US Department of Energy

National Energy Technology Laboratory

Combined Pressure, Temperature Contrast and Surface-Enhanced Separation of Carbon Dioxide for Post-Combustion Carbon Capture

Final Scientific/Technical Report

Reporting Period Start Date: 10/01/2011

Reporting Period End Date: 12/31/2015

Principal Authors:

Zhen Wang, Michael S. Wong*, Mayank Gupta, George J. Hirasaki, Kenneth R. Cox

*Project Director

Phone: 713-348-3511 | E-mail: mswong@rice.edu

Report Issued Date: May, 2016

DOE Award #: DE-FE0007531

Rice University – MS 362

6100 Main St.

Houston, TX 77251-1892

DISCLAIMER

ABSTRACT

The Rice University research team developed a hybrid carbon dioxide (CO_2) absorption process combining absorber and stripper columns using a high surface area ceramic foam gas-liquid contactor for enhanced mass transfer and utilizing waste heat for regeneration. This integrated absorber/desorber arrangement will reduce space requirements, an important factor for retrofitting existing coal-fired power plants with CO_2 capture technology.

Described in this report, we performed an initial analysis to estimate the technical and economic feasibility of the process. A one-dimensional (1-D) CO_2 absorption column was fabricated to measure the hydrodynamic and mass transfer characteristics of the ceramic foam. A bench-scale prototype was constructed to implement the complete CO_2 separation process and tested to study various aspects of fluid flow in the process. A model was developed to simulate the two-dimensional (2-D) fluid flow and optimize the CO_2 capture process. Test results were used to develop a final techno-economic analysis and identify the most appropriate absorbent as well as optimum operating conditions to minimize capital and operating costs. Finally, a techno-economic study was performed to assess the feasibility of integrating the process into a 600 megawatt electric (MWe) coal-fired power plant. With process optimization, $82/MWh of COE can be achieved using our integrated absorber/desorber CO_2 capture technology, which is very close to DOE's target that no more than a 35% increase in COE with CCS. An environmental, health, and safety (EH&S) assessment of the capture process indicated no significant concern in terms of EH&S effects or legislative compliance.

TABLE OF CONTENTS

EXECUTIVE SUMMARY

Rice University researchers developed a new concept to capture CO_2 from coal-fired power plants and hypothesized lower capital and operating costs compared to the conventional amine-based process by combining absorber and stripper columns into a single, integrated process unit.

It was determined that ceramic foam with highly-interconnected structures is an appropriate material to accomplish the integration of the absorber and desorber into a single unit. The hydrodynamic and mass transfer studies of α-Al_2O_3 ceramic foam demonstrated that 20-ppi ceramic foam has a better hydrodynamic and mass transfer performance than random packings (*e.g.*, 25-mm Raschig rings). A 1-D mathematical model was developed to simulate the gas/liquid flow and CO_2 absorption in 1-D ceramic foam column. Model predictions agreed well with the experimental results. More than 90% CO_2 removal can be achieved using ceramic foam as packing material.

Based on the experimental and simulation results in 1-D ceramic foam reactor, Rice University successfully designed a stainless steel prototype of integrated absorber/desorber unit and a steam generator, suitable for conducting the proof-of-concept demonstration. CO_2 capture experiments were conducted in this bench-scale prototype with using 30 wt% diglycolamine and simulated flue gas. 90 percent CO_2 removal is achievable under the selected gas and liquid flow conditions. Following the demonstration studies, a 2-D model to simulate gas and liquid flow in the integrated absorber/desorber unit was developed to perform a parametric sensitivity analysis and process optimization. The operating parameters include operating parameters such as CO_2 lean solvent loading, stripper operating temperature and gas flow rate to liquid flow rate ratio, and geometric parameters,

such as stripper size, absorber/striper overlapping height and membrane thickness.

Rice University evaluated the impact of a series of solid catalysts to enhance the decomposition of MEA-CO_2 complex during regeneration of MEA. Pure metal oxides MoO_3, V_2O_5, and WO_3 and supported metal oxide (on γ-Al_2O_3) have shown to be promising catalytic materials as they increased CO_2 release up to 70% during stripping of CO_2 from MEA. It was also found that γ-Al_2O_3 helps in mitigating this issue/problem. The lowest leaching was observed for WO_x/γ-Al_2O_3, indicating prospects for improved catalyst design that fully stop the leaching.

Finally, a techno-economic evaluation (TEA) of a subcritical PC power plant with integrated absorber/desorber ceramic foam CO_2 capture process was completed. Integrated absorber/desorber CO_2 capture shows a higher net plant efficiency of 30.10%, than conventional Fluor Econamine CO_2 capture (27.01%). In terms of COE, integrated absorber/desorber CO_2 capture presents a lower COE of 100.12 $/MWh, than 110.11 $/MWh of the Fluor Econamine CO_2 capture. With optimization of these parameters, 82 $/MWh of COE can be achieved with using integrated absorber/desorber CO_2 capture technology, which is very close to DOE's target that no more than a 35% increase in COE with CCS. This indicates integrated absorber/desorber CO_2 capture is a promising technology for future carbon capture from coal fired power plants.

1. Background

The mission of the U.S. Department of Energy/National Energy Technology Laboratory (DOE/NETL) Carbon Capture Research & Development (R&D) Program is to develop innovative environmental control technologies to enable full use of the nation's vast coal reserves, while at the same time allowing the current fleet of coal-fired power plants to comply with existing and emerging environmental regulations. The Carbon Capture R&D Program portfolio of carbon dioxide (CO_2) emissions control technologies and CO_2 compression is focused on advancing technological options for new and existing coal-fired power plants in the event of carbon constraints.

Pulverized coal plants burn coal in air to generate steam and comprise 99 percent of all coal-fired power plants in the United States. Carbon dioxide is exhausted in the flue gas at atmospheric pressure and a concentration of 10 to 15 percent by volume. Post-combustion separation and capture of CO_2 is a challenging application due to the low pressure and dilute concentration of CO_2 in the waste stream, trace impurities in the flue gas that affect removal processes, and the parasitic energy cost associated with the capture and compression of CO_2. Post-combustion CO_2 control technologies include the use of solvents, solid sorbents, and membranes, alone or in beneficial combinations. Improvement in the performance of these technologies as well as the development of novel cost-effective processes using these technologies are key to affordable carbon capture for coal-fired power plants.

2. Project description and objective

Rice University proposed to develop a novel gas absorption process for CO_2 capture. The unique process combines the absorber and desorber columns, separated by a microporous ceramic membrane, into a single integrated unit. Conventional CO_2 capture processes consist of a column that absorbs CO_2 with a liquid solvent, and a separate column that desorbs CO_2 from the solvent. The integrated absorber/desorber arrangement would reduce space requirements, an important factor for retrofitting existing coal-fired power plants with CO_2 capture technology.

This novel capture process would use ceramic foam contactors with complex, highly-interconnected structures for the absorption and desorption of CO_2. The ceramic gas-liquid contactors have favorable characteristics for mass transfer with large geometric surface areas, up to ten times that of conventional packing. Additionally, the contactors would be chemically functionalized by solid catalysts (*e.g.* metal oxides) to enhance CO_2 desorption, to achieve lower heats of regeneration using commercially available solvents. In the integrated unit, a microporous ceramic membrane would allow for selective permeation of the CO_2-rich liquid from the absorber section through the membrane and into the CO_2 desorbing side. The desorber section could be operated under moderate vacuum to separate the CO_2 from the solvent at reduced temperatures, which provides the cost-saving advantage of using low-grade heat from the plant.

The unique features of this CO_2 capture process have the potential to reduce the capital and operating costs as well as the resulting cost of electricity with carbon capture at coal-fired power plants. An integrated absorber and desorber unit would result in significant reductions in capital costs, and the use of high-geometric

surface-area packing, along with surface enhancement by functionalization, could reduce the size of the contacting towers. The use of waste heat—instead of high quality steam—for solvent regeneration would reduce the parasitic load for the power plant and lead to a reduction in operating costs.

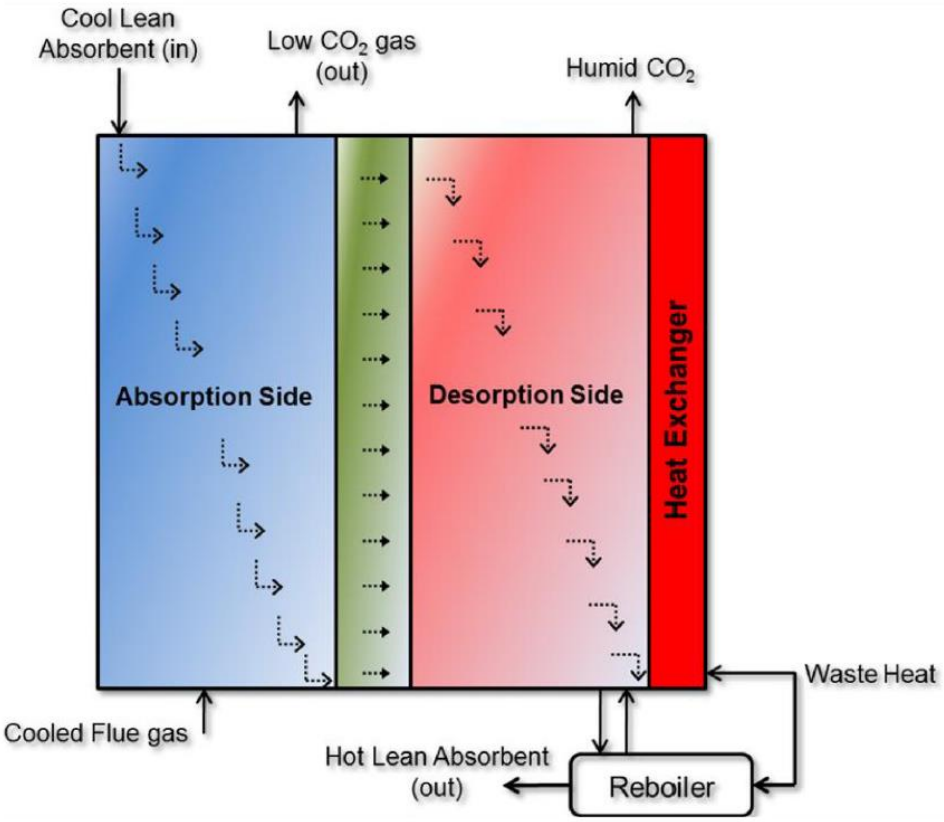

Fig. 2-1 Schematic representation of combined absorber and stripper unit

The primary project goal was to develop, test, and optimize (at bench scale) a novel gas separation process with the potential to reduce the cost of CO_2 capture from coal-fired power plants and meet the DOE goals of capturing 90 percent of the CO_2 with less than a 35 percent increase in the cost of electricity. The specific project objectives were to (1) develop a CO_2 capture process that uses a single integrated unit that combines the absorber and desorber columns, (2) study the

hydrodynamic and mass transfer performance on different grades of un-functionalized ceramic foam, (3) catalyze the CO_2 desorption in ceramic gas-liquid contactors for enhanced gas desorption, and (4) develop a 2-D model to simulate the CO_2 absorption process and optimize the operation to attain the best process performance. Additional objectives were to assess the technoeconomic feasibility of the process using the model experimental and simulation results and the EH&S impact.

3. Gas-liquid heat and mass transfer studies on un-functionalized ceramic foam

We have laid out the theoretical concepts for designing a novel process consisting of an integrated absorber and stripper for the removal of carbon dioxide (CO_2) from coal fired power plant flue gas. The key to advancing these theoretical concepts into a demonstrable bench-scale process is the choice of suitable advanced process materials.

A rigorous search was conducted to determine suitable materials, the outcome of which was the discovery of a class of materials called ceramic foams. Ceramic foams are highly porous cellular ceramic structures. Fig. 3-1 shows a sample of commercial alumina (Al_2O_3) foam. Ceramic foams can be made by a variety of methods. However, the most common approach to manufacturing ceramic foams on a commercial scale is to coat a sample of open cell polyurethane (PU) foam template of required shape and dimensions with a slurry of the required ceramic material followed by removal of the foam template by pyrolysis. Alumina (Al_2O_3) is the most frequently used ceramic, though others such as zirconia (ZrO_2), silicon carbide (SiC) can be used for specialized applications.

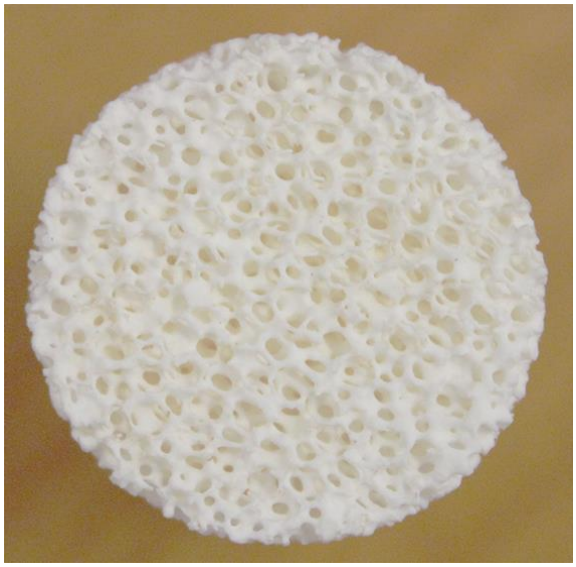

Fig. 3-1 Endview of the α-Al_2O_3 ceramic foam

Table 3-1 shows a comparison between the ceramic foams and several commonly used tower packing materials.

Table 3-1. Structural parameters for different packings

Packing Type	Structure	Porosity (%)	Specific surface area (m^2/m^3)	Bulk density[a] (g/cm^3)	Equivalent pore diameter (mm)	Permeability[b] (m^2)
α-Al_2O_3 Ceramic Foam	20-PPI	85	700	0.60	1.28	8.0×10^{-9}
	30-PPI	85	900	0.65	1.00	7.3×10^{-9}
	45-PPI	84	1400	0.71	0.60	6.2×10^{-9}
Random Packing[20]	Raschig Ring	62.6	239	0.58	1.5	3.87×10^{-8}

	Pall Ring	94.2	232	0.48	2.5	3.53×10^{-7}

(a) Data are available at www.ask-chemicals.com and http://www.tower-packing.com;

(b) Permeability of packing was calculated using $k=\frac{3\varepsilon d_e^{\,2}}{50}$, the parameters and units of this equation can be found in the Nomenclature section.

Clearly, ceramic foam has a significantly higher geometric surface area as compared to conventional packing. The higher of pores per inch (ppi) number, geometric surface area of the ceramic foam is higher. Since, the rate of mass transfer is proportional to the gas-liquid interfacial surface area; a greater geometric surface area in the tower packing promotes better mass transfer. Thus, ceramic foams possess all the features required of the gas-liquid contacting material. Having selected ceramic foam as the material of choice for gas-liquid contacting, the next logical step in process development is to characterize the ceramic foam for its hydrodynamic and mass transfer behavior.

3.1 Design of a 1-D experimental setup for studying hydrodynamic behavior of ceramic foam

Selection of a tower packing material for gas absorption operation is an optimization problem with several variables to consider. Some of the factors considered are the geometric surface area of the packing material, pressure drop, hydrodynamic behavior under different gas-liquid flow conditions and corrosion resistance. The geometric surface of packing materials increases by reducing the void fraction or pore sizes. However, as the void fraction and pore-sizes decrease;

the resistance offered by the packing material to fluid flow which results in greater pressure drops.

In commercial operation, it is often economical to operate a column at gas and liquid flow-rates close to their maximum limits. One of the main constraints on determining this limit is the hydrodynamic behavior of the packing material; more specifically, the flooding point. Flooding in case of an absorption or distillation column is the condition at which the vapor flow-rate and the pressure drop in the column is large enough to disrupt the unhindered downward flow of liquid. When it is flooded, liquid entrainment begins to take place in the column which results in a sharp increase in the differential pressure in the column and a reduced separation efficiency. It is clear from this description of flooding that increasing the surface area of tower packing by reducing the void fraction and pore size will result in lowering of the flooding point - an unfavorable characteristic. It is clear from this discussion that while ceramic foams possess several favorable characteristics; developing an understanding of their hydrodynamic behavior is critical to further development of the novel process.

Experimental setup

In order to study the hydrodynamic behavior of the ceramic foams, a simple experimental setup was developed in-house. We have designed an experimental setup consisting of a glass column, a gas and liquid flow control system and an analytical setup for conducting the hydrodynamic and mass transfer studies on the ceramic foam. The details of this experimental setup are given below.

Figure 3-2 shows a schematic representation of the experimental setup designed for studying the hydrodynamic characteristics of ceramic foam. The experimental

setup involves a glass tube with an ID of 1.1’’. The glass tube is designed to encase 7 foam plugs, each of which is 2’’ in length with 2’’ headspace at the top and 1’’ space at the bottom. Ceramic foam plugs composed of 99.5% α-alumina (Al_2O_3) with 1’’ diameter and 2’’ length were ordered from Ask-Chemicals, Alfred, NY. Three different grades of ceramic foams – 20, 30 and 45 ppi (pores-per-inch) were procured out of which two – 20 and 30 ppi have been tested. 6 foam plugs of the same grade were wrapped tightly, end-to-end in heat-shrink Teflon tubing to prevent the bypass of gas or liquid on the side of ceramic foam plugs. The 7^{th} foam is used as a “sacrificial” plug – it serves to hold the water build up due to capillary end effects in the foam plugs. The 7^{th} foam plug is inserted into the glass tube below the 12’’ long rod. Both the 12’’ rod and the 7^{th} foam plug are held in place using Viton fluoroelastomer O-rings (Dash #21). The O-rings prevent the bypass of gas or liquid through any empty spaces between the glass walls and the ceramic foam rod.

Nitrogen gas (N_2) was introduced above the last plug from the bottom. In order to prevent any escape of the entering gas with the exiting liquid, a plastic graduated cylinder was added to the experimental setup as shown to provide a “liquid seal”. The “liquid seal” works by providing a static head of water which acts as a very low pressure back pressure regulator and prevents the escape of inlet gas through the liquid outlet port. Pressure drop across the column was measured using a water manometer built in-house. Since water is used as the manometer fluid, pressure differences as low as 20 Pa can be detected. This degree of sensitivity is particularly important with our experimental setup due to the relatively short column of packing and the low pressure drops encountered in such porous materials.

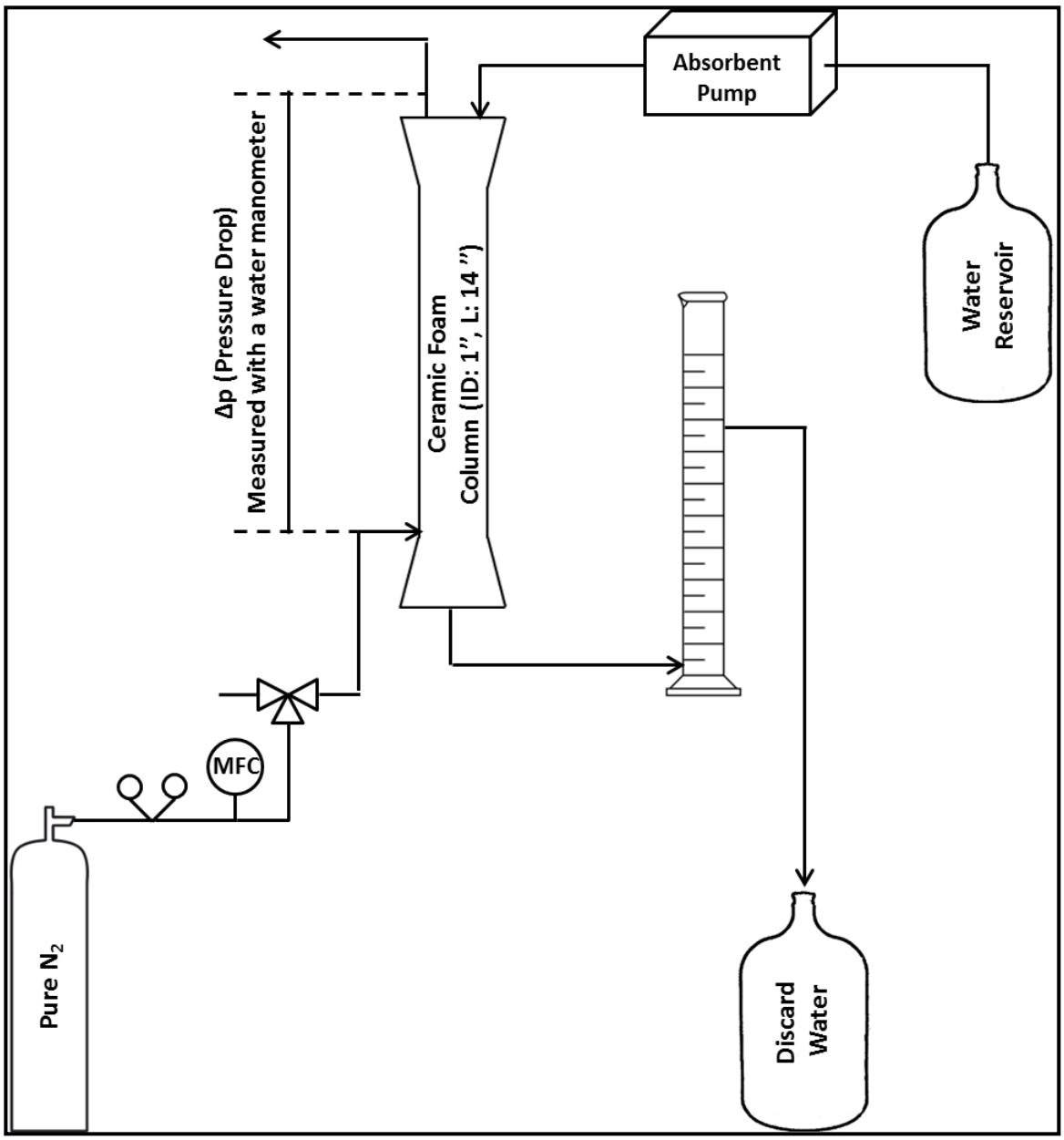

Fig.3-2 Schematic of experimental setup used for conducting hydrodynamic studies

Water was delivered to the column using a peristaltic pump (FPU500, FPUMT) supplied by Omega Engineering. Liquid was distributed on the ceramic foam with a piece of stainless steel wool at the top of the ceramic foam column. Nitrogen (N_2) supplied by Matheson TRIGAS was used as the feed gas for conducting the

hydrodynamic experiments. Gas flux was controlled accurately using a mass flow controller (MFC) (FMA6528ST) manufactured by Omega Engineering.

Experimental Procedure

Figure 3-3 is the photo of experimental setup for studying the hydrodynamic behavior of ceramic foams. When studying the hydrodynamic behavior of ceramic foam, the key parameters of interest are the dependence of pressure drop on gas and liquid flux and the flooding behavior of the material. Flooding in case of tower packing is defined as the condition in operation of a tray or packed column when the energy potential of the vapor is greater than that of the liquid which results in the liquid reversing the direction of flow from downwards to upwards with the gas flow. The flooding point can typically be determined by a change in the slope of the pressure drop vs. gas flux curve.

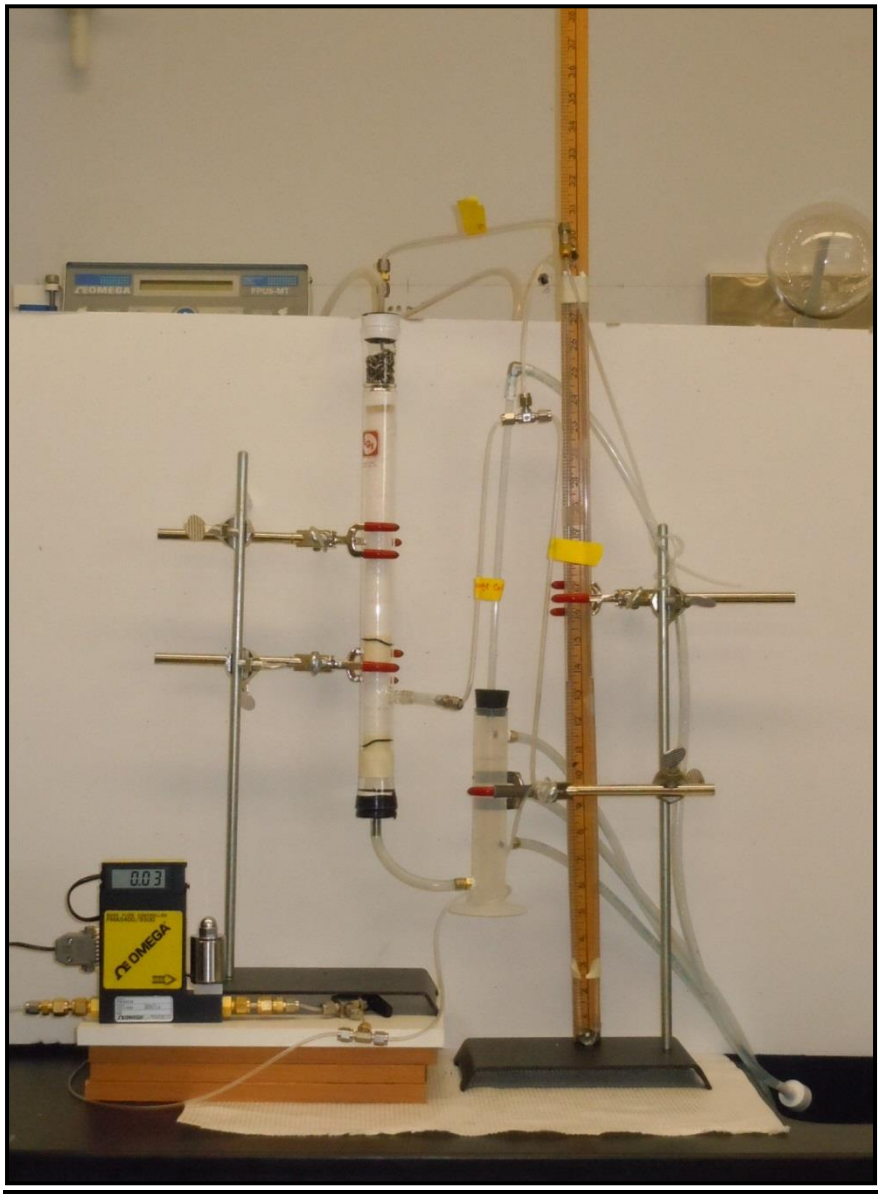

Figure 3-3: Photo of experimental setup for studying the hydrodynamic behavior of ceramic foams

As a part of this study, we explored ceramic foam hydrodynamics between a wide range of gas and liquid flux. The gas flux was varied between 0 and 9 standard liters per minute (SLPM) and the liquid flowrate was varied between 0 and 0.1 liters per minute (LPM). The range of values was selected on the basis of the potential gas and liquid flux that are of interest for a later proof-of-concept

demonstration. When performing the experiments, the gas flux was held constant at a specific value and the liquid flux was varied. For each flux, it was ensured that the system was operationally stable for at least 20 minutes. Pressure drops in the column corresponding to these operating conditions were recorded after the water levels in the manometer reached steady state.

Since pressure drops in the ceramic foams are small, it is important to account for all external sources of pressure drop that contribute to the experimentally measured values. The most important of these factors are the tubing and fittings that are a part of the experimental setup. To quantify the value of these pressure drops, we conducted measurements on the empty glass tube with fittings and tubing unchanged from the hydrodynamic measurements. As before, the gas flux is varied to measure the corresponding pressure drop values. The pressure drop measurements conducted on the ceramic foam are then corrected for these external pressure drop resistances to derive the contribution of the ceramic foams to the pressure drop.

3.2: Studies on hydrodynamic behavior of ceramic foam

Experimental Results

Figure 3-4 is a plot of the pressure drop versus flow-rate for 45 ppi alumina foam for the range of gas and liquid flow-rates measured as a part of this study. As can be seen in the plot, the pressure drop per meter of packing varies linearly with the gas flow-rate. Under the conditions explored in this study, we found that liquid flow-rate has little effect on the pressure drop in the ceramic foam column.

Under all the operating conditions explored, no flooding behavior was observed in this ceramic foam column; suggesting that flooding point had not been reached and the system was within the limits of operating conditions. Assuming a linear relationship between pressure gradient and gas flow-rate till the flooding point is reached allows for the estimation of the flooding point gas flow-rate by balancing the pressure gradient with the product of fluid density and gravitational acceleration. This is expressed in Equation 3-1.

$$\frac{dp}{dx} = \rho \cdot g \qquad (3\text{-}1)$$

For diglycolamine, ρ =1040 (kg/m_3) at 100 ^{o}F. This results in an approximate flooding point pressure gradient (dp/dx) of 10202.5 (Pa/m). Linear extrapolation of the experimental data in Figure 3-4 for the liquid flow-rate of 0.1 liter per minute (LPM) results in a mass flux of 0.93 kg-$m^{-2}S^{-1}$ at the approximate flooding point for the 45 ppi ceramic foam. For the 2.8 centimeter (cm) diameter glass column, this corresponds to a gas flow-rate of 22.5 standard liters per minute (SLPM). Figure 3-4 is a plot of the pressure drop versus flux for 30 ppi alumina foam. Comparing Figures 3-4 and 3-5 clearly shows that the 45 ppi grade ceramic foam has a greater pressure drop as compared to the 30 ppi grade material. This is clearly a result of an increase in the size of the macropores in the latter material. Performing the same calculation for pressure gradient and corresponding vapor flow-rates results in a flooding point gas flow-rate of 28.1 standard liters per minute (SLPM) or a mass flux of 1.16 kg-$m^{-2}s^{-1}$.

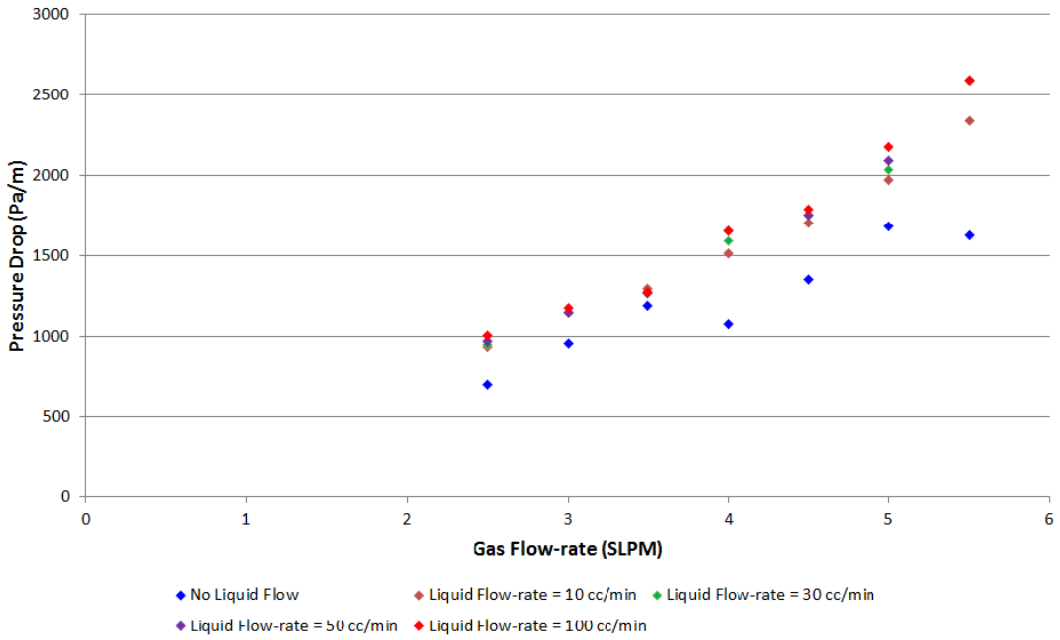

Fig. 3-4 Pressure drop in 45 pores per inch (ppi) ceramic foam at varying gas and liquid flow-rates

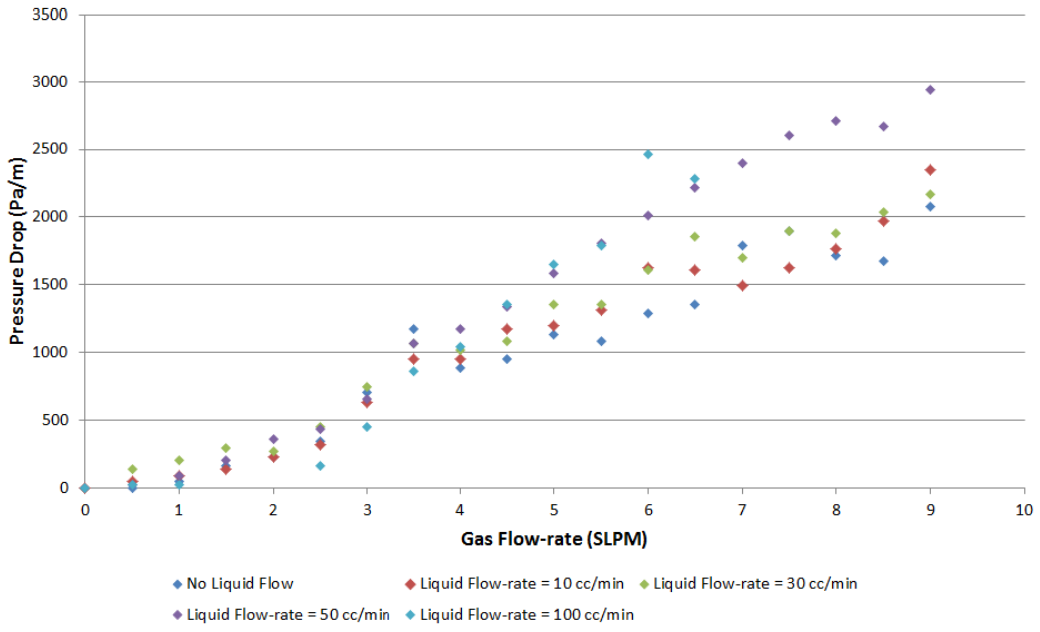

Fig.3-5 Pressure drop in 30 pores per inch (ppi) ceramic foam at varying gas and liquid flow-rates

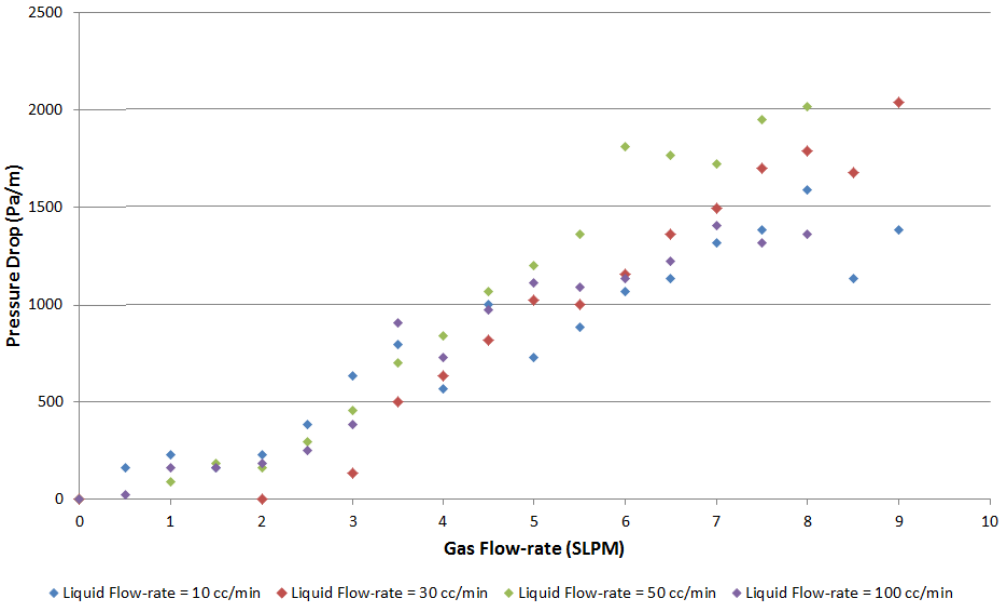

Fig. 3-6 Pressure drop in 20 pores per inch (ppi) ceramic foam at varying gas and liquid flow-rates

Figure 3-6 shows the dependence of pressure gradient on the gas and liquid flow-rates for 20 pores per inch (ppi) grade alumina foam. Clearly, there is a noticeable decrease in the pressure drop as compared to the 30 and 45 pores per inch (ppi) samples due to an increase in the size of the macropores in the foam. Using the same methodology for estimating flooding point yields a flooding point at a gas flow-rate of 33.5 standard liters per minute (SLPM) or a gas mass flux of 1.385 kg-$m^{-2}s^{-1}$.

We have compared the values measured as a part of our study with those reported for 40 pores per inch (ppi) metal foams in published literature. The pressure drops for metal foams are roughly $1/10^{th}$ as compared to our measurements [1]. This can be attributed to the higher thickness of struts in alumina foam as compared to those in metal foams. Thicker struts result in smaller pores and lower porosity which eventually results in greater pressure drops in the

column. Strut thickness is a variable that can be controlled during the manufacture of ceramic foam and thus a factor that can be worked upon with the ceramic foam manufacturer. Optimized ceramic foam materials will result in significantly lower pressure drops than what we are currently using for our studies. This would also mean significantly higher gas-flux at the flooding point. In conclusion, we remark that commercially available ceramic foams performed satisfactorily in the hydrodynamic studies. Next, we conduct experimental studies to determine the mass transfer performance of ceramic foams using simulated flue gas and aqueous diglycolamine (DGA).

3.3: Studies on mass transfer behavior of ceramic foam

When selecting tower packing for gas absorption operation, in addition to the hydrodynamic properties; mass transfer performance plays a critical role. Irrespective of physical or chemical gas absorption, the first step in the process is the transfer of the component of interest from the gas phase to the liquid. The rate of mass transfer from gas to liquid depends on the gas-liquid interfacial surface area and the driving force for mass transfer (difference in concentrations). Increasing the geometric surface of a packing generally increases the rate of mass transfer. The exact magnitude of this change, however, is dependent on several factors such as the actual increase in the interfacial surface area, effect of tower packing fluid flow properties and flow dynamics itself. Since most advanced packing materials such as ceramic foams possess extremely complex 3-dimensional structures; it is impossible to analytically predict their mass transfer performance. In this section, we describe the experiments performed to study the mass transfer behavior of various ceramic foam samples. In addition, we use these

results to start determining the dimensions of a stainless steel prototype that will be developed further for a proof-of-concept demonstration.

Experimental setup

Figure 3-7 is the schematic representation of the experimental setup that we have developed for conducting comparative mass transfer studies between ceramic foam and the reference tower packing – 6 mm Raschig rings. Conceptually, the setup is very similar to the one used for the hydrodynamic studies except we don't need the water manometer in these experiments. As can be seen, the core elements of the setup like the glass column, gas delivery to the column on the side, below the 6^{th} ceramic foam plug from the top haven't been changed.

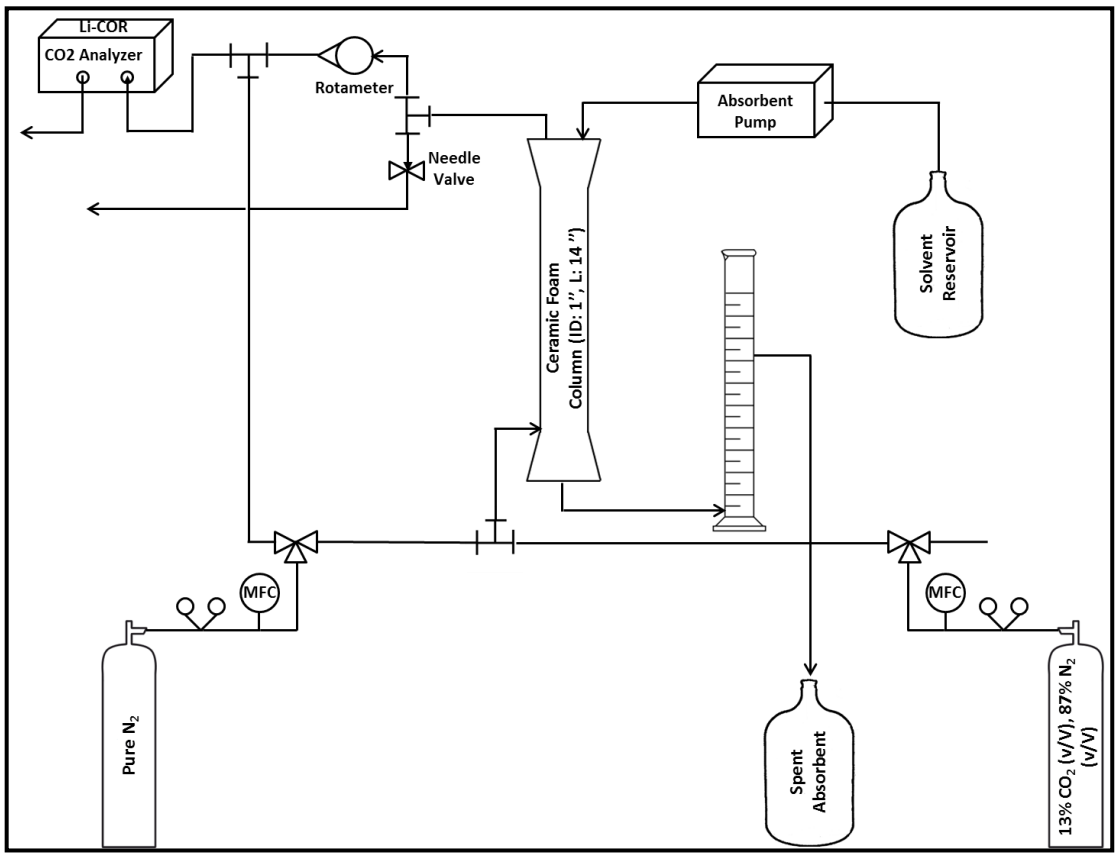

Fig. 3-7 Schematic representation of experimental setup for comparative mass transfer studies

For mass transfer measurements, we are using a CO_2/N_2 mixture with 13% CO_2; balance N_2 supplied by Matheson TRIGAS as the "simulated" flue gas. 30 wt% diglycolamine solution prepared from 99.5% pure diglycolamine agent supplied by Huntsman Chemicals is used as the absorbent. This absorbent solution is delivered from the solvent reservoir on to the ceramic foam plug by a peristaltic pump. Spent absorbent is collected in a carboy for discarding.

As shown in Figure 3-7, gas supply to the glass column can be switched between pure N_2 and simulated flue gas using a 3-way valve. This arrangement has been implemented in order to facilitate purging the air in the glass column before commencing a trial. Outlet gas is analyzed for its CO_2 concentration with a non-

dispersive infrared detector (LI 820) supplied by LI-COR Biosciences. The detector can measure CO_2 concentrations between 0 and 20,000 ppm with 3% accuracy (measured value) and can handle inlet gas flow-rate up to 1 SLPM. Since, the simulated flue gas has a CO_2 concentration of 130,000 ppm; we have implemented a dilution system as shown in Figure 6, wherein we sample a small part of the outlet gas stream from the glass column and dilute it with a known flow-rate of N_2, controlled using a mass flow controller (MFC). The quantity of exit stream being sampled is controlled using a needle valve and measured with a rotameter. The dilution ratio can be calculated using the following equation.

$$D = \frac{(\dot{Q}_{N2} + \dot{Q}_{sample})}{(\dot{Q}_{sample})} \qquad (3\text{-}2)$$

In the above equation, D is the dilution ratio, $\dot{Q}_{N2}$ is the Nitrogen (N_2) flow-rate and $\dot{Q}_{sample}$ is the flow-rate of sampled exit gas.

Experimental Method

When conducting the comparative mass transfer studies to evaluate the effectiveness of ceramic foam and Raschig rings, the key parameter of interest is the degree of CO_2 removal under the same operating conditions (i.e. gas and liquid flux). Even if the geometric surface areas of the two packing materials are known to be the same, their surface properties, composition, geometry and arrangement in the column are critical factors that affect the extent of mass transfer.

As a part of this study, we have conducted the comparison between ceramic foam and Raschig rings under 2 different conditions of gas and liquid flux. These are:

(a) Gas flow-rate = 3 standard liter per minute (SLPM), Liquid flow-rate = 0.02 liter per minute (LPM)

(b) Gas flow-rate = 5 standard liter per minute (SLPM), Liquid flow-rate = 0.04 liter per minute (LPM)

The gas to liquid ratio in both these cases is similar to that maintained in industrial scale absorbers. In addition, we conduct trials at the above gas and liquid flux with 30 wt% and 60 wt% diglycolamine (DGA) solutions respectively to study the effect of absorbent concentration on the degree of CO_2 pickup.

Before commencing a trial, we purge the ceramic foam column with pure N_2 to remove most of the air and residual CO_2 from previous experiments. Once the CO_2 concentration in the column is down to around 10 ppm, nitrogen flow is stopped and simulated flue gas is introduced into the column while simultaneously switching on the dilution N_2 stream to the detector. In all the trials conducted, a flow-rate of 0.8 SLPM was maintained for the dilution N_2 stream using a mass flow controller. The outlet CO_2 levels measured by the analyzer are recorded using a desktop computer and data acquisition software provided by LI-COR Biosciences. The float level in the rotameter is recorded as a function of time since it is sensitive to fluctuations in the inlet gas flux as well as the composition of the outlet gas. After the experiment is complete, the analyzer is purged with the dilution N_2 stream till CO_2 levels are down to almost zero.

Experimental Results

Figure 3-8 shows a plot of the comparison of the degree of carbon dioxide (CO_2) pickup taking place in a 30.5 centimeters (cm) long glass column filled with 45

pores per-inch (ppi) and 20 pores per inch (ppi) ceramic foams and 6 millimeter (mm) Raschig rings corresponding to a gas flow-rate of 3 standard liters per minute (SLPM), a liquid flow-rate of 0.02 liters per minute (LPM) and an absorbent concentration of 30 wt%. As can be seen from the above plot, the use of 6 millimeter (mm) Raschig rings results in around 60% carbon dioxide (CO_2) pickup, 20 pores per inch (ppi) ceramic foam achieves around 40% removal and 45 pores per inch (ppi) ceramic foam results in only 25% carbon dioxide (CO_2) pickup. The performance of the 20 and 45 pores per inch (ppi) ceramic foams, however, seems contrary to expectations. The 45 pores per inch (ppi) foam sample has almost 2x the geometric surface area that of the 20 pores per inch (ppi) foam. Since a larger geometric surface area is largely a favorable characteristic for good mass transfer, the 45 pores per inch (ppi) foam maybe expected to have a better carbon dioxide (CO_2) removal performance than the 20 pores per inch (ppi) sample. A closer examination of the 45 and 20 pores per inch (ppi) foams reveals that the macropores in the 45 pores per inch (ppi) foam are significantly smaller than the ones in the 20 pores per inch (ppi) sample. Whereas a large geometric surface area can aid in increasing the rate of mass transfer, it is of far greater importance that a high gas-liquid interfacial area be available. We hypothesize that during gas absorption operation, macropores in the 45 pores per inch (ppi) foam - now filled with liquid absorbent offer a smaller interfacial surface area as compared to the 20 pores per inch (ppi) sample. This could result from the presence of insufficient gas in the macropores of the foam or could result from a segregation of flow, wherein there is almost a separate flow of gas and liquid through the pores of the foam resulting in poor mass transfer. The 20 pores per inch (ppi) foam has a relatively poorer performance as compared to the 6 millimeter (mm) Raschig rings even

though their geometric surface areas are comparable. We believe this is also a result of the smaller pore spaces for gas-liquid flow in the ceramic foam as compared to the 6 millimeter (mm) Raschig rings.

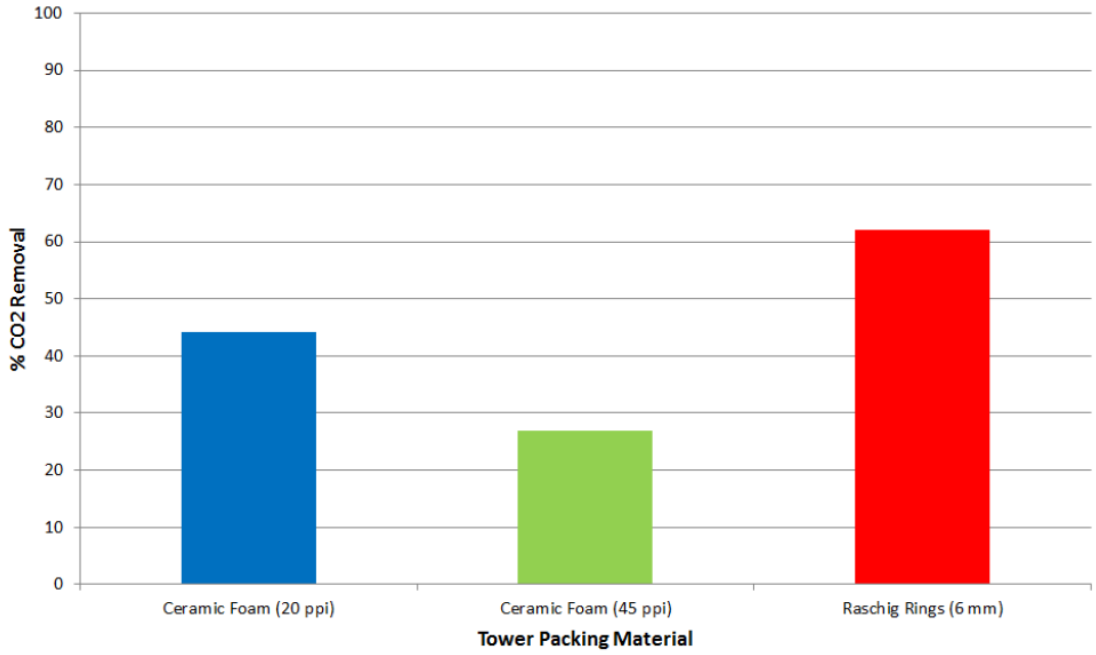

Fig. 3-8 Degree of CO_2 pickup with different tower packing (30 wt% DGA, gas at 3 SLPM, liquid at 0.02 LPM)

Figure 3-9 shows a comparison of the degree of carbon dioxide (CO_2) removal with the use of 20 pores per inch (ppi) ceramic foam and 6 millimeter (mm) Raschig rings. These experiments are conducted at a gas flow-rate of 5 standard liter per minute (SLPM), a liquid flow of 0.04 liter per minute (LPM) and absorbent concentration of 30 wt% diglycolamine (DGA). As can be seen from the plot, there is a slight change in the degree of carbon dioxide (CO_2) removal by both the ceramic foam and the Raschig rings. Whereas the ceramic foam shows a reduction in the carbon dioxide (CO_2) pickup (by around 7%), the Raschig rings exhibit an increase of around 5% in the carbon dioxide (CO_2) uptake. We believe

that the explanation for this lies in the experimental conditions in the bench-scale column in which the experiments are being conducted.

When the gas flow rate is changed from 3 standard liter per minute (SLPM) to 5 standard liter per minute (SLPM), the residence time of the gas in the column reduces by 40%. A smaller time for gas-liquid contacting will result in lesser uptake of carbon dioxide (CO_2). However, the flow-rate of the absorbent solution is doubled as well which results in an increased carbon dioxide (CO_2) uptake. With two competing factors are play, the effectiveness of mass transfer depends on good gas-liquid contacting and the presence of sufficient interfacial surface area. We suggest that the smaller pore spaces in ceramic foam as compared to Raschig rings result in the observed changes in the carbon dioxide (CO_2) uptake.

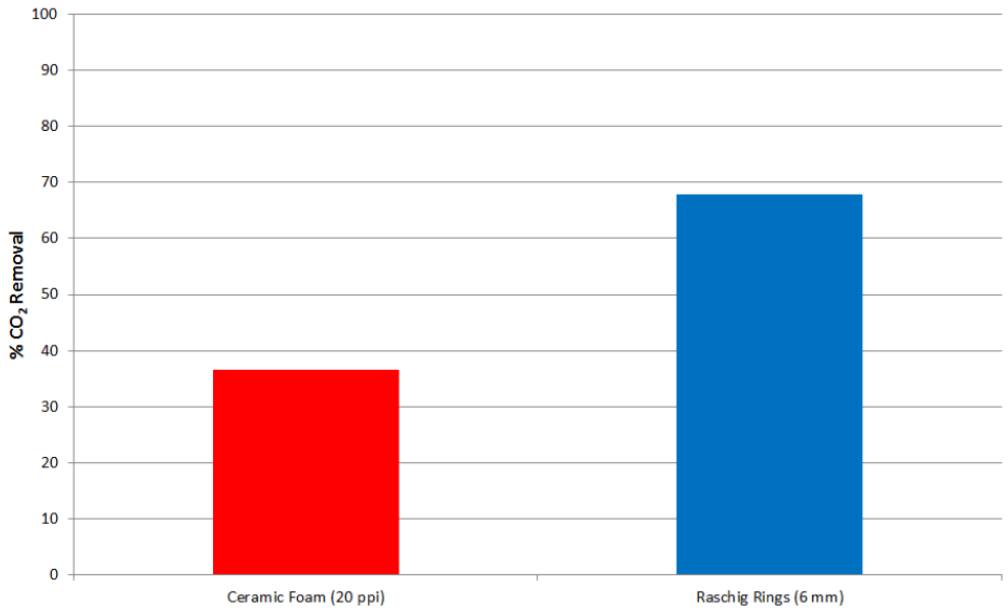

Fig. 3-9 Degree of CO_2 pickup with different tower packing (30 wt% DGA, gas at 5 SLPM, liquid at 0.04 LPM)

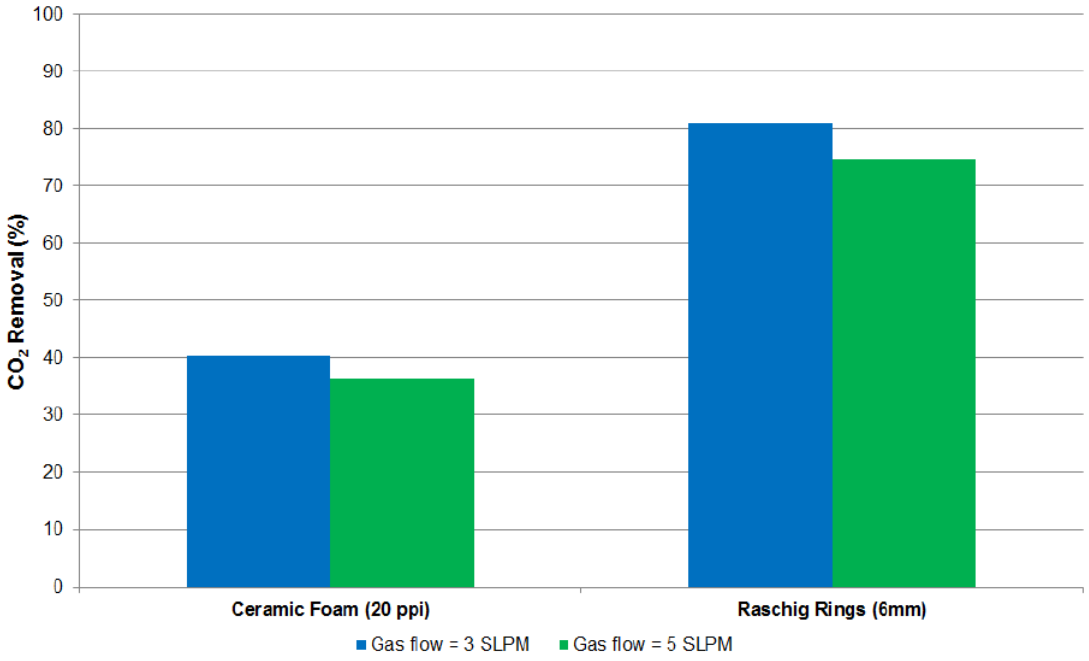

Fig. 3-10 Degree of CO_2 pickup with different tower packing (60 wt% DGA, gas at 3 & 5 SLPM, liquid at 0.02 & 0.04 LPM)

Figure 3-10 shows a comparison of the degree of carbon dioxide (CO_2) uptake with 60 wt% diglycolamine (DGA) as the absorbent with gas flow-rates at 3 and 5 standard liter per minute (SLPM) and liquid flow-rate of 0.02 and 0.04 liter per minute (LPM). In the first case of lower gas and liquid flow-rates, carbon dioxide (CO_2) pickup with the ceramic foam sample is almost the same as that with 30% diglycolamine (DGA) whereas that with Raschig rings increases by around 30%. In the latter case involving higher gas and liquid flow-rates, we observe that the 20 pores per inch (ppi) ceramic foam picks up around 36% of the entering carbon dioxide (CO_2) whereas the Raschig rings result in around 74% pickup. An increase in the amine concentration can normally be expected to increase the extent of carbon dioxide (CO_2) uptake except under a scenario where the degree of carbon dioxide (CO_2) removal isn't limited by the availability of unreacted amine

molecules. This effect can clearly be observed in the case of Raschig rings, however in case of ceramic foam the carbon dioxide (CO_2) uptake surprisingly exhibits no change. Industrial absorbers are suitably optimized to maintain operating conditions to minimize mass transfer resistances in both gas and liquid phases. In case of carbon dioxide (CO_2) absorption, liquid phase resistances are crucial in particular since the carbon dioxide (CO_2) must first dissolve in the liquid absorbent and then undergo hydration to be able to react with the amine. The experimental conditions in the bench-scale apparatus we have setup in our lab are not optimized. Results from the carbon dioxide (CO_2) absorption experiments conducted thus far suggest the presence of liquid phase mass transfer resistances in the ceramic foam system and to a lesser extent in the Raschig ring setup. Thus, an increase in the amine concentration fails to have any significant effect on the extent of carbon dioxide (CO_2) removal in ceramic foam system. This clearly suggests that carbon dioxide (CO_2) absorption is limited by its mass transfer from gas to liquid as opposed to the unavailability of unreacted amine molecules. In case of Raschig rings, mass transfer does not appear to be a significant limiting factor likely due to the larger macro-pores. Consequently, an increase in the diglycolamine (DGA) concentration results in an increase in the carbon dioxide (CO_2) uptake rate.

3.4 Optimization design of CO2 absorption in a ceramic foam column

The results presented in 3.3 describe the mass transfer characteristics of the 20 pores per inch (ppi) ceramic foam. However, in all the cases considered; the degree of carbon dioxide (CO_2) removal is less than 90%. Thus, further experiments

needed to be performed to determine the gas-liquid flow-rates and the height of ceramic foam sufficient for removal of 90% of the inlet carbon dioxide (CO_2). It is important to clarify at this point that a proof-of-concept prototype is far from optimized. Thus, the gas-liquid flow-rates used in this design study for achieving 90% carbon dioxide (CO_2) removal are not representative of the performance of an optimized system.

The experimental setup used for conducting these studies and experimental procedure have been described previously. For all experiments, 30 wt% diglycolamine (DGA) was used as the absorbent. The key parameter of interest in these studies is the dependence of the degree of carbon dioxide (CO2) removal on (i) gas flow rate, (ii) liquid flow rate and (iii) height of ceramic foam packing. As a part of this study, we have compared the performance of 20 pores per inch (ppi) ceramic foams of 4 different lengths under different conditions of gas and liquid flow. These are:

1) Ceramic foam lengths = 10.2, 15.2, 20.3 and 25.4 centimeters (cm)

2) Gas flow-rate = 0.25 standard liter per minute (SLPM), Liquid flow-rate = 0.01, 0.02, 0.03 liter per minute (LPM)

3) Gas flow-rate = 0.50 standard liter per minute (SLPM), Liquid flow-rate = 0.01, 0.02, 0.03 liter per minute (LPM)

4) Gas flow-rate = 0.75 standard liter per minute (SLPM), Liquid flow-rate = 0.01, 0.02, 0.03 liter per minute (LPM)

5) Gas flow-rate = 1.0 standard liter per minute (SLPM), Liquid flow-rate = 0.01, 0.02, 0.03 liter per minute (LPM)

Experimental results

Figure 3-11 is a plot of the comparison of the degree of carbon dioxide (CO_2) pickup in a 20 pores per inch (ppi) ceramic foam column of 10.2 centimeters (cm) length under the different gas and liquid flow conditions listed above. As can be seen, there is a gradual increase in the carbon dioxide (CO_2) removal both as the liquid flowrate is increased and the gas flow rate is decreased. The closest configuration to the required 90% carbon dioxide (CO_2) pickup is at a liquid flow-rate of 0.03 liter per minute (LPM) and a gas flow rate of 0.25 standard liter per minute (SLPM), under which condition, around 80% of the incoming carbon dioxide (CO_2) is removed.

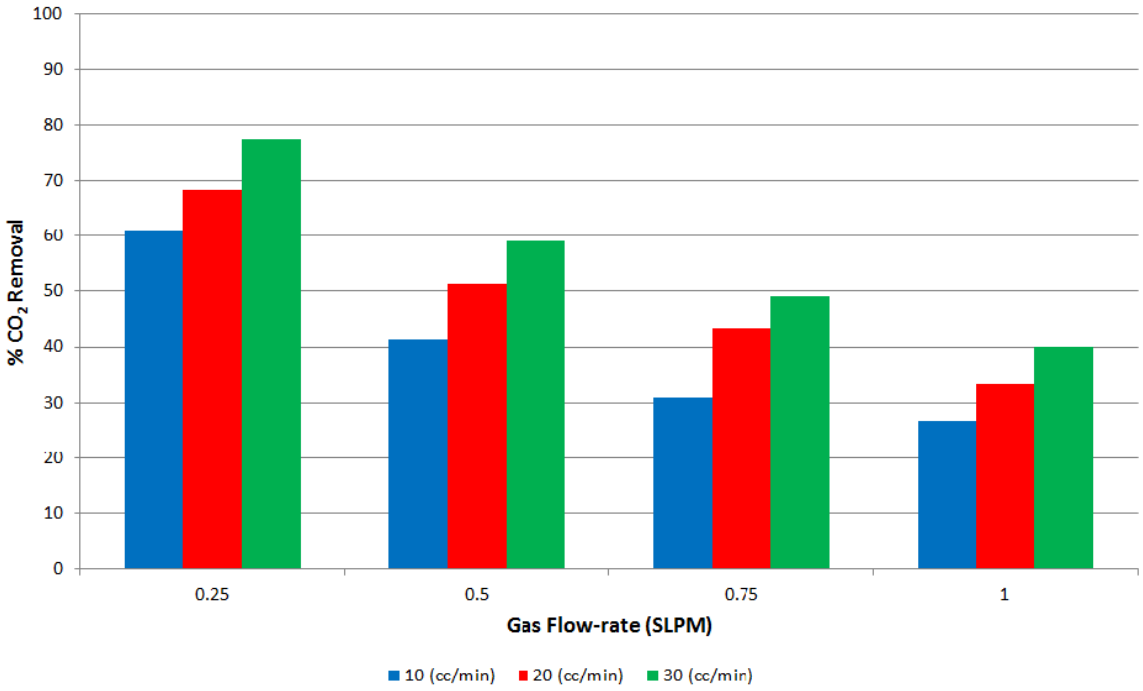

Fig. 3-11 Comparison of CO_2 removal performance under different gas and liquid flow conditions (10.2 cm long ceramic foam column)

Figure 3-12 is a plot of the performance of a 15.2 centimeters (cm) long ceramic foam column for carbon dioxide (CO_2) removal under different gas and liquid flow rates. It can be seen from the plot that the optimal configuration for 90% removal of inlet carbon dioxide (CO_2) is a gas flow-rate between 0.25 standard liter per minute (SLPM) and 0.5 standard liter per minute (SLPM) and liquid flow-rate between 0.02 and 0.03 liter per minute (LPM). Figure 3-13 is a plot of the degree of carbon dioxide (CO_2) removal in a ceramic foam column with a length of 20.3 centimeters (cm).

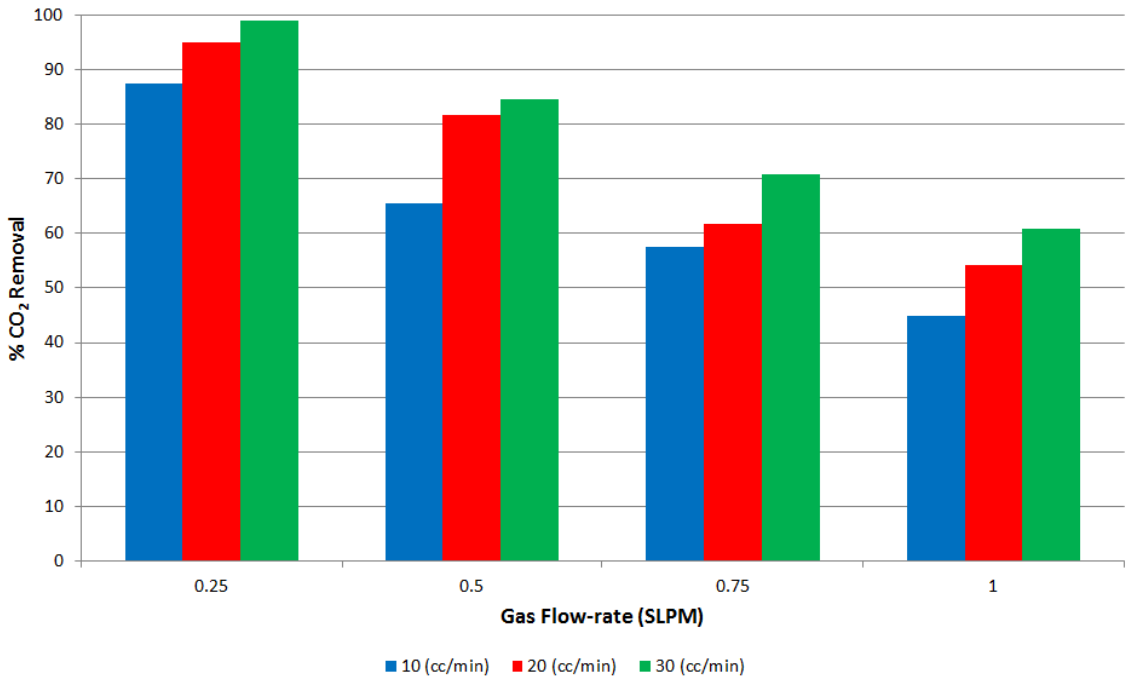

Fig. 3-12 Comparison of CO_2 removal performance under different gas and liquid flow conditions (15.2 cm long ceramic foam column)

The trend observed in the dependence of carbon dioxide (CO_2) removal on gas and liquid flow-rates is consistent with that noticed in Figures 3-12 and 3-13. However, while there is a significant change (increase) in the carbon dioxide (CO_2)

removal with an almost identical change in system conditions between Figures 3-12 and 3-13, there is almost no change in the data represented in Figures 3-12 and 3-13. This suggests that the gains in carbon dioxide (CO_2) removal achieved by adding an extra 5.1 centimeters (cm) of ceramic foam is minimal.

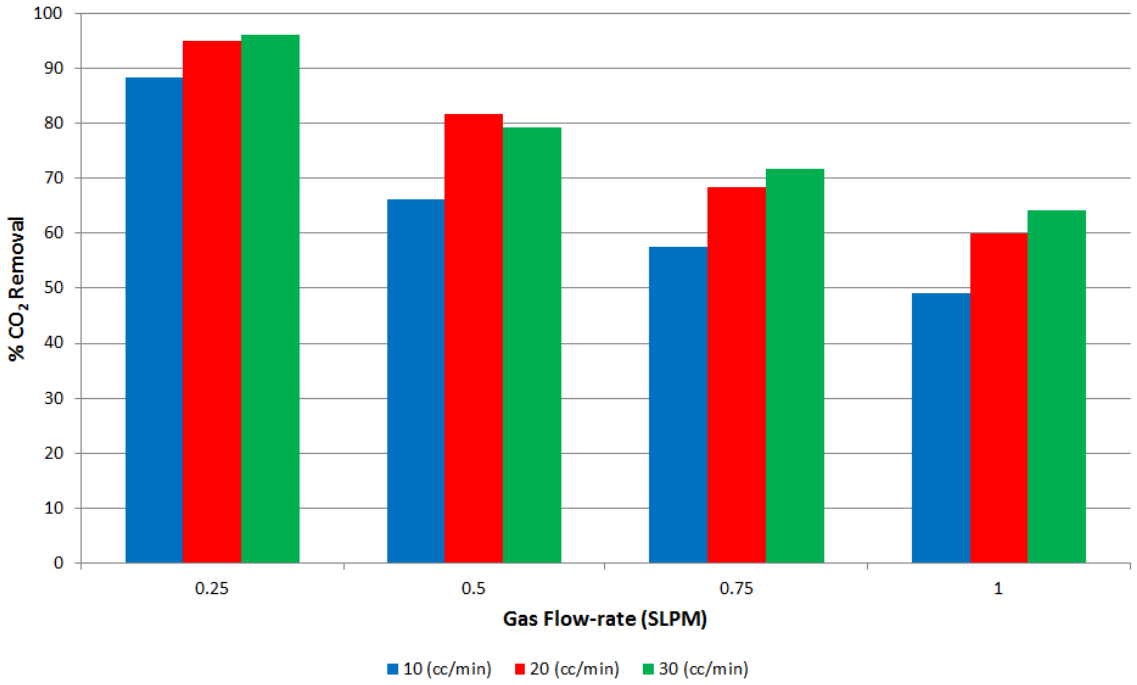

Fig. 3-13 Comparison of CO_2 removal performance under different gas and liquid flow conditions (20.3 cm long ceramic foam column)

Figure 3-14 is a plot of the degree of carbon dioxide (CO_2) removal with a ceramic foam column of 25.4 centimeters (cm) length. As seen, there is only a marginal improvement in carbon dioxide (CO_2) pickup with the addition of the 5.1 centimeters (cm) ceramic foam plug to the 20.3 centimeter (cm) column used previously. Clearly, the addition of tower packing had little effect in increasing the removal of carbon dioxide (CO_2). This can be attributed to the macro-structure and

the size of pore-spaces in the ceramic foam. The porespaces in ceramic foam are significantly smaller than those in the 6 millimeter (mm) raschig rings. The smaller pores in ceramic foam can result in liquid flow that is dominated by surface tension as compared to gravity. An outcome of this is be the channeling of liquid absorbent in the ceramic foam which could result in the observed, poor mass transfer performance in spite of large geometric surface area

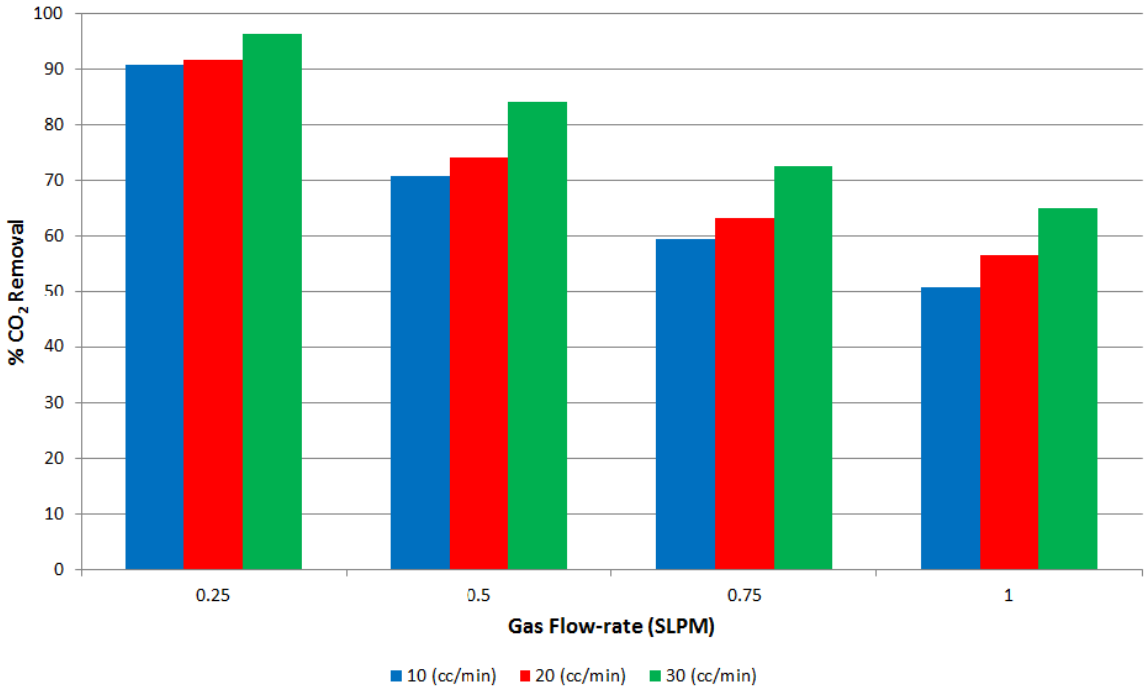

Fig.3-14 Comparison of CO_2 removal performance under different gas and liquid flow conditions (25.4 cm long ceramic foam column)

4. Design, fabrication and setup of stainless steel prototype of the combined absorption/desorption unit

We worked with the Rice Advanced Design Center to design a stainless steel prototype and a steam generator, suitable for conducting the proof-of-concept demonstration. The design work was completed in January 2013, after which the design was used by the Rice University Machine shop for fabricating the actual prototype. The design sheets for the stainless steel prototype and the steam generator were generated by LumaDyne.

5. CO_2 capture demonstration in the bench-scale stainless steel combined absorber/desorber setup

5.1 Development of the experimental prototype

From the experiments conducted and described previously, we have concluded that in order to achieve 90% carbon dioxide (CO_2) removal at a gas flow-rate of 0.25 standard liters per minute (SLPM) and an absorbent flow-rate of 0.02 liters per minute (LPM); the minimum height of ceramic foam required is 20.3 centimeters (cm). It is understood at this point that the more accurate measure of tower packing is its volume. However, in the present scenario; gas-liquid distribution on ceramic foams is not very well understood, thus requiring using the height of tower packing as a parameter. For the proof-of-concept demonstration, it was decided to construct a stainless steel prototype capable of withstanding high temperatures.

Choice of materials

20 pores per inch (ppi) alumina foam was selected as the material for gas-liquid mass transfer on the absorption and stripping sides. 99.5% α-alumina (Al2O3) foam blocks, 20.3 x 10.2 x 2.54 centimeters (cm) were procured from ASK-Chemicals, Alfred, NJ. The choice of a suitable material for the gas-liquid separator membrane was slightly challenging. Using a single microthin membrane is risky since it can easily get damaged (e.g. tear, punctures, etc.). Thus, it was decided to use a porous ceramic membrane of high permeability and lower entry pressure as a support for a micro-thin membrane. Such a 99.5% α-alumina (Al_2O_3) porous membrane was purchased from Refractron Technologies, Newark, NJ. The

properties of this membrane are summarized in the Table 5-1 below. Capillary connectivity between the ceramic foam and the microthin membrane was maintained using a hydrophilic fiber glass wool blanket purchased from the Ceramic Store Inc., Houston, TX as a wicking material.

Table 5-1. Properties of porous alumina membrane

Property	**Value**
Material	Alumina (99.5 %)
Dimensions (mm)	203.2 x 101.6 x 25.4
Mean pore-size (μ)	19.3
Porosity (%)	43.4
Bubble point pressure (kPa)	5.8
Gas permeability (@ 30 psi) (m^2)	5.3 E-12 (5.38 Darcy)

For the gas-liquid separator membrane, several commercially available polymeric membranes were considered. One important characteristic required of this membrane material is for it to be hydrophilic or water-wetting. Additional requirements include good chemical resistance under alkaline conditions and thermal stability at temperatures up to 150^{o}C. Based on these properties, polyethersulfone (PES) was identified as the membrane material. Polyethersulfone (PES) has excellent chemical resistance against bases and has a glass transition temperature of 230^{o}C. Polyethersulfone (PES) membranes were provided by Pall Life Sciences Corporation, Port Washington, NY (Part # S80720). The properties of these membranes are summarized in Table 5-2.

Table 5-2. Properties of porous alumina membrane

Property	Value
Material	Polyethersulfone Membrane (Hydrophilic)
Glass transition temperature (^oC)	220
Membrane thickness (μ)	114.3 – 165.1
Dimensions (mm)	203.2 x 101.6
Mean pore-size (μ)	0.8
Liquid Permeability ($Ls^{-1}m^{-2}$)	13.3 – 63.3
Bubble point pressure (kPa)	103.4 – 213.7

Design considerations

Stainless steel was selected as the main material of construction with an aim of providing sufficient structural strength and avoiding corrosion problems. Several important design objectives that were critical towards the success of the proof-of-concept demonstration were identified. These are presented below:

- No gas or liquid bypass around the ceramic foam blocks
- No gas channeling along with liquid exiting the absorber or stripper at the bottom
- No gas leakage from absorption chamber to stripping chamber
- No leakage of ambient air into stainless steel prototype
- Staggered configuration for absorption and stripping side ceramic foams to maximize the gas-liquid contacting effect of ceramic foam

- Suitable distribution mechanisms for gases and liquids entering the prototype
- Capillary contact between ceramic foam and polyethersulfone (PES) membrane (using hydrophilic fiber glass wool)

After identifying the required features in the stainless steel prototype, LumaDyne LLC., a Houston based scientific design, analysis and manufacturing company was selected to design the prototype. Designers at LumaDyne, used SolidWorks - a 3D CAD design software to accomplish this task. The absorption and stripping chambers are sealed using mechanisms such as Teflon spacers and O-rings. Additionally, lateral forces are exerted on the ceramic foam blocks on both sides with the use of incompressible Teflon spacers to achieve good capillary contact which is crucial for lateral flow of the absorbent solution. In order to prevent gas bypass around the absorption or stripping side ceramic foam blocks, all the non-flowing faces of the ceramic foam blocks are sealed by painting them with waterproof epoxy paint McMaster Part # 7617T5). The epoxy paint prevents any escape of liquid through the non-flowing faces of the ceramic foam, thereby channeling all fluid flow through the main body of the ceramic foam. Finally, stainless steel ‘tee’ fittings purchased from Swagelok with appropriate sized bore holes were used for distributing all incoming gases and liquids. Since, a part of the proof-of-concept demonstration involves injecting steam into the stripping chamber; a steam generator is required.

Commercially available steam generators were considered for this application; however, analysis showed that their capacity was too large for the present application. Hence, a miniature steam generator was designed by LumaDyne LLC. Five 80 Watt (W) cartridge heater elements purchased from Omega Engineering

were installed in the miniature steam generator. A temperature controller purchased from Schneider Electric was used to control the heating elements. When operating with water at boiling temperature (i.e. 100^{o}C at 101.3 kilopascals (kPa), the miniature steam generator can generate steam at 0.64 kilograms per hour (kg/h).

Setup of experimental prototype

Having fabricated the stainless steel prototype and the miniature steam generator, the next step towards the proof-of-concept demonstration was to design the experimental setup for performing the experiments. Figure 4 shows a schematic representation of the experimental setup developed for performing the proof-of-concept demonstration. Conceptually, this setup is quite similar to that described in our previous quarterly research reports. However, unlike the mass transfer setup which was operated at atmospheric pressure; the absorption chamber in the stainless steel prototype is pressurized between 0 and 20.7 kilopascals (kPa). This required making certain design changes to the setup, specifically to prevent the channeling of gas along with exiting absorbent. Whereas a liquid seal could be used in the experimental setup used for the CO_2 absorption studies, application of a similar concept in the present case would result in the requirement of an improbably long liquid seal if water were used. To overcome this problem, a spent absorbent reservoir was added to the system as shown in Figure 5-1. The spent absorbent reservoir acts both as a reservoir for any spent absorbent leaving the absorption or stripping sides and prevents the escape of any gas. In order to maintain a set pressure

in the absorption chamber, an adjustable back pressure regulator is installed downstream of the stainless steel prototype.

When in operation, a peristaltic pump draws absorbent from a fresh absorbent reservoir and delivers it at the top of the stainless steel prototype where it is distributed on the ceramic foam surface. Simulated flue gas containing 13% carbon dioxide (CO_2) and 87 % nitrogen (N_2) is introduced at the required flow-rate by a mass flow controller. The decarbonized flue gas exiting the absorption chamber through the adjustable back pressure regulator is analyzed using a LI-COR carbon dioxide (CO_2) detector. Spent absorbent flows across to the stripping chamber and exits the prototype at the bottom on the stripping chamber.

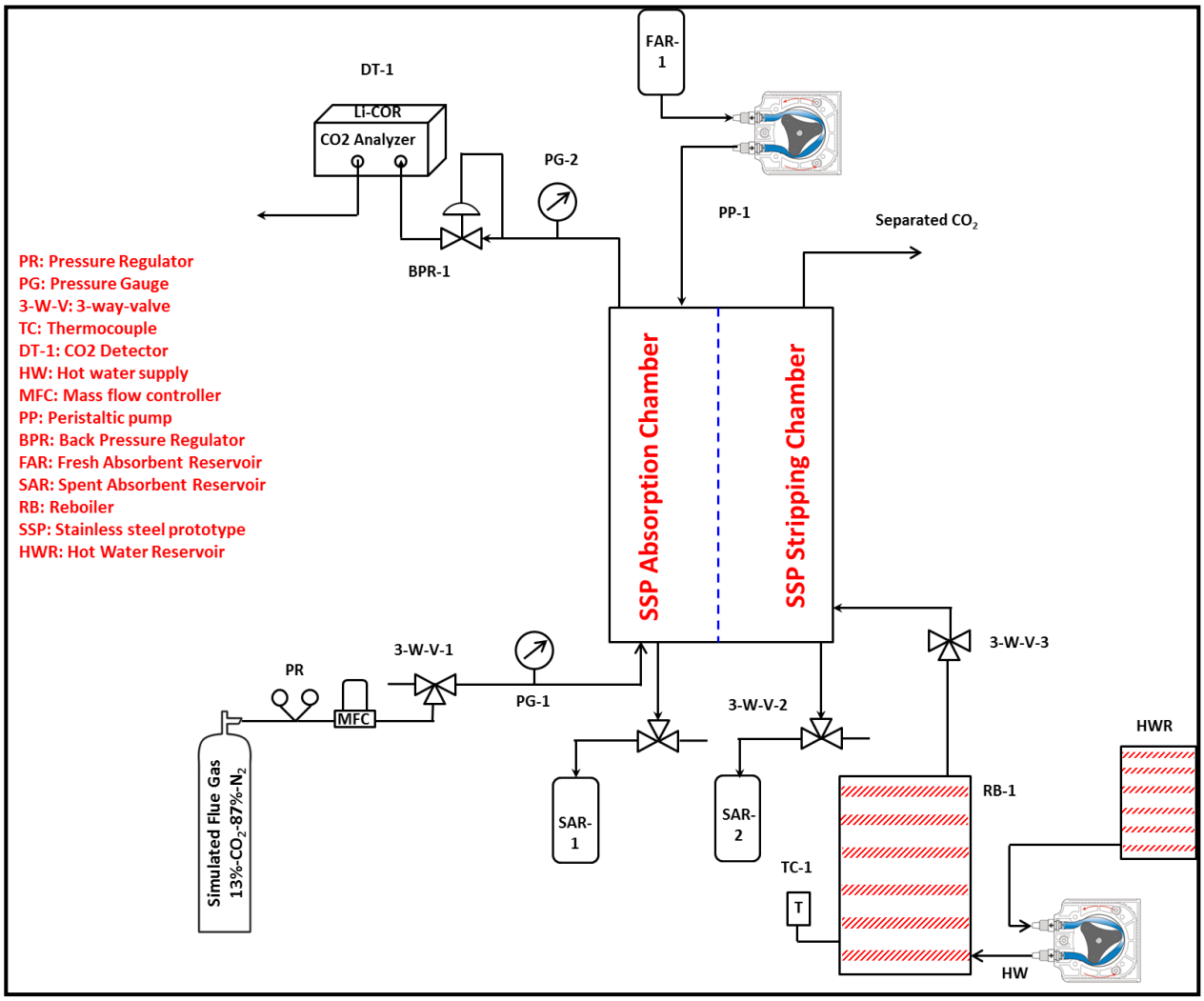

Fig. 5-1 Schematic representation of the experimental setup developed for the proof-of-concept demonstration

When demonstrating simultaneous absorption and stripping operation, steam generated in the steam generator is introduced into the stripping chamber of the stainless steel prototype at the bottom. Hot water at a temperature in excess of 95°C produced in a metallic hot water reservoir is constantly delivered to the miniature

steam generator using a second peristaltic pump. Absorbent along with steam condensate exits the chamber at the bottom where it accumulates in the solvent reservoir. Figure 5 shows the experimental setup developed for the proof-of-concept demonstration of the novel process with a combined absorber and stripper unit. As seen in this image, the external surface of the stripping side chamber is covered with a thermal insulation material made of alumina fiber material. The thermal insulation was purchased from McMaster-Carr and has a K-factor of 0.48 at 800 ^{o}F (Part # 87575K84). Metal fittings used for steam inlet and stripping side effluent were also wrapped in thermal insulation to prevent excessive heat loss. The hot water reservoir and peristaltic pump assembly used to operate the miniature steam generator on a continuous basis is also seen in this image.

5.2 Proof-of-concept demonstration

Choice of operating parameters

The objective of the proof-of-concept demonstration is threefold. The first of these is to demonstrate the feasibility of the proposed concept of achieving a lateral flow of the absorbent solution, from the absorption chamber to the stripping side. This involves a complex operation of the prototype in which the simulated flue gas and lean absorbent enter the absorption chamber and steam enters the stripping side. A second goal is to operate the system at lower temperatures (without steam supply to the stripping chamber) but wider range of operating pressures and flow-rates to

collect experimental data which can be used later to validate the results generated using a computer model developed for this process.

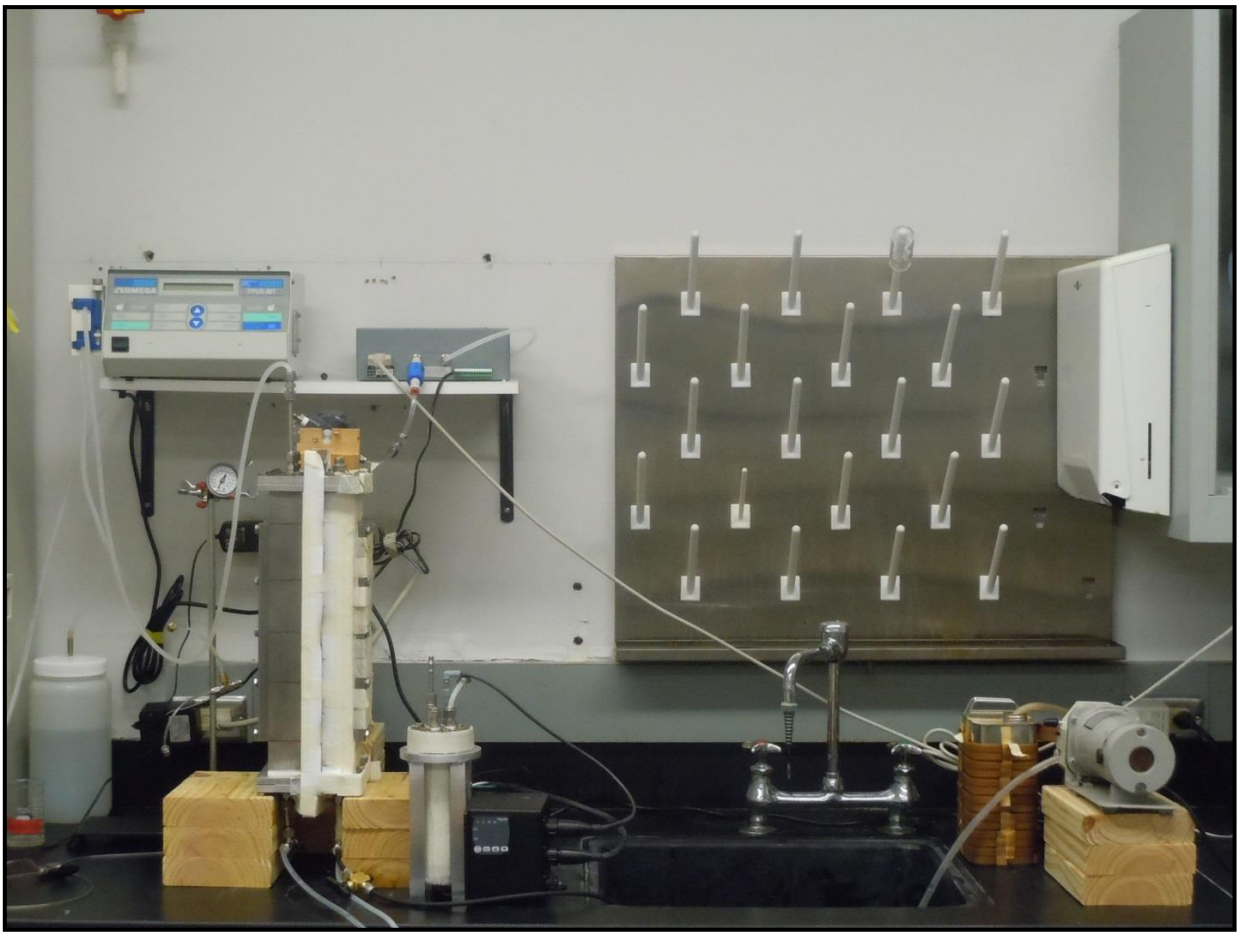

Fig.5-2 Photograph of the experimental setup developed for the proof-of-concept demonstration

Finally, this proof-of-concept demonstration provides the first opportunity to test the proposed concept for the novel carbon dioxide (CO_2) separation process and thus, is an opportunity to observe it for design and operational issues. As a part of the complete proof-of-concept demonstration, thus, we have operated the process with a pressure differential of 20.7 kilopascals (kPa) while injecting simulated flue

gas at flow-rates of 0.25, 0.5 and 1.0 standard liters per minute (SLPM) and 30 wt% diglycolamine (DGA) at 0.01 liters per minute (LPM). Steam was introduced into the stripping chamber at a temperature of 102 ^{o}C and 109 kilopascals (kPa-absolute). When operating without steam, the differential pressures between the absorption and stripping chambers were varied between 6.9 and 20.7 kilopascals (kPa), simulated flue gas flow-rate was maintained at 0.25, 0.35, 0.5 and 1.0 standard liters per minute (SLPM) and the absorbent flow-rates studied were 0.01, 0.02 and 0.03 liters per minute (LPM).

Experimental procedure

The objectives of the proof-of-concept demonstration experiments have been clearly described previously. Since this stainless steel prototype was the first opportunity to test the concept of an integrated absorber and stripper, establishing experimental protocol was considered critical to collecting reliable experimental data. When operating the stainless steel prototype without steam, the absorption chamber was first purged with nitrogen. When the measured carbon dioxide (CO_2) concentration of the exiting gas reduced to very low levels (e.g. 50 ppm); simulated flue gas was introduced into the chamber. Simultaneously, the back pressure regulator installed downstream of the stainless steel prototype was adjusted to achieve the required pressure in the absorption chamber. This pressure was monitored with a pressure gauge connected to the back pressure regulator. The gauge pressure is also the pressure differential across the absorption and stripping chambers since the stripping side is maintained at atmospheric pressure. Once, the absorption chamber was pressurized, 30 wt% diglycolamine (DGA) was flowed into the absorption chamber.

It was observed that when the system operation was started from a dry condition (meaning the ceramic foam, fiber glass wool packing and alumina membrane were completely dry), all the absorbent flowed across laterally into the stripping chamber even at the lowest pressure difference tested (6.9 kilopascals (kPa)). However, when the effluent flow-rate from the stripping chamber was measured; it was found to be lower than the input rate. The lateral flow can be attributed to the existence of a large pressure gradient between the absorption and stripping chambers which promotes the flow of liquid. The difference between the input and outlet flow-rates, suggested the accumulation of the absorbent liquid in the prototype. This can be attributed to an increase in the liquid saturation of the ceramic foam, the alumina membrane and the fiber glass wool. Collection of experimental data during this transient phase would lead to faulty interpretation of system behavior and was carefully avoided. After allowing the absorbent flow to continue in excess of 60 minutes, collection of experimental data was commenced.

The parameters measured were the degree of carbon dioxide (CO_2) removed in the absorption column and the lateral throughput of liquid absorbent. Since the measurement of absorption side liquid effluent would result in a disruption of the system operation, stripping side liquid effluent was measured and a mass balance performed to determine the lateral flow-rate. Corresponding to each operating condition (i.e. gas and liquid flow-rate and pressure difference), at least three readings were made for the absorbent mass balance. Once these were found to be repeatable, the experimental data was noted. In Figures 8 and 9, the points corresponding to no data represent the cases under which no measurements were made because the lateral transport of the absorbent solution was significantly smaller

than the inflow-rate. Specific precautions were taken to avoid absorbent accumulation in the absorption chamber by draining the any accumulated solution periodically.

Operating the stainless steel prototype with steam was conceptually similar but practically significantly more complicated due to the introduction of steam into the stripping chamber. When operating with steam, the electrical heating tape on the metallic hot water reservoir was switched on before commencing the flow experiments. The heat rate was set to raise the water temperature to around 100 ^{o}C. Once this set temperature was reached, the miniature steam generator was switched on. The boiler vessel in the steam generator has a volume of 0.2 liters. This was loaded with approximately 0.2 liters of hot water to expedite steam generation. Once a steady flow of steam was observed coming out of the steam generator, the peristaltic pump supplying hot water to the steam generator was turned on and set to flow at 0.01 liters per minute (LPM).

Simultaneously, simulated gas flow was turned on and the absorption side chamber was pressurized. Once the chamber was pressurized, absorbent flow was initiated. After allowing the flow to reach steady state, steam was introduced into the stripping chamber. Simultaneously, temperature readings were made at the 10 equispaced nodes located on the side-faces of the stainless steel prototype. Measuring these temperatures using a conventional thermometer (e.g. thermocouple thermometer) is impractical due to the significant time lag involved in attaining a steady reading. Hence, a hand-held infrared thermometer purchased from McMaster-Carr was used for making the temperature measurements. The thermometer has a response time of around 1 second, a resolution of 0.1 ^{o}F and an accuracy of ± 1.8 ^{o}F.

Temperature measurements were made every 10 minutes till the temperatures reached a steady state. It was observed that the heat losses, especially through the stripping side of the stainless steel prototype were quite significant despite the use of thermal insulation. This resulted in steam condensation occurring in the stripping chamber. During constant operation, this steam condensate was periodically drained from the stripping chamber by opening a 3-way valve installed on the liquid outlet port. Since both the steam condensate and the laterally transported absorbent solution exit the stainless steel prototype through the same outlet port, a direct measurement of the lateral flow-rate is not possible. An indirect approach was developed to detect the presence of diglycolamine (DGA) in the stripping chamber effluent. Several samples of the stripping chamber effluent were collected in glass vials. A known quantity of the effluent was then titrated against 0.1 N hydrochloric acid (HCl) using phenolphthalein as an indicator. Diglycolamine (DGA) is a base and reacts with hydrochloric acid (HCl) to form its chloride salt. Thus, the lateral flow of absorbent liquid can be confirmed by using the indirect acid-base titration technique. In the subsequent section, we present the results of the proof-of-concept demonstration experiments. Also presented are the results of the acid-base titration conducted to detect the presence of diglycolamine (DGA) in the stripping side effluent.

5.3 Experimental results and analysis

Figure 5-3 shows a plot of the degree of carbon dioxide (CO2) removal taking place in the absorption chamber of the stainless steel prototype when operating without steam at a temperature of 23 ^{o}C and a liquid flow-rate 0.01 liters per minute

(LPM). As expected, the extent of carbon dioxide (CO2) removal taking place decreases gradually as the gas flow-rate is increased. However, it appears that the degree of carbon dioxide (CO2) removal has some dependence on the pressure differential maintained across the absorption and stripping sides. It can be observed that the degree of carbon dioxide (CO2) removed decreases as the pressure differential is increased. This can likely be attributed to the dependence of the lateral flow of absorbent on the pressure differential. As shown in Figure 5-4, the maximum lateral flow of absorbent solution at a pressure difference of 6.9 kilopascals (kPa) is around 0.006 liters per minute (LPM). This would result in the excess absorbent flowing down on the entirety of the absorption side ceramic foam and exiting the chamber at the bottom. For the 13.8 and 20.7 kilopascals (kPa) cases, the maximum lateral flow-rates are both greater than 0.01 liters per minute (LPM) resulting in all of the absorbent flowing across to the stripping side. The dependence of lateral throughput on pressure drop is observed to be linear except when the pressure differential was maintained at 20.7 kilopascals (kPa). The linear behavior is consistent with Darcy's law.

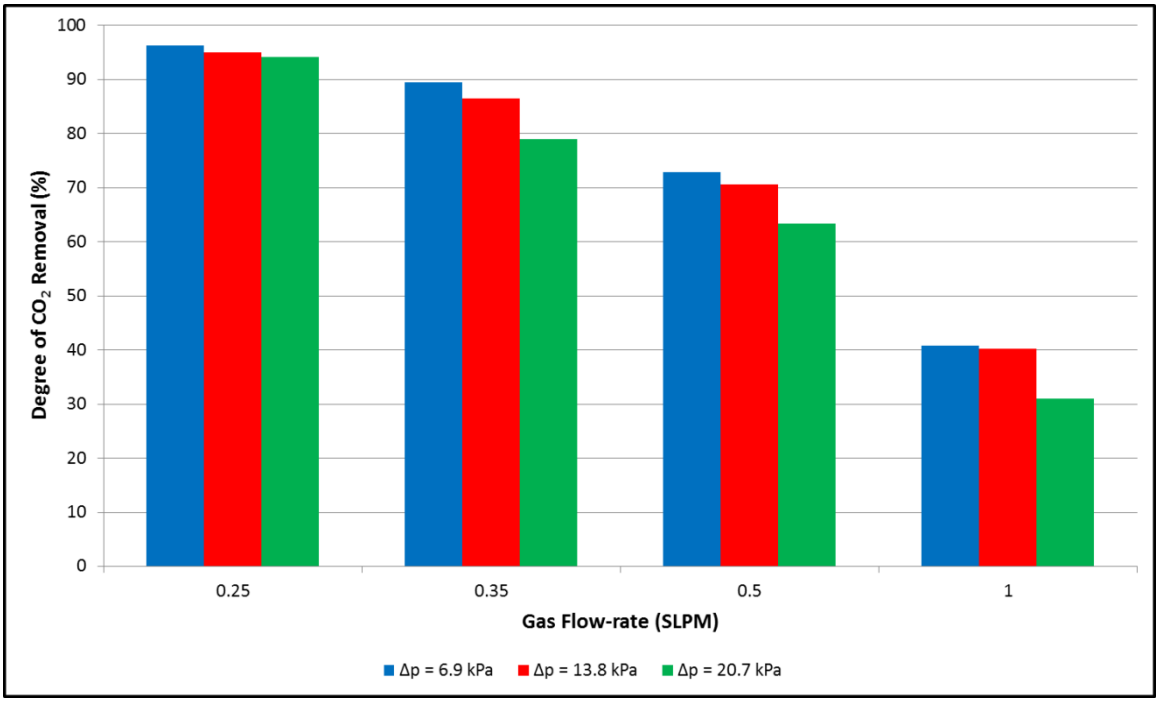

Fig.5-3 Degree of CO_2 removal at variable gas flow-rates and absorbent flow-rate of 0.01 liters per minute (LPM)

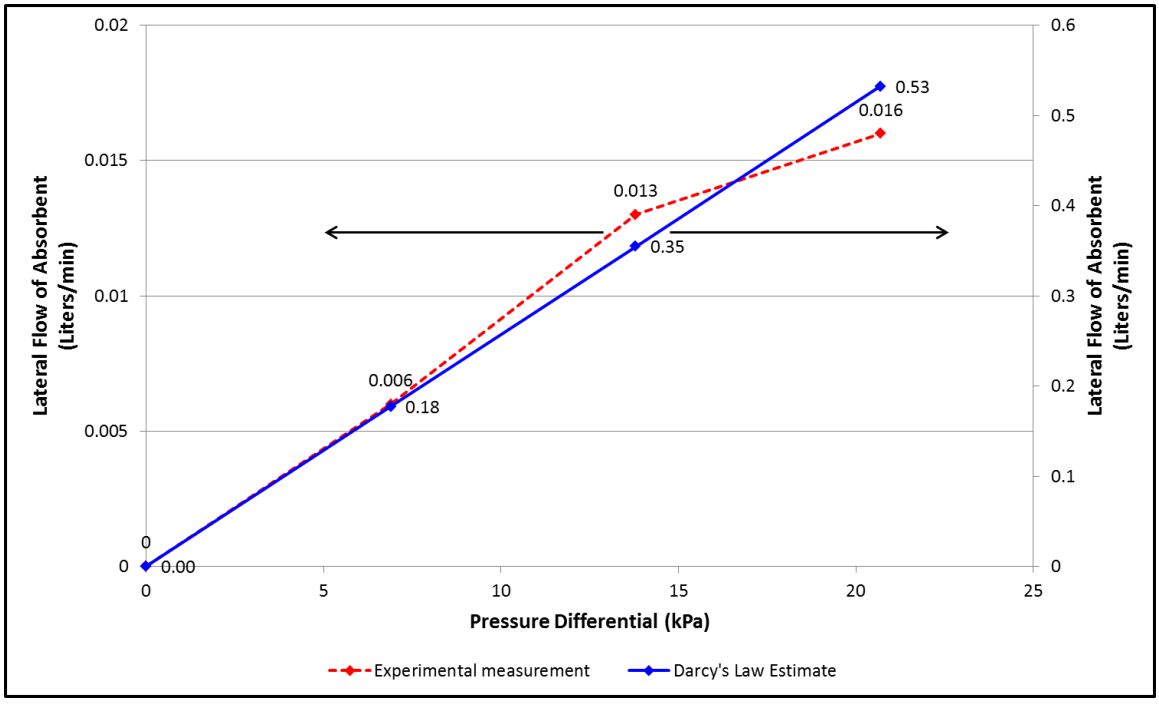

Fig 5-4 Dependence of maximum lateral flow-rate of absorbent on pressure difference across absorption and stripping chambers

At 20.7 kilopascals (kPa), however, it is possible that the absorbent solution flowing laterally to the stripping side did not wet the entire length of the absorption side resulting in the observed trend. As seen in Figure 5-5, however, the experimentally measured flow-rates are at least one order of magnitude lower than the calculated maximum flow-rate across the polyethersulfone (PES) and porous alumina membrane. This can be explained on the basis of the flow resistance offered by the microporous matrix of the ceramic foam. While the polyethersulfone (PES) and the porous alumina membranes have very high liquid permeability, the microporous ceramic matrix offers a much higher flow resistance and acts as the rate-limiting process.

The difference between the extents of carbon dioxide (CO_2) removal corresponding to pressure differentials of 6.9, 13.8 and 20.7 kilopascals (kPa) at an absorbent flowrate of 0.01 liters per minute (LPM) can be attributed to variations in the lateral transport of the absorbent. At lower pressure differentials, the absorbent flows down a greater length of the ceramic foam before either draining at the bottom or completely flowing across to the stripping side. At higher pressure differentials, the liquid flows across laterally without wetting the entire ceramic foam surface which results in decreased carbon dioxide (CO_2) pickup. Figure 5-5 shows the extent of carbon dioxide (CO_2) removal for the two cases of 13.8 and 20.7 kilopascals (kPa) when operating at an absorbent flow-rate of 0.02 liters per minute (LPM). No experiment was conducted corresponding to a pressure differential of 6.9 kilopascals (kPa) case since the absorbent flow-rate significantly exceeded the maximum lateral flow achieved at that pressure. The trend observed for the dependence of carbon dioxide (CO_2) removal on pressure difference in this plot is different from that in Figure 6. At an absorbent flow-rate of 0.02 liters per minute (LPM), excess absorbent flows down the entire length of the ceramic foam in both cases.

Figure 5-7 shows the degree of carbon dioxide (CO_2) removal at an absorbent flow-rate of 0.03 liters per minute (LPM) and a pressure differential of 20.7 kilopascals (kPa). Better carbon dioxide (CO_2) removal is observed in this case as compared to the previous two cases involving lower flow-rates. Based on these results, it can be concluded that it is possible to achieve more than 90% removal of inlet carbon dioxide (CO_2) in the combined absorption/desorption process while achieving lateral flow absorbent.

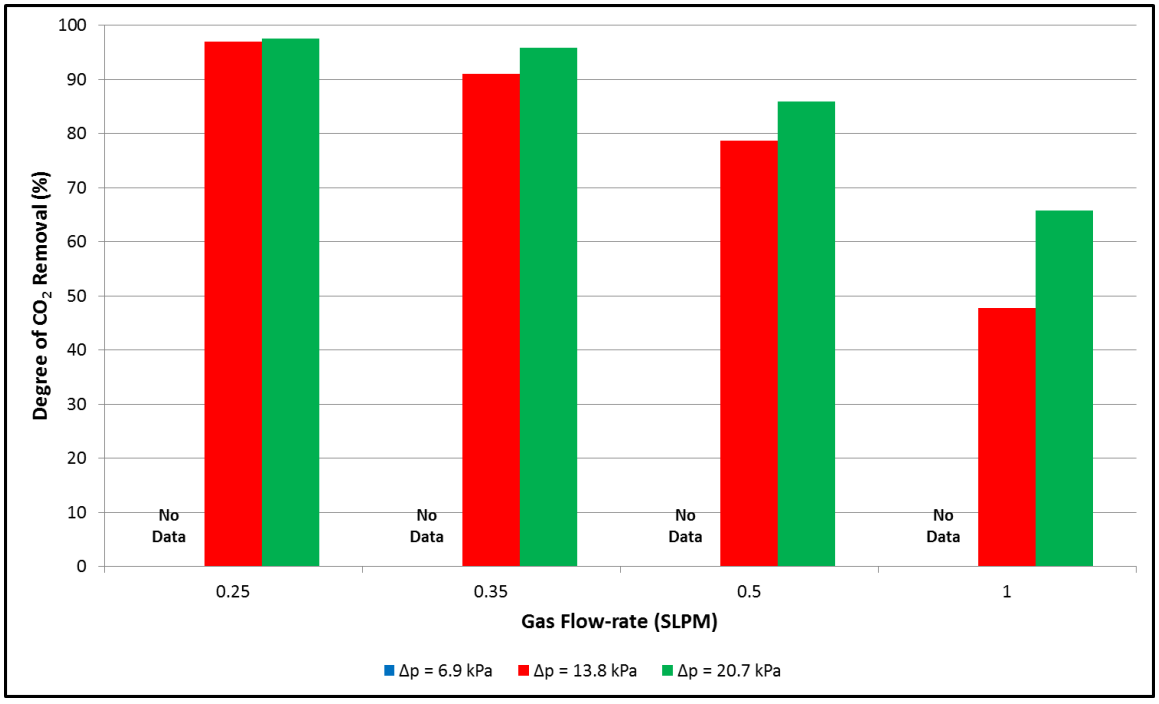

Fig. 5-5. Degree of CO_2 removal at variable gas flow-rates and absorbent flow-rate of 0.02 liters per minute (LPM)

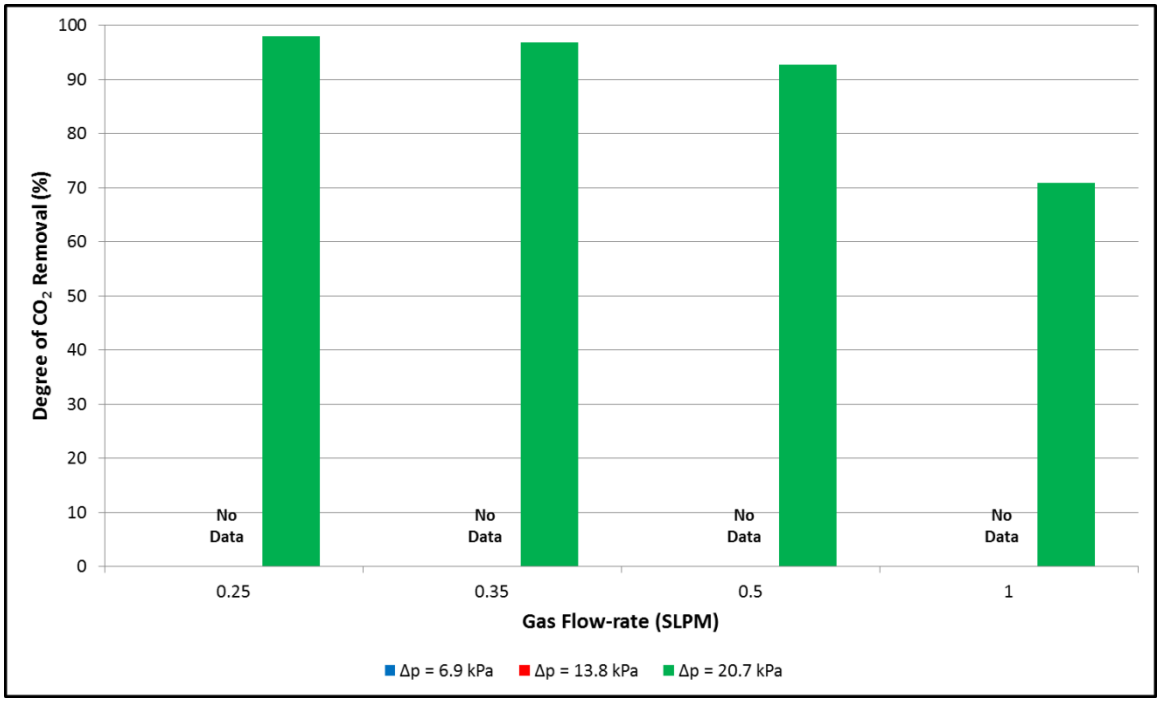

Fig.5-61. Degree of CO_2 removal at variable gas flow-rates and absorbent flow-rate of 0.03 liters per minute (LPM)

Figure 5-7 shows a comparison of the degree of carbon dioxide (CO_2 removal taking place in the absorption chamber of the stainless steel prototype when operating without and with steam flowing into the stripping chamber. The simulated gas flow-rates maintained were 0.25, 0.5 and 1.0 standard liters per minute (SLPM), the absorbent flow-rate was 0.01 liters per minute (LPM) and the pressure differential between the absorption and stripping chambers was 20.7 kilopascals (kPa). During the experiment, it was observed that there was a constant flow of liquid exiting the absorption chamber. This observation is in contrast to the results of our previous experimental studies conducted without steam (see Figure 5-4). This significant reduction in lateral transport of absorbent solution can be attributed to the changes in its physical properties such as viscosity. Steam entering the stripping

chamber increases the temperature in the absorption chamber which results in a reduction of the solution viscosity. This promotes the downwards flow of the absorbent solution by gravity drainage. The trend observed in the dependence of carbon dioxide (CO_2) removal is similar to those observed previously in Figures 6-6.

To verify the lateral flow of liquid from the absorption to stripping side, acid-base titrations were performed. The results of these are summarized in Table 5-3. The significant variance in the titration volumes can be attributed to the ejection of the stripping chamber effluent in spurts as the entering steam escapes along with the liquid. These results clearly show the presence of a base in the stripping chamber effluent.

Since the steam condensate itself is ‘distilled water’ and because no other basic compound is injected into the stainless steel system, the source of this basicity was concluded to be diglycolamine (DGA) flowing across from the absorption chamber.

Figure 5-8 shows a schematic representation of the experimental setup with the various measurements and observations made during the proof-of-concept demonstration with steam.

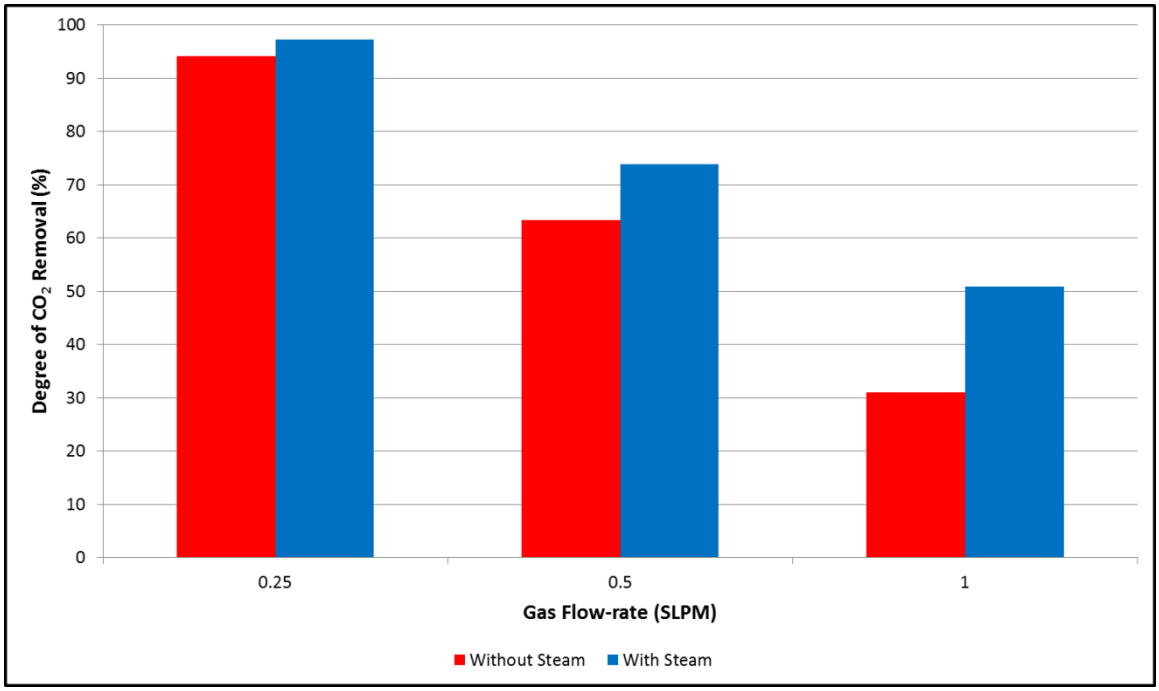

Fig. 5-7 Degree of CO_2 removal at variable gas flow-rates, absorbent flow-rate of 0.01 liters per minute (LPM) and pressure differential (ΔP) of 20.7 kPa - with and without steam

Table 5-3 Diglycolamine (DGA) concentration in stripping chamber effluent

Effluent Case #	Effluent Volume	Acid Concentration	Acid Volume	Base concentration in Effluent (N)
0.5 SLPM #1	10	0.1	11.4	0.114
0.5 SLPM #2	10	0.1	17.2	0.172
1.0 SLPM #1	10	0.1	10.1	0.101
1.0 SLPM #2	10	0.1	9.7	0.097

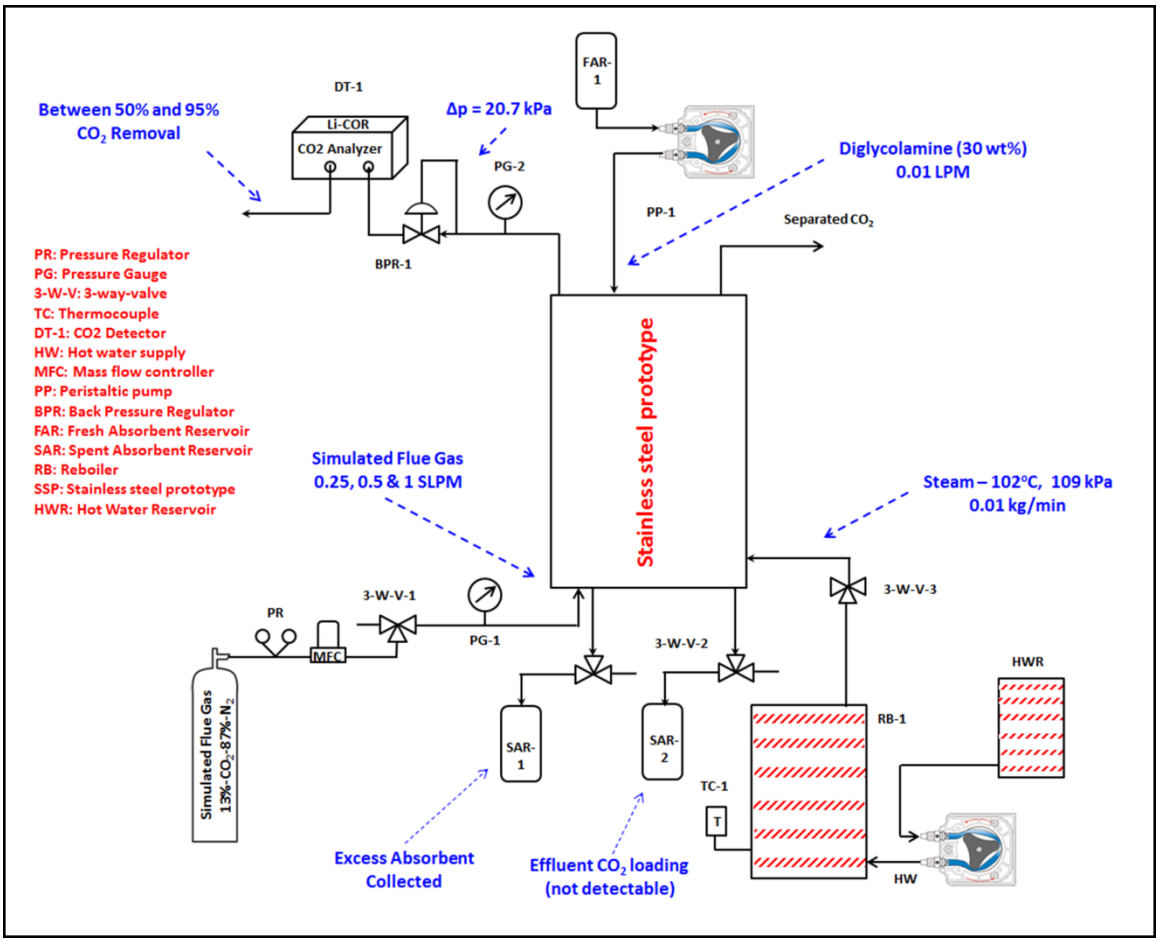

Fig. 5-8 A schematic representation of the experimental setup used for the proof-of-concept demonstration - with experimental measurements and observations

Figure 5-9 and Figure 5-10 show the temperatures measured on the external surfaces on the absorption and stripping sides of the stainless steel prototype. In these figures, the lower number represents nodes at the top of the stainless steel prototype whereas the higher number represents a node at the bottom. Addition of the steam clearly resulted in a heating of the stripping chamber. However, it also resulted in a significant increase in the absorption side temperature; a factor that

could influence both the lateral flow of absorbent solution as well as the degree of carbon dioxide (CO_2) removal.

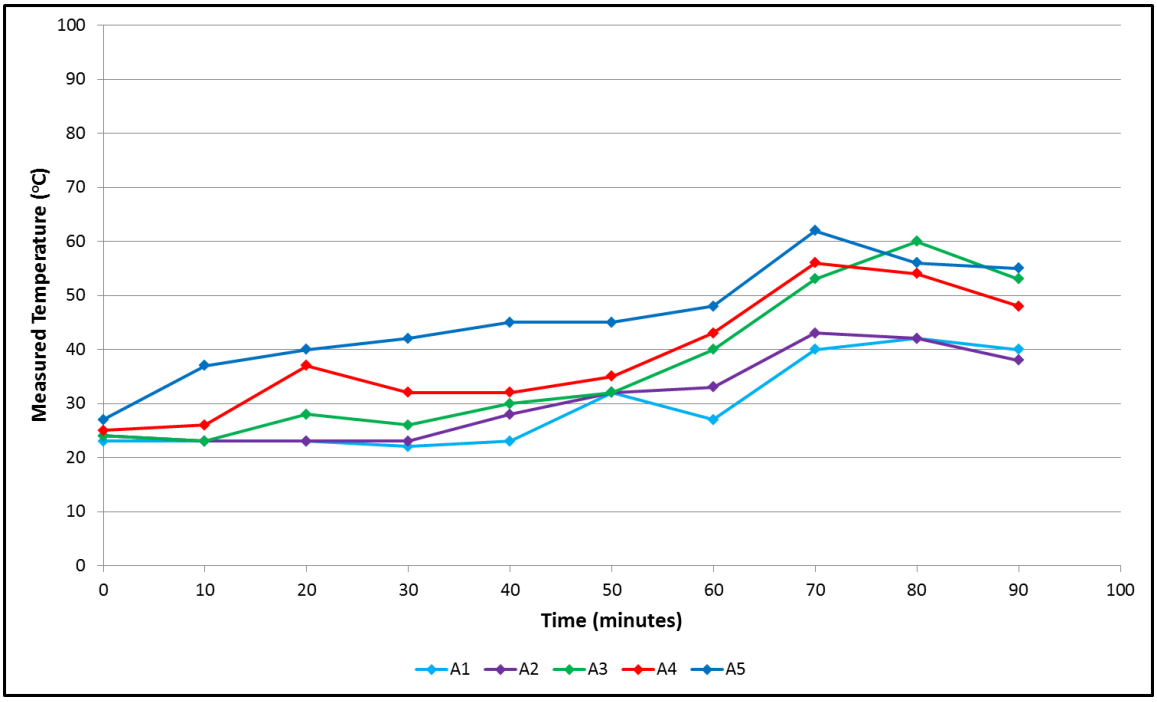

Fig. 5-9 Temporal dependence of absorption side external surface temperatures

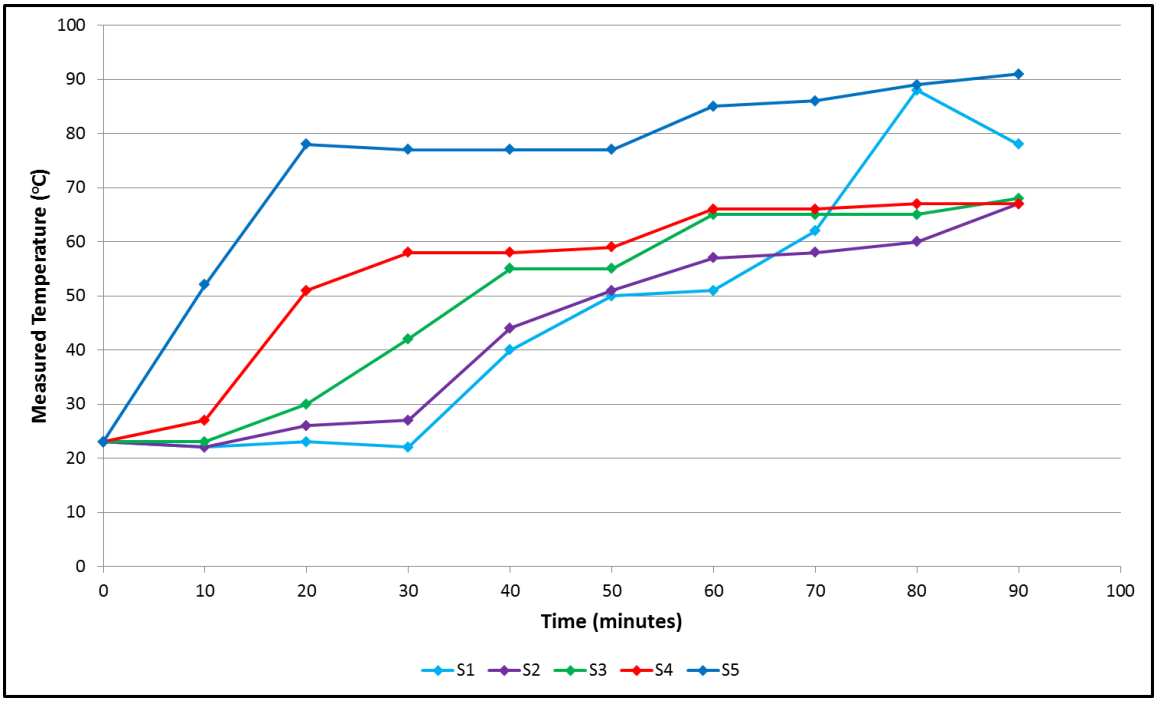

Fig. 5-2 Temporal dependence of stripping side external surface temperatures

6. Catalytic desorption of CO_2 using metal oxides

During the surface functionalization work, we encountered issues with the stability of silicon-based molecular ligands attached to alumina surface, due to instability of the Al-O-Si bond under the high-pH conditions of the amine solution.

To address this, we studied the use of phosphorus-based molecular ligands, testing the hypothesis that Al-O-P bonds are stable under high-pH conditions. Phenylphosphonic acid was successfully attached to the surface of alumina powder. However, after contacting with a water solution of DGA (diglycolamine), the phenylphosphonic acid undesirably detached from the surface. Thus, we concluded that the Al-O-P bond was not stable at basic pH, even after improving the surface chemistry coupling reactions. We were unable to identify any surface functionalization chemistries that would give a functionalized alumina surface that would remain stable with short or long-term exposure to the basic pH environment of aqueous amines.

Instead of restricting ourselves to alumina (which is the material of the ceramic foam), we then studied the functionalization chemistry of silica surfaces, with the hypothesis that Si-O-Si bonds are more stable than Al-O-Si. We functionalized silica powder with (3- aminopropyl)trimethoxysilane successfully. This material had a significantly higher coverage of the ligand ($5.0x10^{-2}$ ligand/nm^2) than a similarly prepared alumina material ($7.4x10^{-4}$ ligand/nm^2). After exposure to a monoethanolamine (MEA) solution, the silica material lost 60% of the surface ligand. Deposition of a silane with a longer carbon chain called 3-(2-aminoethylamino) propyl]trimethoxysilane) led to a material with a higher surface

coverage ($7.0x10^{-3}$ ligand/nm^2). No stability testing was done with this material, but we expected that there would significant ligand loss after exposure to MEA. We performed additional work to improve the stability of silica by preparing alkenyl and alkyl amine-terminated groups on silica surfaces.

Ultimately, we concluded that further work on surface functionalization was not fruitful unless the stability of the un-functionalized alumina and silica materials were studied at high-pH conditions. Instead of attaching chemically active groups onto the alumina surface, we sought to understand what types of metal oxides have chemically active surfaces that can participate in the amine-CO_2 reactions. We narrowed our Task 6 from *functionalization of ceramic foam with both acidic and basic moieties* to *catalytic desorption of CO_2 using metal oxides.*

6.1 The effects of metal oxides on decomposing carbamate intermediates

Experimental Setup

Aqueous solutions of 3 M MEA and 1.5 M piperazine (PZ) were prepared. CO_2 was loaded into 15 mL of the solution 10 wt% CO_2/90 wt % N_2 at either 40 °C (MEA) or 30 °C (PZ) in a 50 mL four-neck round bottom flask (Fig. 6-1) . Following loading of CO_2, the flask was purged with N_2 for 10 minutes to flush the headspace and return the flask to a full N_2 atmosphere.

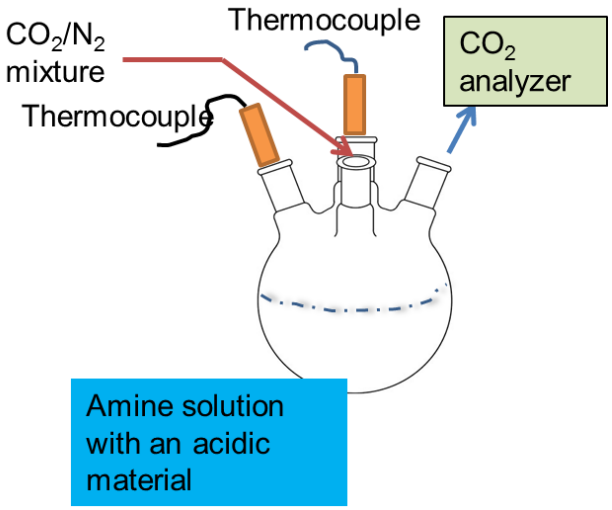

Fig.6-1 Experimental setup for CO_2 absorption and desorption studies

Metal oxide powers were dried under vacuum at 150 °C for 30 minutes prior to desorption studies. 3 M monoethanolamine (MEA) and 1.5 M piperazine (PZ) were prepared and stored under nitrogen prior to use. CO_2 was loaded into 15 mL of the appropriate solutions to 0.3 mol via 100 mL min^{-1} of 10 wt% CO_2/90 wt % N_2 at either 40 °C (MEA) or 30 °C (PZ) in a 50 mL four-neck round bottom flask. Following loading of CO_2, the flask was purged with N_2 for ten minutes to flush the headspace and return the flask to a full N_2 atmosphere, as shown in Fig. 6-2. If required, 1.5 g of appropriately dried metal oxide powder was introduced into the solution and allowed to equilibrate for 15 minutes at absorption temperatures.

The desorption process was initiated by applying heat through a heating mantle controlled by a J-KEM model 210 temperature controller set to heat to 100 °C at 10 °C min^{-1}. CO_2 evolution was monitored at 1 second intervals by an IR detector (Li-Cor Li-820 CO_2 analyzer) on the exit stream of gas after passing through a condenser operating at 10 °C to remove any residual moisture from the solution.

Final temperature of the solution was around ~86 °C, mostly due to the cooling effect by the rate at which nitrogen was bubbling through the solution. High gas flow rates (on the order of 1000 mL min^{-1}) were necessary to provide enough dilution to maintain the concentration of CO_2 entering the detector below the calibration limit of 20000 ppm. Stopping the nitrogen flow caused the solution to achieve the desired 100 °C set-point temperature. UV-vis absorbance measurements were performed with 15 mL of CO_2 free 3 M MEA and 1.5 M PZ. 1.5 g of previously dried metal oxide was added to a 30 mL vial along with a stir bar, capped, and the reaction allowed to progress. 1.6 µL aliquots were removed every 5 min and diluted to 10 mL for an overall amine concentration of 4.8 x 10^{-4} M. UV-vis absorbance measurements were made from 200 to 600 nm at a scan rate of 100 nm min^{-1}.

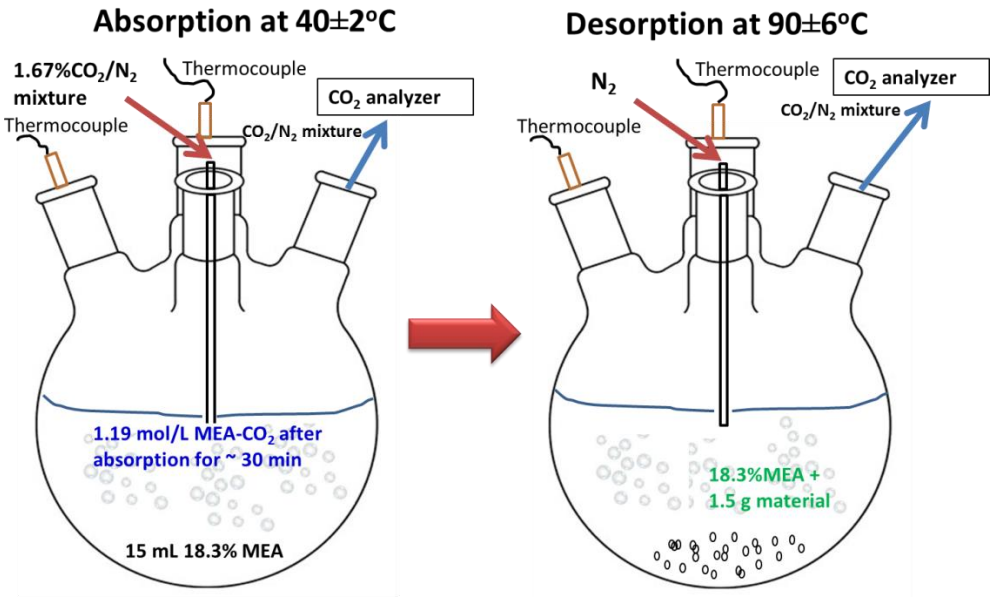

Fig. 6-2. Bubble reactor for CO_2 absorption and desorption experiments

CO_2-amine Reaction Chemistry

Caplow [2] was the first to devise the mechanism for the formation of MEA-carbamate from CO_2 and amine and it was later reintroduced by Danckwerts [3]. This is the commonly accepted mechanism for the MEA-CO_2-H_2O system [4, 5]. The overall reaction between CO_2 and MEA can be represented as shown in scheme I. CO_2 and MEA combine to form an intermediate called 'zwitterion' (Z). In the second step, MEA-carbamate ($HOCH_2CH_2NHCO_2^-$) forms when a proton transfer occurs between the zwitterion and a base. The base can be H_2O, MEA, or OH^-.

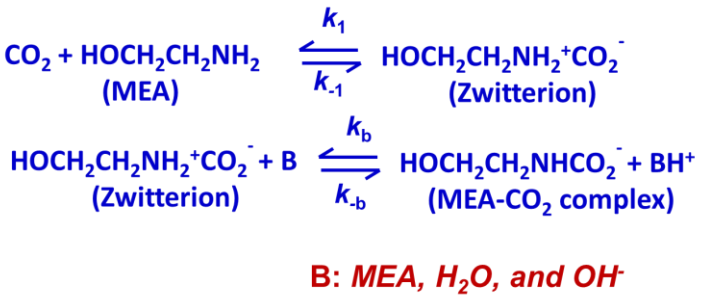

Scheme I: Mechanism for CO_2 absorption and desorption

More details about reactions, reaction mechanism, and rate laws for CO_2 absorption and desorption can be found in the available literature [2, 5-13]. In MEA-CO_2-H_2O system, practically all CO_2 is chemically bound in MEA-carbamate ($MEACOO^-$) at low loadings of CO_2 (<0.4 mol CO_2/mol MEA) [14] which is valid for most of the studies including the present work. MEA-CO_2-H_2O system has several reactions occurring simultaneously as shown in scheme II:

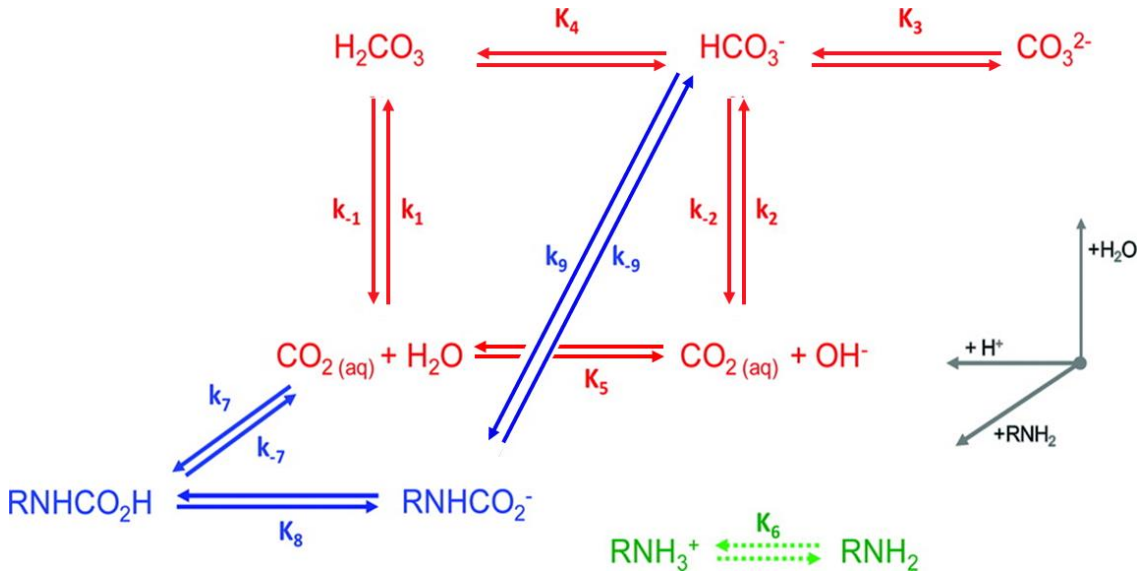

Scheme II. Set of reactions occurring in MEA-CO_2-H_2O system [13]

Experimental Results and Discussion

Figure 6-3 shows an example of CO_2 absorption, desorption, and temperature profiles. These profiles were obtained when the MEA solution loaded with CO_2 and was slowly heated from 40°C (MEA) to maintain the temperature around 84°C. The amount of supplied heat was the same in all the cases. However, slightly different temperatures were observed (not shown here) probably due to different side reactions (exothermic in nature) with various materials. During absorption, some CO_2 was detected probably due to N_2 bubbling, as shown in Fig. 6-3. This CO_2 amount was subtracted from the total CO_2 fed to the reactor to get the total CO_2 absorbed by MEA. During CO_2 desorption, there are two separate regions – 'ramp' and 'soak' stage. During ramp stage, temperature increases to 89 ± 5°C in about 15 min. During soak stage, the temperature remains nearly constant ranging from 84 to 95°C depending upon the material.

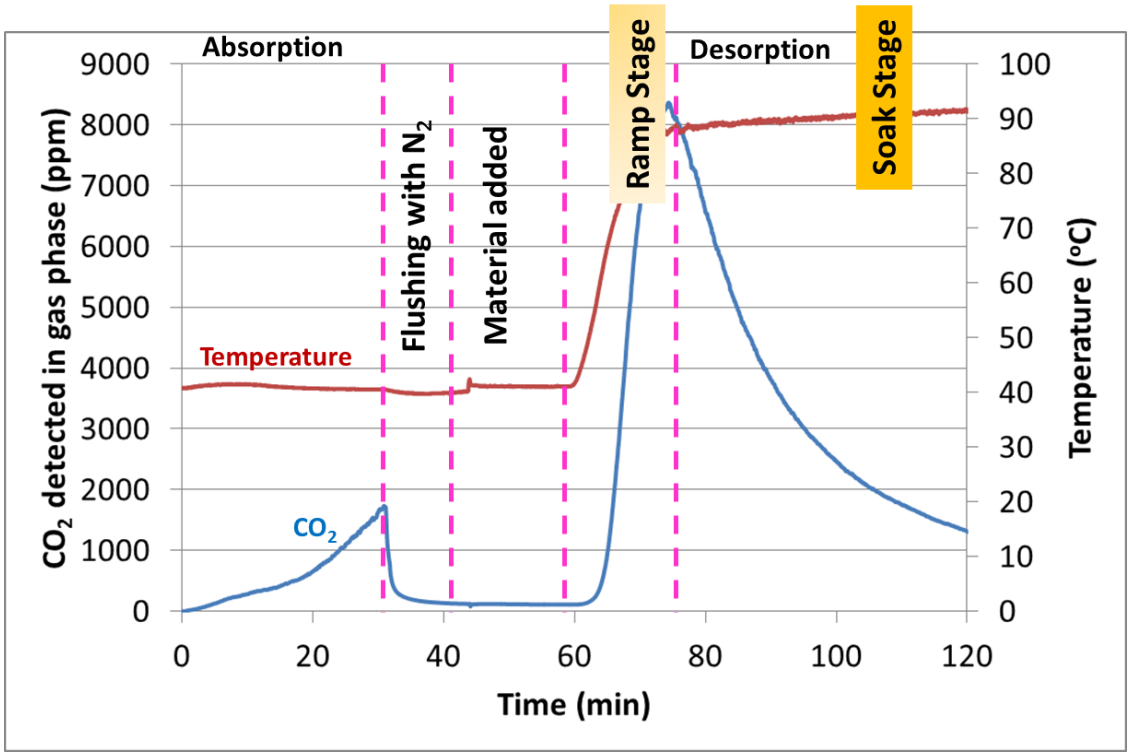

Fig. 6-3 Desorption profile of CO_2 from 3 M MEA with 1.5 g of $WO_3/\gamma\text{-}Al_2O_3$. A typicaltemperature ramp at 2.3°C/min is displayed on the right y-axis.

We studied what happened when eight different, non-functionalized metal oxides came into contact with CO_2-loaded MEA solution, initially to assess the stability of alumina at the high pH conditions. Our findings exciting showed that, while dissolution was observed, improved CO_2 release (in terms of larger quantity and/or lower temperature) was also observed. We had considered the possibility that metal oxides (some with surface acidity) function similarly to liquid acids. The addition of liquid acids, like HCl, lowers the amine solution pH, causing the equilibrium to shift away from carbamate formation to carbamate decomposition, leading to CO_2 desorption. Our hypothesis is that metal oxides can behave like solid acid catalysts

and that the material's tabulated isoelectric point (IEP) correlate with its surface acidity and its ability to influence the rate and quantity of CO_2 desorption.

Two of the metal oxides, vanadium oxide (V_2O_5) and molybdenum dioxide (MoO_2) had the surprising effect of not only increasing the total amount of CO_2 desorbed from the system at increasing temperatures (Fig. 6-4), but CO_2 was also released at 40 °C (during the initial 15-minute equilibrium step prior to raising the temperature of the CO_2-amine/metal oxide system. Tungsten oxide (WO_3), despite being the most acidic metal oxide added had surprising little initial influence on the initial quantities of CO_2 desorbed. Most of the influence from WO_3 came at the period of time after the main desorption event, releasing more CO_2 compared to MEA only while at the main desorption temperature of 86 °C.

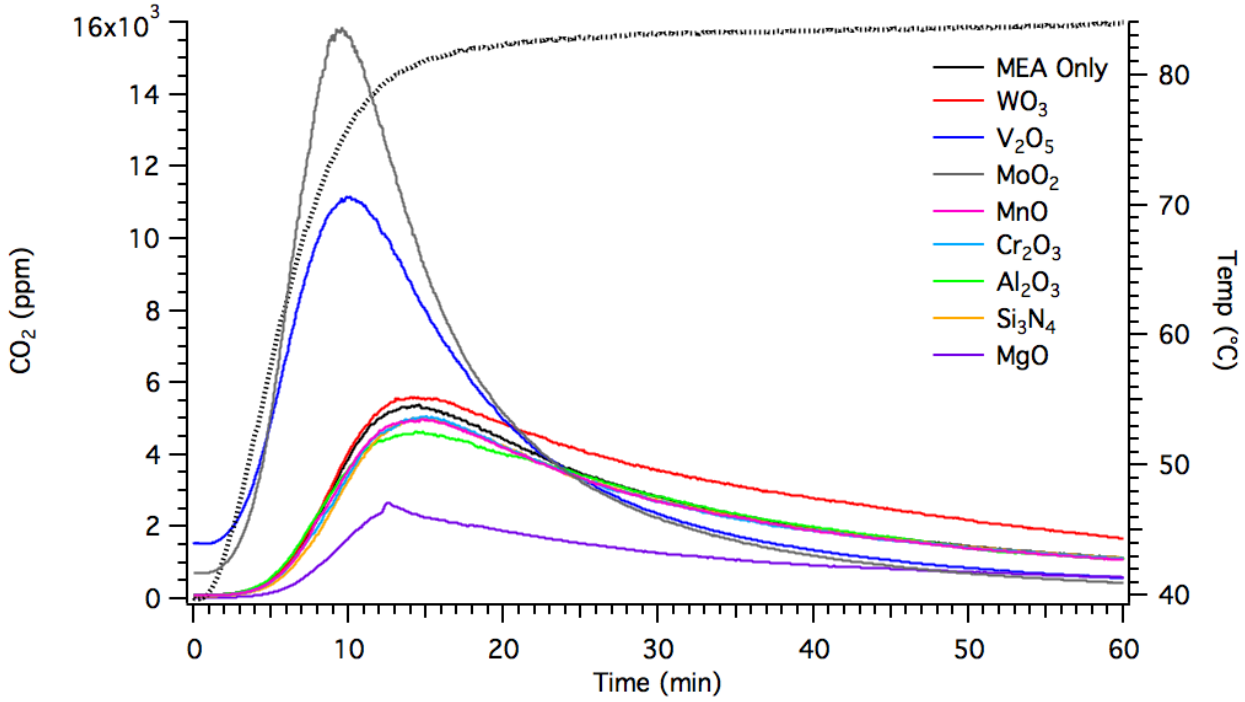

Figure 6-4. Desorption of CO_2 from 3 M MEA with 1.5 g of various metal oxides. A typical temperature ramp (dotted black line) from 40 °C to 86 °C at 10 °C/min is displayed on the right y-axis. Reference typical CO_2 desorption from 3M MEA is displayed on the solid black line. V_2O_5 and MoO_2 experienced CO_2 release during 15-minute equilibration, accounting for the non-baseline appearance of the two curves.

As shown in Table 6-1, both V_2O_5 and MoO_2 released a significant portion of absorbed CO_2 in the course of applying a temperature ramp to 86 °C. WO_3 required a longer period of time for the full effect of the presence of the metal oxide to be revealed, yet the total amount of CO_2 released was still higher after 60 minutes of elevated temperatures compared to the base case of only MEA. These 3 metal oxides increased the overall CO_2 amount released, but the rest of the metal oxides lowered the overall amount of CO_2 released.

Table 6-1. CO_2 desorption data using CO_2-loaded MEA (3M) and 1.5 g of metal oxides.

MO_x	Cumulative %CO_2 released by 30 min at 86 °C	Cumulative %CO_2 released by 60 min at 86 °C	Time (min), temperature (°C) of max CO_2 release peak	IEP[a]
MEA only	31.6	49.2	14, 84	N/A
WO_3	34.7	60.0	13, 73	0.2 – 0.5
V_2O_5	45.8	69.0	10.5, 76	1 – 2
MoO_2	65.8	76.2	10, 82	2.5
MnO_2	29.8	46.8	15, 84	4 – 5
Cr_2O_3	29.7	46.8	15, 84	7

α-Al_2O_3	29.4	47.0	14, 84	8 – 9
Si_3N_4	29.3	46.5	15, 84	9
MgO	13.7	22.3	13, 80	12 – 13

[a] Kosmulski, M. "Chemical Properties of Material Surfaces", Marcel Dekker, 2001.

Time and temperature for the maximum CO_2 release for these three were lower than compared to the MEA-only case (14 minutes, 84 °C): 13 minutes (73 °C) for WO_3, 10.5 minutes (76 °C) for V_2O_5, and 10 minutes (82 °C) for MoO_2. The peak CO_2 release for the other metal oxides were within 1 minute of the MEA-only case, further suggesting that they had little influence on the overall CO_2 desorption process. PZ appears to give similar trends as MEA, but data collection was incomplete to be conclusive.

One materials issue about V_2O_5 and MoO_2 is that they dissolve during the process, which is undesirable for our current process. However, a regeneration and recovery scheme can be a technical solution to this problem, especially if associated costs can be quantified.

UV-vis absorbance measurements of metal oxides in the 3 M solutions of MEA were performed to gain a better understanding of the possible mechanisms of interaction with V_2O_5, MoO_2, WO_3, and α-Al_2O_3. As shown in Figure 6-5, each spectrum represents a five-minute reaction interval between measurements, for a total of 30 minutes.

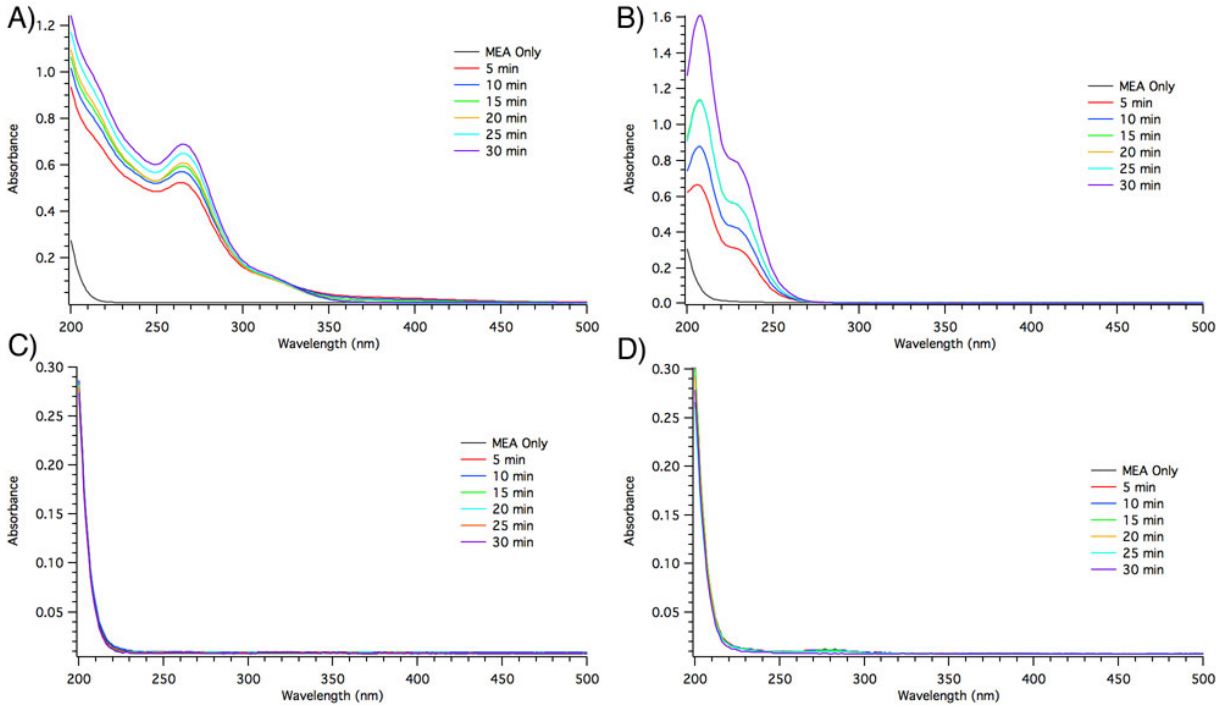

Fig. 6-5 Combined UV-vis absorbance measurements of 1.5 g of metal oxide in 15 mL of 3 M MEA at room temperature, Aliquots were removed every five minutes and analyzed by absorbance measurements. From the top left, A) vanadium oxide (V_2O_5), B) molybdenum oxide (MoO_2), C) tungsten oxide (WO_3), and D) α-alumina (Al_2O_3).

As demonstrated by absorbance measurements in Figure 6-5, WO_3 and Al_2O_3 have no observable interaction with the amine in solution, as evident from the lack of no additional absorbance peaks nor any observable shift in the MEA peak. In the case of addition of V_2O_5 there is a rapid and obvious change in absorbance spectra after five minutes, as detailed by the appearance of peaks at 275 nm and at 320 nm along with changes to the appearance of the MEA absorbance peak by way of a significant increase in overall absorbance intensity and additional shoulders of other absorbance peaks. Figure 6-6 shows the observed color changes in solution as the reaction progresses from initial 0 minutes to conclusion at 30 minutes, followed by a final observation at 60 minutes.

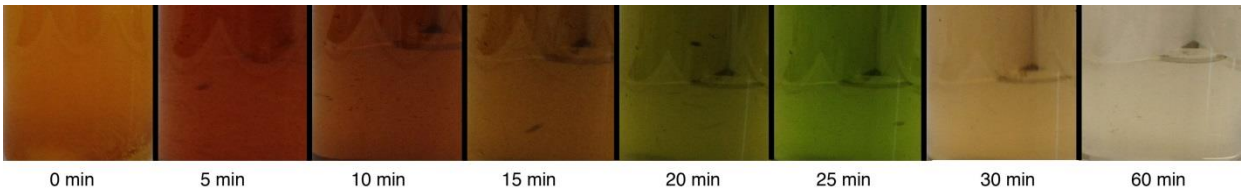

Fig. 6-6 Changes in solution color of 3 M MEA with 1.5 g of V_2O_5 over a 60-minute period. The color change from yellow-orange to green is likely due to the reduction of vanadium in the presence of ethanolamine (V^{5+} to V^{3+}).

There have been previous reports of complexes between reduced vanadium and ethanolamine in aqueous solutions that results in the reduction of vanadium.[1] A proposed possible structure is presented in Figure 6-7. We are unsure of the actual structure, whether or not an actual complex forms, and the oxidation state of the vanadium. All of the presented states are estimated from previous literature observations; we have no experimental evidence to support this structure.

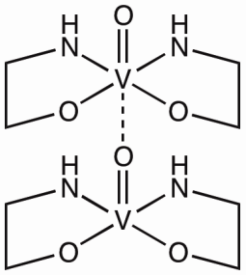

Figure 6-7: Possible $VO(MEA)_2$ complex that forms upon the reduction of V^{5+} to V^{3+} in the presence of ethanolamine.

In an effort to elucidate the possible interaction of V_2O_5 with ethanolamine, two different solvents were employed: dimethyl sulfoxide (DMSO) and methanol (MeOH). The hypothesis was that disrupting both the solvent polarity and the hydrogen bonding ability would alter the interaction of ethanolamine with V_2O_5 and

provide us with some possible information about the structure and nature of the possible $VO(MEA)_2$ complex.

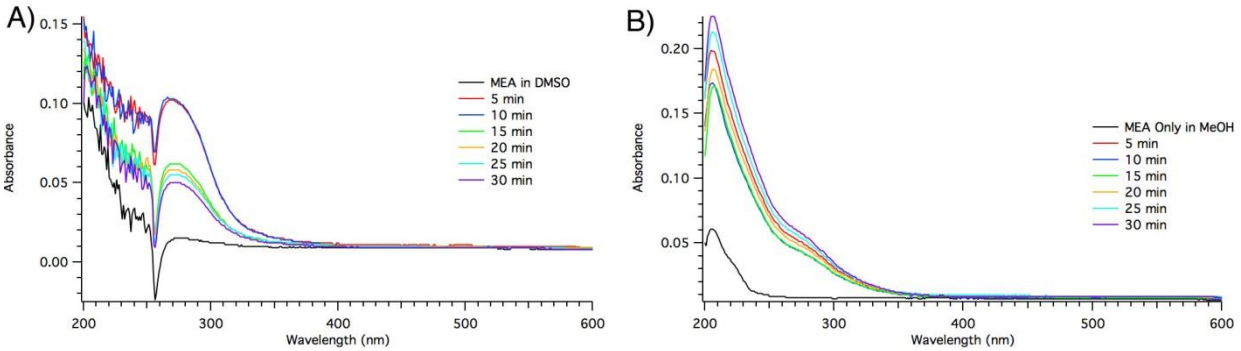

Fig. 6-8 UV-vis absorbance traces of samples from 3 M MEA in A) DMSO and B) MeOH with 1.5 g of V_2O_5 analyzed in five minute intervals for a total of thirty minutes.

Figure 6-8 shows the UV-vis absorbance results for DMSO and MeOH as the primary solvents in 3 M MEA along with 1.5 g of V_2O_5. In DMSO, the peak for MEA is redshifted, landing at 280 nm (compared to below 200 nm in water) and after each five minute aliquot no additional absorption peaks were observed. The increase in absorbance intensity of MEA suggests some interaction with V_2O_5, but no visible reduction occurs, as shown in the solution colors in Figure 6-9.

Fig. 6-9 Solution colors of 3 M MEA in DMSO with 1.5 g of V_2O_5. Beginning from the left: 0 min, 5 min, 10 min, 15 min, 20 min, 25 min, 30 min, and 120 min, no reduction of V^{5+} to V^{3+} was observed in DMSO.

Like DMSO, MeOH does not have any visible reduction in V_2O_5, as shown in Figure 6-10. However, in UV-vis absorbance traces, there is a second peak slowly increasing in intensity at 285 nm, which is likely due to some limited interaction with MEA and V_2O_5. Again, an increase in MEA peak intensity is observed. As to the nature and effects of this interaction, the results are currently unknown with these current limited experiments. In both DMSO and MeOH, V_2O_5 did not fully dissolve, unlike in water.

Fig. 6-10 Solution colors of 3 M MEA in MeOH with 1.5 g of V_2O_5. Beginning from the left: 0 min, 5 min, 10 min, 15 min, 20 min, 25 min, 30 min, 60 min, and 120 min, Like in DMSO, there is no observable color change in the solution, aside from a slight discoloration at the end at 120 minutes, thus suggesting that there was no reduction of V^{5+} to V^{3+}.

Interactions of molybdenum oxide (MoO_2) also had a significant effect on UV-vis absorbance experiments in 3 M MEA. Like V_2O_5, MoO_2 both dissolved and underwent a change in solution color as the experiment progressed. Peaks appeared at 211 nm and at 235 nm, indicating that MoO_2 was somehow interacting with MEA in solution, but as to what extent is unknown as we have yet to find any literature discussing MEA interactions with molybdenum oxides.

The other two metal oxides, WO_3 and Al_2O_3, were examined for stability in MEA solutions showed no significant interactions as evident from any absorbance peaks appearing at any time in the course of the experiment. It is likely that the other metal oxides previously examined, outside of MgO, have little to no interaction with MEA

and were thus not examined. MgO, however, is likely to have a different interaction as it binds CO_2, which likely accounts for the overall decrease in total amount of CO_2 desorbed from a previously loaded amine solution. We have yet to examine what effect CO_2 loaded amine solutions have on the stability of metal oxides. The presence of CO_2 may also alter the interaction and stability of the metal oxides, which may be useful when applying these substances to a desorber-type setup.

In second set of experiments, we used PZ because it is resistant to oxidative degradation, has less volatility than MEA, and is not corrosive to stainless steel [15]. Similar trends were observed for PZ as that of MEA (Figure 6-11). Table 6-2 shows the amount of CO_2 desorbed. Here, both MoO_2 and V_2O_5 showed similar enhancement of CO_2 desorption. Both the oxides increased the amount of CO_2 desorption from 58% to approximately 80%. WO_3 did not dissolve, which implies that foams made of WO_3 may be suitable in a stripper unit. V_2O_5 only partially dissolves in PZ unlike MEA, which can make its recovery easier from PZ than MEA. V_2O_5 can also be used for desorption if it can be recovered after desorption process. Overall, PZ showed better performance than MEA.

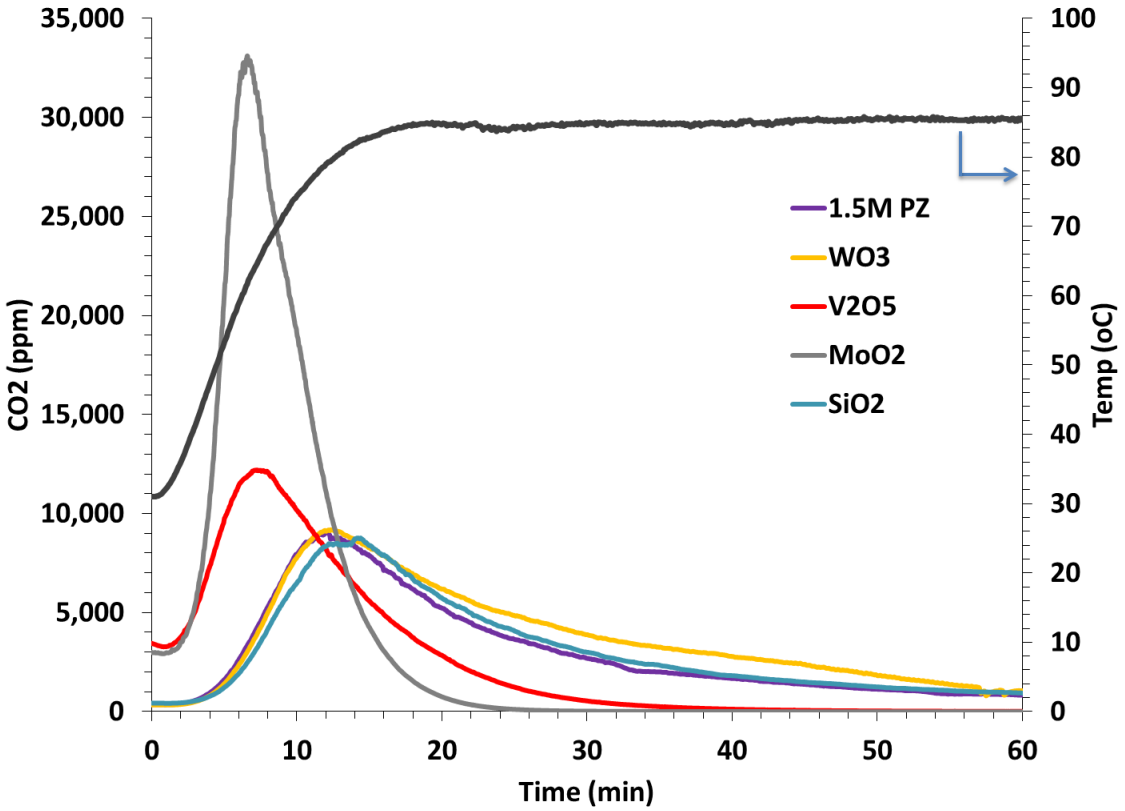

Fig. 6-11 Desorption of CO_2 from 1.5 M PZ with 1.5 g of various metal oxides. A typical temperature ramp at 2.3°C/min is displayed on the right y-axis. Reference typical CO_2 desorption from 1.5 M PZ is displayed with the solid purple curve.

Table 6-2. Amount of CO_2 desorbed from CO_2-loaded PZ

Metal oxide	***%CO_2 desorbed***[a]
No metal oxide	58.1
WO_3	69.2
MoO_2	79.1
V_2O_5	81.1
SiO_2	58.9

[a] %CO_2 desorbed= Total CO_2 desorbed in 60 min*100/total-CO2-absorbed

6.2 Catalytic desorption of CO_2 using supported metal oxides

As we discussed previously, we observed some leaching of the metal oxide materials during the experiment. Leaching of active metal is a common phenomenon in solid-liquid systems [16, 17]. This phenomenon is likely due to the formation of a complex between MEA and metal oxide [18]. Thus we tried to use some supported catalysts which could exhibit less leaching than metal oxides only.

Supported metal oxides were tested for promoting CO2 desorption as a catalyst. Table 6-3 show different materials used in present work, their isoelectric points (IEP), textural, properties, surface area, and surface density. IEP represents the pH at which an immersed solid oxide surface has zero net charge [19]. For solid oxides and hydroxides, IEP is indicative of their acidity and basicity. Acidic materials have low IEP values for e.g., WO_3 and MoO_3, and basic materials have high IEP for e.g., MgO [20].

All the materials were purchased from different vendors except $MOx/\gamma\text{-}Al_2O_3$, which were synthesized in our laboratory. First, an ammonium salt of the desired metal is dissolved in DI water and 10%NH_4OH. Thereafter, $\gamma\text{-}Al_2O_3$ powder is added to the aqueous solution of metal salt, which is left stirring for 20 minutes at room temperature. The material is then placed in the oven to dry for 21 h at 105°C. Activation of the catalyst and removal of moisture from the voids (calcination) is carried in a furnace at 450°C for 8 h in He/air. Supported metal oxides have higher surface areas than unsupported counterparts. This is due to higher surface area of $\gamma\text{-}Al_2O_3$.

Table 6-3. Supported and unsupported metal oxide materials tested

Material	**Isoelectric Point (IEP)**	**Surface Area (m^2/g)**	**Surface Density ($atoms/nm^2$)**
WO_3	0.3	1.2	--
WO_3 (54.9 wt%) /$\gamma\text{-}Al_2O_3$	--	49.3	43.9
V_2O_5	1-2	4.5	--
V_2O_5 (3.0 wt%)/$\gamma\text{-}Al_2O_3$	--	137.9	7.0
MoO_3	2.5	0.9	--
MoO_3 (14.3 wt%) /$\gamma\text{-}Al_2O_3$	--	80.0	24.3
$\gamma\text{-}Al_2O_3$	7-8	144.4	--
MgO	12-13	115.8	--

Table 6-3 shows different materials, CO_2 released/desorbed and the temperature range during ramp stage. It also shows CO_2 released/desorbed and the average

temperature for each material during soak stage, and total CO_2 released/desorbed after 60 min. CO_2 released shown in the table is as calculated as follows:

$$\%CO2\ \text{released/desorbed} = \frac{100 \times \text{Amount of CO2 released from MEA}}{\text{Total CO2 absorbed by MEA}} \qquad (6\text{-}1)$$

In the first column, wt% for supported oxides corresponds to WO_3 for tungsten oxide, MoO_3 for molybdenum oxide, and V_2O_5 for vanadium oxide.

Table 6-4. Amount of CO_2 desorbed from CO_2-loaded MEA

Material	Surface Acidity Characteristic	%CO_2 released (Ramp)	Temperature Range (°C)	%CO_2 released (Soak)	Average Temperature (°C)	% CO_2 released after 60 min
None	---	13.6	41-82	25.3	84	38.9
WO_3	Strongly acidic	21.3	42-83	32.7	85	54.0
WO_x/γ-Al_2O_3 (54.9 wt% WO_3)	Acidic	12.9	41-87	34.6	90	47.5
MoO_3	Strongly acidic	46.3	41-82	20.3	84	66.5
MoO_x/γ-Al_2O_3 (14.3 wt% MoO_3)	Weakly Acidic	24.0	41-85	28.3	84	52.2
V_2O_5	Strongly acidic	36.0	40-83	23.3	84	59.2
VO_x/γ-Al_2O_3 (3.0 wt% V_2O_5)	Weakly acidic	14.8	43-94	48.7	91	63.6
γ-Al_2O_3	Weakly acidic	13.7	42-85	25.7	89	39.4
MgO	Basic	3.6	43-94	21.2	95	24.8

WO_3 enhanced CO_2 release/desorption from 38.9% to 54%. CO_2 release (21.3%) was significantly higher than the baseline case during ramp stage. CO_2 release/desorption increased to 32.7% during soak time. Overall, it released 15.1% more CO_2 than the baseline case.

As expected, $WO_3/\gamma\text{-}Al_2O_3$ enhanced the CO_2 release/desorption from 38.9% to 47.5%. CO_2 release (12.9%) was less than the baseline case during ramp stage. $WO_3/\gamma\text{-}Al_2O_3$ increased the CO_2 release/desorption to 34.6% during soak time. Overall, it released approximately 8.6% more CO_2 than the baseline case but less than WO_3 only.

Addition of MoO_3 resulted in significant increase in total CO_2 release (66.5%). During ramp stage, it increased CO_2 release to 46.3%, a five-fold increase. However, it had less CO_2 release/desorption (20.3% compared to 25.3% of the baseline case) during soak time because it released large amount of CO_2 during ramp stage. Overall, it released 27.6% more CO2 than the baseline case.

$MoO_3/\gamma\text{-}Al_2O_3$ resulted in significant increase in CO_2 release (52.2%), however less than MoO_3 only. During ramp stage, CO_2 release (24%) was around two times more than the baseline case. It also has more CO_2 release/desorption (28.3% compared to 25.3% of the baseline case) during soak time unlike MoO_3. Overall, it released 13.3% more CO_2 than the baseline case.

Addition of V_2O_5 increased the CO_2 release/desorption from 38.9% to 59.2%. CO_2 release (36%) was more than the baseline case during ramp stage. However, it

had slightly less CO_2 release/desorption (23.3%) during soak time. Overall, it released approximately 20.3% more CO_2 than the baseline case.

Addition of $V_2O_5/\gamma\text{-}Al_2O_3$ to MEA during CO_2 desorption step enhances its release/desorption significantly (from 38.9% to 63.6%). CO_2 release is almost the same (~14.8%) as the baseline case during ramp stage. However, during soak time it increased CO_2 release/desorption to 48.7% from 25.3% of the baseline case. Overall, it released approximately 24.7% more CO2 than the baseline case.

Both supported and unsupported metal oxides enhanced the CO_2 release/desorption. For supported metal oxides, this enhancement could be due to $\gamma\text{-}Al_2O_3$ because it is slightly acidic. To test this hypothesis, we conducted experiments with $\gamma\text{-}Al_2O_3$ only and found that it had the same CO_2 release as the baseline case for both during ramp and soak stages. Therefore, CO_2 release is due to MOx not the support.

It can also be inferred from the table that MgO has significantly lower CO2 release than the baseline case because it is basic in nature and absorbs CO_2 [21].

6.3 Material Stability Tests

Figure 6-12 shows MEA before and after an experiment. The supported catalysts exhibited less leaching which shows that $\gamma\text{-}Al_2O_3$ helps reducing the dissolution of metal oxide. For example, the amount of W leached was 53%, however it reduced to 24% when $\gamma\text{-}Al_2O_3$ was used as a support. Similarly, the leaching reduced to 68% from 96% in the case of MoO_3, and 79% from 88% in the case of V_2O_5. We did not

observe the dissolution of γ-Al_2O_3. When the pH of the solution was decreased, the material precipitated back. This pH swing can be used to recover the material.

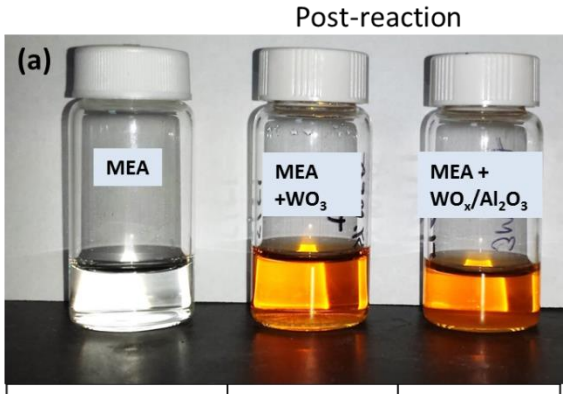

Amount of W dissolved (%)	53	24

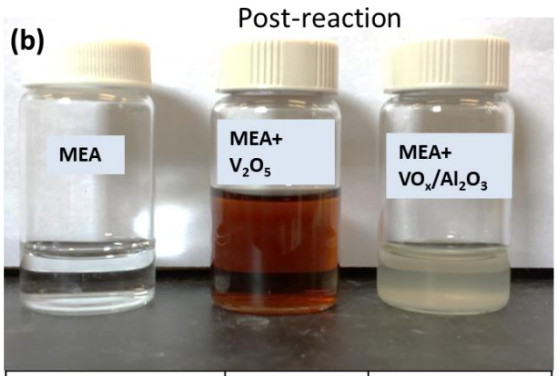

Amount of V dissolved (%)	88	79

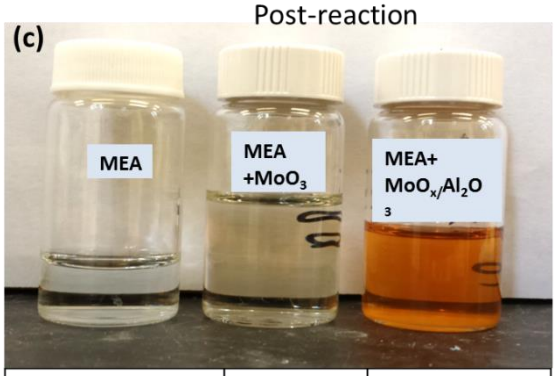

Amount of Mo dissolved (%)	96	68

Fig. 6-12 Change in color of MEA and amount of metal dissolved: (a) WO_3, WO_x/γ-Al_2O_3 ; (b) V_2O_5, VO_x/γ-Al_2O_3(c) MoO_3, MoO_x/γ-Al_2O_3

As discussed above, we observed leaching/dissolution of our materials which is a common phenomenon in solid-liquid systems. Dissolution is likely due to a

reaction between metal oxide and MEA. Dissolution of Al_2O_3 was not observed. Al_2O_3 helps reducing the dissolution of metal oxide.

The lowest leaching was observed for $WO_x/\gamma\text{-}Al_2O_3$. Whereas, MoO_3 leached more than any other material studied in the current work. It was found that $\gamma\text{-}Al_2O_3$ helps in mitigating this issue/problem. For instance, in the case of WO_3, $\gamma\text{-}Al_2O_3$ helped in reducing the leaching by over 50%. This shows that catalyst preparation method can be optimized to stop the leaching.

7. Model development for CO_2 capture in integrated absorber/desorber unit

7. 1 1-D model of CO_2 absorption in ceramic foam column

In this task, we will develop a two-dimensional (2-D) mathematic model to simulate the CO2 capture in combined ceramic foam absorber/desorber unit, and optimize this system to attain the best process performance. Before that, one subtask is to develop a one-dimensional (1-D) mathematical model and numerically simulated CO_2 absorption through a ceramic foam column. After validating the model with the experimental results, we will perform a parametric study on the effects of gas velocity, liquid velocity, and solvent CO2 loading on CO2 removal efficiency, and the influence of liquid-to-gas ratio (L/G) on temperature distribution within the column. In 1-D simulation, we will choose a 30 wt% DGA solution as the liquid amine absorbent. The hydrodynamic characteristics (e.g., pressure drop, flooding point and liquid holdup) of α-Al2O3 ceramic foams with different pores-per-inch (PPI) numbers will be studied in gas-liquid counter current operation.

7.1.1 Chemistry of CO_2 absorption by DGA

DGA, as a primary amine, is widely used for acid gas treatment. The kinetics for the reaction of CO_2 and DGA has previously been studied extensively [22-25]. The following two reversible reactions are usually used to represent the reactions between CO_2 and DGA solution:

$$CO_2 + H_2O + DGA \Leftrightarrow DGACOO^- + H_3O^+ \quad (7\text{-}1)$$

$$CO_2 + OH^- \Leftrightarrow HCO_3^- \quad (7\text{-}2)$$

The contribution of reaction (2) is usually ignored due to the very low OH^- concentration (10^{-5}-10^{-4} M) relative to DGA concentration (~3 M), and the CO_2 reaction rate is assumed to follow the following elementary rate expression:

$$r_{CO_2} = k_{DGA}[CO_2][DGA] - k_{DGA} / K_{DGA,K}[DGACOO^-][H_3O^+] \quad (7\text{-}3)$$

or

$$r_{CO_2} = k_{DGA}[DGA]([CO_2] - [CO_2]_{eq}) \quad (7\text{-}4)$$

where $[CO_2]_{eq}$ is the equilibrium concentration of CO_2 in solvent.

The rate constant k_{DGA} can be expressed as

$$k_{DGA}(m^3 kmol^{-1} s^{-1}) = k_{DGA(298K)} \exp(-\frac{E_a}{R}(\frac{1}{T} - \frac{1}{298.15})) \quad (7\text{-}5)$$

in which $k_{DGA(298K)} = 6.66 \times 10^3 m^3 kmol^{-1} s^{-1}$; E_a=40.1 kJ/mol, and T is the absolute temperature, K [22].

Five reactions were used to describe the equilibrium concentrations of all chemical species in the DGA-H_2O-CO_2 system [26]:

$$2H_2O \xleftrightarrow{K_W} H_3O^+ + OH^- \quad (7\text{-}6a)$$

$$DGAH^{+} + H_2O \xleftrightarrow{K_{DGAH+}} DGA + H_3O^{+} \quad (7\text{-}6b)$$

$$DGACOO^{-} + H_2O \xleftrightarrow{K_{DGACOO^-}} DGA + HCO_3^{-} \quad (7\text{-}6c)$$

$$CO_2 + 2H_2O \xleftrightarrow{K_{CO2}} H_3O^{+} + HCO_3^{-} \quad (7\text{-}6d)$$

$$HCO_3^{-} + H_2O \xleftrightarrow{K_{HCO_3^-}} H_3O^{+} + CO_3^{2-} \quad (7\text{-}6e)$$

The chemical equilibrium constants, which are a strong function of temperature *T*, can be expressed as:

$$\ln K_{eq} = A + B/T + C\ln(T) + DT \quad (7\text{-}7)$$

where K_{eq} is the equilibrium constant for equations 6a-e; A, B, C and D are adjustable parameters, which are available in Table 7-1.

The relationship between gaseous CO_2 and CO_2 in aqueous DGA-H_2O-CO_2 system

can be expressed by Henry's Law,

$$P_{CO_2} = H_{CO_2,L} \times [CO_2] \quad (7\text{-}8)$$

where P_{CO2} is CO_2 partial pressure; $H_{CO_2,L}$ is the Henry's law constant of CO_2 in aqueous DGA solution; and [CO_2] is CO_2 concentration in liquid phase. Calculations of $H_{CO_2,L}$ at different temperatures are detailed in the Appendix A.

Table 7-1. Parameters A, B, C and D for equilibrium constants in Eq. 7-7

Reaction	A	B	C	D	Reference
6a	132.899	-13445.9	-22.4773	0	[27]
6b	-13.3373	-4218.708	0	0	[28]
6c	3.661096	-3696.1689	0	0	[28]
6d	231.465	-12092.1	-36.7816	0	[29]
6e	216.05	-12431.7	-35.4819	0	[27]

7.1.2 Numerical model development

The ceramic foam column was modeled as a 1-D counter-current flow CO_2 absorption process (Fig. 7-1). The following assumptions were applied: (1) steady state operation; (2) the solvent was an incompressible and Newtonian fluid; (3) negligible vapor pressure of water and DGA; (4) uniform liquid velocity and gas velocity fields throughout column; and (5) Henry's law to describe the relation between the solution and gas-phase concentrations for CO_2 in the gas-liquid interface.

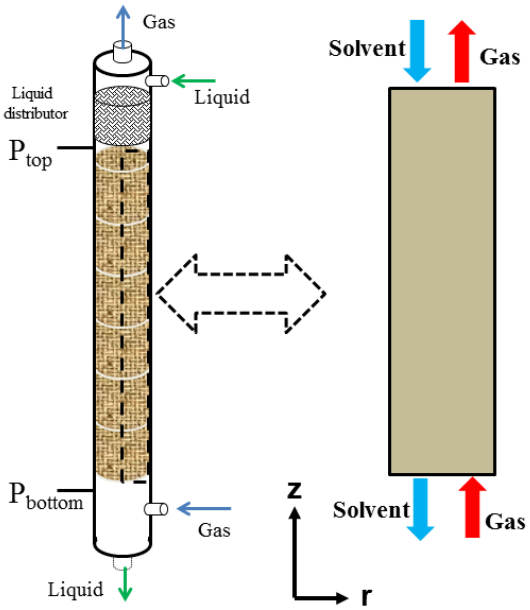

Figure 7-1 Schematic of CO_2 absorption process in the ceramic foam.

Momentum equations

For stationary, creeping and incompressible flow, the inertial terms can be neglected. Therefore, the momentum balance equations for the gas and liquid flows can be simplified into Darcy's Law:

$$-\frac{dP_G}{dz}-\frac{\mu_G}{k_{rg}k}U_G+\rho_G\vec{g}=0 \qquad (7\text{-}9)$$

$$-\frac{dP_L}{dz}-\frac{\mu_L}{k_{rw}k}U_L+\rho_L\vec{g}=0 \qquad (7\text{-}10)$$

Under the assumption of having a uniform velocity throughout the ceramic foam column and the liquid saturation being uniformly distributed, the pressure gradients of respective gas phase and liquid phase are equal. Therefore,

$$\frac{dP_G}{dz} = \frac{dP_L}{dz} \qquad (7\text{-}11)$$

Within the ceramic foam, the pressure difference between the gas and liquid phases (also called gas-water capillary pressure P_c) is a function of liquid saturation (S_L),

$$P_G - P_L = P_c(S_L) \qquad (7\text{-}12)$$

in which, subscripts G or L represents gas or liquid phase, respectively; ρ is the density; g is gravitational acceleration; μ is the viscosity; P is pressure, k is the permeability. k_{rw} and k_{rg} are the relative permeability of liquid phase and gas phase, respectively. S_L is liquid saturation, which presents the fraction of the pore space occupied by liquid in the porous medium.

The relative permeability is assumed to be a function of the saturation of each phase [30]. Therefore, gas phase relative permeability (k_{rg}) and liquid phase relative permeability (k_{rw}) can be expressed in terms of gas saturation (S_G) and liquid saturation (S_L) in the following way [31]:

$$k_{rg} = S_G^{n_1} = (1 - S_L)^{n_1} \qquad (7\text{-}13)$$

$$k_{rw} = \left(\frac{S_L - S_L^0}{1 - S_L^0}\right)^{n_2} \qquad (7\text{-}14)$$

The parameters n_1 and n_2 for different types of ceramic foams with different PPI number are reported by Stemmet *et al.* [32].

In equation (14), S_L^0 is the liquid saturation at the static holdup condition and is correlated by Saez and Carbonell [31],

$$S_L^0 = [\varepsilon(20 + 0.9\,\mathrm{Eo}^*)]^{-1} \qquad (7\text{-}15)$$

in which, the dimensionless parameter *Eo** is defined as,

$$Eo^* = \frac{\rho g d_e^{\,2} \varepsilon}{\sigma(1-\varepsilon)^2} \qquad (7\text{-}16)$$

where ε is the porosity of ceramic foam; g is gravity acceleration; d_e is equivalent diameter of foam; σ is surface tension of liquid.

The liquid saturation can be estimated by the capillary pressure based on the Thomeer model [33],

$$\frac{S_L - S_L^0}{S_{Li} - S_L^0} = \begin{cases} 1.0, & J < J_e = C_1 \\ 1.0 - \exp\left\{ \dfrac{C_2}{\ln\left[\dfrac{C_1}{J}\right]} \right\}, & J > J_e = C_1 \end{cases} \qquad (7\text{-}17)$$

S_{Li} is initial liquid saturation, which is equal to 1 in this study. S_L^0 is the residual liquid saturation, which is defined here as the asymptotic saturation where the capillary pressure approaches infinity. J is the Leverett J function [34], which is a dimensionless function that accounts for capillary pressure as a function of liquid saturation,

$$J = \frac{P_c}{\sigma}\sqrt{\frac{k}{\varepsilon}} \qquad (7\text{-}18)$$

where P_c is capillary pressure, σ is surface tension, k is permeability, ε is porosity.

Mass transport equations

Mass balance of species CO_2 in gas phase and liquid phase can be respectively expressed as

$$\frac{d}{dz}(-D_{CO_2,G}\frac{dC_{CO_2,G}}{dz} + C_{CO_2,G}U_G) = R_{CO_2,\mathrm{G}} \qquad (7\text{-}19)$$

$$\frac{d}{dz}(-D_{CO_2,\mathrm{L}}\frac{dC_{CO_2,\mathrm{L}}}{dz} + C_{CO_2,\mathrm{L}}U_L) = R_{CO_2,L} \qquad (7\text{-}20)$$

in which $D_{CO_2,G}$ and $D_{CO_2,\mathrm{L}}$ are CO_2 diffusion coefficient in gas phase and liquid phase, respectively; $C_{CO_2,G}$ and $C_{CO_2,\mathrm{L}}$ are CO_2 concentration in gas phase and liquid phase, respectively.

The boundary conditions for these equations are as follows,

at z=0, $C_{CO_2,G} = C^0_{CO_2,G}$, $\frac{dC_{CO_2,L}}{dz} = 0$

at z=L, $\frac{dC_{CO_2,G}}{dz} = 0$, $C_{CO_2,\mathrm{L}} = C^0_{CO_2,\mathrm{L}}$

Mass balance of specie DGA in liquid phase can be expressed as,

$$\frac{d}{dz}(-D_{\mathrm{DGA,L}}\frac{dC_{\mathrm{DGA,L}}}{dz}+C_{\mathrm{DGA,L}}U_L)=R_{\mathrm{DGA},L} \qquad (7\text{-}21)$$

subject to the following initial and boundary conditions

at z=0, $\frac{dC_{DGA,L}}{dz}=0$

at z=L, $C_{\mathrm{DGA,L}}=C^0_{DGA,\mathrm{L}}$

in which $D_{\mathrm{DGA,L}}$ is DGA molecular diffusion coefficient in liquid phase; $C_{DGA,\mathrm{L}}$ is DGA concentration in liquid phase.

The source term $R_{CO_2,G}$ for equation (19) is the net mass transfer rate of CO_2 into gas phase, which can be expressed as,

$$R_{CO_2,G}=-K_{ov}a_{eff}[\frac{C_{CO_2,G}}{H}-C_{CO_2,\mathrm{L}}] \qquad (7\text{-}22)$$

The source term $R_{CO_2,\mathrm{L}}$ for equation (20) represents the net CO_2 generation rate in the liquid phase, which is the combination of CO_2 mass transfer and CO_2 reaction,

$$R_{CO2,L}=K_{ov}a_{eff}[\frac{C_{CO2,G}}{H}-C_{CO2,L}]-r_{CO2} \qquad (7\text{-}23)$$

The source term $R_{\mathrm{DGA,L}}$ for equation (21) is the net reaction rate of DGA absorbent in liquid phase, which can be expressed as,

$$R_{DGA,L} = -2r_{CO2} \qquad (7\text{-}24)$$

In equations (22) and (23), K_{ov} is overall mass transfer coefficient for CO_2, which can be described as the combination of liquid phase mass transfer coefficient (K_L) and gas phase mass transfer coefficient (K_G),

$$\frac{1}{K_{ov}} = \frac{1}{K_G} + \frac{1}{K_L} \qquad (7\text{-}25)$$

Gas phase mass transfer coefficient (K_G) in packing column was correlated as [35]

$$\frac{K_G d_e}{D_{CO_2,G}} = 0.054\left(\frac{\mu_G}{\rho_g D_{CO_2,G}}\right)^{0.333}\left(\frac{\rho_g U_G d_e}{\mu_G(1-\varepsilon)}\right)^{0.8} \qquad (7\text{-}26)$$

in which d_e is equivalent pore diameter; μ_G is gas viscosity; and ε is porosity.

Liquid phase mass transfer coefficient (K_L) can be calculated by the following equation,

$$K_L = \sqrt{1 + \frac{k_{obs} C_{DGA,L} D_{CO2,L}}{K_{L,0}^{\ 2}}} \qquad (7\text{-}27)$$

in which k_{obs} is observed reaction rate constant of reaction (1), $K_{L,0}$ is physical mass transfer coefficient in liquid phase.

For laminar liquid flow, the effective interfacial gas-liquid area per unit volume (a_{eff}) can be correlated as [36],

$$a_{eff} = 6.49a^{0.333}\frac{(\rho_L - \rho_g)^{0.5} g^{1/6} \upsilon_L^{1/3}}{\sigma_L^{1/2}} U_L^{1/3} \qquad (7\text{-}28)$$

in which a is geometric surface are of ceramic foam per unit volume, υ_L is kinematic viscosity of solvent, and σ_L is surface tension of liquid.

Energy equations

The differential equations for heat transfer in steady-state in ceramic foam can be described as

For liquid phase

$$\rho_L C_{p,L} U_L \frac{dT_L}{dz} = \frac{d}{dz}(\lambda_L \frac{dT_L}{dz}) + ha_{eff}(T_G - T_L) + R_{CO2,L}\Delta H_R \qquad (7\text{-}29)$$

The boundary conditions imposed on the thermal energy equation for liquid phase are as follows:

at z=0, $\frac{dT_L}{dz} = 0$

at z=L, $T_L = T_L^0$

For gas phase:

$$\rho_G C_{p,G} U_G \frac{dT_G}{dz} = \frac{d}{dz}(\lambda_G \frac{dT_G}{dz}) + ha_{eff}(T_L - T_G) \qquad (7\text{-}30)$$

The boundary conditions imposed on Eq. 30 are as follow

at z=0, $T_G = T_G^0$

at z=L, $\frac{dT_G}{dz} = 0$

The last term in Eq. 29 refers to the heat generation due to the chemical reactions that occur in the solvent phase. The $C_{p,L}$ and $C_{p,G}$ are specific heat capacities for liquid and gas, respectively; λ_L and λ_G are the thermal conductivities for liquid and gas, respectively; ΔH_R is enthalpy change of CO_2 reaction with DGA; and *h* is heat transfer coefficient, which can be approximately calculated by following correlation[37]:

$$h = 1.195 G C_{p,G} [\frac{d_e G}{\mu_G G(1-\varepsilon')}]^{-0.36} Pr_G^{-0.667} \qquad (7\text{-}31)$$

where G is the gas mass flow rate, kg/(m^2s); ε' is operating void space fraction in the packing, $m^3_{void}/m^3_{packed\ volume}$; Pr_G is Prandtl number, and $Pr_G = \frac{\mu_G C_{p,G}}{\lambda_G}$.

Numerical solution

The partial differential equations associated with appropriate boundary conditions, physical and chemical properties, and reaction rate equations were numerically solved via the finite element method using the commercial software COMSOL. The detailed calculations for some physical and chemical properties needed to solve the above model equations are presented in the Appendix A. They include mass transfer coefficients in gas and liquid phase, Henry's Law constants, viscosities, and diffusion coefficients.

7.1.3 Results and discussions

Hydrodynamic behavior study

Liquid holdup and flow regime prediction

The trickle flow regime, *i.e.*, liquid flows down as a laminar film on the foam surface while the gas passes through the remaining void space, only occurs at relatively low liquid holdup. In this regime, gas and liquid have high contact area favorable for mass transfer. With the increase of gas or liquid flow, the liquid holdup increases since the flow of gas opposes the down-flow of liquid in the ceramic foam. As the gas flux or liquid flux increases to a certain value, the trickle flow behavior will begin to change to pulse flow behavior. The trickle-to-pulse flow regime transition point is usually referred to as flooding point.

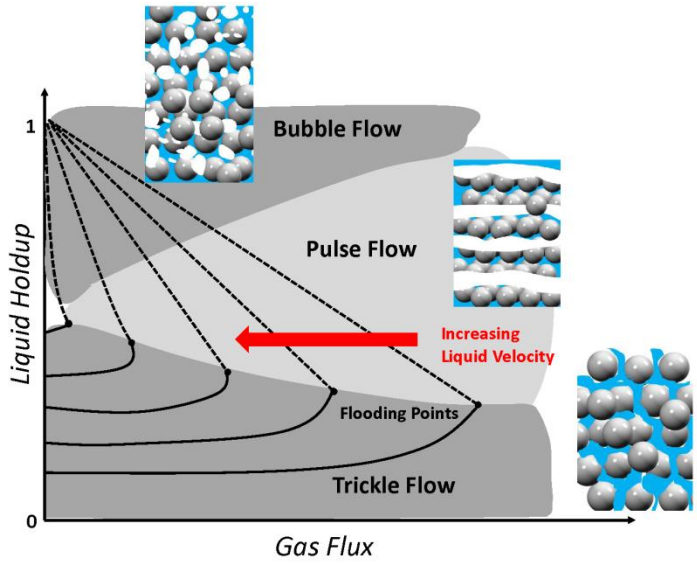

Figure 7-2 Liquid holdup and flow regimes for different gas and liquid fluxes. (Dashed and solid lines represent the contour lines of liquid velocity).

In bubble flow, gas flows up as discrete bubbles through a continuous liquid phase within the foam packing. In this regime, the liquid holdup is usually very high and gas velocity is relatively low. As the gas flux increases or the liquid flux decreases, these bubbles will become larger and coalesce, eventually spanning the width of packing column and developing to the pulse flow regime. For both bubble flow and pulse flow regimes, the mass transfer characteristics deteriorate due to lowered gas-liquid contact area.

Fig. 7-3 shows calculated liquid holdup values for the three ceramic foams with different porosities at varying gas and liquid flow rates. Under trickle flow, we can find that the liquid holdup increases with increasing liquid flow rate at a fixed gas flow rate. As the gas flow rate increases, it opposes the flow of the liquid in the packing column, giving rise to a higher liquid holdup as well. The highest liquid holdup that can be obtained is equal to the porosity of ceramic foam as gas flow rate reduces to zero. The trickle flow regime falls below the loci of points.

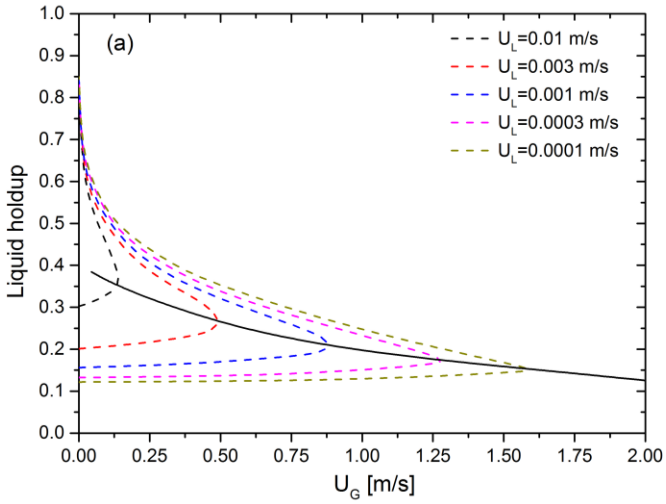
(a)
U_L=0.01 m/s
U_L=0.003 m/s
U_L=0.001 m/s
U_L=0.0003 m/s
U_L=0.0001 m/s
Liquid holdup
U_G [m/s]

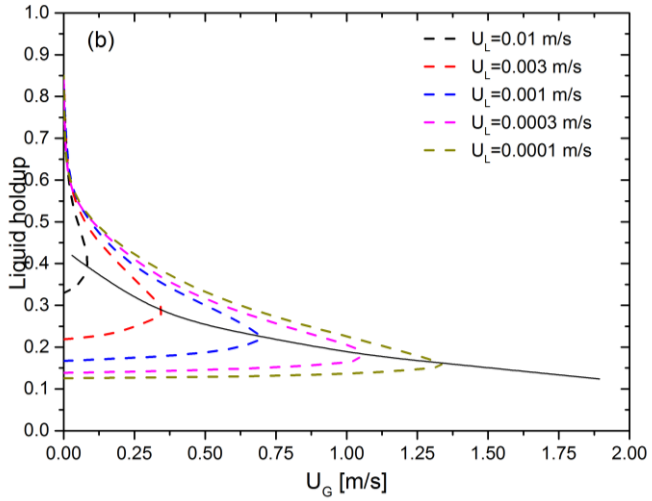
(b)
U_L=0.01 m/s
U_L=0.003 m/s
U_L=0.001 m/s
U_L=0.0003 m/s
U_L=0.0001 m/s
Liquid holdup
U_G [m/s]

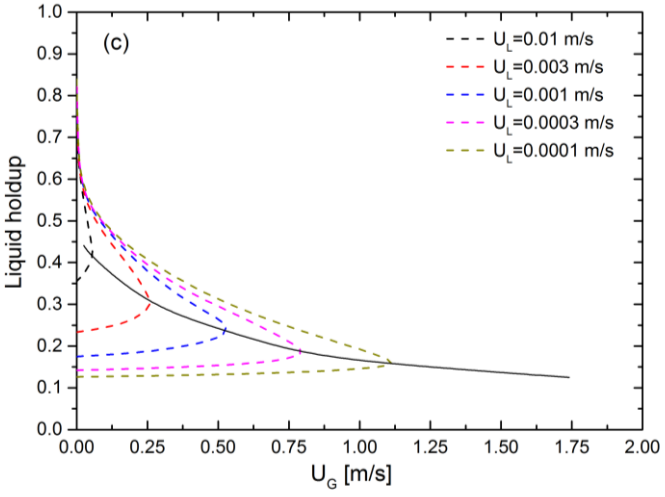
(c)
U_L=0.01 m/s
U_L=0.003 m/s
U_L=0.001 m/s
U_L=0.0003 m/s
U_L=0.0001 m/s
Liquid holdup
U_G [m/s]

Figure 7-3 Modelling results of the liquid holdup versus superficial gas velocity:(a) 20-PPI ceramic foam (b) 30-PPI ceramic foam (c) 45-PPI ceramic foam. (Dashed lines are constant liquid velocities, and solid lines are flooding lines) Operating conditions: packing height: 30.5 cm; liquid phase: water; gas phase: N_2; 25 °C.

By comparing with Fig. 7-3 (a)-(c), we can further find the difference of flooding lines between 20, 30 and 45 PPI ceramic foams. Ceramic foam with a higher PPI number presents a higher risk to reach flooding than ceramic foam with lower PPI. For example, for 20-PPI ceramic foam in Fig.7-3 (a), as the liquid flow rate is 0.0001 m/s, the flooding occurs as gas flow rate increases to 1.6 m/s. However, for 45-PPI ceramic foam in Fig. 7-3(c), the flooding occurs as gas flow rate only exceed 1.125 m/s.

Fig. 7-4 further gives a clear comparison of flooding points for different ceramic foam packings with gas and liquid flow velocities. In a packed column, the gas and liquid flow rates are limited by the tendency of the packing to the liquid flooding. At the flooding point, the pressure drop rises sharply and much of the liquid is carried off mechanically by the gas leaving the top of the packing. As the PPI number of ceramic foam increases, flooding is encountered at lower liquid and gas flow rates. The reason is that the higher PPI ceramic foam has more tortuous flow channels and smaller pore sizes, increasing the restriction to gas and liquid flow.

Therefore, the ceramic foam with lower PPI number may have larger operating flexibility than ceramic foam with higher PPI number.

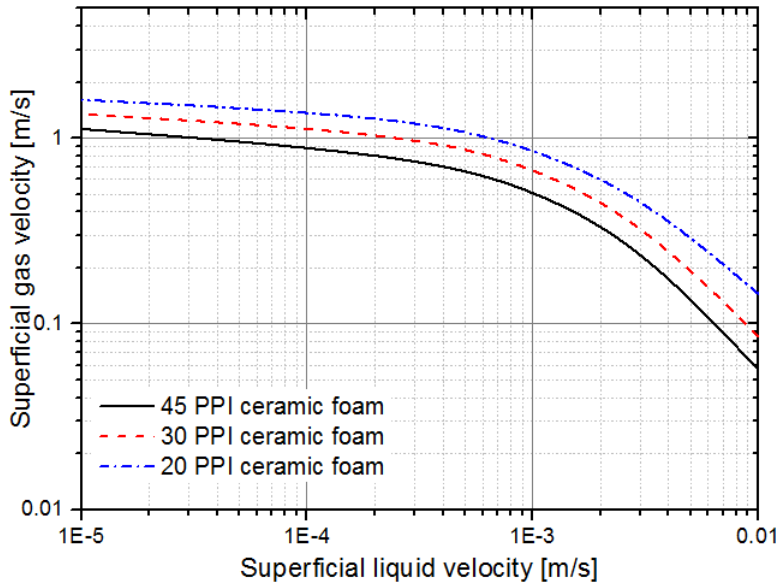

Figure 7-4 Modelling results of gas and liquid velocities at the flooding point for 20, 30 and 45 PPI ceramic foams Operating conditions:packing height: 30.5 cm; liquid phase: water; gas phase: N_2; temperature: 25 °C.

We further investigated the flooding characteristics of the ceramic foam by comparing with other conventional packings via generalized pressure drop correlation (GPDC) charts, as shown in Fig. 8. GPDC chart describes the balance between the vapor momentum and gravity forces acting on the liquid droplets, which is commonly used to predict packing flooding and pressure drops in industry [38]. The abscissa and ordinate of the GPDC chart are the flow parameter and capacity factor, respectively [39]:

$$\text{flow parameter} = \left(\frac{L}{G}\right)\left(\frac{\rho_G}{\rho_L}\right)^{0.5} \quad (7\text{-}32)$$

$$\text{capacity factor} = \frac{G^2 F_p \xi^2 \mu_L^{0.2}}{\rho_G \rho_L g} \quad (7\text{-}33)$$

where F_p is the wet packing factor; and ξ is the ratio between the density of water and the density of liquid. The flow parameter represents the ratio of liquid kinetic energy to vapor kinetic energy, and the capacity factor describes the balance between the up-flowing vapor momentum force, that acts to entrain swarms of liquid droplets, and the gravity force, that resists the upward entrainment.

As can be seen, ceramic foam performed better than the random packing in terms of avoiding liquid flooding, with twice the capacity factor limit of the latter. However, the ceramic foam had a lower capacity factor limit than the structured packing. Thus, ceramic foam has intermediate hydrodynamic performance based on GPDC studies.

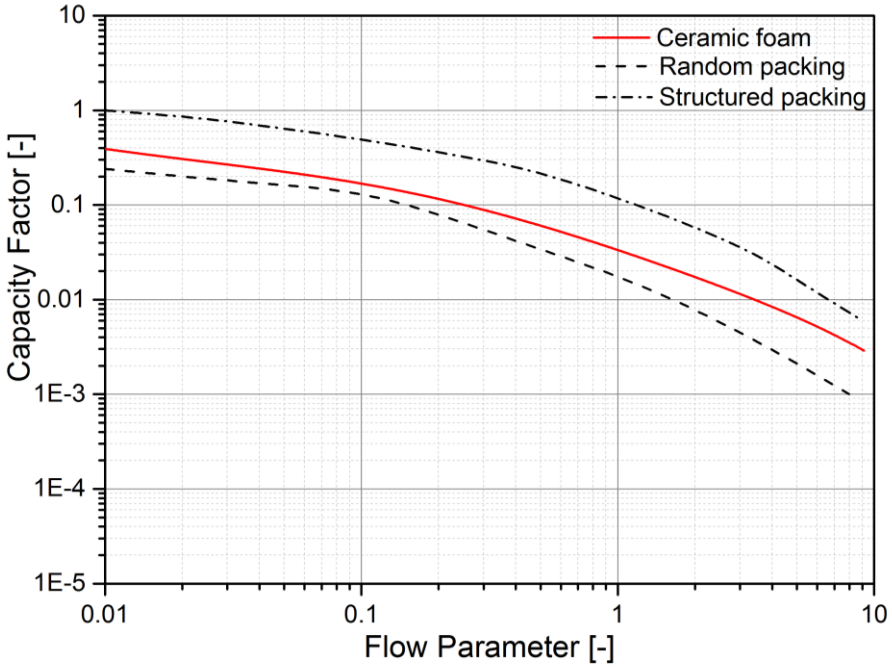

Figure 7-5 Comparison of different packings in generalized pressure drop correlation (GPDC) chart.

Pressure drop prediction of ceramic foams with different PPI number

The pressure drop measurements were performed using N_2-water system at room temperature in the hydrodynamic test setup as shown in section 4. In the measurement, the gas and liquid flow were controlled in the trickle flow regime. 20, 30 and 45 PPI ceramic foam packings were used.

Fig. 7-6(a) shows the predicted and experimental pressure drops in 20, 30 and 45 PPI ceramic foams as a function of gas flow rate. The predicted pressure drops of ceramic foams had fair agreement with measured pressure drops, considering there were no adjustable parameters in the pressure drop model. Pressure drops

increased with faster gas flow velocities or with higher PPI numbers (or lower permeabilities) of the foam. Fig. 7-6(b) shows a similar comparison of the predicted and experimental pressure drops at different liquid and gas flow rates in a 20 PPI ceramic foam column. Higher liquid flow rates increase the pressure drops of the ceramic foam, which can be explained by the decrease of the gas phase relative permeability (k_{rg}) with faster liquid flow velocities. Higher liquid flow rates result in the increase of liquid saturation (S_L) and decrease of gas saturation (S_G), which will decrease the gas phase relative permeability in the ceramic foam, as shown in Equation (13) and (14).

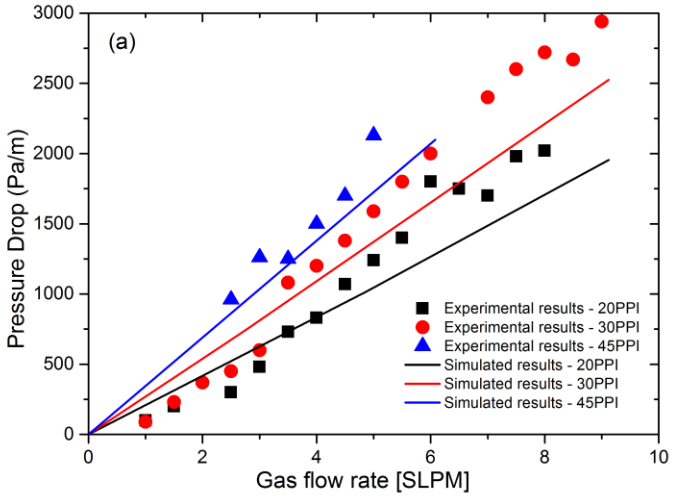

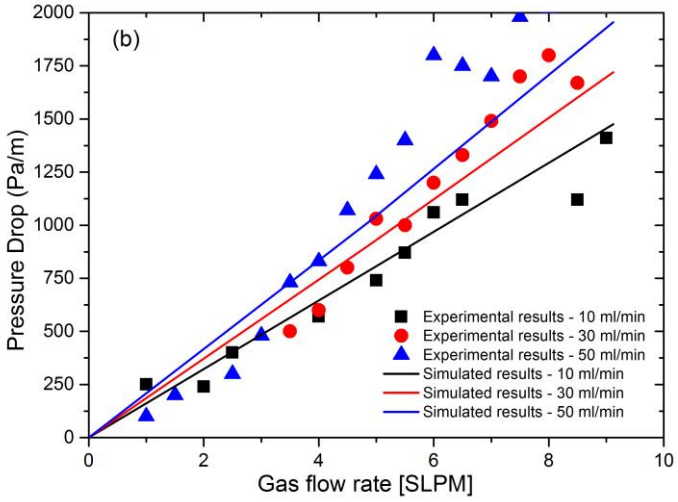

Figure 7-6 Predicted and experimental the pressure drops in ceramic foams as a function of gas flow rate: (a) ceramic foam with different PPI number, liquid flow rate: 50 mL/min; (b) 20-PPI ceramic foam at different liquid flow rates. Operating conditions: Packing height: 30.5 cm; liquid phase: water; gas phase: N_2; temperature: 25 °C.

CO_2 absorption in ceramic foam column

Model validation

CO_2 absorption using 30 wt% DGA was conducted experimentally in a counter-current column packed with a 20-PPI ceramic foam. Fig. 7-7 shows a comparison of experimentally determined and simulated CO_2 removal efficiencies at various gas and liquid flow rates. The predictions agreed well with the experimental results as the height of ceramic foam column is 10.2 cm in Fig.7-7(a). CO_2 removal efficiency increased with higher ceramic foam height (Fig. 7-7(b)). When the packing height doubled to 20.4 cm, a general good accordance between simulation

and experiments was seen, with the exception of CO_2 removal efficiencies at the lowest gas flow rate tested (0.25 SLPM), which were under-predicted.

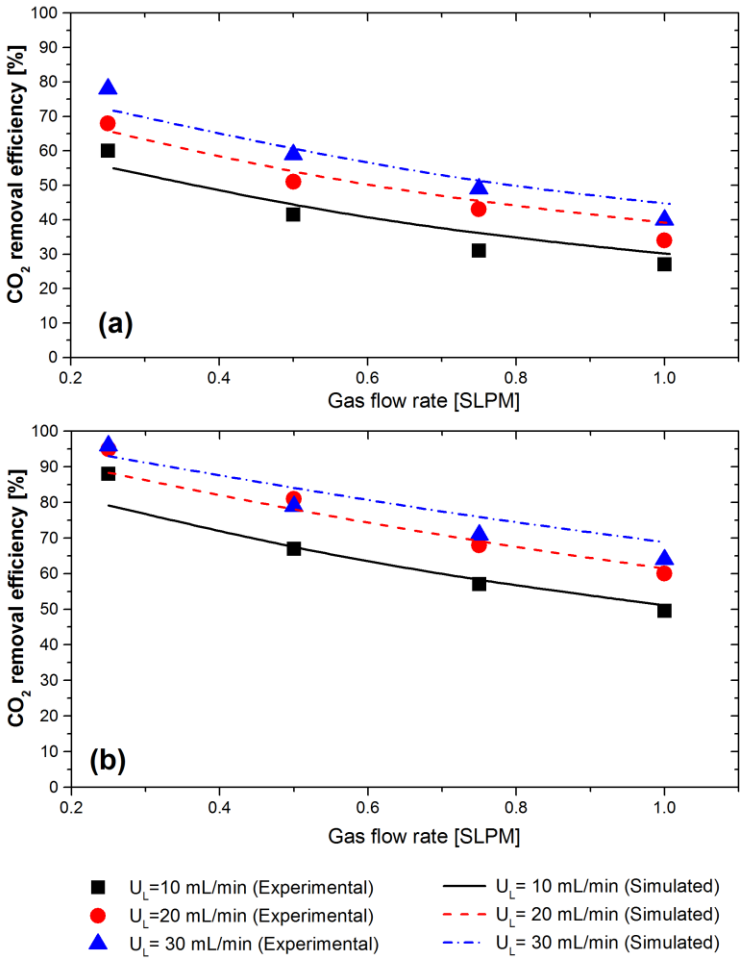

Figure 7-7 Simulated and experimental CO_2 removal efficiency, as a function of gas flow rate at different liquid flow rates: (a) ceramic foam height = 10.2 cm; (b) ceramic foam height = 20.4 cm. Operating conditions: ceramic foam type: 20 PPI; liquid phase: 30 wt.% DGA, gas phase: 13% CO_2/87% N_2; absorption temperature: 25 °C; lean loading: 0.2 mol CO_2/mol DGA.

Parametric study of CO_2 absorption in ceramic foam

Fig. 7-8 shows the simulated concentrations and temperatures profiles along the ceramic foam column. Ordinate describes the dimensionless height of ceramic foam packing. The CO_2 loading of lean DGA solvent is 0.2 mol CO_2/mol DGA at the top of the column (z=H); gas-phase CO_2 concentrations at the bottom of column (z=0) is 13 v/v%. A typical concentration profile of CO_2 in gas phase decreasing along the column height can be seen in Fig. 7-8(a). The CO_2 loading of DGA solvent has a similar distribution along the column, as shown in Fig. 11(b). Fig. 7-8(c) presents the temperature profiles of gas and liquid phases along the column. A maximum temperature (a "temperature bulge ") can be observed near the bottom of the column.

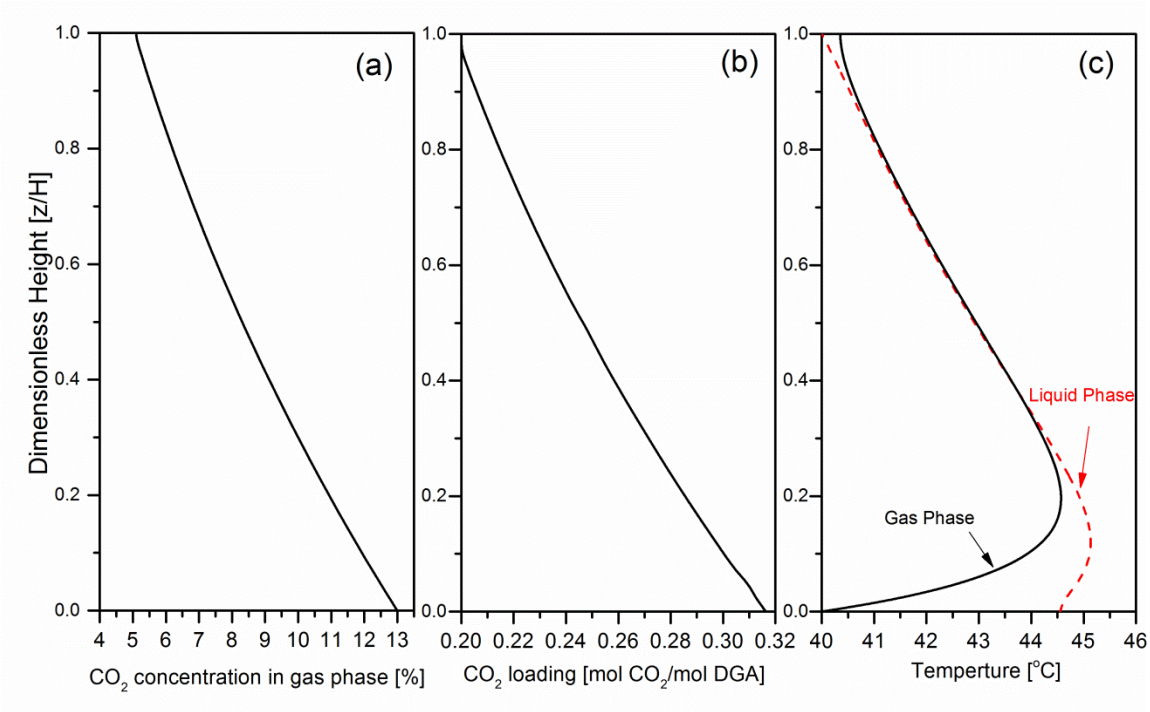

Figure 7-8 Simulation results for CO_2 capture using DGA in a ceramic foam column: (a) CO_2 concentration in gas phase; (b) liquid-phase CO_2 loading; (c) column temperature. Operating conditions:ceramic foam height: 25.4 cm; ceramic foam type: 20 PPI; gas flow velocity: 0.01 m/s; liquid flow velocity: 0.01 cm/s; liquid phase: 30% DGA solvent; gas phase: 13% CO_2/87% N_2; absorption temperature: 40 °C; lean loading: 0.2 mol CO_2/mol DGA.

Effects of liquid and gas velocities

Fig. 7-9 plots the CO_2 concentration profiles in gas phase along the column's length under different liquid flow velocities. A decreasing trend of CO_2 concentration is found along the column's length. But, for the cases with high liquid flow rates, the CO_2 concentration is decreasing slowly gradually. This phenomenon becomes more significant with slower gas flow rate. This is because near the top end of the column, CO_2 concentration is becoming extremely low and close to CO_2 equilibrium, which will lead to a very low CO_2 absorption driving force. The optimal liquid velocities should be those at which CO_2 concentration decreases linearly along the column.

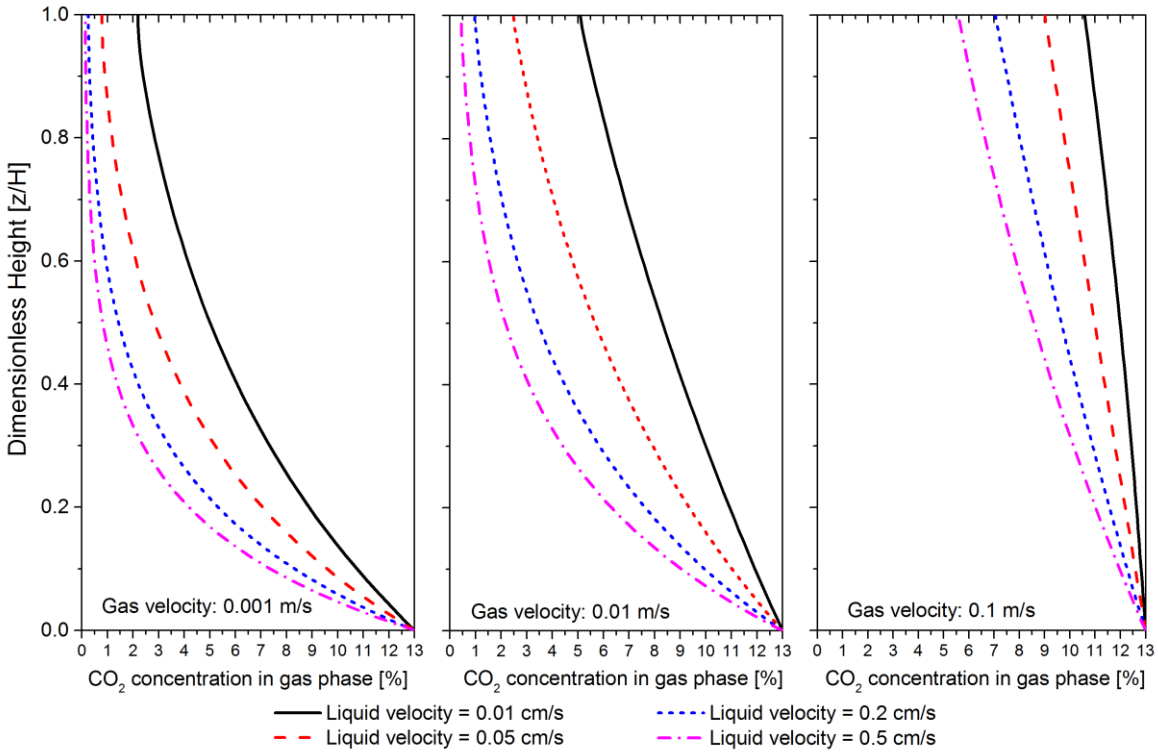

Figure 7-9 Simulated CO_2 concentration profiles of gas phase along ceramic foam column for four different liquid velocities at three different gas velocities. Operating conditions: ceramic foam height: 25.4 cm; ceramic foam: 20 PPI; liquid phase: 30% DGA sovlent; gas phase: 13% CO_2/87% N_2; absorption temperature: 40°C; lean loading: 0.2 mol CO_2/mol DGA.

Fig. 7-10 simulated CO_2 removal efficiencies as the function of liquid velocity and gas velocity for DGA solvents. CO_2 removal efficiency increased as gas flow rate decreased. This can be explained by the change of residence time of CO_2 gas in ceramic foam column as the gas flow rate increases. A higher gas flow rate will result in a shorter residence time, which decreases the reaction time between CO_2 and the DGA absorbent. CO_2 removal efficiency also increased as the liquid flow

rate became faster. This is due to more reactive absorbent to gaseous CO_2 at faster liquid velocity. In the other hand, faster liquid flow will also lead to the increase of effective gas-liquid contacting area and the intensified mass transfer in the liquid phase. However, as the CO_2 removal efficiency exceeds 90%, increased liquid flow rate has minor effect on CO_2 removal efficiency since CO_2 equilibrium is achieved between the gas and liquid phase.

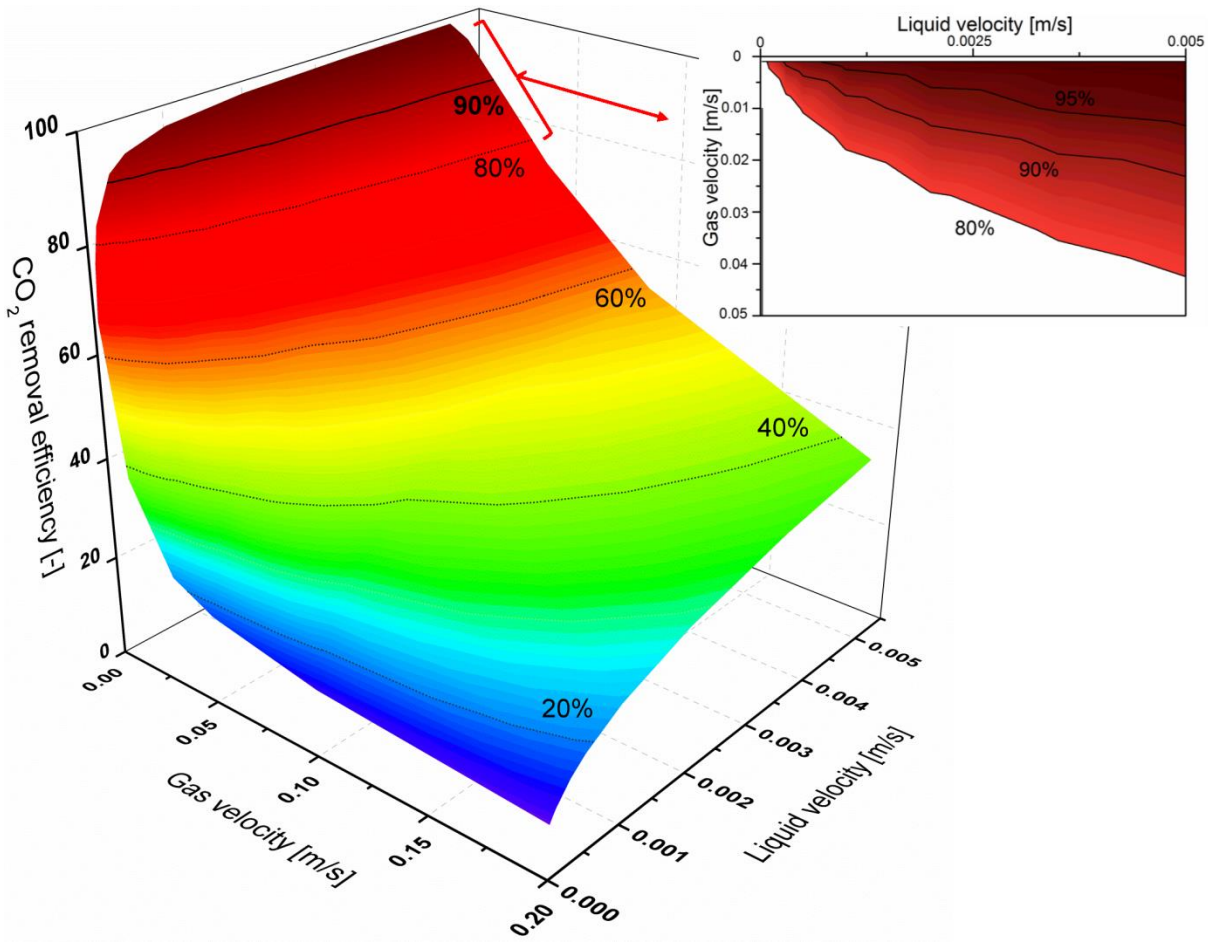

Figure 7-10 Change of CO_2 removal efficiencies under different gas and liquid flow velocities (Inset: gas and liquid velocities yielding >80 % CO_2 removal efficiency). Operating conditions: ceramic foam height: 25.4 cm; ceramic foam type: 20 PPI; liquid phase: 30% DGA solvent; gas phase: 13% CO_2/87% N_2; absorption temperature: 40°C; lean loading: 0.2 mol CO_2/mol DGA.

Effect of CO_2 loading

Fig. 7-11 investigates the change of CO_2 removal efficiency for DGA absorbent with different CO_2 loadings at gas flow velocity of 0.01 m/s. CO_2 removal efficiency decreased as initial CO_2 loading increased. The maximum removal efficiency was achieved when the DGA solvent was free of CO_2. As CO_2 loading increased from 0 to approximately 0.35 mol CO_2/mol DGA, CO_2 removal efficiency was slightly decreased. However, as CO_2 loadings above 0.35 mol CO_2 /mol DGA, CO_2 removal efficiency declined sharply with CO_2 loading. Therefore, the recommended initial CO_2 loading of DGA solution should be less than 0.35 mol CO_2/mol DGA. This phenomenon can be explained by two negative effects of CO_2 loading: the reduction of free amine, and the increase of CO_2 equilibrium pressure in the liquid phase, respectively. Increasing CO_2 equilibrium pressure will decrease CO_2 driving force. As the CO_2 loading is relatively low, the second negative effect is limited, and the decrease of free amine plays a more important role. As CO_2 loading increases to a high level, CO_2 equilibrium pressure will climb sharply. At this moment, the second negative effect becomes significant, which leads to a rapid drop of CO_2 removal efficiency. In Fig. 7-11, a negative CO_2 removal efficiency can even be seen as CO_2 loading reached to 0.5 mol CO_2/mol DGA. This indicates that CO_2 equilibrium pressure is greater than the inlet CO_2 gas phase pressure, thus CO_2 desorption occurs in this condition.

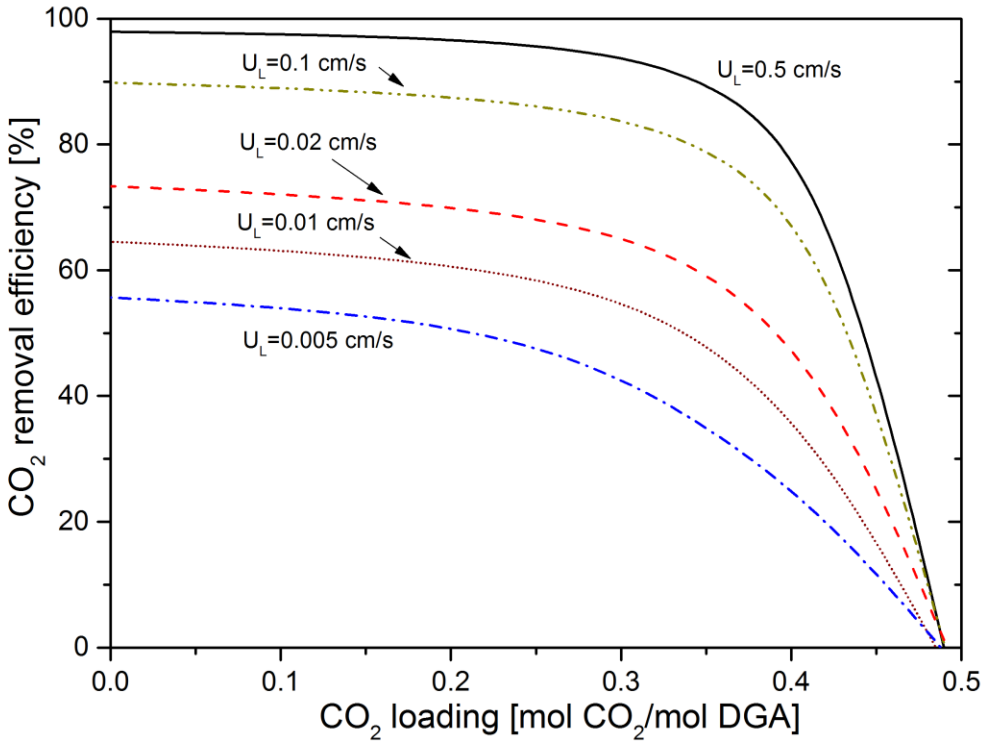

Figure 7-11 Change of CO_2 removal efficiency for DGA solvent with different CO_2 loadings. Operating conditions: ceramic foam height: 25.4 cm; ceramic foam type: 20 PPI; liquid phase: 30 wt.% DGA solvent; gas phase: 13% CO_2/87% N_2; gas flow velocity: 0.01 m/s; absorption temperature: 40 °C.

Temperature profile in ceramic foam column

Fig. 7-12 shows the temperature profiles for gas phase and liquid phase at different liquid flow velocities and gas flow velocities. It can be clearly seen that for all cases, a temperature bulge can be found in the column. The gas phase and liquid phase temperature profiles look similar in shape but will be lagged due to the difference in heat capacities of the two phases and the solvent-to-gas ratio (L/G). Varying solvent-to-gas ratio (L/G) will change the magnitude of

temperature bulge. Lower L/G will result in a more significant temperature bulge in the column.

Fig. 7-12 also reveals the information about the effect of varying the L/G with respect to the temperature bulge location. The primary negative effect of temperature bulge is the reduction of the equilibrium driving force. If there is insufficient solvent related to gas, the greatest absorption rate will occur at the top part of the column. Excess solvent relative to the gas will make the greatest absorption rate near the bottom of the column. The greater heat capacity of the liquid relative to the gas will also tend to push the heat of reaction to the bottom [40]. Therefore, with the increase of solvent flow rate or the decrease of gas flow rate, the location of the temperature bulge shifts from the top of the column to the bottom.

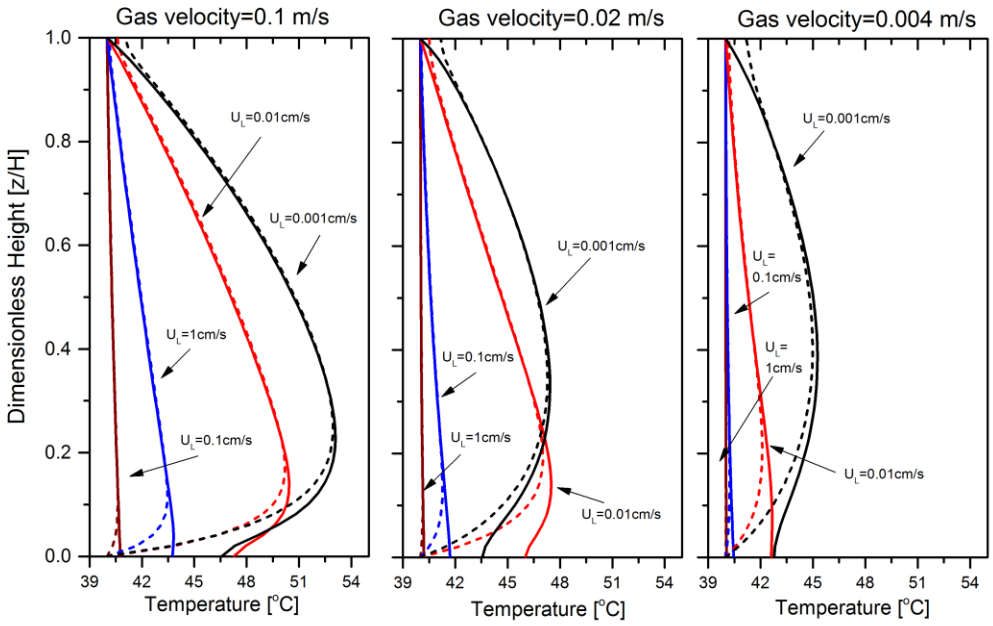

Figure 7-12 Temperature profiles for gas and liquid phases at different liquid flow rate, solid line: liquid phase; dashed line: gas phase. Operating conditions: ceramic foam height: 25.4 cm; ceramic foam type: 20 PPI; liquid phase: 30 wt.% DGA sovlent; gas phase: 13% CO_2/87% N_2; absorption temperature: 40°C; lean loading: 0.2 mol CO_2/mol DGA.

7.2 2-D model for integrated absorber/desorber ceramic foam reactor

In this subtask, we will further develop our model from 1D column to 2D integrated absorber/desorber ceramic foam reactor unit. In 2D model, the gas/liquid flow, pressure profile and CO_2 absorption/stripping were predicted. Additionally, an optimization and parametric study for the integrated absorber/desorber ceramic foam reactor, based on 2D model with using 30 wt.% MEA as absorbent were performed. The operating parameters include operating parameters such as CO_2 lean solvent loading, stripper operating temperature and gas flow rate to liquid flow rate ratio, and geometric parameters, such as stripper size, absorber/striper overlapping height and membrane thickness.

7.2.1 The process of CO_2 capture in combined absorber/stripper system

Figure 7-13 shows the developed CO_2 capture process with integrated absorber/stripper ceramic foam unit. The unique process combines the absorber and desorber columns, separated by a microporous ceramic membrane, into a single integrated unit, as shown in Figure 4. In this process, flue gas comes into the bottom while the solvent is fed into the top of the absorption side. The flue gas

flows up through the ceramic foam, making contact with the solvent as it falls down. Then the CO_2 is chemically absorbed by the solvent so that the gas that comes out of the top of the absorption side contains very little CO_2. The rich CO_2 loaded solvent after absorption permeates through the membrane section (middle section) to the desorber section (right section) by the driving force of pressure difference. The middle membrane is hydrophilic membrane which only allows liquid pass through. Gas will not pass through the membrane unless the pressure difference across the membrane exceeds the breakthrough pressure. In the desorption side, rich solvent falls down through the ceramic foam where it is heated to desorption temperature, then the CO_2 is released from the rich solvent. The solvent after regeneration will send back to the absorption side for next absorption after cooling down to the absorption temperature by a cross heat exchanger. Conventional CO_2 capture processes consist of a column that absorbs CO_2 with a liquid solvent, and a separate column that desorbs CO_2 from the solvent. In our previous research, we have determined that it is possible to integrate the absorber and desorber sections into a single unit. The integrated absorber/desorber arrangement will reduce space requirements, an important factor for retrofitting existing coal-fired power plants with CO_2 capture technology.

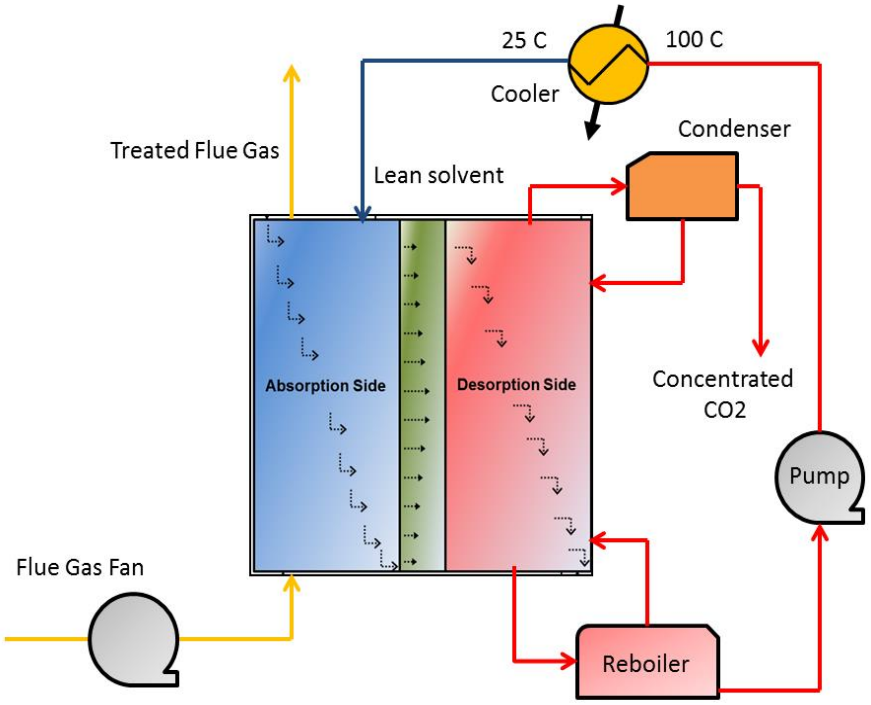

Figure 7-13 The process of CO_2 capture in combined absorber/stripper ceramic foam unit

7.2.2 Baseline case definition and simulation

Figure 7-14 gives the schematic diagram of integrated absorber/desorber ceramic foam unit. In both absorption side and desorption side, commercial ceramic foam of 20 PPI is chosen as the packing material.

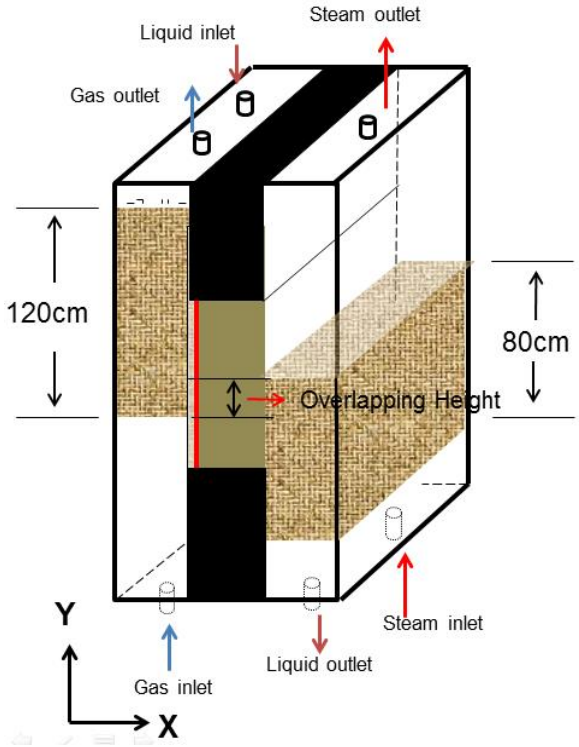

Figure 7-14 Schematic diagram of integrated absorber/desorber ceramic foam unit

The dimension of this integrated unit is presented in Table 7-2.The simulated flue gas flow rate and gas composition which have been used in the study are presented in Table 7-3. Other base case are defined as follow: (1) a 30 wt.% MEA absorbent; (2) solvent inlet temperature is 25 °C, (3) gas to liquid flow ratio (G/L) is 200, (3) stripper temperature is 100 °C.

Table 7-2 The dimension of integrated absorber/desorber ceramic foam unit

Absorber	Desorber	Membrane	Absorber/desorber overlapping height

Height (cm)	Thickness (cm)	Height (cm)	Thickness (cm)	Height (cm)	Thickness (cm)	Height (cm)
120	10	90	10	70	10	30

Table 7-3 The simulated flue gas flow rate and gas composition

Item	Unit	Value
Flue gas flow rate	m/s	0.1
Flue gas outlet pressure	kPa	101.6
Flue gas inlet temperature	°C	25
Flue gas composition	/	13 v/v% CO_2
	/	87 v/v% N_2

7.2.3 Optimization and parametric study based on 2D model

In this study, some of the main parameters affecting the CO_2 capture process will be varied as an initial step towards an optimization of the process. Starting from the baseline case, the following parameters will be varied:

1. The CO_2 lean solvent loading (0.17, 0.22, 0.27 and 0.31 mol CO2/mol MEA);

2. The stripper operating temperature (358K, 363K, 373K, 383K and 393K);

3. Gas flow rate to liquid flow rate ratio (100, 150, 200, 250 and 300);

4. Size of stripper section(140 cm×20 cm, 130 cm×14 cm, 90 cm×10 cm, 80 cm×8 cm, 70 cm×6 cm,);

5. Membrane section thickness (2.5 cm, 5 cm, 7.5 cm, and 10 cm);

6. Shape of absorber and stripper sections (rectangular to non-rectangular);

7. Absorber/stripper overlapping height (20 cm, 30 cm, 50 cm, 70 cm, 100 cm and 120 cm)

The following performance indicators in the absorption/desorption process were used to investigate the effect of the parameters:

1) CO_2 removal efficiency in absorber (target is 90%)

2) The thermal energy required in the stripper(MJ energy/kg CO_2 removed)

These two indicators were chosen because they present information on both the operating and the capital costs. The CO_2 removal efficiency in absorber will affect the size of the absorber, which in turn influences the capital costs. The thermal energy consumption for CO_2 stripping is expected to be a major contributor to the production cost and a change in the energy required, which will give a clear effect on the operating costs.

Operating parameters

Effect of different solvent CO_2 lean loading on CO_2 capture performance

The lean solvent loading of the MEA solution was varied to find the optimum solvent loading for a minimal thermal energy requirement. Figure 7-15 shows simulated CO_2 loading profiles in the integrated absorber/desorber ceramic foam reactor at different CO_2 lean loadings. We can clearly see the difference of CO_2 loading profile in the reactor as the CO_2 lean loading changes from 0.17 to 0.31 mol CO2/mol MEA. For CO_2 desorption, a significant CO_2 loading gradient at top half part of the stripper side can be observed, which means CO_2 desorption mainly occurred near the top of the stripper side. For CO_2 absorption, CO_2 loading profiles in Figure 7-15 are quite different, which means that the position of CO_2 absorption reaction changes with CO_2 lean loading. With the increase of solvent CO_2 lean loading, we can see the decrease of height with CO_2 absorption in the absorption side.

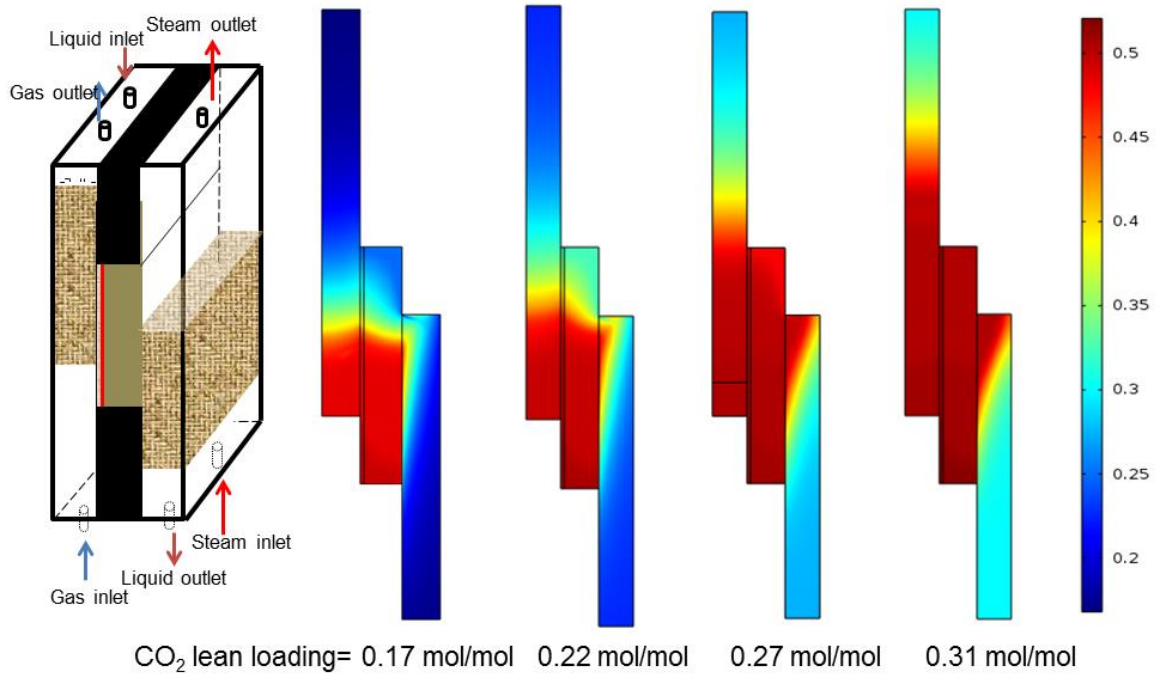

Figure 7-15 CO_2 loading profile in integrated absorber/desorber ceramic foam reactor

Figure 7-16 is the CO_2 concentration profiles in gas phase for different lean loading cases. By this we can see the CO_2 absorption at different CO_2 lean loading cases more clearly in the absorption side. For all the cases, flat CO_2 concentration profile can be found near the bottom of the absorber. As solvent CO_2 lean loading increases, the height of flat CO_2 concentration profile increases. It means that solvent with higher CO_2 lean loading will be much easier to reach equilibrium in the CO_2 absorption process.

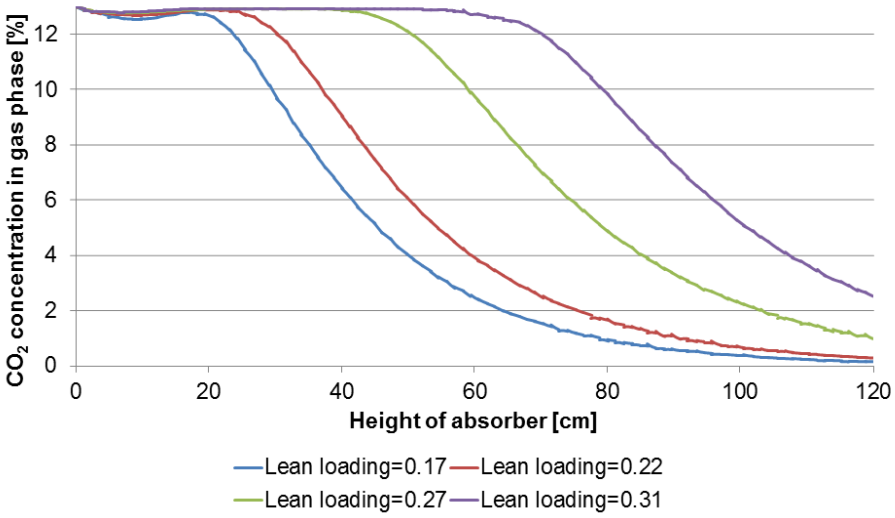

Figure 7-16 CO_2 concentration profiles in gas phase for different lean loading cases

CO_2 removal efficiency at different lean loading cases is presented in Figure 7-17. The case with a lower CO_2 lean loading has a better CO_2 removal efficiency than higher CO_2 lean loading cases. For example, as the CO_2 lean loading is 0.17 mol CO_2/mol MEA, 99% of CO_2 could be removed from flue gas by the MEA solvent; as the CO_2 lean loading increases to 0.31 mol CO_2/mol MEA, the CO_2 removal efficiency is reduced to 80.59%. This is contributed to the change of amount of free MEA molecules in the solvent with different CO_2 lean loadings. Lower CO_2 lean loading means the more free MEA molecules exists in the solvent, which will provide faster CO_2 reaction rate. We also notice that the targeted 90% removal efficiency can be realized in our study if the CO_2 lean loading is operated at around 0.27 mol CO_2/mol MEA.

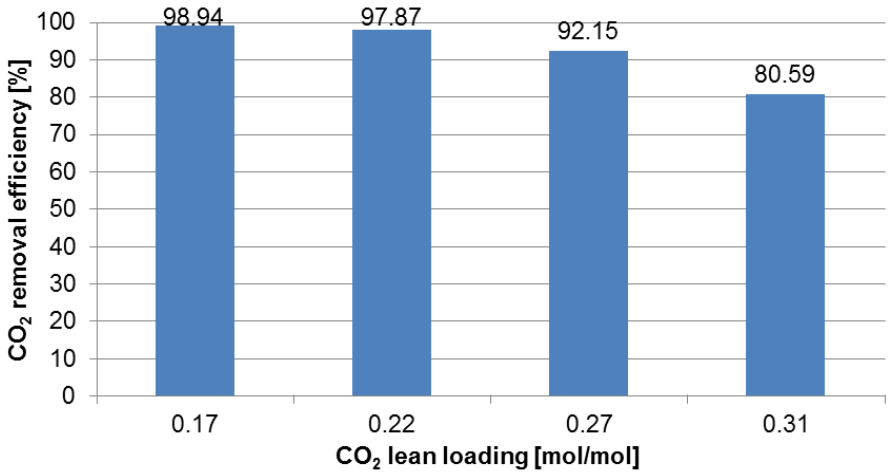

Figure 7-17 CO_2 removal efficiency for different lean loading cases

Figure 7-18 presents the regeneration heat consumption for different lean loading cases. At low values of lean solvent loading, the amount of stripping steam required (latent heat) to achieve this low solvent loading is dominant in the thermal energy requirement. With increase of lean solvent loading values, the latent heat reduce sharply but the energy to heat up of the solvent (sensible heat) gradually becomes more significant in the thermal energy requirement. As a consequence, thermal energy requirement decreases with increasing solvent lean loading.

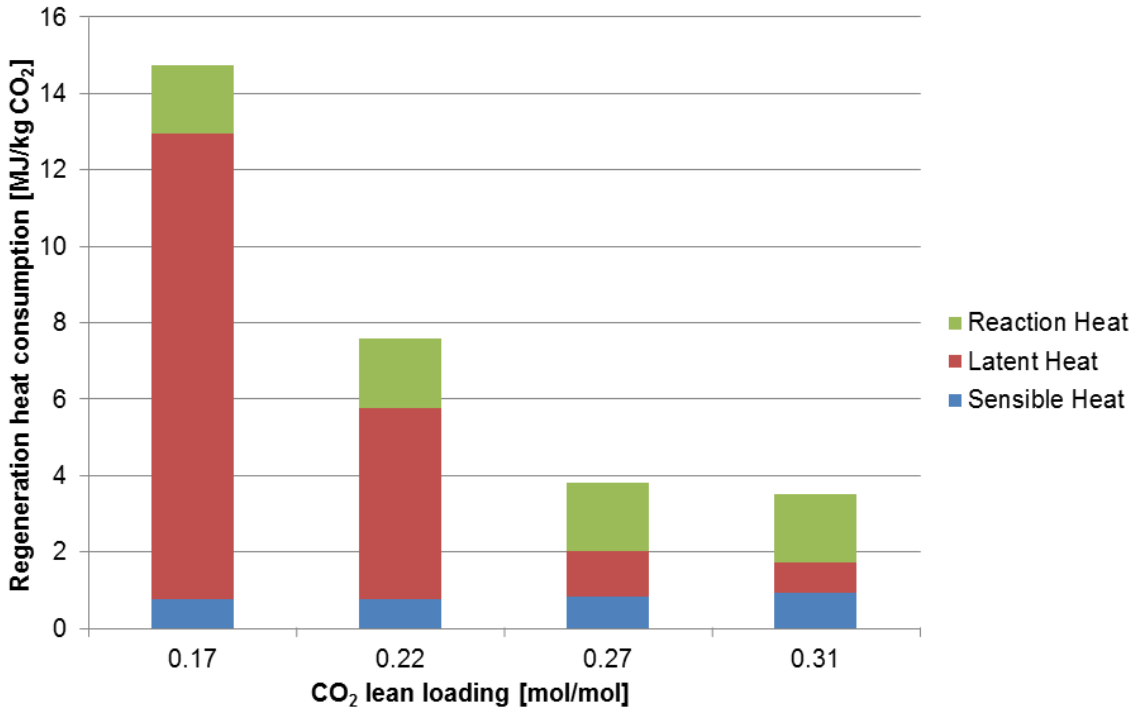

Figure 7-18 The change of regeneration heat consumption with solvent CO_2 lean loading

Effect of G/L ratio on CO_2 capture performance

G/L ratio is one of the important parameters for absorbent based CO_2 capture process, which presents a significant influence on CO_2 removal efficiency and regeneration heat consumption. Figure 7-19 shows the change of CO_2 removal efficiency with G/L ratio. It seems attractive to use lower G/L ratio to reach better CO_2 removal efficiency. With the increase of G/L ratio, the CO_2 removal efficiency reduces. CO_2 removal efficiency, for example, reaches to almost 100% as G/L ratio ss 100; but the CO_2 removal efficiency decreases to 61.09% as G/L ratio raises to 300.

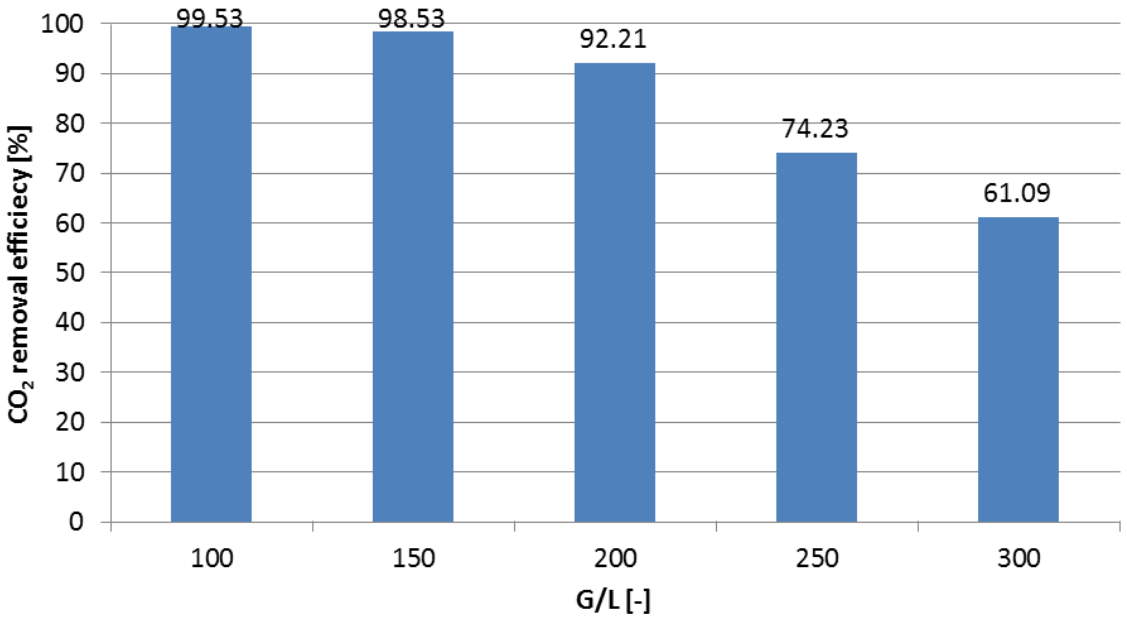

Figure 7-19 CO_2 removal efficiency for different G/L ratio cases

G/L ratio also plays a significant effect on temperature profile along absorber, as shown in Figure 7-20 It can be clearly seen that for all cases, a temperature bulge (a "warm spot") can be found in the absorption side due to exothermic reaction of CO_2 absorption. The highest temperature can reach to about 323K. As the G/L ratio is 100, the location of the maximum temperature bulge occurs in the bottom of the absorber. With increase of G/L ratio, the location of the temperature bulge shifts up along the absorber and the range of temperature bulge increases. In addition, the location of the maximum temperature bulge is known as the maximum CO_2 absorption point. Therefore, by investigating the temperature profiles along the absorber; we can optimize the G/L ratio in CO_2 capture process.

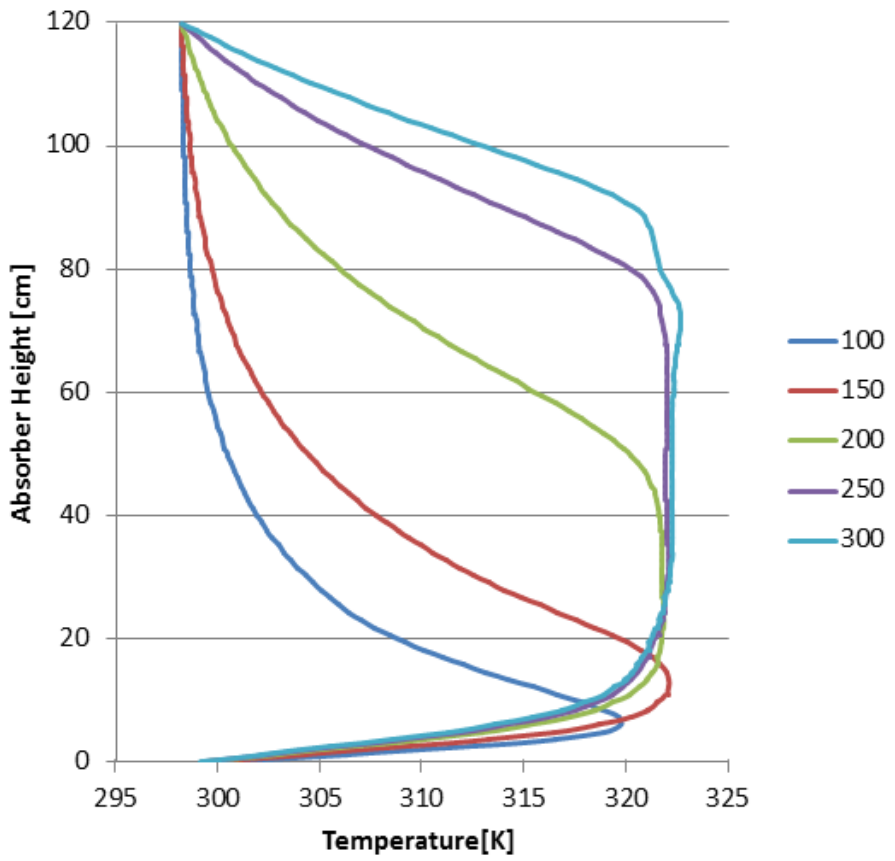

Figure 7-20 Temperature profiles along the absorber for different G/L ratio cases

Figure 7-21 presents the CO_2 loading profile in the integrated absorber/desorber ceramic foam reactor for different G/L ratio cases. In the absorption side, we can find the most CO_2 absorption occurred near the bottom of absorber as G/L ratio is 100. Increasing G/L ratio will result in the position of most CO_2 absorption shifting up from the bottom to the top of absorber. This information will help us to conduct the parametric optimization in the integrated absorber/desorber ceramic foam reactor.

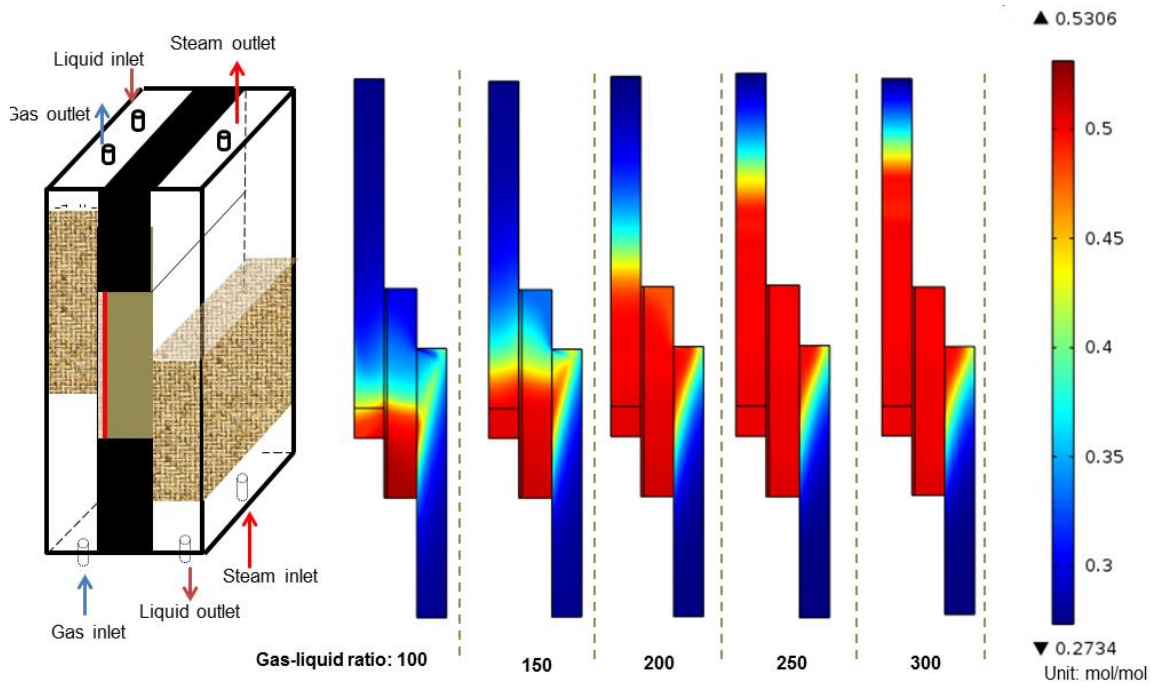

Figure 7-21 CO_2 loading profiles in the integrated absorber/desorber ceramic foam reactor for different G/L ratio cases

Thermal energy required for CO_2 desorption at different G/L ratio.is investigated in Figure 7-22 The lowest thermal energy required is found to be 3.8 MJ/kg CO_2 as G/L ratio is 200. The higher G/L ratio means higher solvent circulation flow rate, which will lead to an increase on sensible heat. However, as the G/L ratio lower than 200, latent heat is found to increase substantially with the decrease of G/L ratio. Therefore, in terms of regeneration heat consumption, the optimum G/L ratio is expected to be around 200 in this study. Mangalapally et al. also reported similar phenomenon in the packed tower system [41].

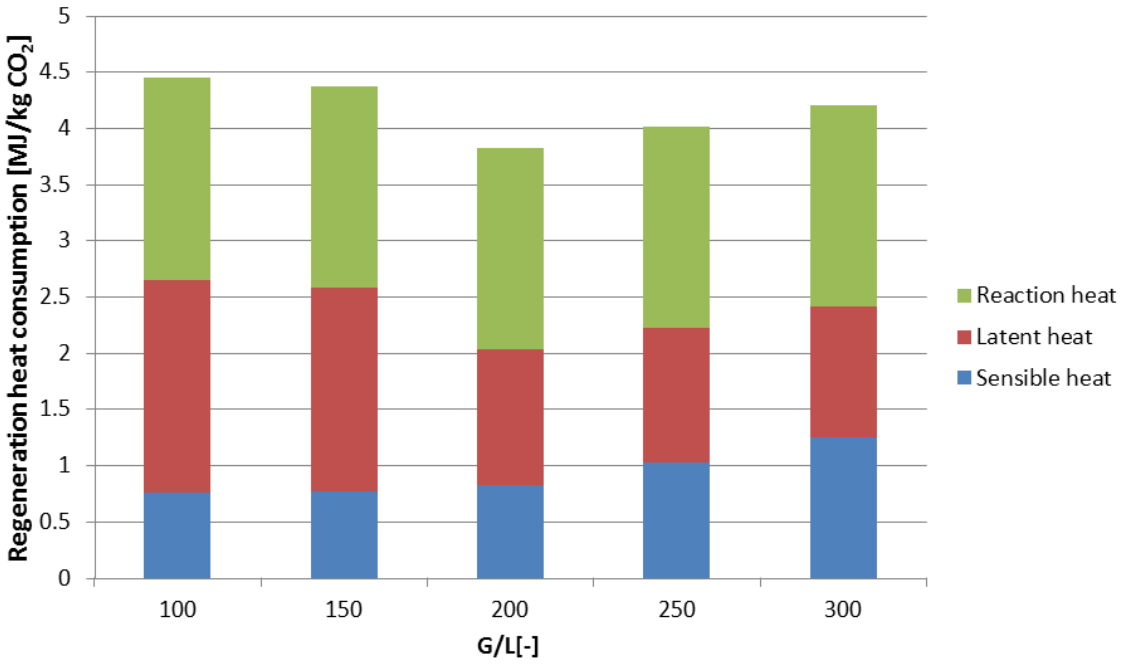

Figure 7-22 Regeneration heat consumption for different G/L ratio cases

Effect of stripping temperature on CO_2 capture performance

The operating pressure in stripper is strongly dependent on stripping temperature, as shown in Figure 7-23. As the temperature lower than 373K, stripper is required to operate at vacuum condition; as the temperature higher that 373K, stripper is operated at pressurized condition. As a result, we usually require that the stripper is with larger size as operating at lower temperature, not only because the lower pressure it is, but also the CO_2 desorption kinetics will be slower under a lower stripping temperature. Therefore, we need a larger stripper to provide more residence time (reaction time) and gas-liquid contact area to make sure rich solvent could be regenerated adequately. Table 7-4 shows the change of stripper size with stripping temperature in this study.

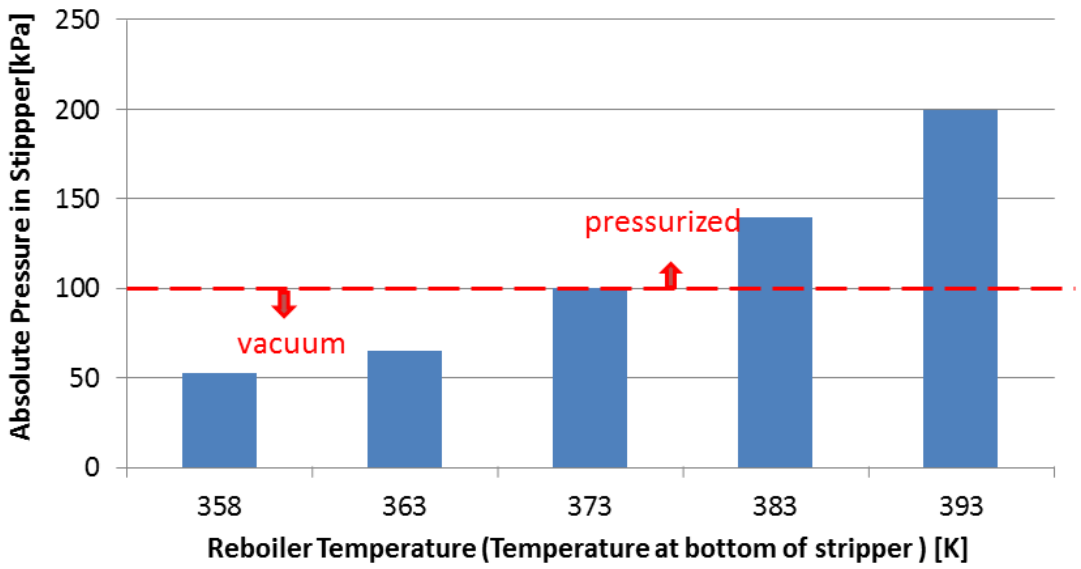

Figure 7-23 The relationship of reboiler temperature and stripping pressure in the integrated absorber/desorber ceramic foam unit.

Table 7-4 The change of stripper size with stripping temperature in this model

Stripper Temperature [K]	Stripper Height [cm]	Stripper Width [cm]
358	140	20
363	130	14
373	90	10
383	80	8
393	70	6

The CO_2 removal efficiency at different stripping temperatures is investigated in Figure 7-24. It has been found that CO_2 removal efficiencies are all kept at around

92% for different cases, which means the variation of stripping temperature will not affect CO2 reaction in absorption side.

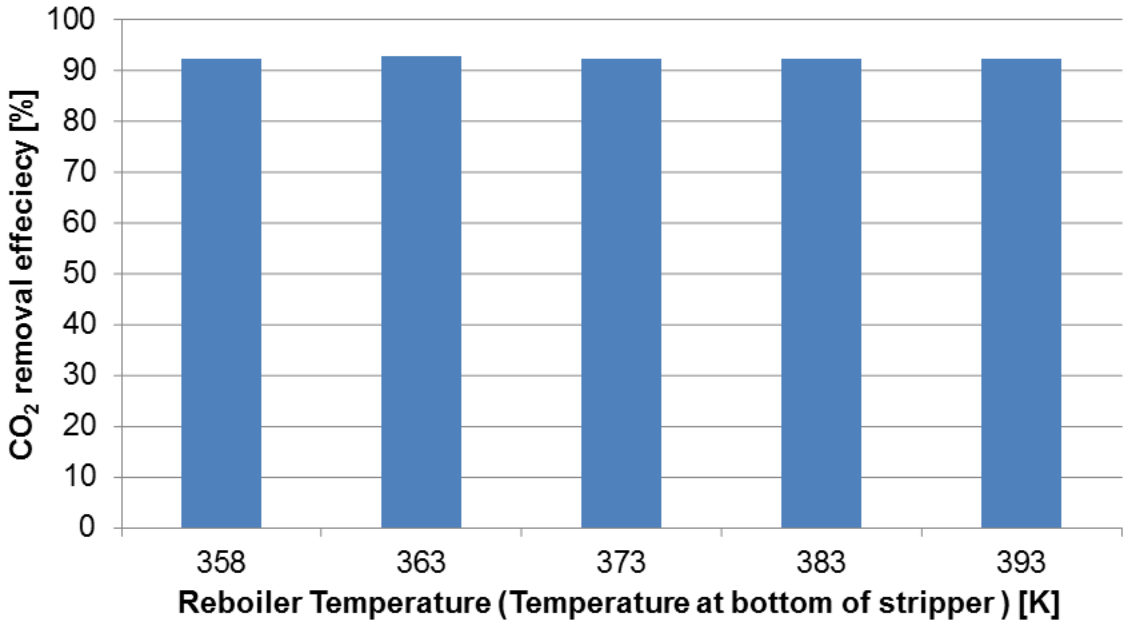

Figure 7-24 CO_2 removal efficiency at different reboiler temperatures

Figure 7-25 is the CO_2 loading profiles in the reactor for different stripping temperature cases. We can also find that the CO_2 loading profiles in the absorption side are uniform at different stripping temperature cases. But in the desorption side, the change in solvent CO_2 loading is more significant at higher stripping temperature. This could be explained by the faster desorption reaction at higher stripping temperature.

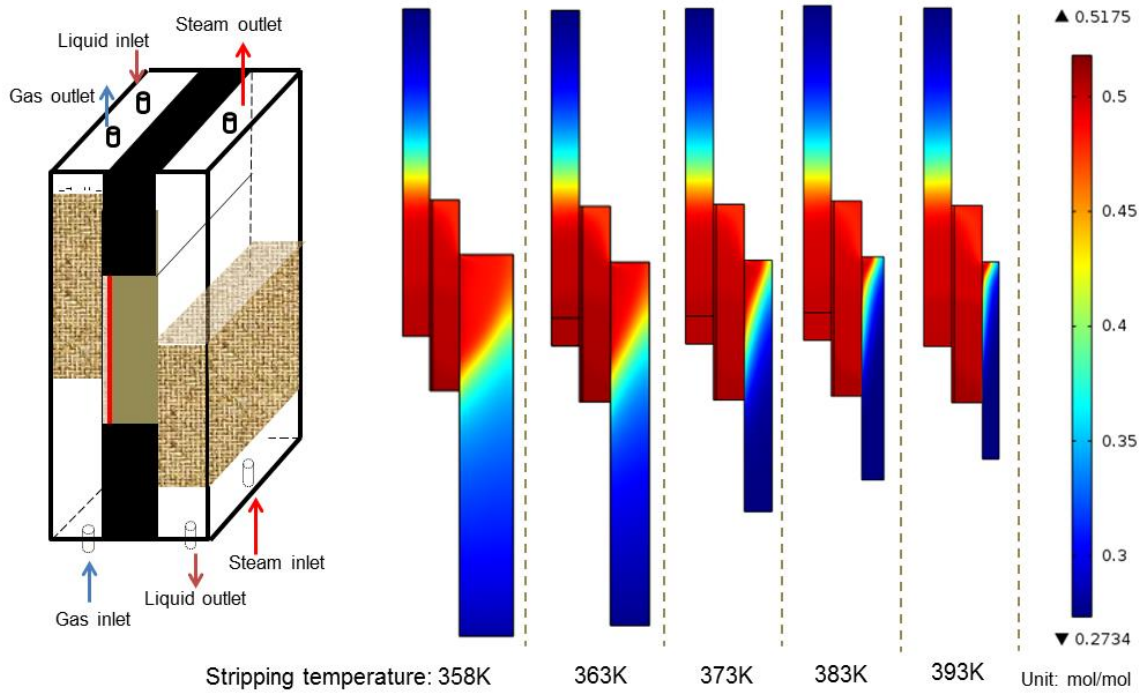

Figure 7-25 CO_2 loading profiles in the integrated absorber/desorber ceramic foam reactor at different stripping temperature

The solvent temperature profile for different stripping temperature cases is described in Figure 7-26. Almost no change of temperature distribution in the absorption side as the stripping temperature increases from 358 to 393 K. In the desorption side, a big difference in temperature profile can be found in different cases.

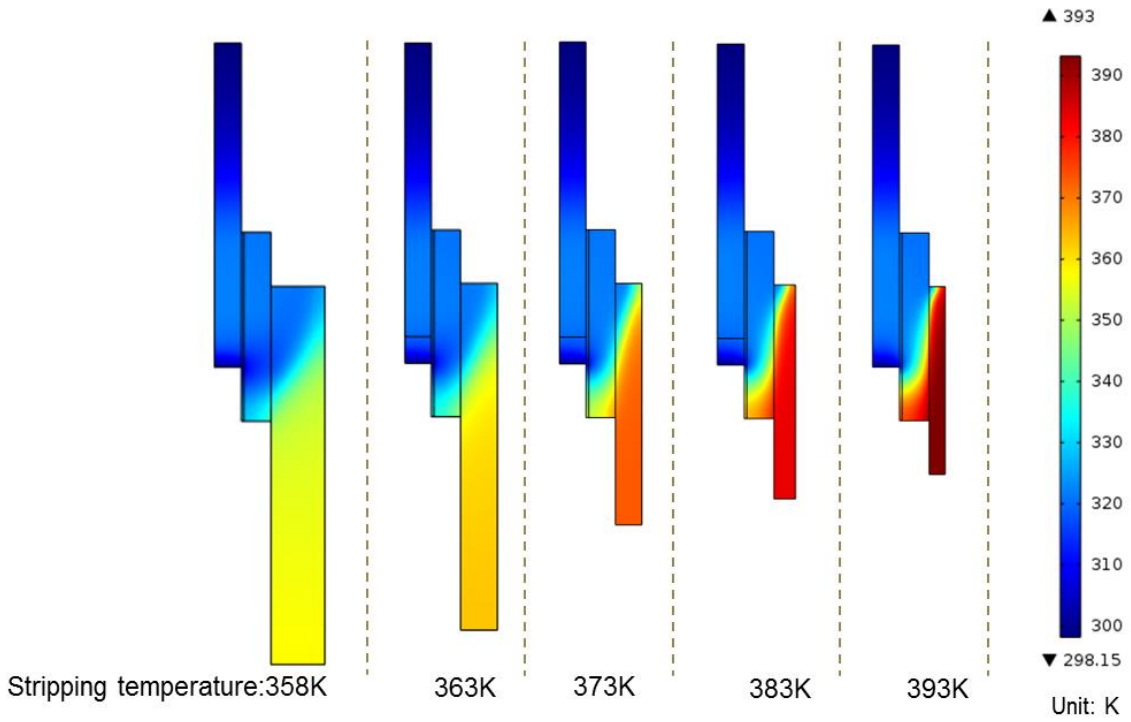

Figure 7-26 Solvent temperature profiles in the integrated absorber/desorber ceramic foam reactor at different stripping temperatures

The thermal heat consumption for CO_2 desorption is investigated in Figure 7-27. Stripping temperature has a significant influence on regeneration consumption. The lowest regeneration heat consumption is found as stripping temperature is 363-373K. But it should be noted that it is at the cost of using large size of stripper. When we choose low temperature stripping, the capital cost in desorber will increase compared to the high temperature stripping cases.

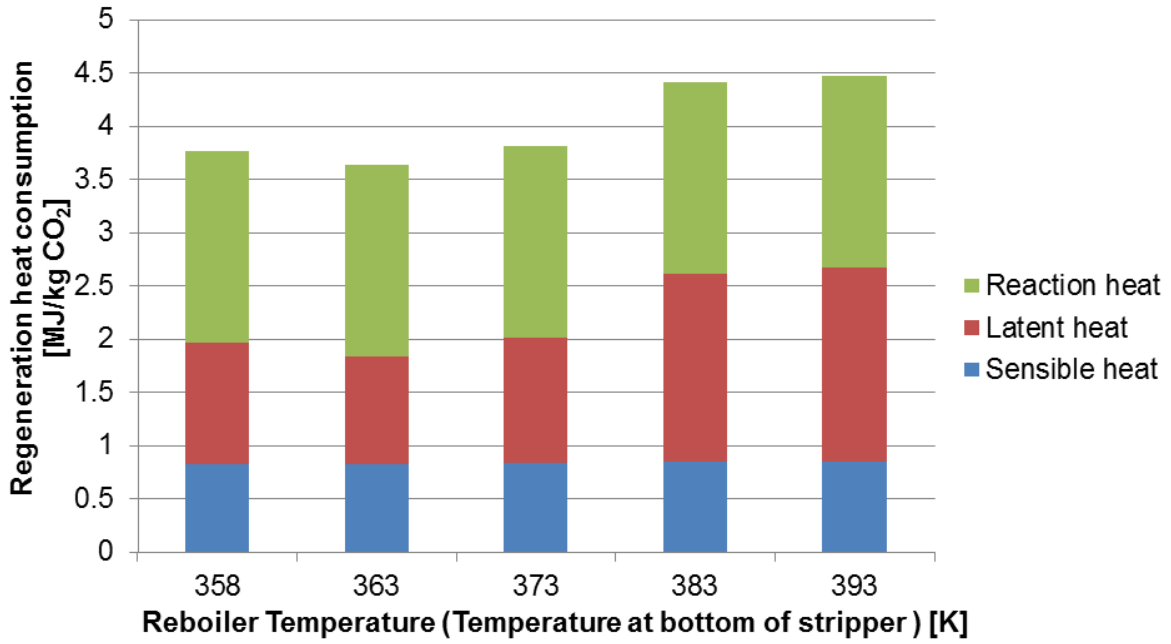

Figure 7-27 Regeneration energy consumption for different stripping temperature cases

Geometric parameters

Effect of stripper size on CO_2 capture performance

The size of stripper was varied to find the optimum stripper size for a maximal CO_2 removal efficiency and minimal thermal energy requirement. Fig. 7-28 shows simulated CO_2 loading profiles in the integrated absorber/desorber ceramic foam reactor at different stripper size cases. In the absorber section, the CO_2 loading profile doesn't presents any significant change with stripper size. This implies that the operating performance of absorption side will not be affected by the change of stripper size, at least in term of solvent CO_2 loading profile. In the stripper section, we can clearly see the difference of CO_2 loading profile as the stripper size changes from 140 cm×20 cm to 70 cm×6 cm. However, it should be noted that a significant

CO_2 loading gradient at top half part of the stripper side can be observed for all cases. It indicates CO_2 desorption mainly occurred near the top of the stripper side whatever the size of stripper. It is also interesting to find that the lean CO_2 loading at the bottom of the stripper almost has no change even the stripper size double or half compared to the base case. This is very important information to tell us that CO_2 loading of lean solvent in the stripper mainly depends on the stripping temperature not the size of stripper. Therefore, it is better to choose a more compact stripper if the stripping temperature is given.

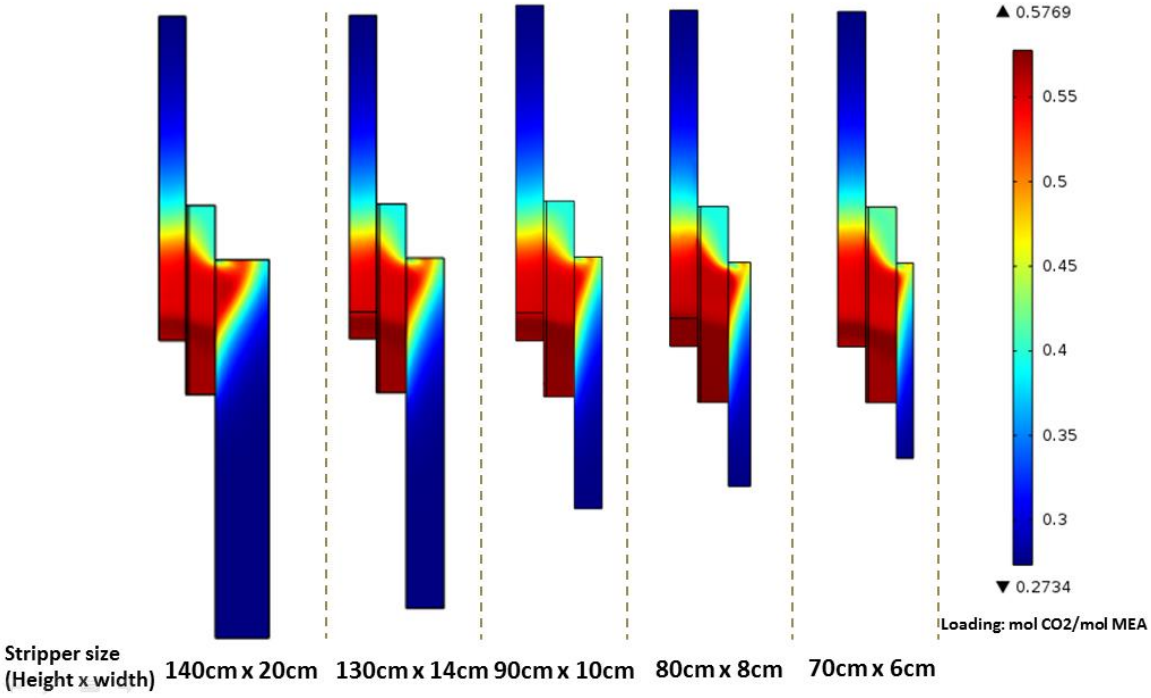

Figure 7-28 CO_2 loading profile in integrated absorber/desorber ceramic foam reactor with the change of stripper size

CO_2 removal efficiency for different stripper size cases is presented in Fig. 7-29. We can clearly see that CO_2 removal efficiencies with different stripper sizes are very similar. This phenomenon further proves that operating performance of absorption side will not be affected by change of stripper size. We also notice that the targeted 90% removal efficiency can be realized in our study for all the cases.

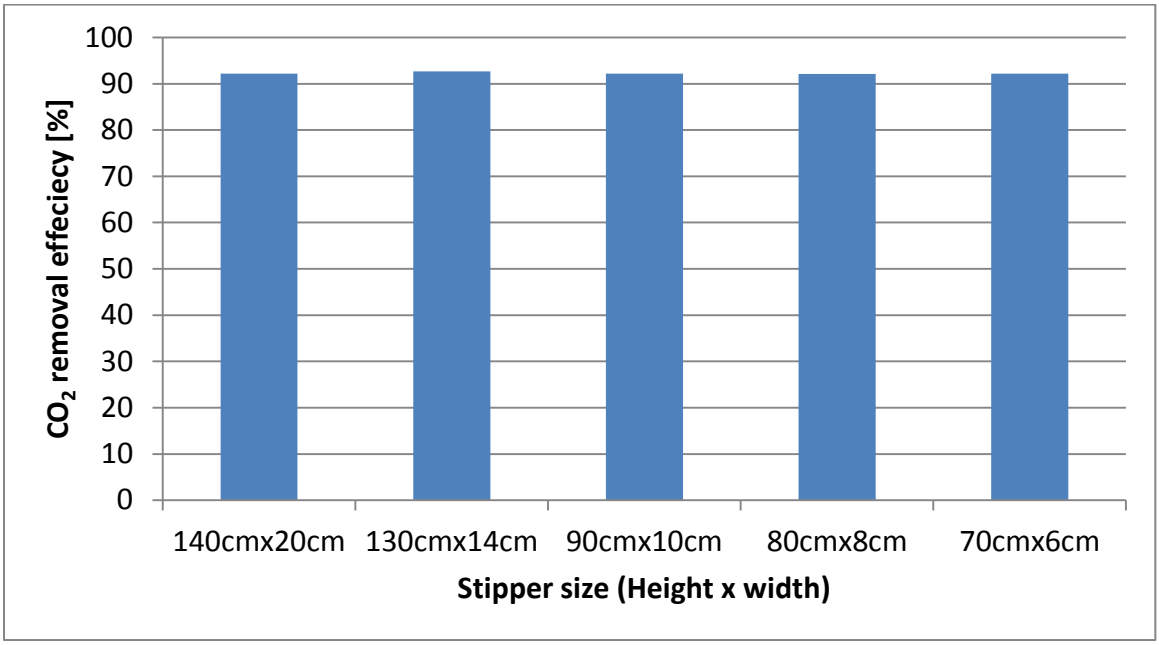

Figure 7-29 CO_2 removal efficiency for different stripper size cases

Fig. 7-30 presents the regeneration heat consumption for different size strippers. Stripper size doesn't have very significant effect on regeneration heat consumption, but we can still find an optimal stripper size with lowest regeneration heat consumption, which is 80cm x 8 cm. A larger or smaller stripper will increase regeneration heat consumption slightly. However, in terms of capital cost, smaller stripper size is preferred. Therefore, for a given stripping temperature, choosing an

optimal stripper size should take into account the trade-off between regeneration heat consumption and capital cost.

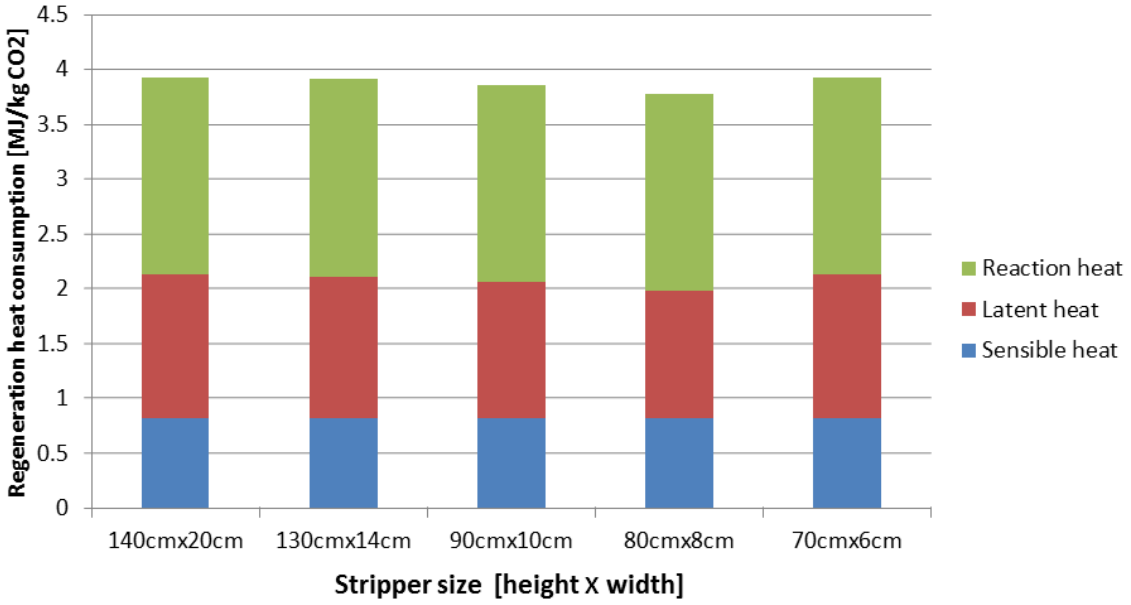

Figure 7-30 The change of regeneration heat consumption with stripper size

Effect of membrane thickness on CO_2 capture performance

Besides absorber and stripper section, membrane section is also an important part of ceramic foam reactor to connect the absorber side and stripper side. The thickness of membrane section is one of important geometric parameters for CO_2 capture, which plays an important role on the mass transfer and heat transfer between absorber and desorber. Fig. 7-31 shows the change of CO_2 removal efficiency with membrane thickness. Increasing membrane thickness will result in a slightly improvement on CO_2 removal efficiency. For example, CO_2 removal

efficiency only increases from 91.82% to 92.24% as membrane thickness increases from 2.5 cm to 10 cm.

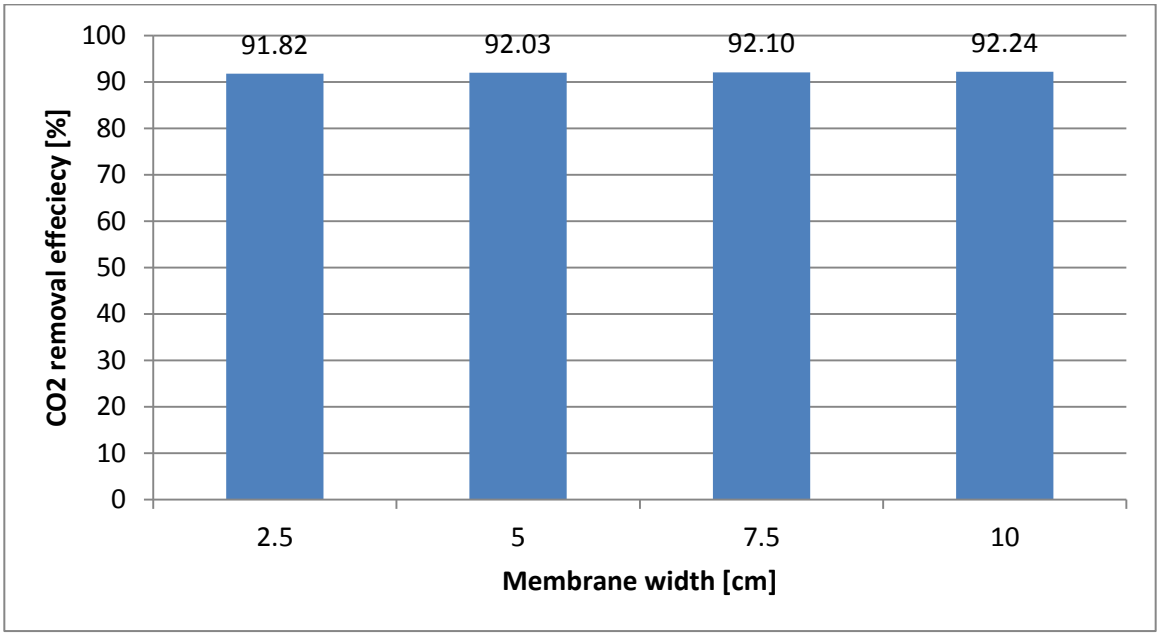

Figure 7-31 CO_2 removal efficiency with different membrane thickness

The effect of membrane thickness on temperature profile along absorber is shown in Fig. 7-32. As the membrane thickness is 10 cm, a temperature bulge (a "warm spot") can be found in the absorption side due to exothermic reaction of CO_2 absorption. The highest temperature can reach to about 320K. As the membrane thickness less than 10 cm, we can clearly see a “secondary temperature bulge” occurs near the bottom of the absorber. The magnitude of this “secondary temperature bulge” increases significantly with the decrease of membrane thickness. As shown in Fig. 11, maximum “secondary temperature bulges” are 322 K, 328 K and 337 K for membrane thickness of 7.5 cm, 5 cm and 2.5 cm, respectively. This is contributed to the heat conduction from high temperature

stripper side to low temperature absorber side. With the decease of membrane thickness, the effect of heat conduction from stripper side to absorber side will be more significant, which will result in a bigger temperature bulge near the bottom of absorber.

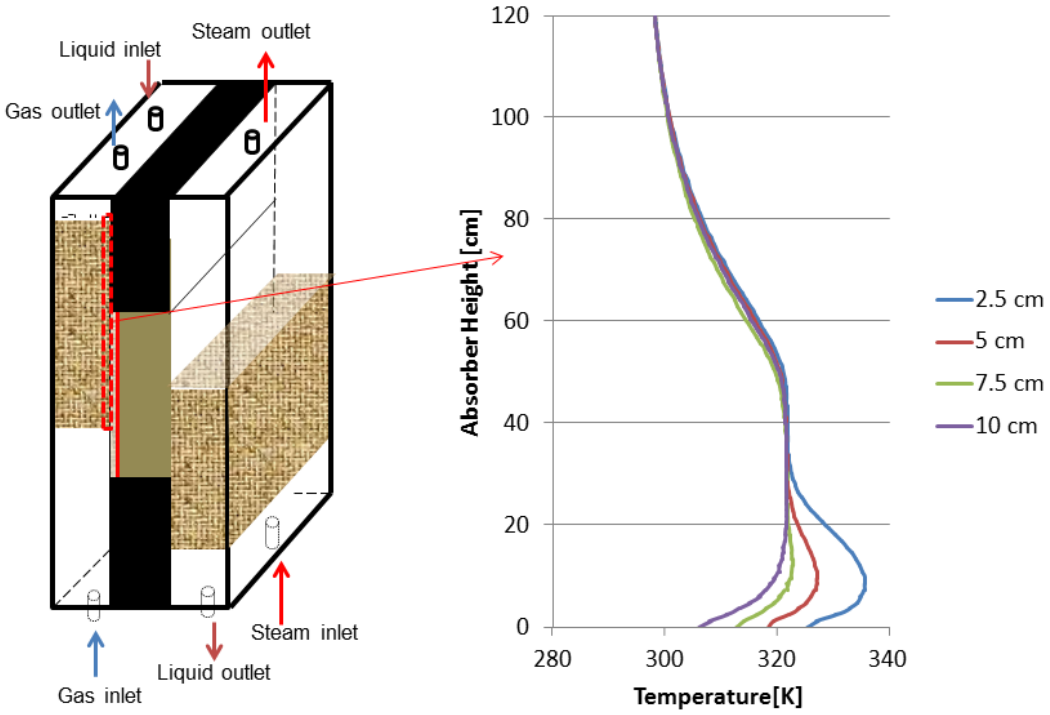

Figure 7-32 Temperature profiles along the absorber for different membrane thickness cases

Fig. 7-33 presents the 2D temperature profiles of absorber side for different membrane thickness cases. It can be more clearly to see the difference of temperature distributions with the change of membrane thickness. For example, as the membrane thickness is 2.5 cm, a high-temperature region can be found near the bottom right corner of absorber, next to the membrane section. As it is far from the membrane section, the temperature gradually decreases. This also proves the

hypothesis that the secondary temperature profile results from the heat conduction from stripper side to absorber side. Usually, considering CO_2 absorption is exothermic reaction and CO_2 desorption is endothermic reaction, a significant temperature contrast between absorber and stripper is recommended. Therefore, we prefer a thicker membrane to avoid a "secondary temperature bulge" in the absorber side.

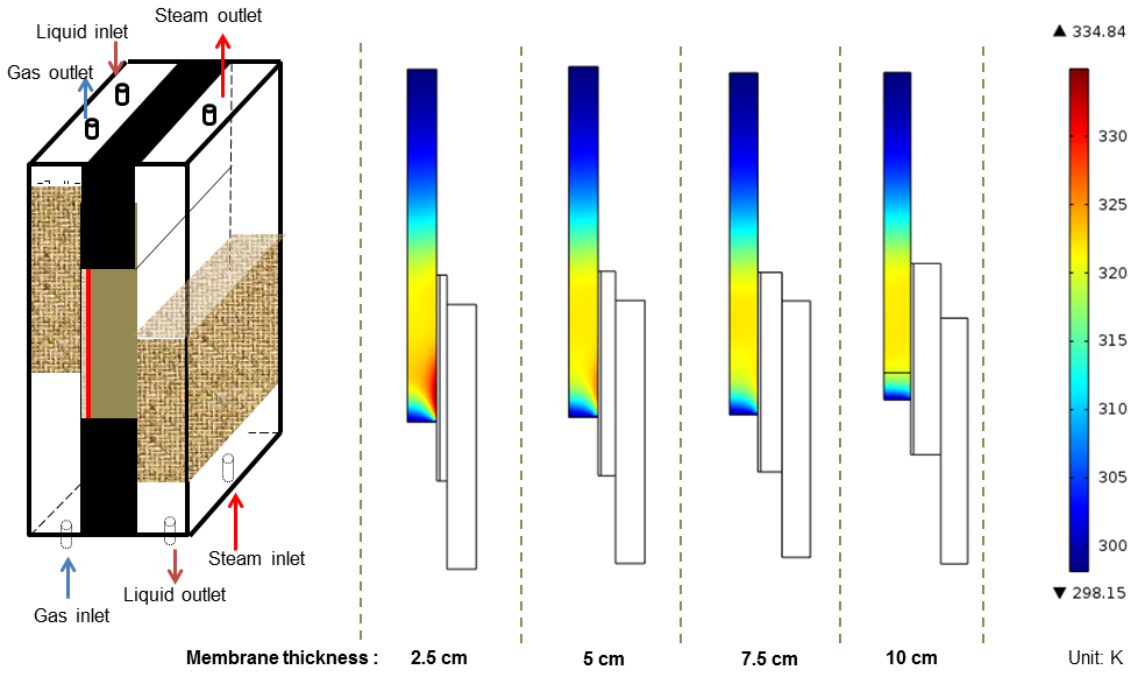

Figure 7-33 Temperature profiles in the absorber side with different membrane thickness

Fig. 7-34 presents the CO_2 loading profile in the integrated absorber/desorber ceramic foam reactor for different membrane thickness cases. We can find that the CO_2 loading profiles in the integrated absorber/desorber ceramic foam reactor are almost uniform at different membrane thickness cases. It indicates membrane thickness doesn't have a significant influence on CO_2 loading profile.

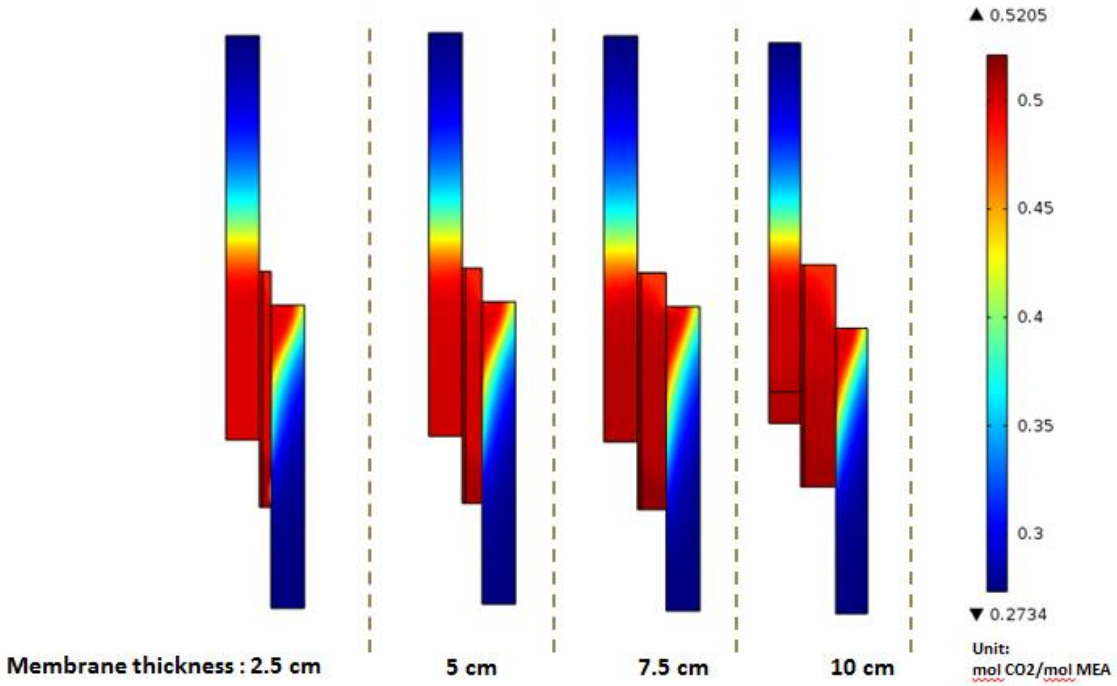

Figure 7-34 CO_2 loading profiles in the integrated absorber/desorber ceramic foam reactor for different membrane thickness cases

Thermal energy required for CO_2 desorption at different membrane thickness cases.is investigated in Fig. 7-35. The regeneration heat consumption increases with the increase of membrane thickness. The lowest thermal energy required is found to be 3.74 MJ/kg CO_2 as membrane thickness is 2.5 cm. As the membrane thickness increases to 10 cm, regeneration heat consumption increases to 3.83 MJ/kg CO_2.

In conclusion, increasing membrane thickness will result in a slight decrease of regeneration heat consumption, but in the other hand, will reduce CO_2 removal efficiency slightly. Therefore, an optimum membrane thickness is recommended to be a compromising value between 5 cm and 7.5 cm in our study.

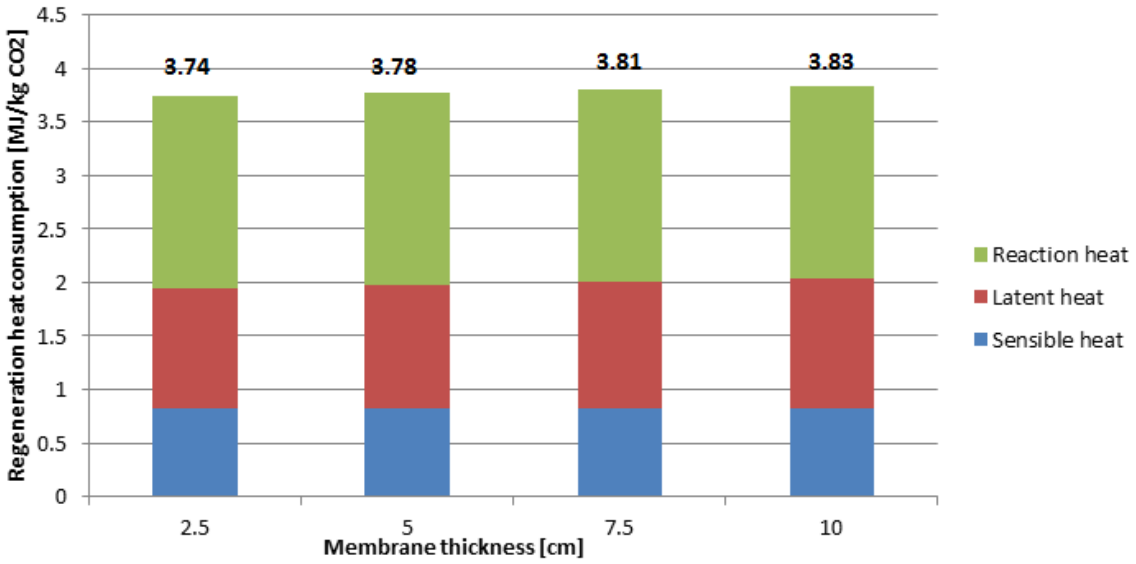

Figure 7-35 Regeneration heat consumption for different membrane thickness cases

Effect of absorber/stripper shape on CO_2 capture performance

In our previous study, the shapes of absorber and stripper are both rectangular. In this section, we will investigate the feasibility of ceramic foam reactor with non-rectangular shape of absorber and stripper for CO_2 capture. Fig. 7-36 shows the cases we studied with different shape of absorber and desorber. The left one is base case with traditional rectangular shape, right ones are three different non-rectangular shapes of absorber and desorber. The width of absorber bottom varies from 10 cm to 3 cm.

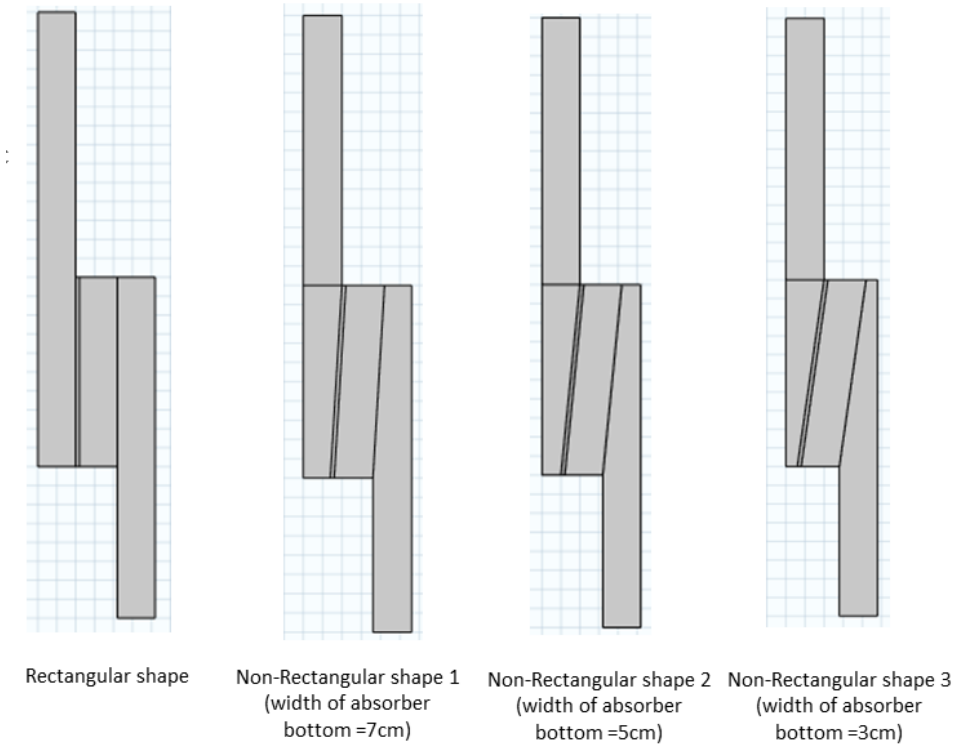

Figure 7-36 Different non-rectangular shapes of absorber and desorber

Fig. 7-37 presents the comparison of liquid flow profiles in different shape reactors. For non-rectangular shape reactor, as the width of absorber bottom decreases, we doesn't see any velocity increase in the absorber side compared to the liquid flow velocity profile of rectangular shape reactor. It means this kind of shape reactor has the tendency to facilitate liquid flow through the membrane. For the rectangular shape reactor, the membrane section is perpendicular; the driving force of liquid permeating through the membrane is the capillarity and pressure difference between absorber and desorber. For the non-rectangular shape reactors, the membrane section is sloped. Therefore, besides capillarity and pressure difference, gravity force is another driving force to accelerate liquid flow through the membrane.

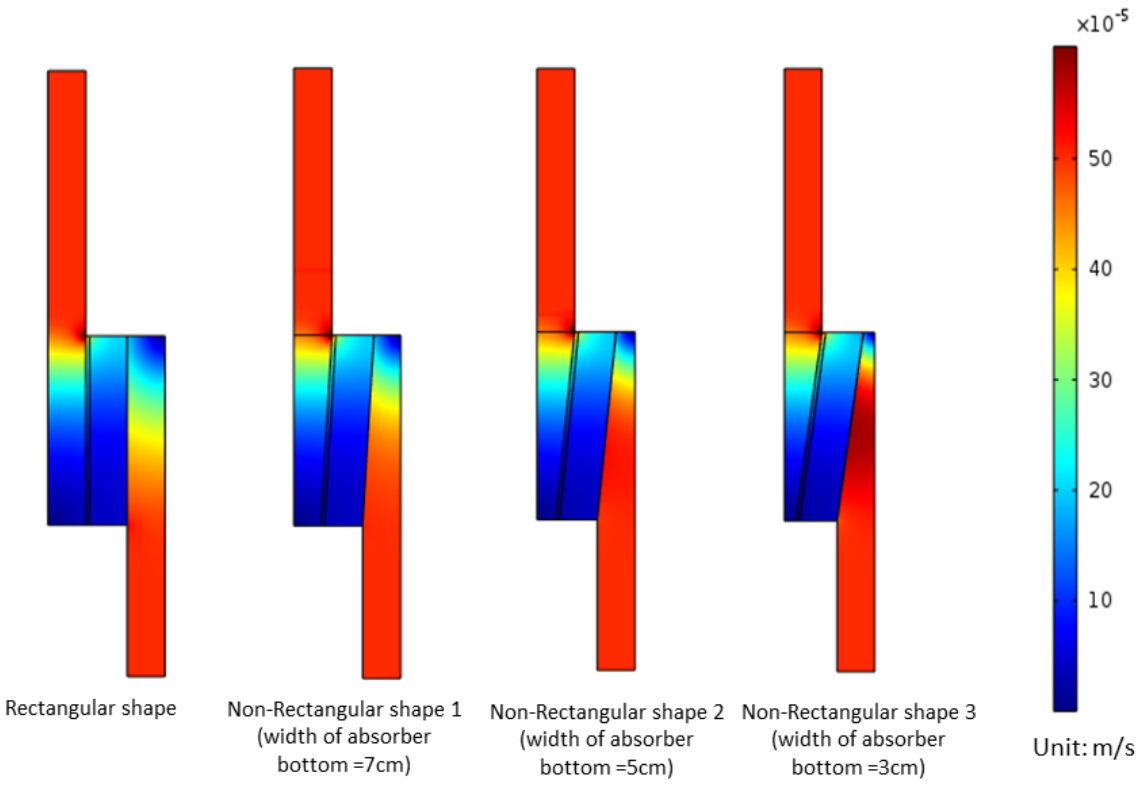

Figure 7-37 Liquid flow velocity profiles in different shape of reactors

The liquid temperature profile of different shape of reactors was also investigated, as shown in Fig. 7-38. It can be seen that the change of reactor shape doesn't affect the liquid temperature profile in the ceramic foam reactor. The non-rectangular shape reactors show similar temperature profiles with rectangular shape reactor.

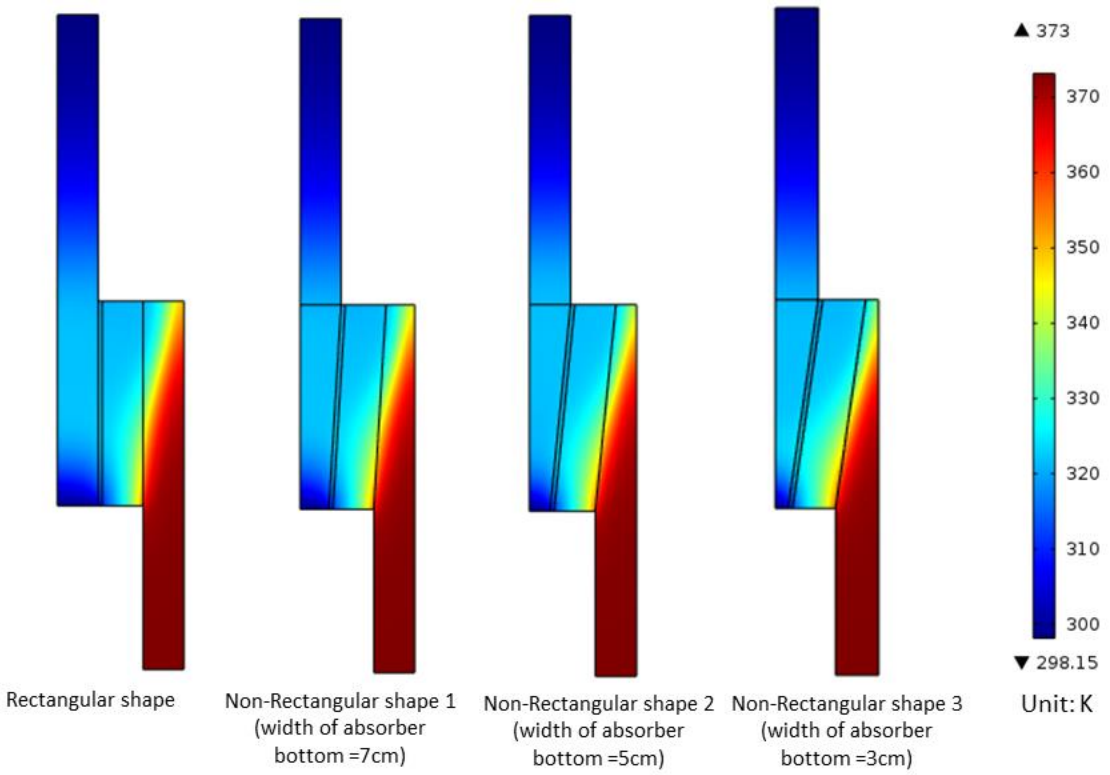

Figure 7-38 Liquid temperature profiles in different shape of reactors

The CO_2 removal efficiency at different stripping temperatures is investigated in Fig.7-39. It has been found that CO_2 removal efficiencies all reach to around 91% for different cases, which indicate the variation of reactor shape will not affect CO_2 absorption reaction in absorber side.

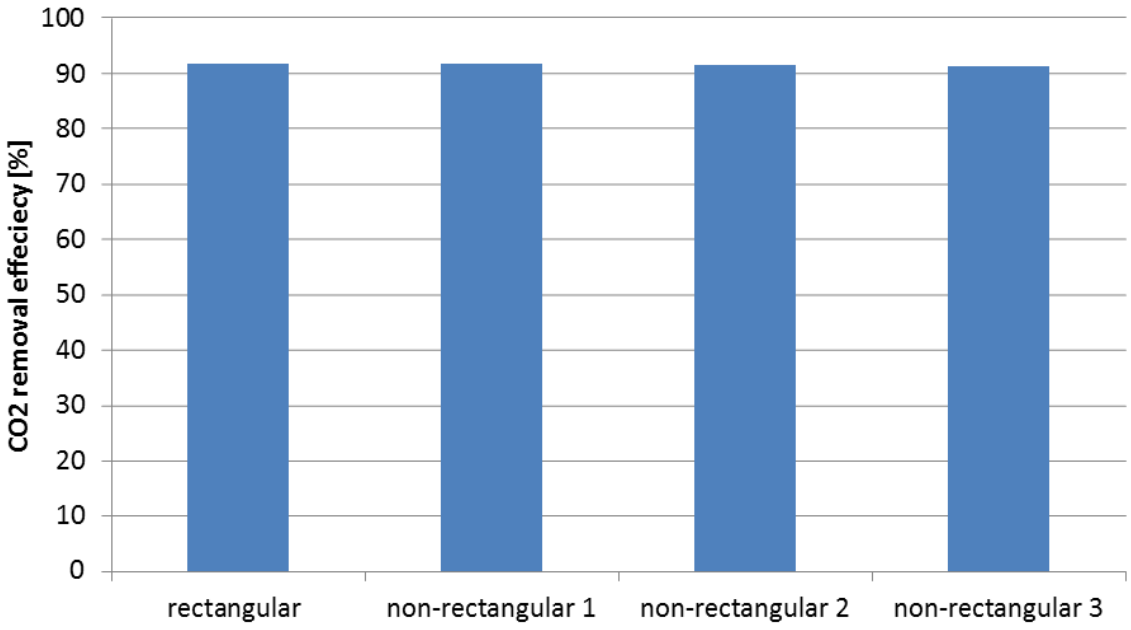

Figure 7-39 CO_2 removal efficiency for different shape of reactors

Fig. 7-40 is the comparison of total gas phase pressure drop in the absorber side for rectangular shape and non-rectangular shape reactor. Pressure drop increases as reactor changes to be more non-rectangular. A lowest gas phase pressure drop can be found as the shape of reactor is rectangular. For the non-rectangular shape reactors, with the decrease of the width of absorber bottom, the gas phase pressure drop in the absorber side raises dramatically. This is mainly because the decrease of the width of absorber bottom means a narrower channel for gas flowing, which will lead to a larger restriction of gas to flow through the absorber.

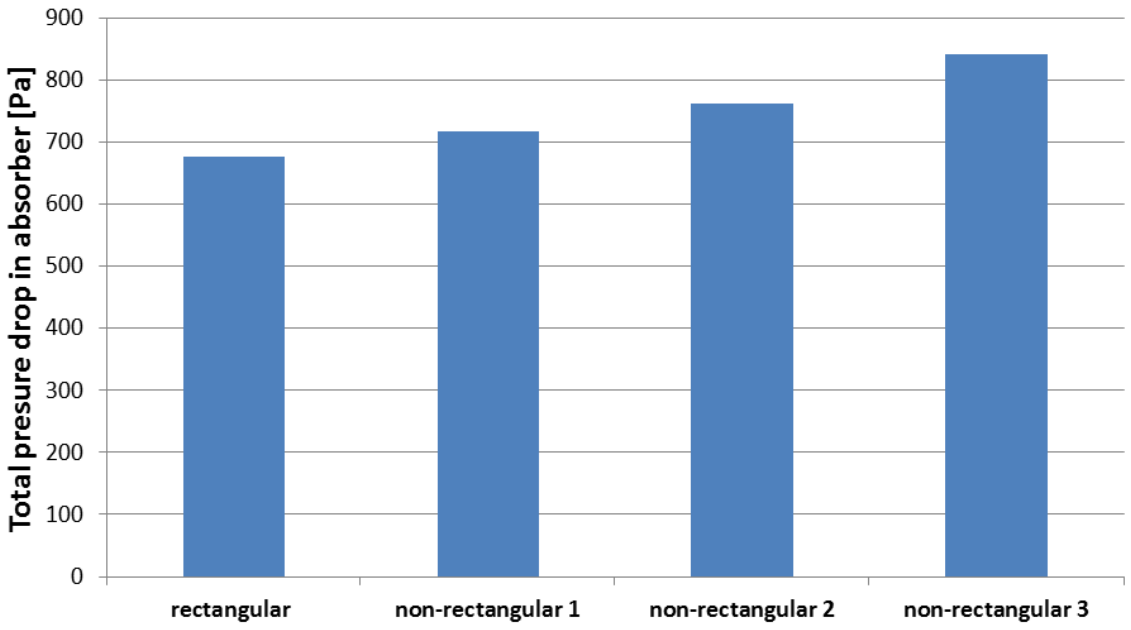

Figure 7-40 Total pressure drop (gas phase) in absorber side for different cases

Fig. 7-41 is the CO_2 loading profiles in the reactor for different reactor shape cases. We can find that even though the shapes of reactors are obviously different, CO_2 loading profiles in the reactor are almost uniform at different cases. Specially, in the stripper side, high CO_2 loading gradient can be found at the top-half of the stripper; at the bottom half of the stripper, CO_2 loading of solvent only presents a small change.

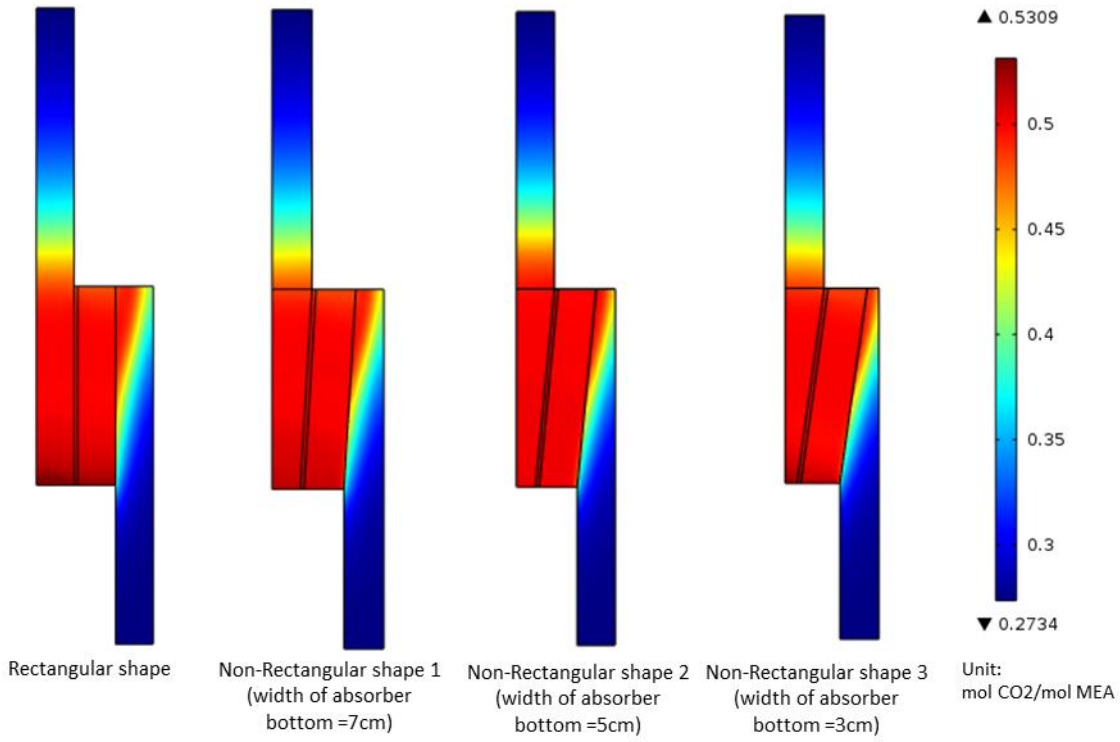

Figure 7-41 CO_2 loading profiles in the integrated absorber/desorber ceramic foam reactor for different cases

The thermal heat consumption of CO_2 desorption for different reactor shape cases is investigated in Fig. 7-42. With the decrease of width of absorber bottom, the regeneration heat consumption decreases. Therefore, rectangular shape reactor presents the highest regeneration heat consumption, which is 3.946 MJ/kg CO_2. Non-rectangular shape 3 reactor with 3 cm width of absorber bottom has the lowest regeneration heat consumption of 3.737 MJ/kg CO_2. 6% of regeneration heat consumption could be reduced for non-rectangular shape 3 compared with rectangular shape reactor.

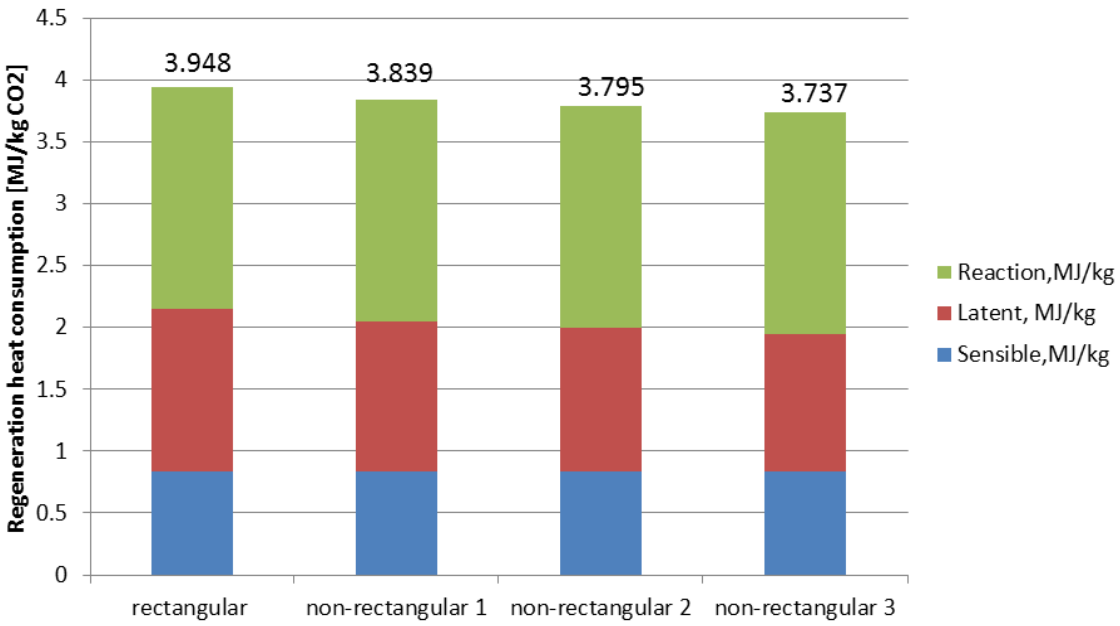

Figure 7-42 Regeneration energy consumption for different reactor shape cases

Effect of absorber/stripper overlapping height on CO_2 capture performance

Absorber/stripper overlapping height is an important geometric parameter that determines the fluid flow and CO_2 capture performance in the ceramic foam reactor. The height of absorber/stripper overlapping was varied to find the optimum overlapping height for a maximal CO_2 removal efficiency and minimal thermal energy requirement. Fig. 7-43 presents the predicted liquid flow velocity distributions in the reactors with different overlapping height. It is very easy to understand that higher overlapping height can provide larger flow section. Therefore, we can find that higher absorber/stripper overlapping height will facilitate the flow of liquid through the membrane to the stripper side. It can also be concluded by the comparison of pressure difference across the membrane for different overlapping height cases, as shown in Fig. 7-44. As the overlapping

height is 120 cm, the average pressure difference across membrane is only 0.046 atm. However, as the overlapping height decreases to 20 cm, the average pressure difference that pushes liquid to pass through the membrane increases to 0.173 atm. A higher pressure difference means more work required to compress the flue gas and liquid to the absorber.

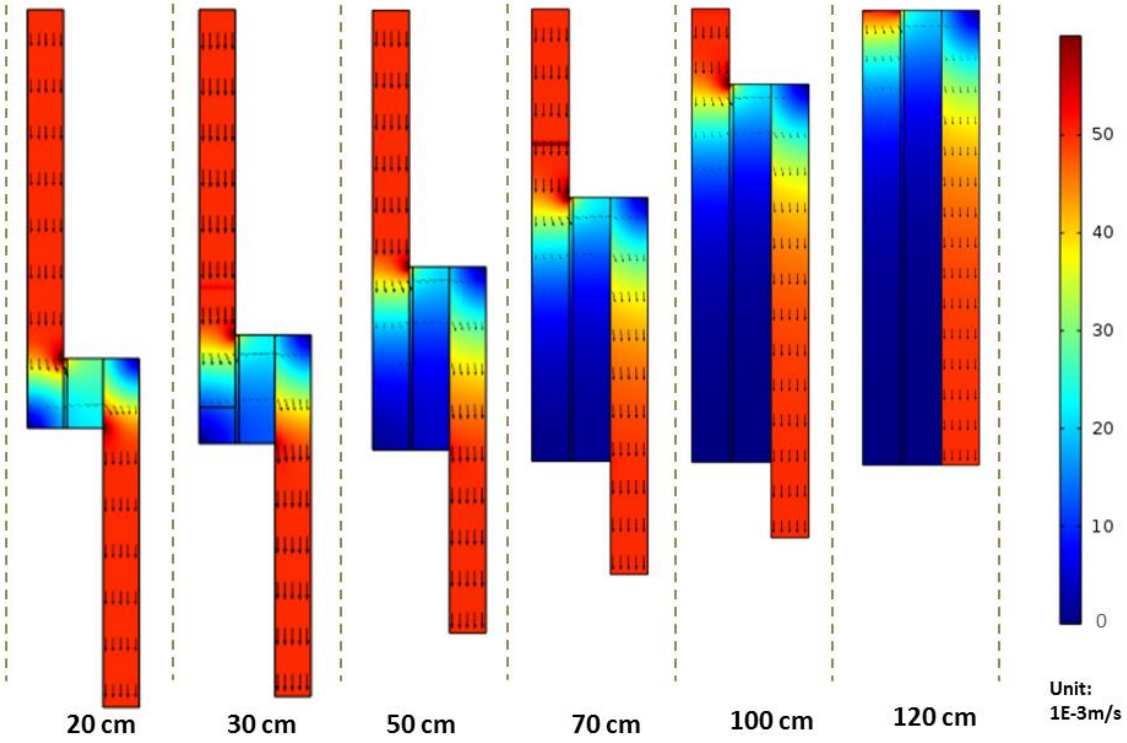

Figure 7-43 Liquid flow velocity profiles for different absorber/stripper overlapping height reactors.

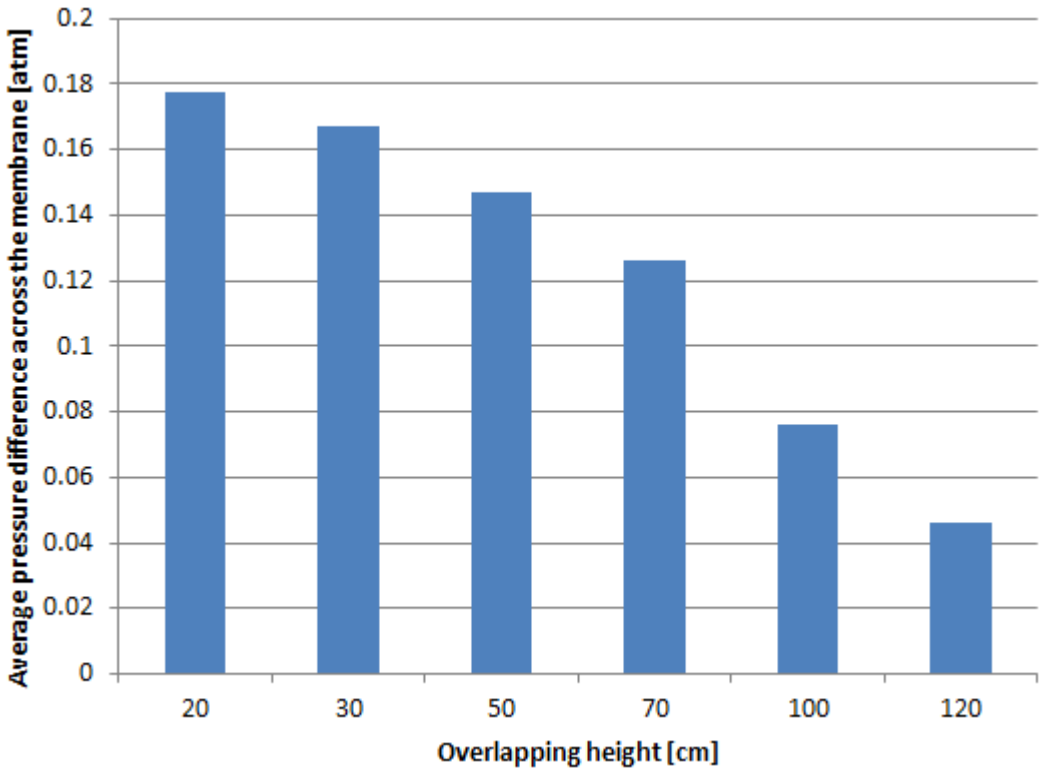

Figure 7-44 Comparison of average pressure difference across the membrane for different overlapping height cases

But higher overlapping height will result in the less efficiency of absorber. In Fig. 7-45, we can find that almost no liquid flows down in the lower part of absorber as the overlapping height is as high as 120 cm, which means CO_2 gas flowing up will not be absorbed in this lower part of absorber due to very small amount of solvent. As the overlapping height is as low as 20 cm, most part of absorber will be full of flowing liquid, as shown in Fig. 7-45. Fig. 7-46 gives a more clear comparison of the influences of overlapping height on the absorber efficiency at different cases. With the increase of absorber/stripper overlapping height, the CO_2 removal efficiency presents a decreasing tendency. Especially, as

the overlapping height higher than 50 cm, CO_2 removal efficiency decreases sharply with the increase of overlapping height. CO_2 removal efficiency reduces to 51.87% as overlapping height increases to 120 cm. We also notice that the targeted 90% removal efficiency can be realized as the overlapping height is less than 70 cm. Therefore, overlapping height less than 70 cm is preferable for CO_2 removal from flue gas in this study.

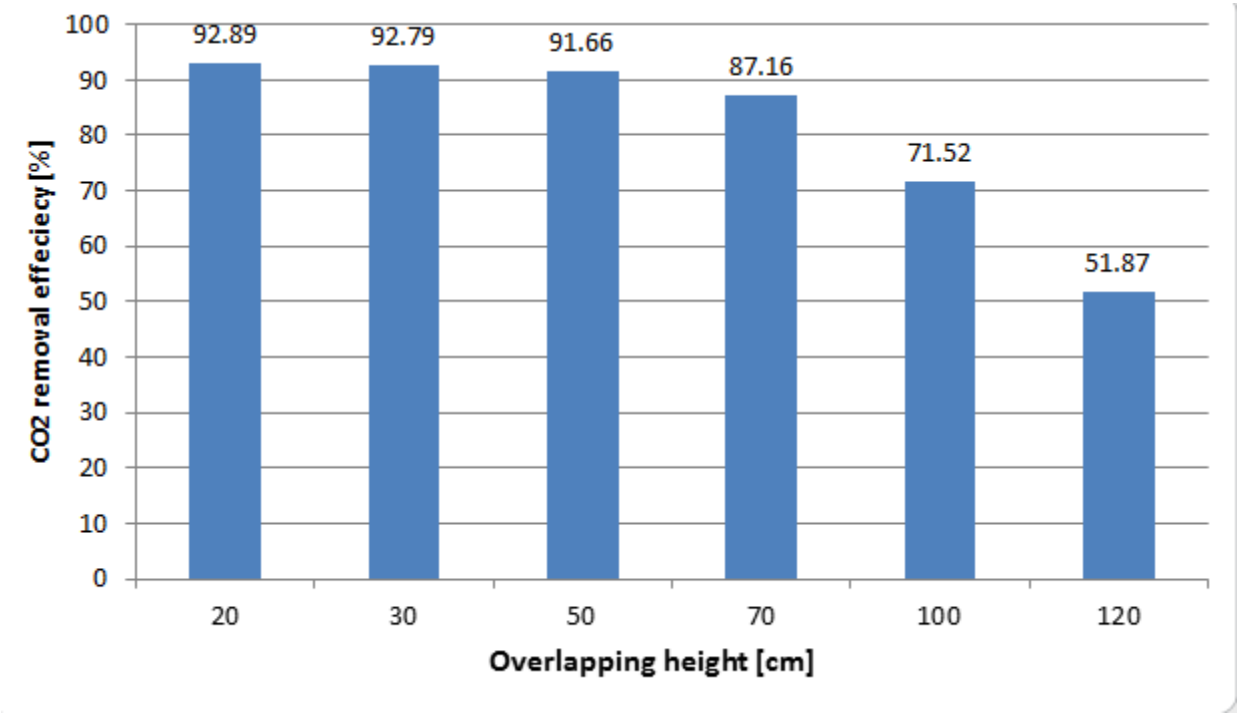

Figure 7-45 The change of CO2 removal efficiency with absorber/stripper overlapping height

Fig. 7-46 shows the liquid temperature profiles in the ceramic foam reactor for different overlapping height cases. It is interesting to notice that with the increase of overlapping height, the magnitude of temperature bulge in the absorber increases. The reason is that higher overlapping height increases the effective area

of heat transfer, which promotes the heat to conduct from high temperature stripper side to low temperature absorber side.

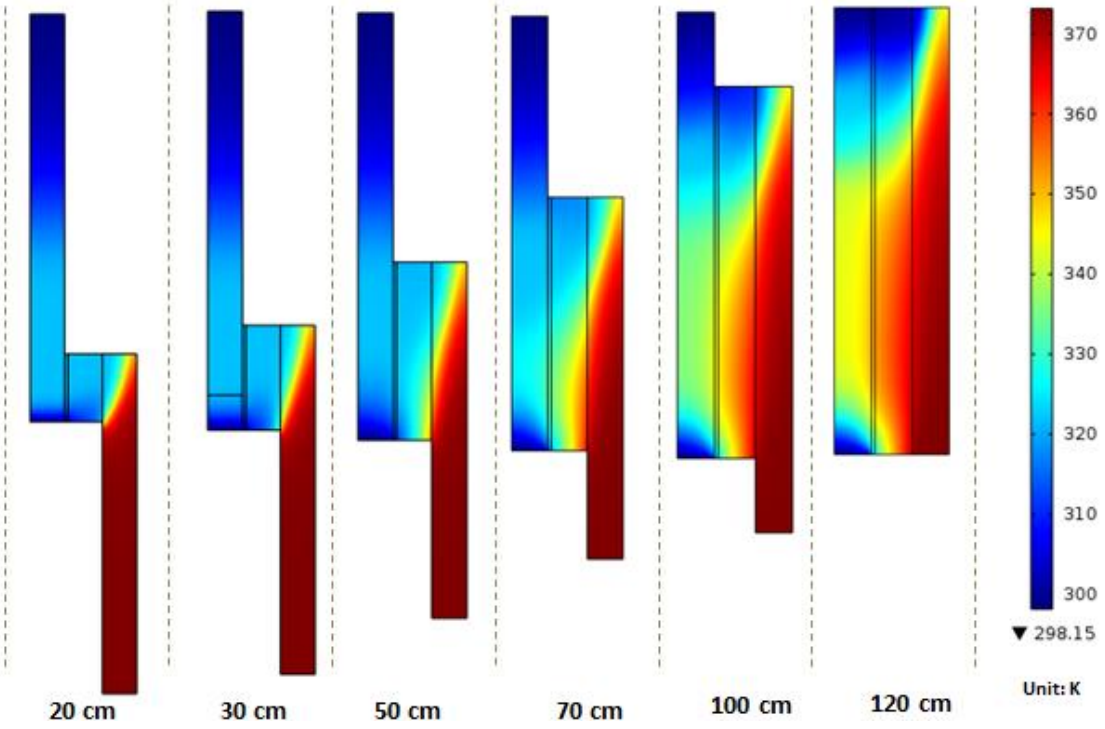

Figure 7-46 Liquid temperature profiles in the integrated absorber/desorber ceramic foam reactor for different overlapping height cases

The solvent CO_2 loading profile in the integrated absorber/desorber ceramic foam reactor for different overlapping height cases is shown in Fig. 7-47. It can be found the cases with overlapping height 20 cm, 30 cm and 50 cm have the similar CO_2 loading profiles in the absorber side. The largest CO_2 loading gradient locates at the middle part of absorber. At the bottom half part of absorber, CO_2 loading is almost kept unchanged with a high CO_2 loading of over 0.5 mol CO_2/mol MEA. However, as the overlapping height further increases to higher than 70 cm, the largest CO_2 loading gradient locates at the top part of absorber.

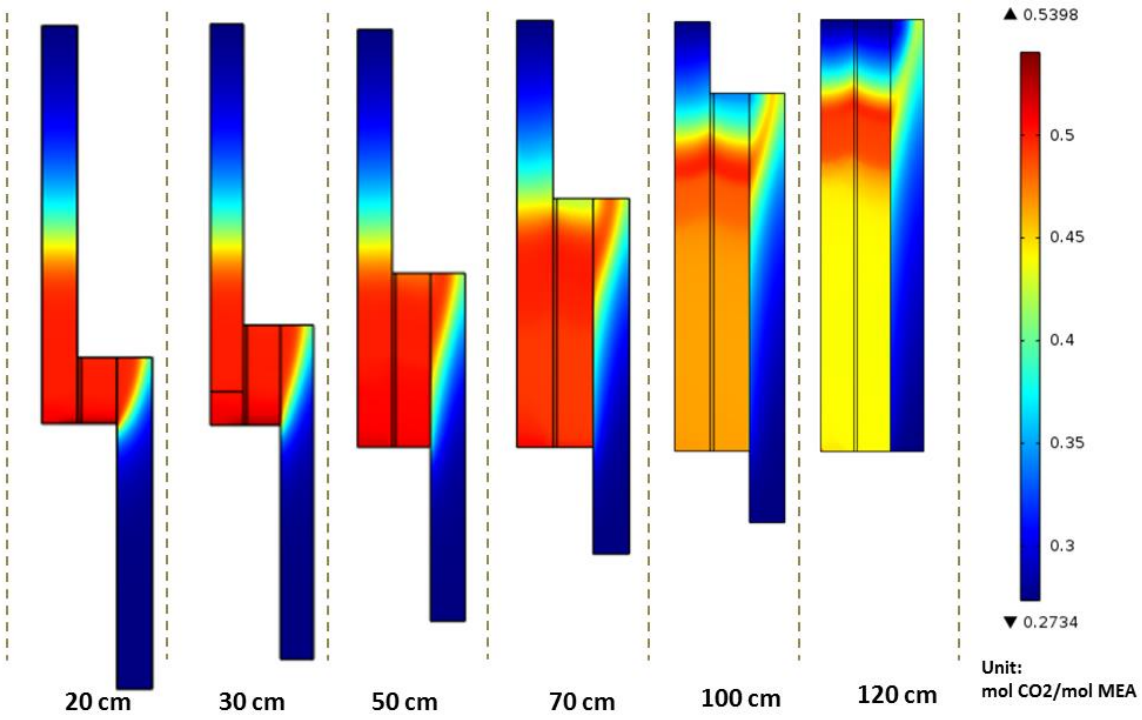

Figure 7-47 CO_2 loading profiles in the integrated absorber/desorber ceramic foam reactor for different overlapping height cases

Thermal energy required for CO_2 desorption with different absorber/stripper .is investigated in Fig. 7-48. As the overlapping height increases from 20 cm to 50 cm, regeneration heat consumption decreases slightly. The lowest thermal energy required is found to be 3.87 MJ/kg CO_2 as overlapping height is 50 cm. With the further increase of overlapping height from 50 cm to 120 cm, the regeneration heat consumption increases significantly, from 3.87 MJ/kg to 5.19 MJ/kg. Therefore, in terms of regeneration heat consumption, the optimum overlapping height of absorber and stripper is expected to be around 50 cm (about half length of the absorber) in this study.

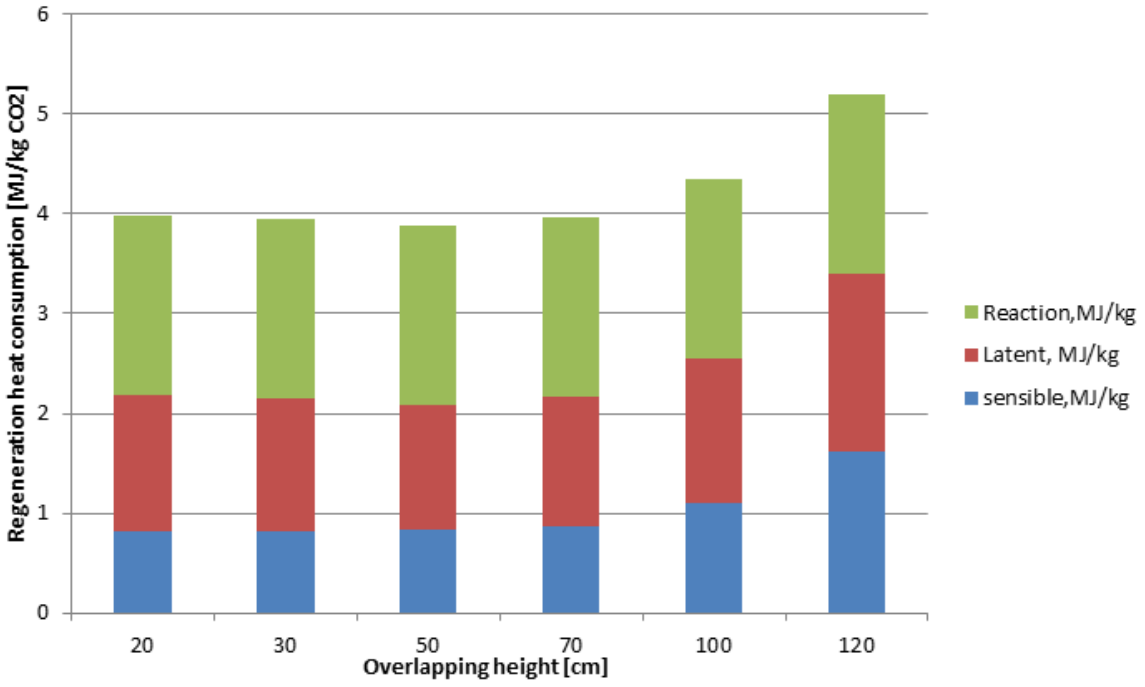

Figure 7-48 Regeneration heat consumption for different overlapping height cases

7.2.4 Simulation of CO_2 capture in ceramic foam unit based on commercial-scale 2D model

Our previous parametric studies of integrated absorber/desorber ceramic foam reactor concluded some optimized operating and geometric parameters for CO_2 capture using 30 wt.% MEA absorbent. However, these predicted results are based on the simulation of a bench-scale 2D model. In order to establish a reasonable comparison between the DOE's baseline process for CO_2 capture and our novel ceramic foam technology, we need to scale up our 2D model from bench-scale to

commercial-scale, and use the simulation results of commercial-scale 2D model to initiate the techno-economic analysis.

Table 7-5 gives the system operating parameters of commercial-scale integrated absorber/desorber ceramic foam CO_2 capture unit, which are based on optimized simulation results of bench-scale 2D model in our previous studies.

Table 7-5 System operating parameters in commercial-scale integrated absorber/desorber ceramic foam CO_2 capture unit

Operating parameters	Value
Absorbent type	30 wt% MEA
Lean CO_2 loading	0.27 mol CO_2/mol MEA
Flue gas to solvent volumetric flow ratio (G/L)	200
Flue gas velocity	0.4 m/s
Flue gas inlet temperature	313 K
Solvent inlet temperature	313 K
Stripper bottom temperature	373 K

It is important to notice that the flue gas flow velocity in the ceramic foam unit (Table 7-5) is determined by the flooding velocity of ceramic foam. The operating flue gas velocity is usually 0.8 times of flooding velocity. Fig. 7-49 investigates the flooding characteristic of ceramic foam in generalized pressure drop correlation (GPDC) charts. GPDC describes the balance between the vapor momentum force and the gravity force acting on the liquid droplets, has been commonly used as the

standard for predicting packing flooding and pressure drops in industry [38]. The GPDC is constituted of the flow parameter on the abscissa and the capacity factor on the ordinate [39]:

$$\text{flow parameter} = \left(\frac{L}{G}\right)\left(\frac{\rho_G}{\rho_L}\right)^{0.5} \quad (1)$$

$$\text{capacity factor} = \frac{G^2 F_p \xi^2 \mu_L^{0.2}}{\rho_G \rho_G g} \quad (2)$$

where F_p is the wet packing factor; ξ is the ratio between the density of water and the density of liquid; L and G are the liquid and vapour mass fluxes; μ_L is the liquid viscosity, cP; ρ_G and ρ_L are the densities of vapour and liquid;

In Fig. 7-49, we can find as G/L equal to 200, the flooding gas velocity in ceramic foam will be around 0.5 m/s. We choose 0.8 times of flooding velocity as the operating flue gas velocity, therefore, the operating flue gas velocity is 0.4 m/s in ceramic foam unit.

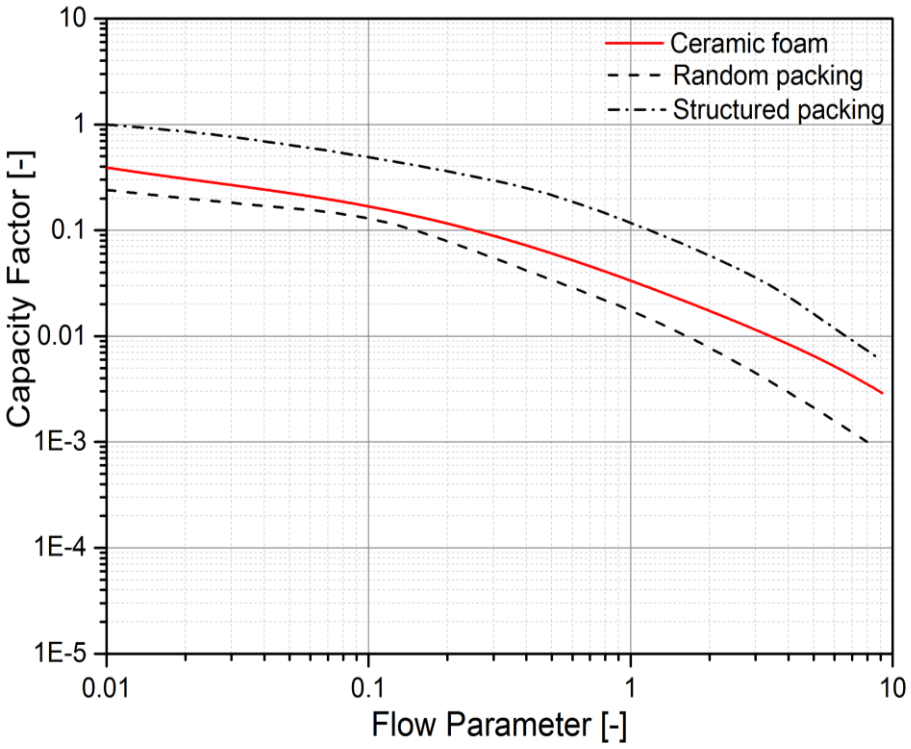

Figure 7-49 Comparison of flooding lines for different packings in generalized pressure drop correlation chart.

The DOE report (#DOE/NETL-2010/1397) provides the system parameters of baseline case (case 9) for CO_2 capture. In this case, the subcritical PC plant with a nominal net output of 550 MWe, with a single reheat 16.5 MPa/566°C/566°C (2400 psig/1050°F/1050°F) cycle, the total flue gas flow rate is about 1.97E6 Nm^3/h.

Fig. 7-50 gives the schematic diagram of integrated absorber/desorber ceramic foam unit. In both absorption side and desorption side, commercial ceramic foam of 20 PPI is chosen as the packing material.

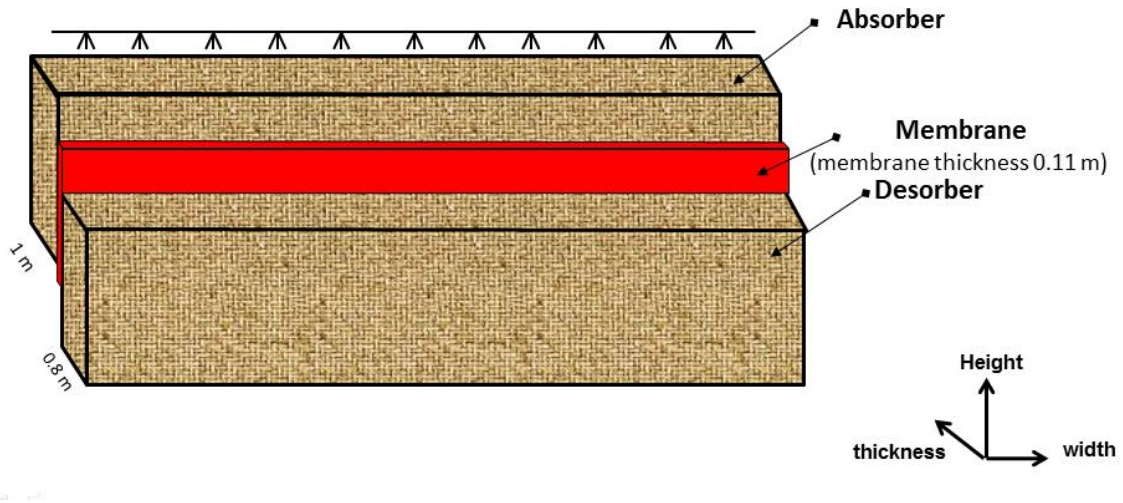

Figure 7-50 Schematic diagram of integrated absorber/desorber ceramic foam unit

The dimensions of this integrated unit are presented in Table 7-6. In order to choose the optimal absorber and stripper heights, we simulated two cases which have different heights of absorber and desorber for comparison.

Table 7-6 The dimension of integrated absorber/desorber ceramic foam unit

	Absorber		Desorber		Membrane	Absorber/desorber overlapping height
	Height (m)	Thickness (m)	Height (m)	Thickness (m)	Thickness (cm)	Height (m)
Case1	8	1	6	0.8	11	3
Case 2	5	1	4	0.8	11	3

The simulated flue gas flow rate and gas compositions which have been used in this study are presented in Table 7-6.

Table 7-7 The simulated flue gas flow rate and gas composition

Item	Unit	Value
Flue gas flow rate	m/s	0.4
Flue gas outlet pressure	kPa	101.6
Flue gas inlet temperature	°C	40
Flue gas composition	/	13 v/v% CO_2
	/	87 v/v% N_2

Fig. 7-51 presents the simulated solvent flow velocities in ceramic foam unit for different cases. For both cases, we can clearly find the change of liquid velocity along the absorber column. A uniform liquid down flow velocity can be found in the top half of the absorber column. As the liquid reaches the bottom half of the absorber column which has overlapping area with stripper, the liquid flow velocity decreases gradually. This is because in the bottom part of absorber, some of the liquid permeates through the membrane layer and flow to the stripper side. And at the bottom end of the absorber, the liquid flow velocity almost becomes zero, meaning no liquid left in the absorber anymore and all the liquid has crossed into the stripper side. By comparing with two different cases, we can also find change the heights of absorber and stripper will not affect the flow distribution of liquid in the ceramic foam unit.

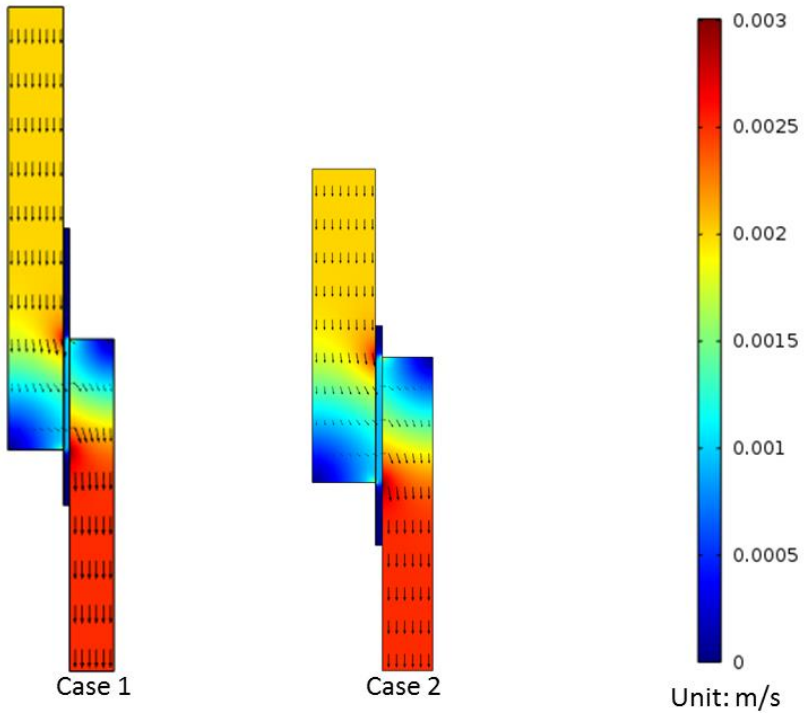

Figure 7-51 solvent flow velocity distribution in ceramic foam unit (arrow direction indicates the solvent flow direction; arrow size indicates the magnitude of flow velocity).

The change of gas phase CO_2 concentration along the height of absorber column can be seen in Fig. 7-52. For both cases, a very small change in CO_2 concentration can be found near the bottom part of the absorber. Small change of CO_2 concentration in gas phase means CO_2 absorption process almost reaches equilibrium in this area.

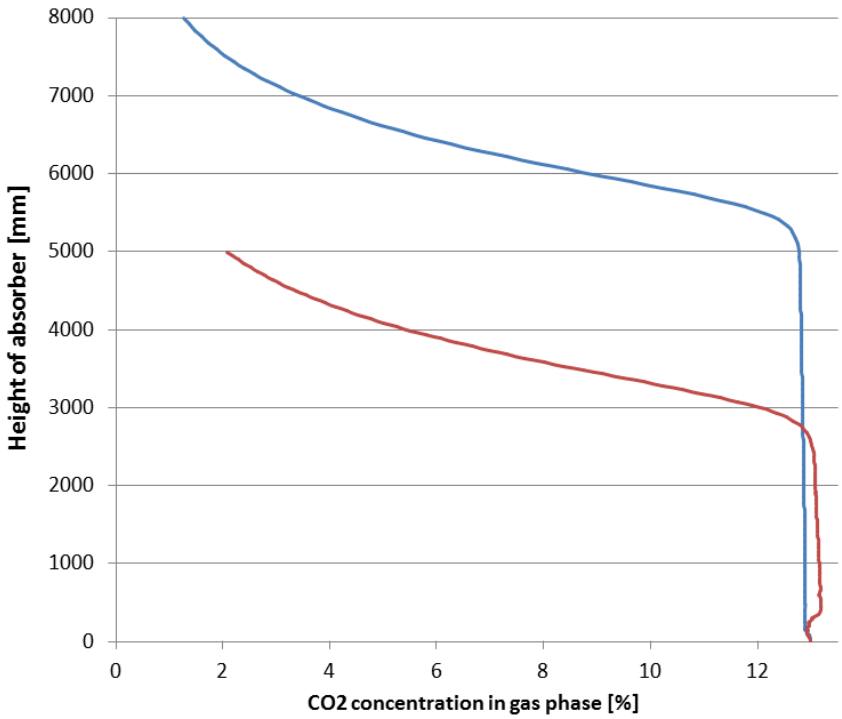

Figure 7-52 The change of CO_2 concentration in gas phase along the height of absorber column (blue line: case 1, red line: case 2).

CO_2 removal efficiency for different cases is presented in Fig. 7-53. Increasing absorber column height results in an improvement on CO_2 removal efficiency. CO_2 removal efficiency increases from 85% to 90% as absorber column height increases from 5 m (case 2) to 8 m (case 1). We also notice that the targeted 90% removal efficiency cannot be realized in our study if the absorber height is less than 8 m.

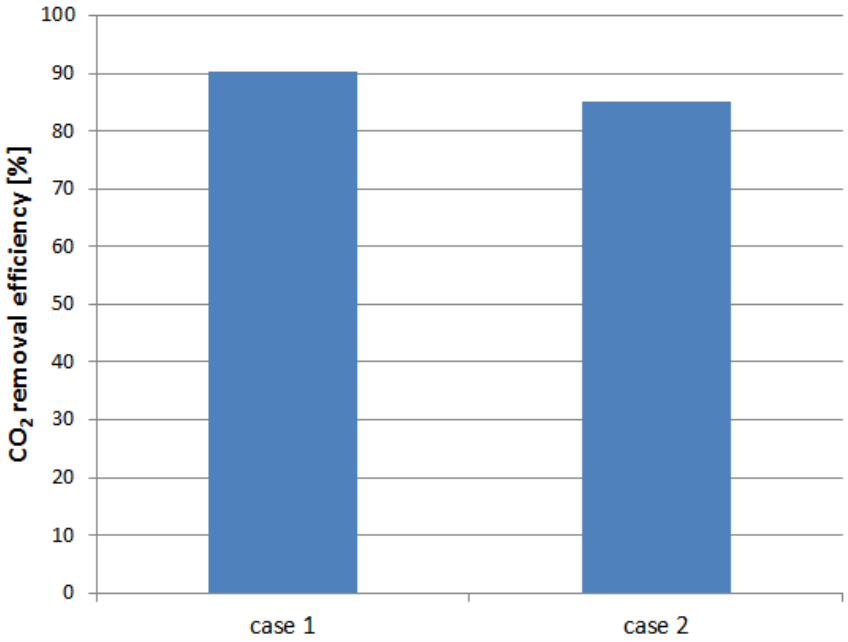

Figure 7-53 CO_2 removal efficiency for different cases

The predicted solvent temperature profiles in ceramic foam unit for different cases are shown in Fig. 7-54. While change of absorber and stripper height does not affect the profile of solvent temperature, some clear temperature boundaries can be found in the ceramic foam unit. The highest temperature region is located at the bottom part of stripper column; lowest temperature region is located at the top part of absorber column. In the absorber/stripper overlapping region, the temperature is almost unchanged and keeping at around 335 K. This temperature profile is also similar with the temperature profile predicted by bench-scale 2D model reported previously.

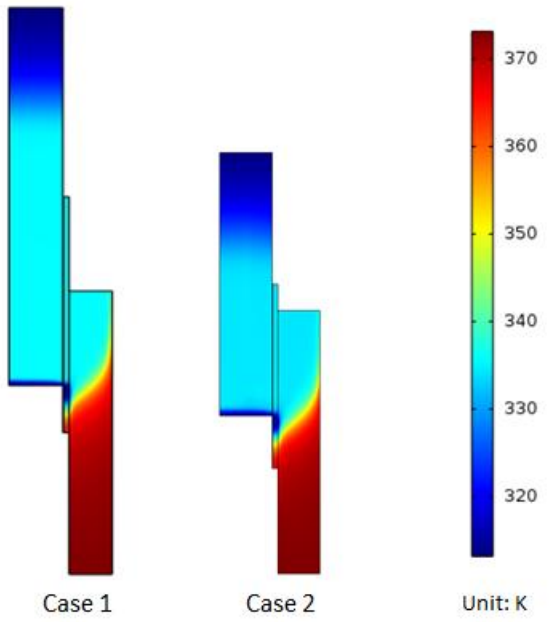

Figure 7-54 Solvent temperature profiles in the integrated absorber/desorber ceramic foam reactor for different cases

Fig. 7-55 further gives the predicted solvent temperature profiles along absorber column for different cases. For both cases, we can found a temperature bulge (a "warm spot") at the bottom part of absorber due to exothermic reaction of CO_2 absorption. The highest temperature can reach to about 335 K. Case 1 with absorber height 8 m presents a bigger temperature bulge than case 2 with absorber height 6 m. It is also interesting to notice that solvent temperature change very sharply near the bottom of the absorber. It could be explained by the very small liquid flow velocity near the bottom (due to most of the liquid having permeated through the membrane to the stripper side before reaching the bottom), resulting in the hot liquid being cooled down quickly by the upward gas flow.

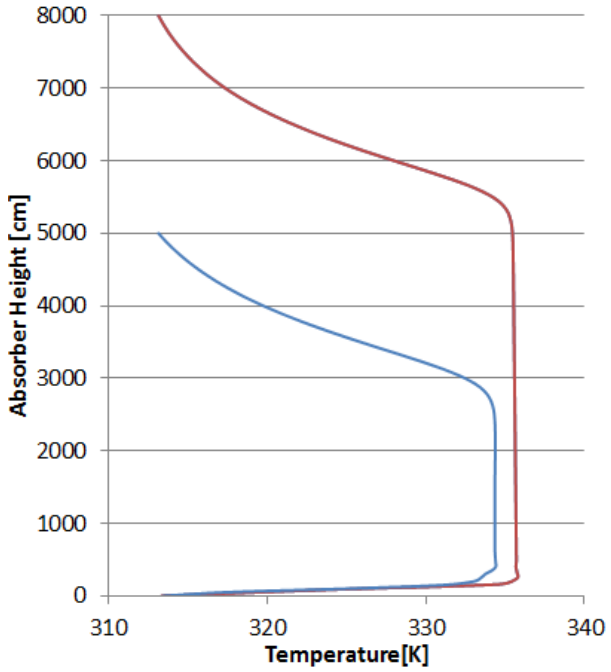

Figure 7-55 The change of temperature in liquid phase along the height of absorber column (red line: case 1, blue line: case 2).

Fig. 7-56 shows simulated CO_2 loading profiles in the integrated absorber/desorber ceramic foam unit at different cases. In the top part of absorber section, the CO_2 loading presents a significant change with absorber height. However, in the bottom half of the absorber, the CO_2 loading almost keeps unchanged. The unchanged of CO_2 loading means no CO_2 is absorbed in the region. In the stripper section, a significant CO_2 loading gradient at top half part of the stripper side can be observed the CO_2 absorption reach to equilibrium in this area. It indicates CO_2 desorption mainly occurred near the top of the stripper side. This phenomenon is also similar with the simulation results of bench-scale 2D model.

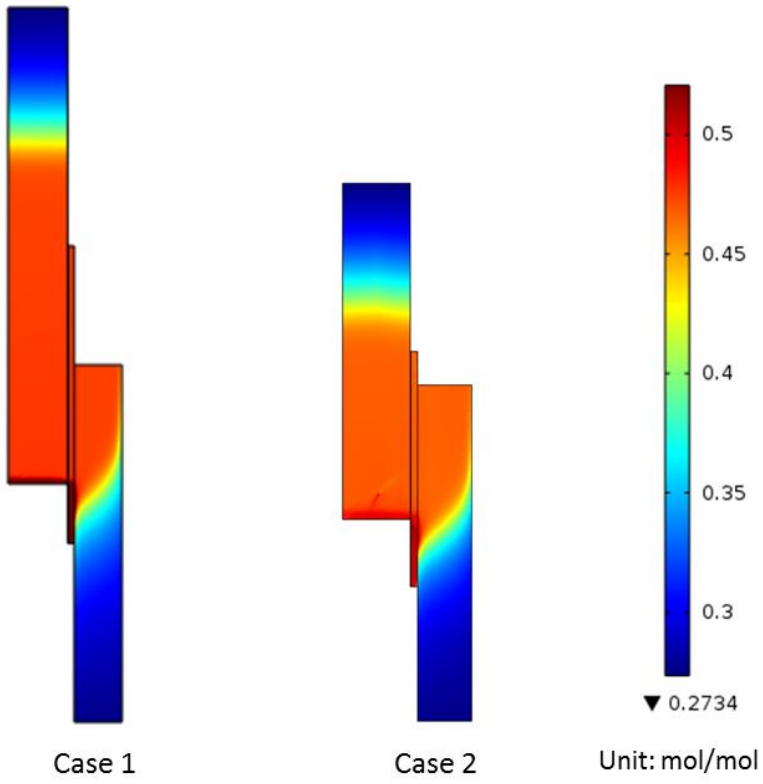

Figure 7-56 CO_2 loading profiles in the ceramic foam unit at different cases

Fig. 7-57 presents the regeneration heat consumption for different cases. Higher absorber and stripper height will result in a decrease in regeneration heat consumption. For case 1, the regeneration heat consumption is around 3.8 MJ/kg CO_2; for case 2, the regeneration heat consumption is around 3.9 MJ/kg CO_2. These regeneration heat consumption values are also similar with the predicted heat consumption from bench-scale 2D model.

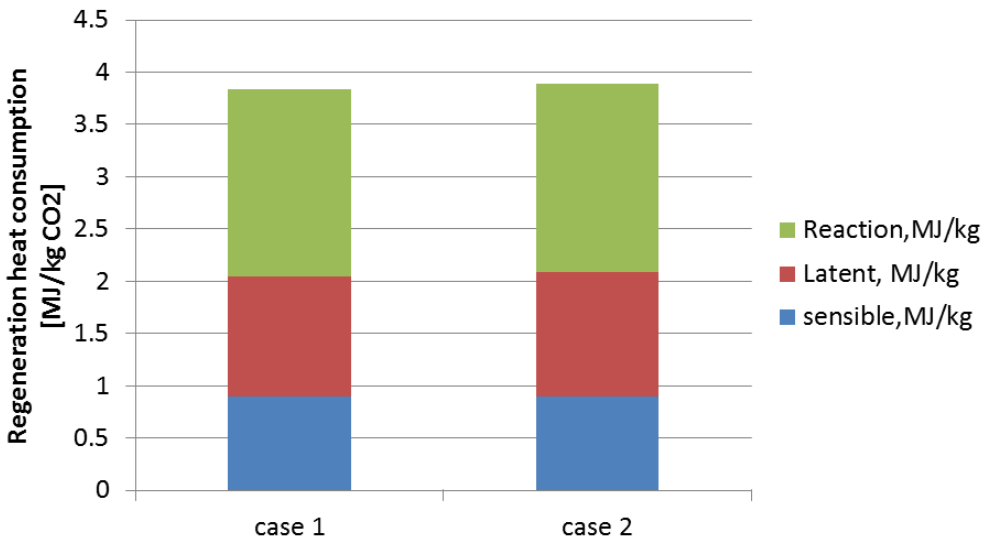

Fig. 7-57 Regeneration heat consumption for different cases

8. Techno-economic feasibility study

8.1 Background and generating unit configurations

This section is to present an accurate, independent assessment of the cost and performance of a new-built subcritical PC power plant with integrated ceramic foam CO_2 capture process developed by Rice University. The study evaluates CCS plants based on current technology and predicts the performance and costs of CCS plants that operate in 2012.

A subcritical PC power plant with a nominal net output of 550 MWe and a single reheat 16.5 MPa/566°C/566°C (2400 psig/1050°F/1050°F) cycle (DOE Case 9- Subcritical PC plant) is selected to act as a reference base without CO_2 capture and compression. The techno-economic evaluation for two PC Cases (Case A and Case B) with CO_2 capture will be performed and compared with the techno-economic results from the DOE reports. Both Cases use a single reheat 16.5 MPa/566°C/566°C (2400 psig/1050°F/1050°F) cycle. The only difference is Case A is subcritical PC plant with Fluor Econamine CO_2 capture process (DOE Case 10); while Case B is subcritical PC plant with the Rice University integrated ceramic foam CO_2 capture process.

A summary of plant configurations in this study is presented in Table 8-1. Both PC cases are evaluated on a common 550 MWe net basis. The SOx, NOx and PM emissions control technologies of both PC Cases are also common to each plant configuration.

Table 8-1 Case descriptions

Case	Unit Cycle	Steam cycle, Mpa/°C/°C	Boiler Technology	Oxidant	SO_X removal	PM Control	NO_X Control	CO_2 Capture Technology	CO_2 Removal efficiency	CO_2 Sequestration
A	PC	16.5/566/566	Subcritical PC	Air	Wet FGD/Gypsum	ESP	LNB/OFA and SCR	Fluor Econamine	90%	Off-site
B	PC	16.5/566/566	Subcritical PC	Air	Wet FGD/Gypsum	ESP	LNB/OFA and SCR	Ceramic Foam	90%	Off-site

8.2 General evaluation bases

8.2.1 Coal characteristics

The design coal is Bituminous Coal Illinois No. 6 with characteristics presented in Table .

Table 8-2 Characteristics of Design Coal

Item	Unit	Value
Heating value	kJ/kg	27140
Carbon	wt %	63.75
Hydrogen	wt %	4.50
Oxygen	wt %	6.88
Chlorine	wt %	0.29
Sulfur	wt %	2.51
Nitrogen	wt %	1.25
Ash	wt %	19.70
Moisture	wt %	11.12
Total	wt %	100

8.2.2 Environmental targets

For the environmental targets of the PC reference plant, some factors should be considered, such as EPA emission standards and the emission regulation trends. In this study, only air pollutants were taken into consideration. Emission standards for air pollutants are shown in Table . But as the CO_2 capture system is integrated into

the PC plant, SO_X concentration in the flue gas before the CO_2 absorber should be reduced to about 10 ppmv or less in order to reduce the MEA losses caused by reaction with SO_2. The gas exiting the FGD system passes through an SO_2 polishing step to achieve this objective. Particulates concentration in the flue gas should be limited to about 20 mg/Nm^3. NO_2 concentration in the flue gas should be reduced to about 5 ppmv after LNB, OFA and SCR technologies.

Table 8-3 Environmental targets for subcritical PC reference base

Pollutant	Environmental Target	Possible Control Technology
Particulates	50 mg/Nm^3	Electrostatic Precipitator (ESP) or Fabric Filter
SO_X	400 mg/Nm^3	Wet limestone scrubber
NO_X	V_{daf}<10%, 1100 mg/Nm^3; 10%≤V_{daf}≤20%, 650 mg/Nm^3; V_{daf}>20%, 450 mg/Nm^3	Low NO_X burners, overfire air (OFA) and SCR or SNCR

8.2.3 Raw water withdrawal

Water demand represents the total amount of water required for a particular process. A water balance was performed in some major subsystems of the CCS PC power plant, such as the boiler, condenser, lean solution cooler, CO_2 product cooling & drier system and cooling tower. The total water demand for each subsystem was calculated, and some water is recovered within the process and is reused as internal recycle.

Raw water withdrawal is defined as the water removed from the ground or diverted from a surface-water source for use in the plant. For the reference PC plant, raw water withdrawal can be estimated by estimating all the water makeups in the plant process, such as boiler feedwater makeup, cooling tower makeup, slurry preparation makeup, ash handling makeup, and FGD system makeup. For the CCS PC plant, it was assumed that the raw water withdrawal for the PC plant without CO_2 capture is constant, so we only need to calculate the raw water withdrawal for CO_2 capture and compression system, such as the recirculated cooling water makeup and desalinated water makeup, to assess the total raw water withdrawal for CCS PC plant. In this study, all the raw water makeup was assumed to be provided by river water. The water withdrawal of the PC power plant without CO_2 capture will be used as a reference baseline to indicate the impact of CO_2 capture on water usage.

The largest raw water consumer in this power plant is cooling tower makeup. It was assumed that the reference base adopted a natural draft, evaporative cooling tower. The cooling water inlet temperature was designated as 15 ^oC and the outlet temperature was taken as 26 ^oC. The average raw water withdraw of the PC reference base plant was assumed to be about 0.8 $m^3/(s \cdot GW)$. The cooling water makeup rate was determined using the following procedures:

- *Evaporative losses were calculated as follows:*

Evaporative losses= (specific heat of water)*(cooling water range)*(circulating water flow rate)/2260.

- *Windage losses of 0.1 percent of the circulating water flow rate.*

- *Blowdown losses were calculated as follows:*

Blowdown losses = Evaporative losses / (Cycles of Concentration – 1).

8.2.4 Configuration of power plants

This section gives an overview of the chosen plant configuration and the basic engineering data used for the study basis.

Subcritical pulverized coal fired power plants

The configurations of Case A and Case B are shown in Fig. 8-1 and Fig. 8-1**(b)**. For both cases, SO_X and NO_X concentrations of the flue gas must be further reduced to approximately 10 ppmv to minimize formation of amine heat stable salts (HHS) during the CO_2 absorption process.

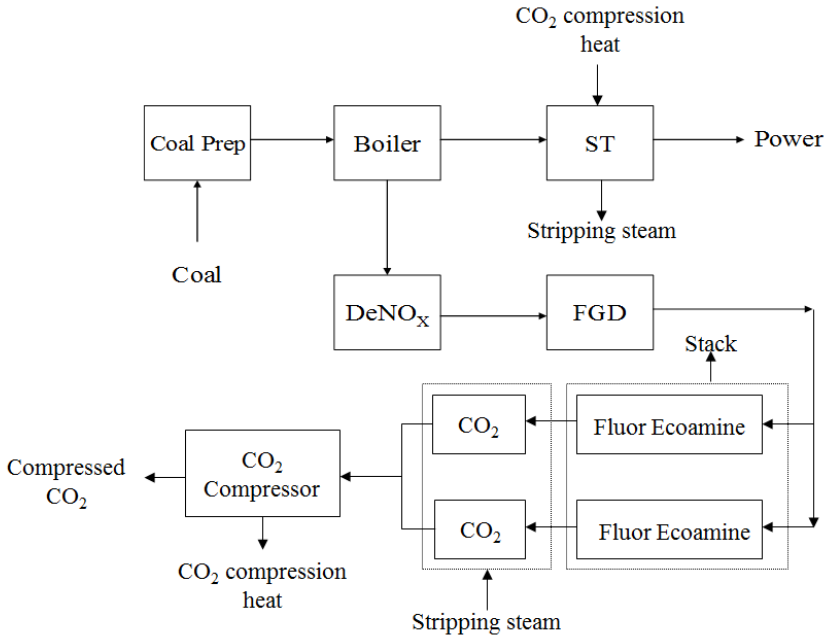

Fig. 8-1(a) Subcritical PC plant with Fluor Ecoamine CO_2 capture process (Case A).

Fig. 8-1(a) shows the flow diagram of subcritical PC plant with Fluor Ecoamine CO_2 capture process (Case A). After $DeNO_X$ and FGD system, the flue gas is sent to the Fluor Econamine system for CO_2 separation. In this case, two identical CO_2 capture units are employed to removal CO_2 from flue gas. IP/LP steam will be extracted from the steam line between IP turbine and LP turbine to regenerate the rich-amine, but it will lead to a loss of power output of the plant. In addition, CO_2 compression heat can be recovered for the steam turbine (ST) system to offset part of the power loss. The effect of steam extraction and CO_2 compression heat recovered on power output can be estimated by using the method and results provided by Romeo [4].

Fig.8-1(b) shows the flow diagram of subcritical PC plant with Rice University ceramic foam CO_2 capture process (Case B). The main difference between these two flow diagrams is the number of CO_2 capture units. In Fig. 8-1(b), 20 identical ceramic foam CO_2 capture units are employed to removal CO_2 from flue gas, while there are two identical Fluor Ecoamine units in Fig. 8-1(a).

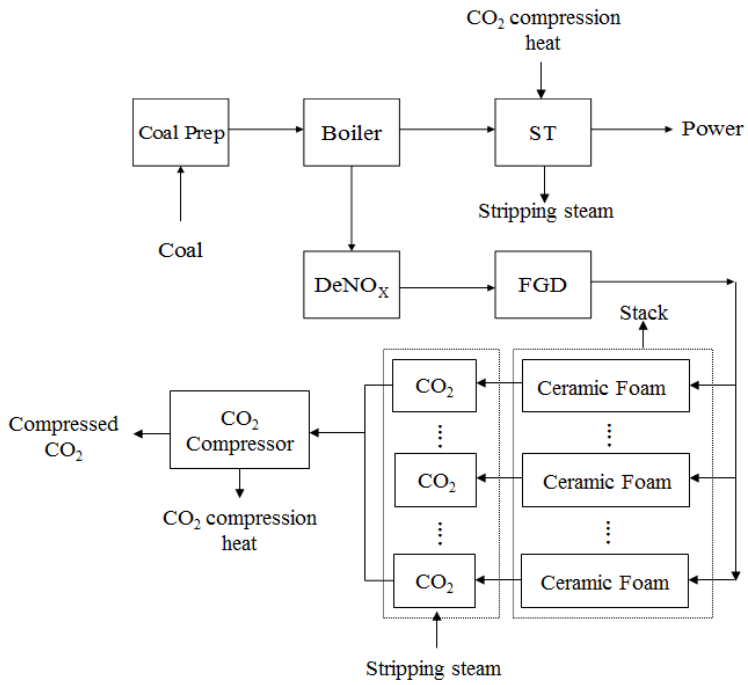

Fig. 8-1(b) Subcritical PC plant with cer1amic foam CO_2 capture process (Case B).

Configuration of commercial-scale ceramic foam CO_2 capture unit

Table 8-4 gives the system operating parameters of commercial-scale integrated absorber/desorber ceramic foam CO_2 capture unit, which are based on optimized simulation results of bench-scale 2D model in our previous studies.

Table 8-4. System operating parameters in commercial-scale integrated absorber/desorber ceramic foam CO_2 capture unit

Operating parameters	Value
Absorbent type	30 wt% MEA
Lean CO_2 loading	0.27 mol CO_2/mol MEA

Flue gas to solvent volumetric flow ratio (G/L)	200
Flue gas velocity	0.4 m/s
Flue gas inlet temperature	313 K
Solvent inlet temperature	313 K
Stripper bottom temperature	373 K

It is important to notice that the flue gas flow velocity in the ceramic foam unit (Table 8-4) is determined by the flooding velocity of ceramic foam. The operating flue gas velocity is usually 0.8 times of flooding velocity.

The DOE report (#DOE/NETL-2010/1397) provides the system parameters of baseline case (case 9) for CO_2 capture. In this case, the subcritical PC plant with a nominal net output of 550 MWe, with a single reheat 16.5 MPa/566°C/566°C (2400 psig/1050°F/1050°F) cycle, the total flue gas flow rate is about 1.97×10^6 Nm^3/h.

Fig. 8-2 gives the schematic diagram of integrated absorber/desorber ceramic foam unit. In both absorption side and desorption side, commercial ceramic foam of 20 PPI is chosen as the packing material.

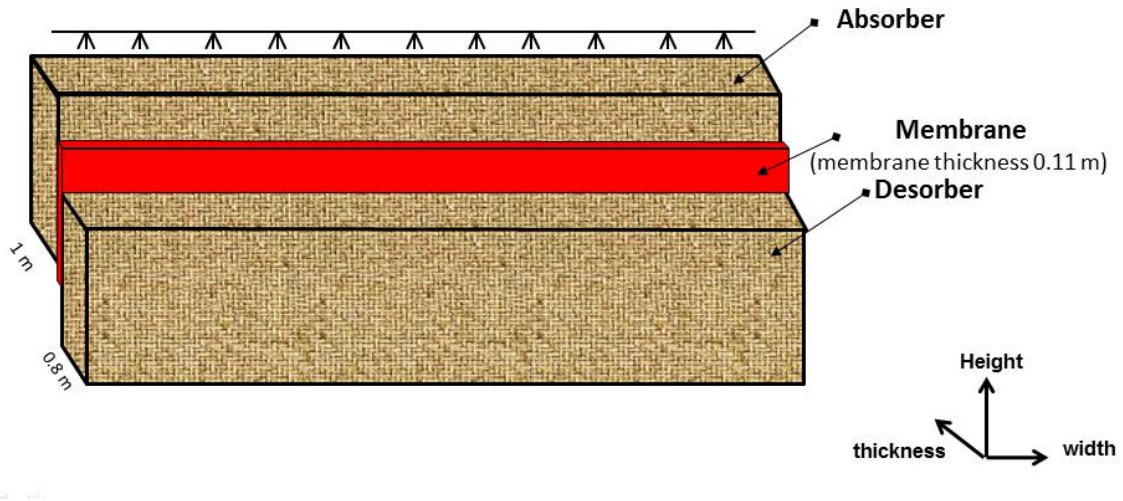

Figure 8-2. Schematic diagram of integrated absorber/desorber ceramic foam unit

The dimensions of this integrated unit are presented in Table 8-5. In order to choose the optimal absorber and stripper heights, we simulated two cases which have different heights of absorber and desorber for comparison.

Table 8-5 The dimension of integrated absorber/desorber ceramic foam unit

Absorber		Desorber		Membrane	Absorber/desorber overlapping height
Height (m)	Thickness (m)	Height (m)	Thickness (m)	Thickness (cm)	Height (m)
8	1	6	0.8	11	3

The simulated flue gas flow rate and gas compositions which have been used in this study are presented in Table 8-6.

Table 8-6 The simulated flue gas flow rate and gas composition

Item	Unit	Value
Flue gas flow rate	m/s	0.4
Flue gas outlet pressure	kPa	101.6
Flue gas inlet temperature	°C	40
Flue gas composition	/	13 v/v% CO_2
	/	87 v/v% N_2

Gross and net power output of cases

The gross and net power outputs for Case A and Case B are given below in Table 8-7 respectively. The net power output of Case A is lower than Case B. In Case A, about 151 MWe power is lost due to CO_2 capture; in Case B, CO2 capture power loss is 138.3 MWe. CO_2 capture power loss includes the power loss due to steam extraction and power consumption for CCS system running. The detailed energy consumption in CCS plant will be discussed in subsequent section.

Table 8-7 Gross and net power outputs for Case A and Case B

	CASE A	**CASE B**
	Subcritical PC+Fluor Ecoamine CO2 Capture	**Subcritical PC+Rice Ceramic Foam CO2 Capture**
Gross output, MWe	672	672
Power plant loss, MWe	53.1	53.1

CO_2 capture loss, MWe	151.0	138.3
Total loss, MWe	204.2	191.4
Net output, MWe	467.9	480.6
Net thermal efficiency, %	27.8	28.6

8.2.5 Other basic data

The flue gas parameters using for CO_2 capture plant design can be found in Table 8-8. The basic data for economic analysis of the CO_2 capture system are shown in Table 8-9.

Table 8-8 Flue gas parameters at the air heater exit

Flue Gas Component	Unit	**Value**
N_2	kg/MWh	3,110
O_2	kg/MWh	217.2
H_2O	kg/MWh	398.3
CO_2	kg/MWh	850
HCl	kg/MWh	1.085
SOx	kg/MWh	0.373
NOx	kg/MWh	0.256
Particulates	kg/MWh	0.063

Ar	kg/MWh	52.94

Table 8-9 Economical data

Description	Units	Value
Coal price	$/ton	38.18
MEA price	$/t	2200
Ceramic foam price	$/m^3	2780
Packing price	$/m^3	1800
Al_2O_3 membrane price	$/ m^3	8330
PES membrane price	$/m^2	50
Industrial water price	$/t	1
Cooling water price	$/t	0.2
Activated carbon price	$/t	2000
Liquid ammonia price	$/t	3000
NaOH price	$/t	500
Limestone price	$/t	60
DeNOx catalyst price	$/m^3	10000

8.2.6 Cost estimating methodology

Design and construction

Subcritical PC cases have been evaluated with the following investment profiles:

Year 1	10% CAPEX
Year 2	30% CAPEX
Year 3	25% CAPEX
Year 4	20% CAPEX
Year 5	15% CAPEX

Total design and construction period is 5.0 years.

Load factor (Capacity factor)

As suggested by DOE, the load factors for two PC Cases are both assumed to be 85% during the operating years.

Project life and startup date

This is 30 years for the two subcritical PC cases. The project is assumed to start operation in 2012.

Discount rate

The two main cases are using a 11% nominal discount rate.

Cost of debt

This is ignored as finance structures have not been taken into consideration.

Contingencies

Process and project contingencies are included in estimates to account for unknown costs that are omitted or unforeseen due to a lack of complete project definition and engineering.

Process contingency is intended to compensate for uncertainty in cost estimates caused by performance uncertainties associated with the development status of a technology. Process contingencies are applied to each plant section based on its current technology status, AACE International Recommended Practice 16R-90 provides guidelines for estimating process contingency based on EPRI philosophy, as shown in Table 8-10.

The project contingency is estimated to be 29 percent of Bare Erected Cost.

Table 8-10 AACE Guidelines for Process Contingency

Technology Status	Process Contingency (% of associated process capital)
New concept with limited data	40+

Concept with bench-scale data	30-70
Small pilot plant data	20-35
Full-sized modules have been operated	5-20
Process is used commercially	0-10

CAPEX

CAPEX is estimated using the methodology defined at Table 8-11. In the Table 8-11 CAPEX estimates 40% contingency costs are assumed for Case B because this is a new concept only with bench-scale data.

Table 8-11 CAPEX estimating methodology

Description	Type	Value
Direct equipment cost (DEC)	Input	Assessment
Construction cost (CC)	Input	30%DEC
Bare erected cost (BEC)		**BEC = DEC + CC**
Eng'g CM H.O.& Fee (ECF)	Input	12.5% BEC
Process contingency	Input	20% BEC (Fluor Ecoamine) 40%BEC (Rice Ceramic Foam)

Project contingency	Input	29% BEC
Owners cost	Input	30% BEC
CAPEX	Output	**CAPEX=BEC+ECF+Contingences+Owner cost**

Operating costs

The annual operating costs consist of three parts: fuel costs, fixed O&M costs and variable costs. The methodology to estimate annual operating costs is listed in Table 8-12. In this study, fixed O&M costs contain maintenance cost, insurance and taxes costs, operating labor costs, and administration & support labor cost. Variable O&M costs include chemical and consumable costs and waste disposal costs. CO_2 transport and storage costs and CO_2 emission costs (for residual emissions) are not taken into consideration in this study.

Table 8-12 Annual operating costs

Parameters	**Units**	**Case A**	**Case B**
Fixed O&M Costs			
Maintenance	$/yr	1% CAPEX	
Insurance and taxes	$/yr	2% CAPEX	
Operating labor cost	$/yr	Operator No.×Salary×Time	
Salary	$/h	40	
Operator NO.	/	16	

Admin. & support labor cost	$/yr	30% of operating labor cost	
Fixed O&M costs	$/yr	**Sum of above**	
Variable O&M Costs			
MEA loss caused by oxidative degradation	kg MEA/tCO_2	~ 0.4	~ 0.1
MEA loss caused by SO_2	molMEA/mol SO_2	2	2
MEA loss caused by NO_2	molMEA/mol NO_2	2	2
MEA loss caused by HCl	molMEA/mol HCl	1	1
MEA loss (exhaust gas)	ppmv	2	2
Inhibitor additive consumption [14]	$/yr	20% of cost of MEA make-up	20% of cost of MEA make-up
Caustic consumption in MEA reclaimer [15]	kg / t CO_2	0.13	0.13
Activated carbon use in CO_2 capture system [15]	kg / t CO_2	0.075	0.075
Limestone consumption	$/yr	Calculation	
Industrial water	$/yr	Calculation	
Cooing water	$/yr	Calculation	
Chemicals and Consumables Costs	$/yr	**Sum of above**	
Waste disposal cost	$/yr	3.6×10^6	
Variable O&M Costs	$/yr	**Chemicals and Consumables Costs + waste disposal costs**	

COE calculation

An economic model has been developed to calculate the cost of electricity (COE) on a levelized basis. This economic model calculates a revenue stream equal to the discounted production costs plus the discounted capital costs. The sum is adjusted by the model in a series of iterations to produce a zero net present value (*NPV*) of the operating and capital expenditure costs over the project life.

The model thus calculates the selling price of electricity that returns a zero net present value over the project life. This is equivalent to the levelized production cost of power determined at the battery limit of the plant. It does not include any distribution cost [6]. NPV can be determined using the following equation:

$$NPV = \sum_{t=1}^{n} (CI - CO)_t \, (1 + i_C)^{-t} = 0 \qquad (8\text{-}1)$$

where CI represents the cash inflows in one year; CO represents the cash outflows in one year; $(CI - CO)_t$ is the net cash flow for the "t" year; i_C represents the nominal discount rate.

In this study, CO includes fixed capital expenditure and operating costs which consists of the fuel costs, fixed O&M costs and variable O&M costs. CI includes the electricity sales revenue and by-product sales revenue.

Breakdown of COE

In this study COE can be calculated by the formula "*NPV*=0". For the levelized cost of electricity (LCOE), if we use another calculating method to estimate it in which the amortised capital costs, fixed O&M costs, variable O&M costs and coal costs are separately considered, we can obtain a breakdown of COE. In this study COE of Case A or Case B consists of four main parts: COE derived from capital cost, COE derived from fixed O&M costs, COE resulted from variable O&M costs and COE derived from coal costs. COE due to these factors can be calculated by the following equations:

$$\begin{aligned}\mathrm{COE} &= \frac{(CCF)*CAPEX + FC + VC + CC}{(LF)*E_N*8760} \\ &= \frac{(CCF)*(CAPEX_{\mathrm{Membrane}} + CAPEX_{\mathrm{Others}})}{(LF)*E_N*8760} + \frac{FC_{\mathrm{Membrane}} + FC_{\mathrm{Others}}}{(LF)*E_N*8760} + \frac{VC + CC}{(LF)*E_N*8760} \\ &= \mathrm{COE}_{\mathrm{Membrane}} + \mathrm{COE}_{\mathrm{Others}} + \frac{FC_{\mathrm{Membrane}} + FC_{\mathrm{Others}}}{(LF)*E_N*8760} + \frac{VC_{\mathrm{F}} + CC_{\mathrm{F}}}{E_N*8760}\end{aligned} \quad (8\text{-}2)$$

where COE is the calculated cost of electricity by using the method "*NPV*=0", \$/MWh; E_N is the net power output of Case A or Case B, MWe; $(CCF)*CAPEX$ is the amortised capital cost per year, \$/year; CCF is the capital charge factor; *VC* is the variable O&M cost per year, \$/year ; FC is the Fixed fixed O&M cost per year, \$/year; CC is the coal cost per year, \$/year.

CO_2 avoided cost

CO_2 avoided cost can be defined as the following equation:

$$\text{CO}_2 \text{ avoided cost} = \frac{\left\{(\text{COE})_{\text{capture}} - (\text{COE})_{\text{ref}}\right\} \$/\text{MWh}}{\left\{(\text{Emissions})_{\text{ref}}^{\text{CO}_2} - (\text{Emissions})_{\text{capture}}^{\text{CO}_2}\right\} \text{tCO}_2/\text{MWh}} \quad (8\text{-}3)$$

Energy penalties

The net electrical efficiency (ϕ) can use the following formula to calculate:

$$\phi = \frac{E_{\text{N}}}{H_{\text{T}}} = \frac{E_{Gross} - (\text{Loss}_{\text{Auxiliary}} + Loss_{\text{capture}} + Loss_{\text{compression}} + Loss_{\text{steam}})}{H_{\text{T}}} \quad (8\text{-}4)$$

where E_{N} is the net power output of Case A or Case B, MWe; H_{T} is the total heating value energy of all input fuels (LHV), MWth.

The net power output can be estimated by the following equation:

$$E_N = \frac{E_{Gross} - (\text{Loss}_{\text{Auxiliary}} + Loss_{\text{capture}} + Loss_{\text{compression}} + Loss_{\text{steam}})}{H_{\text{T}}} \quad (8\text{-}5)$$

Where E_{Gross} is the gross power output, MWe; $\text{Loss}_{\text{Auxiliary}}$ is auxiliary power consumption by coal-fired power plant only, MWe; $Loss_{\text{capture}}$ is the electrical power consumptions in the CO_2 capture system (pumps and blowers consumptions), MWe; $Loss_{\text{compression}}$ is the electrical power consumption due to CO_2 compression,

MWe; $Loss_{steam}$ is the power output reduction or loss caused by the extraction of IP/LP steam.

IECM software

The IECM (Integrated Environmental Control Model) is chosen as a reference to be compared with the results calculated by self-developed techno-economic model. IECM is a computer-modeling program that performs a systematic cost and performance analyses of emission control equipment at coal-fired power plants. It is free download and available at https://www.cmu.edu/epp /iecm/history.html.

Before self-developed techno-economic model, the techno-economic evaluation of DOE-Case 10 (Subcritical PC plant with Fluor Econamine CO_2 capture process) is performed and compared with the results using the IECM (Integrated Environmental Control Model) software and the results in the DOE reports. Our calculations agree well with the results in the DOE reports and IECM-calculated values. In our calculation, 68 MWe electric power will be used to run the CCS unit, which is also very close to DOE's 71 MWe and IECM software's 67 MWe. The total auxiliary load calculated is 122 MW3, which is also close to DOE's 123 MWe and IECM software's 124 MWe. This proved that our self-developed techno-economic model is reliable.

8.3 Subcritical PC power plant with CO_2 capture

8.3.1 Process flow diagram

The simplified process flow diagram of the subcritical PC plant with CO_2 capture is shown in Fig. .

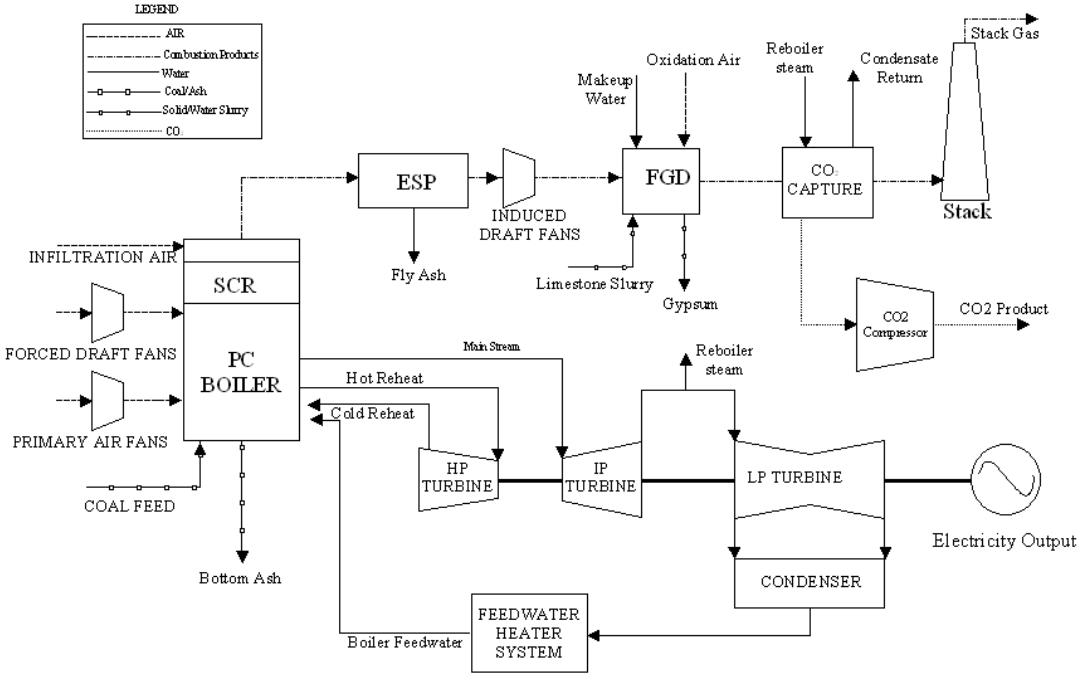

Fig. 8-3 Block flow diagram of subcritical PC with CO_2 capture

8.3.2 Steam cycle flow diagram

The proposed subcritical steam cycle flow diagram for Case B is presented in this subsection. Steam cycle flow is affected by the stripping temperature, thus two different scenarios are provided respectively, as shown in Fig. 8-4 (a) and Fig. 8-4(b)

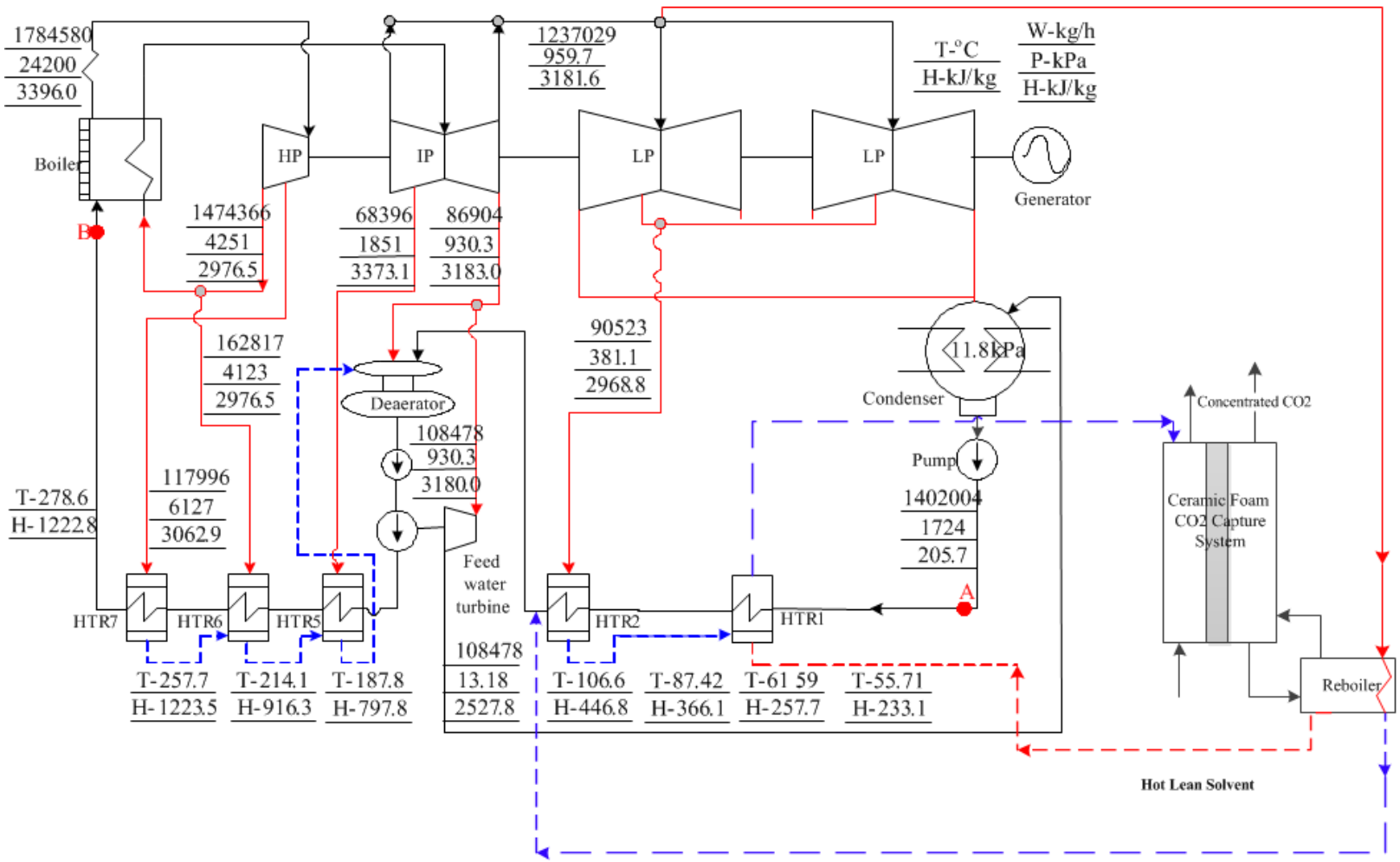

Fig. 8-4(a) Steam cycle flow diagram of Case B (stripping temperature >100C)

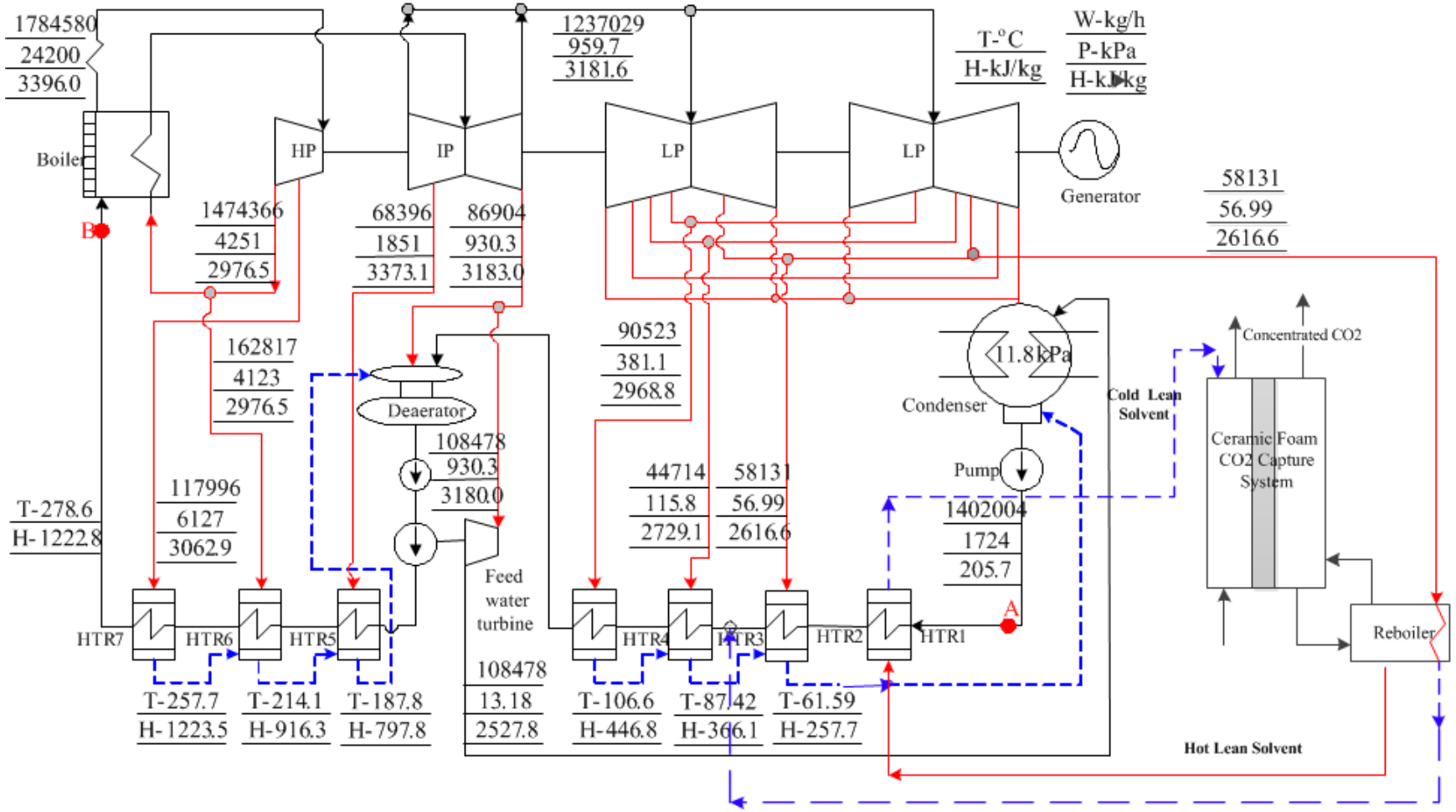

Fig. 8-4(b) Steam cycle flow diagram of Case B (stripping temperature <100C)

8.3.3 Chemicals and consumables summaries

The chemicals and consumables summaries for Case A and Case B are calculated and shown in Table 8-13. It should be noted that the amount of solid waste is given in these tables, but the solid waste disposal costs are not included in the COE calculations.

Table 8-13 Chemicals and consumables summaries of Case A and Case B

Item	Units	Case A	Case B
		Fluor Ecoamine	**Ceramic Foam**
		(Value)	**(Value)**
Gross power output	MWe	672	672
Net power output	MWe	467.9	480.6
CO_2 emission	t/h	464	464
CO_2 recovered	t/h	418	418
Coal feed rate	t/d	7380	7380
Chemicals and Consumables			
Makeup water	t/h	2660	2660
Limestone	t/h	8.64	8.64
ammonia	t/h	0.7	0.7
MEA solvent	kg/tCO_2	0.297	0.197

Amine inhibitors	$/t$CO_2$	0.13	0.09
Activated carbon	kg/tCO_2	0.075	0.075
NaOH	kg/tCO_2	0.7	0.7
Catalyst for DeNO_X	M$/yr	0.875	9.875
Waste Disposal			
Bottom ash	t/h	2.9	2.9
Fly ash	t/h	26.134	26.134
Cinder	t/h	5.124	5.124
Mill rejects	t/h	0.5	0.5
Gypsum	t/h	7.065	7.065
Chloride	t/h	0.61	0.61
Amine unit waste	t/tCO_2	0.003	0.003
Waste water	t/h	370	370

8.3.4 Capital Cost Estimation

For economic evaluation, the most important is how to estimate the capital cost, which is usually classified as fixed-capital investment and working capital. Fixed-capital investment is divided into manufacturing fixed capital investment, or direct cost, and nonmanufacturing fixed-capital investment, or indirect cost. Following items are recommended by DOE as the major components of capital cost:

- Direct Equipment Cost
- Material Cost
- Direct & Indirect Labor Cost
- Eng'g CM H.O.& Fee
- Process Contingency
- Project Contingency
- Owner's Cost

There are various methods for capital cost estimation, such as detailed item estimate method; unit cost estimate method, percentage of delivered equipment cost method, power factor applied to plant/capacity ratio method, etc. [8]. Choosing a specific method depends on detail information available and desired accuracy. In this study, the percentage of delivered equipment cost method was used based on the detail information available. In this method, the cost of major equipment is estimated from the literature, existing plants with similar configuration, or vendors. The cost of delivering the equipment is represented as a percentage of the purchased equipment cost. Other components of capital cost are calculated as a percentage of the delivered-equipment cost. The accuracy of this method is in the range of ±20 to 30 percent. The more equipment that is included in the major equipment list, the more accurate this method becomes.

Major Equipment list

Table 8-14 lists the major equipment for different units and subsystems. Some minor equipments have not been considered in this research because their costs and importance are less than that of major equipment.

Table 8-14 Major Equipment list (Case A for example)

NO.	**Item**	**Equipment**
1	Absorber system	Absorber column
		Amine emission control Tower
2	Stripper system	Stripper column
		Reboiler
		Condenser
		Condensate reflux kettle
3	Heat exchanger system	Lean/rich heat exchanger
		Lean solvent cooling system
		CO_2 cooling & drying system
4	Amine recovery system	Reclaimer
5	Compression system	Flue gas booster fan
		CO_2 compressor
6	Pump system	Rich solvent pump
		Lean solvent pump

		Lean solvent cooling pump
		Condensed water reflux pump
		Cooling water pump for stripper
		CO_2 cooling & drying pump
		Cooling water pump for CO_2 compressor
		Circulation pump for amine emission control
		Cooling water circulation pump
		Cooling water make-up pump
		Desalting-water pump for amine emission control
		Desalting-water pump in stripper
7	Tank	MEA solvent tank
		Pure MEA Tank
		Desalting water make-up tank
8	Liquid filtration system	Liquid filtrate
9	CO_2 compression heat recovery system	First
		Second
		Third
		Fourth

Equipment sizing and purchase cost

To calculate the equipment cost, a parameter that represents the size of the equipment is required. Size parameters are calculated from the data in material balance and data from the simulations. It is often necessary to estimate the cost of a piece of equipment when cost data are not available for the particular size or capacity involved. Prediction can be made by using the power relationship known as the *six-tenths factor rules*, as shown in Equation 8-6:

$$\textit{cost of equipment a} = \textit{(cost of equipment b)}\ X^{0.6} \qquad (8\text{-}6)$$

According to this rule, if the cost of ***a*** given unit ***b*** at one capacity is known, the cost of a similar unit ***a*** with X times the capacity of the first is $X^{0.6}$ times the cost of the initial unit.

The size parameter for the absorber, stripper and wash water column is weight. For calculating the weight of these columns, column length and diameter are required. Diameter of packed columns can be calculated from the pressure drop correlation. Length, or height of the column, can be estimated by the number of ideal stages times HETP.

The size parameter for heat exchangers, condensers, and coolers is heat transfer area. Area (m^2) of the heat exchangers is calculated from following equations:

$$A = \frac{Q}{h \cdot LMTD} \qquad (8\text{-}7)$$

$$LMTD = \frac{\Delta T_A - \Delta T_B}{\ln(\frac{\Delta T_A}{\Delta T_B})} = \frac{\Delta T_A - \Delta T_B}{\ln \Delta T_A - \ln \Delta T_B} \qquad (8\text{-}8)$$

where ΔT_A is the temperature difference between the two streams at end *A*; and ΔT_B is the temperature difference between the two streams at end *B*; LMTD is the logarithmic mean temperature difference; A is the heat transfer area for the heat exchanger; Q is the exchanged heat duty; h is the heat transfer coefficient.

Heat transfer coefficients (*h*) are listed in Table 8-15 for different heat exchanger systems.

Table 8-15 Overall heat transfer coefficients in tubular heat exchangers

Shell side	**Tube side**	**Overall Heat Transfer Coefficient (Btu/°F.ft2.h)**
water	Air, N2	20-40
water	water	180-200
MEA	MEA	120-130
water	amine	100-110
steam	water	400-1000
water	100 psia Gas	35-40
water	300 psia Gas	40-50
water	700 psia Gas	60-70
water	1000 psia Gas	80-100

The size parameter for pumps is volumetric flow rate (m^3/s)×discharge pressure (kPa).

8.4 Techno-Economic Analysis Results

8.4.1 Major Equipment Cost

The estimation and calculation of major equipment costs for Case A and Case B are listed in Table 8-16, respectively. It can be found ceramic foam CO_2 capture process has the advantage in terms of reducing direct equipment purchase cost. For Case A, the total major equipment cost is 191.26 M$; for Case B, the total major equipment cost will reduce to 143.75M$.

Table 8-16 Summary of major equipment cost for case A and case B

NO.	Item	Equipment	Price, K$ (Case A)	Price, K$ (Case B)
1	Absorber system	Absorber column	77203.69	/
		Amine emission control Tower	342.94	342.94
2	Stripper system	Stripper column	32942.37	/
		Reboiler	7811.72	6249.38
		Condenser	1169.57	1169.57
		Condensate reflux kettle	252.12	252.12
3		Ceramic foam reactors	/	56466.26
4	Heat exchanger system	Lean/rich heat exchanger	7902.12	6337.57
		Lean solvent cooling system	374.16	374.16
		CO_2 cooling & drying system	617.56	617.56
5	Amine recovery system	Reclaimer	1721.87	1721.87
6	Compression system	Flue gas booster fan	8623.62	8623.62

		CO_2 compressor	40481.25	48577.50
7	Pump system	Rich solvent pump	297.74	297.74
		Lean solvent pump	297.74	297.74
		Lean solvent cooling pump	42.06	42.06
		Condensed water reflux pump	67.74	67.74
		Cooling water pump for stripper	64.40	64.40
		CO_2 cooling & drying pump	15.28	15.28
		Cooling water pump for CO_2 compressor	11.99	11.99
		Circulation pump for amine emission control	80.11	80.11
		Cooling water circulation pump	48.25	48.25
		Cooling water make-up pump	12.39	12.39
		Desalting-water pump for amine emission control	3.72	3.72
		Desalting-water pump in stripper	2.32	2.32
		Subtotal	***992.52***	***992.52***
8	Tank	MEA solvent tank	339.73	339.73
		Pure MEA Tank	236.17	236.17
		Desalting water make-up tank	92.53	92.53
		Subtotal	***668.43***	***668.43***
9	Liquid filtration system	Liquid filtrate	105.39	105.39
10	CO_2 compression heat recovery system	First	670.09	2141.24
		Second	1188.96	1188.96
		Third	1182.12	1182.12
		Fourth	1274.62	1274.62
		Subtotal	***4315.78***	***5786.94***

Total Equipment Cost	**191263.12**	**143752.90**

8.4.2 CAPEX Estimation

Table 8-17 lists the CAPEX of Case A and Case B.

Table 8-17 Total Capital Cost components

Description	**Case A**	**Case B**
Direct equipment cost (DEC)	191263.12	143752.90
Construction cost (CC)	57378.94	43125.87
Bare erected cost (BEC)	248642.05	186878.77
Eng'g CM H.O.& Fee (ECF)	31080.26	23359.85
Process contingency	49728.41	74751.51
Project contingency	72106.20	54194.84
Owners cost	74592.62	56063.63
CAPEX	**476149.53**	**395248.59**

8.4.3 Fuel Cost and O&M Cost Estimation

The estimated fuel cost and operating& maintenance cost are listed in Table 8-18.

Table 8-18 Fuel cost and O&M cost for Case A and Case B

Parameters	Case A		Case B	
Unit	Annual Cost (M$/yr)	Annual Unit Cost ($/kW-net)	Annual Cost (M$/yr)	Annual Unit Cost ($/kW-net)
		Fuel Cost		
Fuel Cost	**87.42**	**158.94**	**87.42**	**155.55**
		Fixed O&M Costs		
Maintenance	17.21	31.30	16.40	29.19
Insurance and taxes	34.43	62.59	32.81	58.38
Operating labor cost	4.77	8.66	4.77	8.48
Admin. & support labor cost	1.43	2.60	1.43	2.54
Fixed O&M costs	**57.84**	**105.15**	**55.41**	**98.59**
		Variable O&M Costs		
Limestone consumption	6.06	11.02	6.06	10.78
Ammonia consumption	4.91	8.92	4.91	8.73
Water consumption	2.70	4.91	2.70	4.81
Waste disposal cost	3.60	6.55	3.60	6.41
MEA loss	2.04	3.71	1.35	2.41
NaOH consumption	1.09	1.98	1.09	1.94
Active carbon consumption	0.70	1.27	0.70	1.25
Other material cost	15.00	27.27	15.00	26.69
Variable O&M Costs	**36.10**	**65.63**	**35.41**	**63.01**

8.4.4 Cost of Electricity (COE)

The calculated COE of case A and case B are compared in Fig. 8-5. The DOE case 9 is the reference PC plant without CCS system, which has the COE of 59.3 mills/kWh (= 59.3 $/MWh). When the Fluor Econamine CO_2 capture process was installed in the reference PC plant, the COE increased to 104.21 mills/kWh. Rice University's ceramic foam CO_2 capture technology (Case B) increased the COE comparatively less (Case A), with a calculated COE of 98.6 mills/kWh.

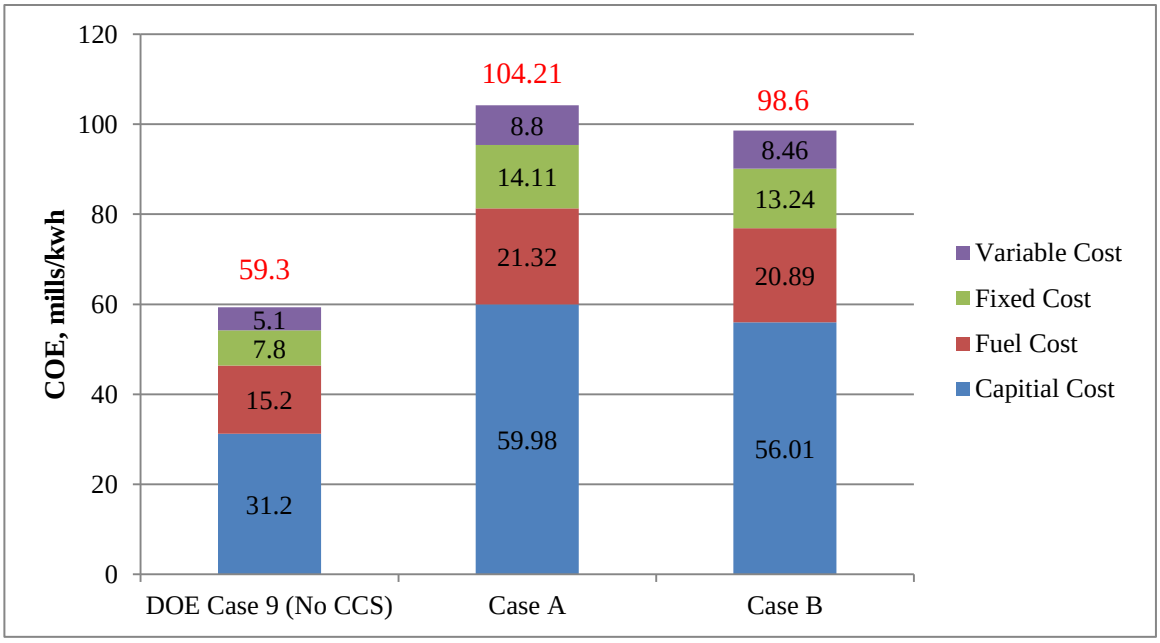

Fig. 8-5 Cost of electricity for Case A and Case B

8.4.5 Cash flow analysis for Case A and Case B

Table 8-19 and Table 8-20 present the cash flow of Case A and Case B during the construction period and operating period. It can be found that as COE

of Case A and Case B are 104.21 and 98.6 mills/kWh respectively, the NPV for Case A and Case B are both equal to zero.

Table 8-19 NPV for Case A

	YEAR	2007	2008	2009	2010	2011	2012	2013	2014	2015	2016	2017	2018	2019	2020	2021	2022	2023	2024	2025	2026	2027	2028	2029	2030	2031	2032	2033	2034	2035	2036	2037	2038	2039	2040	2041
		-4	-3	-2	-1	0	1	2	3	4	5	6	7	8	9	10	11	12	13	14	15	16	17	18	19	20	21	22	23	24	25	26	27	28	29	30
	Net output, MW	550.68																																		
	Load factor, Φ						85.00%	85.00%	85.00%	85.00%	85.00%	85.00%	85.00%	85.00%	85.00%	85.00%	85.00%	85.00%	85.00%	85.00%	85.00%	85.00%	85.00%	85.00%	85.00%	85.00%	85.00%	85.00%	85.00%	85.00%	85.00%	85.00%	85.00%	85.00%	85.00%	85.00%
	Operating hours, h						7446	7446	7446	7446	7446	7446	7446	7446	7446	7446	7446	7446	7446	7446	7446	7446	7446	7446	7446	7446	7446	7446	7446	7446	7446	7446	7446	7446	7446	7446
	Expenditure factor	10.00%	30.00%	25.00%	20.00%	15.00%																															
	Electricity produced, MWh/yr						4100363.3	4100363.28	4100363.3	4100363	4100363	4100363.3	4100363	4100363.3	4100363.3	4100363.3	4100363.3	4100363	4100363	4100363	4100363.3	4100363.3	4100363	4100363	4100363	4100363	4100363	4100363	4100363	4100363	4100363	4100363	4100363	4100363.28	4100363.28	4100363.28	4100363.28
	COE, $/MWh	104.207																																		
CI-1	Electricity revenues, M$/yr						427.28656	427.286556	427.28656	427.2866	427.2866	427.28656	427.2866	427.28656	427.28656	427.28656	427.28656	427.2866	427.2866	427.28656	427.28656	427.2866	427.2866	427.2866	427.287	427.2866	427.287	427.2866	427.2866	427.2866	427.2866	427.2866	427.2865563	427.2865563	427.2865563	427.2865563
CO-1	**CAPEX**																																			
	CAPEX, M$	1721.34																																		
	Fixed CAPEX, M$	172.134	516.402	430.335	344.268	258.201																														
CO-2	**Annual operating costs**																																			
1)	Coal consumption, tons/yr	2693700																																		
	Coal price, $/ton	38.18																																		
	Coal costs, M$/yr						87.418646	87.4186461	87.418646	87.41865	87.41865	87.418646	87.41865	87.418646	87.418646	87.418646	87.418646	87.41865	87.41865	87.418646	87.418646	87.41865	87.41865	87.41865	87.4186	87.41865	87.4186	87.41865	87.41865	87.41865	87.41865	87.41865	87.4186461	87.4186461	87.4186461	87.4186461
2)	**Fixed O&M costs, M$/yr**																																			
	Annual salary of one operator, $/h	40																																		
	Operator number	16																																		
	Labor cost, M$/yr						4.76544	4.76544	4.76544	4.76544	4.76544	4.76544	4.76544	4.76544	4.76544	4.76544	4.76544	4.76544	4.76544	4.76544	4.76544	4.76544	4.76544	4.76544	4.76544	4.76544	4.76544	4.76544	4.76544	4.76544	4.76544	4.76544	4.76544	4.76544	4.76544	4.76544	4.76544
	Administrative & Support Labor, M$/yr						1.429632	1.429632	1.429632	1.429632	1.429632	1.429632	1.429632	1.429632	1.429632	1.429632	1.429632	1.429632	1.429632	1.429632	1.429632	1.429632	1.429632	1.429632	1.42963	1.429632	1.42963	1.429632	1.429632	1.429632	1.429632	1.429632	1.429632	1.429632	1.429632	1.429632	1.429632
	Matainance fee, M$/yr						17.2134	17.2134	17.2134	17.2134	17.2134	17.2134	17.2134	17.2134	17.2134	17.2134	17.2134	17.2134	17.2134	17.2134	17.2134	17.2134	17.2134	17.2134	17.2134	17.2134	17.2134	17.2134	17.2134	17.2134	17.2134	17.2134	17.2134	17.2134	17.2134	17.2134	17.2134
	Insurance&Tax fee, M$/yr						34.4268	34.4268	34.4268	34.4268	34.4268	34.4268	34.4268	34.4268	34.4268	34.4268	34.4268	34.4268	34.4268	34.4268	34.4268	34.4268	34.4268	34.4268	34.4268	34.4268	34.4268	34.4268	34.4268	34.4268	34.4268	34.4268	34.4268	34.4268	34.4268	34.4268	34.4268
	Fixed O&M costs, M$/yr						57.835272	57.835272	57.835272	57.83527	57.83527	57.835272	57.83527	57.835272	57.835272	57.835272	57.835272	57.83527	57.83527	57.83527	57.835272	57.835272	57.83527	57.83527	57.83527	57.8353	57.83527	57.8353	57.83527	57.83527	57.83527	57.83527	57.83527	57.835272	57.835272	57.835272	57.835272
3)	Variable O&M costs, M$/yr						36.09	36.09	36.09	36.09	36.09	36.09	36.09	36.09	36.09	36.09	36.09	36.09	36.09	36.09	36.09	36.09	36.09	36.09	36.09	36.09	36.09	36.09	36.09	36.09	36.09	36.09	36.09	36.09	36.09	36.09	36.09
	Annual operating costs, M$/yr						181.34392	181.343918	181.34392	181.3439	181.3439	181.34392	181.3439	181.34392	181.34392	181.34392	181.34392	181.3439	181.3439	181.34392	181.34392	181.3439	181.3439	181.3439	181.344	181.3439	181.344	181.3439	181.3439	181.3439	181.3439	181.3439	181.3439181	181.3439181	181.3439181	181.3439181
CI-2	Working capital, M$/yr						0	0	0	0	0	0	0	0	0	0	0	0	0	0	0	0	0	0	0	0	0	0	0	0	0	0	0	0	0	0	0
	Total yearly cash flow, MRMB/yr	-172.134	-516.402	-430.335	-344.268	-258.201	245.94264	245.942638	245.94264	245.9426	245.9426	245.94264	245.9426	245.94264	245.94264	245.94264	245.94264	245.9426	245.9426	245.94264	245.94264	245.9426	245.9426	245.9426	245.943	245.9426	245.943	245.9426	245.9426	245.9426	245.9426	245.9426	245.9426382	245.9426382	245.9426382	245.9426382
NPV	Nominal discount rate					11%																															
	Discount rate to get 2011 values	1.51807041	1.367631	1.2321	1.11	1	0.9009009	0.81162243	0.7311914	0.658731	0.593451	0.5346408	0.481658	0.4339265	0.3909248	0.3521845	0.3172833	0.285841	0.257514	0.2319948	0.2090043	0.188292	0.169633	0.152822	0.13768	0.124034	0.11174	0.100669	0.090693	0.081705	0.073608	0.066314	0.059741975	0.053821599	0.048487927	0.043682817
	Yearly NPV	-261.311532	-706.2474	-530.21575	-382.13748	-258.201	221.56994	199.612562	179.83114	162.01	145.955	131.49098	118.4603	106.72103	96.14507	86.61718	78.033495	70.30045	63.33374	57.057419	51.40308	46.30908	41.71989	37.58549	33.8608	30.50523	27.4822	24.75873	22.30516	20.09474	18.10337	16.30934	14.69309884	13.23702598	11.92524863	10.74346724
	Total NPV	0																																		

Table 8-20 NPV for Case B

	YEAR	2007	2008	2009	2010	2011	2012	2013	2014	2015	2016	2017	2018	2019	2020	2021	2022	2023	2024	2025	2026	2027	2028	2029	2030	2031	2032	2033	2034	2035	2036	2037	2038	2039	2040	2041
		-4	-3	-2	-1	0	1	2	3	4	5	6	7	8	9	10	11	12	13	14	15	16	17	18	19	20	21	22	23	24	25	26	27	28	29	30
	Net output, MW	562																																		
	Load factor, Φ						85.00%	85.00%	85.00%	85.00%	85.00%	85.00%	85.00%	85.00%	85.00%	85.00%	85.00%	85.00%	85.00%	85.00%	85.00%	85.00%	85.00%	85.00%	85.00%	85.00%	85.00%	85.00%	85.00%	85.00%	85.00%	85.00%	85.00%	85.00%	85.00%	85.00%
	Operating hours, h						7446	7446	7446	7446	7446	7446	7446	7446	7446	7446	7446	7446	7446	7446	7446	7446	7446	7446	7446	7446	7446	7446	7446	7446	7446	7446	7446	7446	7446	7446
	Expenditure factor	10.00%	30.00%	25.00%	20.00%	15.00%																															
	Electricity produced, MWh/yr						4184652	4184652	4184652	4184652	4184652	4184652	4184652	4184652	4184652	4184652	4184652	4184652	4184652	4184652	4184652	4184652	4184652	4184652	4184652	4184652	4184652	4184652	4184652	4184652	4184652	4184652	4184652	4184652	4184652	4184652
	COE, $/MWh	98.6																																		
CI-1	Electricity revenues, M$/yr						412.60669	412.606687	412.60669	412.6067	412.6067	412.60669	412.6067	412.60669	412.60669	412.60669	412.6067	412.6067	412.6067	412.6067	412.60669	412.60669	412.6067	412.6067	412.6067	412.607	412.6067	412.607	412.6067	412.6067	412.6067	412.6067	412.6067	412.6066872	412.6066872	412.6066872	412.6066872
CO-1	**CAPEX**																																			
	CAPEX, M$	1640.44																																		
	Fixed CAPEX, M$	164.044	492.132	410.11	328.088	246.066																														
CO-2	**Annual operating costs**																																			
1)	Coal consumption, tons/yr	2693700																																		
	Coal price, $/ton	38.18																																		
	Coal costs, M$/yr						87.418646	87.4186461	87.418646	87.41865	87.41865	87.418646	87.41865	87.418646	87.418646	87.418646	87.418646	87.41865	87.41865	87.418646	87.418646	87.41865	87.41865	87.41865	87.4186	87.41865	87.4186	87.41865	87.41865	87.41865	87.41865	87.41865	87.4186461	87.4186461	87.4186461	87.4186461
2)	**Fixed O&M costs, M$/yr**																																			
	Annual salary of one operator, $/h	40																																		
	Operator number	16																																		
	Labor cost, M$/yr						4.76544	4.76544	4.76544	4.76544	4.76544	4.76544	4.76544	4.76544	4.76544	4.76544	4.76544	4.76544	4.76544	4.76544	4.76544	4.76544	4.76544	4.76544	4.76544	4.76544	4.76544	4.76544	4.76544	4.76544	4.76544	4.76544	4.76544	4.76544	4.76544	4.76544	4.76544
	Administrative & Support Labor, M$/yr						1.429632	1.429632	1.429632	1.429632	1.429632	1.429632	1.429632	1.429632	1.429632	1.429632	1.429632	1.429632	1.429632	1.429632	1.429632	1.429632	1.429632	1.429632	1.42963	1.429632	1.42963	1.429632	1.429632	1.429632	1.429632	1.429632	1.429632	1.429632	1.429632	1.429632	1.429632
	Matainance fee, M$/yr						16.4044	16.4044	16.4044	16.4044	16.4044	16.4044	16.4044	16.4044	16.4044	16.4044	16.4044	16.4044	16.4044	16.4044	16.4044	16.4044	16.4044	16.4044	16.4044	16.4044	16.4044	16.4044	16.4044	16.4044	16.4044	16.4044	16.4044	16.4044	16.4044	16.4044	16.4044
	Insurance&Tax fee, M$/yr						32.8088	32.8088	32.8088	32.8088	32.8088	32.8088	32.8088	32.8088	32.8088	32.8088	32.8088	32.8088	32.8088	32.8088	32.8088	32.8088	32.8088	32.8088	32.8088	32.8088	32.8088	32.8088	32.8088	32.8088	32.8088	32.8088	32.8088	32.8088	32.8088	32.8088	32.8088
	Fixed O&M costs, M$/yr						55.408272	55.408272	55.408272	55.40827	55.40827	55.408272	55.40827	55.408272	55.408272	55.408272	55.408272	55.40827	55.40827	55.40827	55.408272	55.408272	55.40827	55.40827	55.40827	55.4083	55.40827	55.4083	55.40827	55.40827	55.40827	55.40827	55.40827	55.408272	55.408272	55.408272	55.408272
3)	Variable O&M costs, M$/yr						35.41	35.41	35.41	35.41	35.41	35.41	35.41	35.41	35.41	35.41	35.41	35.41	35.41	35.41	35.41	35.41	35.41	35.41	35.41	35.41	35.41	35.41	35.41	35.41	35.41	35.41	35.41	35.41	35.41	35.41	35.41
	Annual operating costs, M$/yr						178.23692	178.236918	178.23692	178.2369	178.2369	178.23692	178.2369	178.23692	178.23692	178.23692	178.23692	178.2369	178.2369	178.23692	178.23692	178.2369	178.2369	178.2369	178.237	178.2369	178.237	178.2369	178.2369	178.2369	178.2369	178.2369	178.2369181	178.2369181	178.2369181	178.2369181
CI-2	Working capital, M$/yr						0	0	0	0	0	0	0	0	0	0	0	0	0	0	0	0	0	0	0	0	0	0	0	0	0	0	0	0	0	0	0
	Total yearly cash flow, M$/yr	-164.044	-492.132	-410.11	-328.088	-246.066	234.36977	234.369769	234.36977	234.3698	234.3698	234.36977	234.3698	234.36977	234.36977	234.36977	234.36977	234.3698	234.3698	234.36977	234.36977	234.3698	234.3698	234.3698	234.37	234.3698	234.37	234.3698	234.3698	234.3698	234.3698	234.3698	234.3697691	234.3697691	234.3697691	234.3697691
NPV	Nominal discount rate					11%																														
	Discount rate to get 2011 values	1.51807041	1.367631	1.2321	1.11	1	0.9009009	0.81162243	0.7311914	0.658731	0.593451	0.5346408	0.481658	0.4339265	0.3909248	0.3521845	0.3172833	0.285841	0.257514	0.2319948	0.2090043	0.188292	0.169633	0.152822	0.13768	0.124034	0.11174	0.100669	0.090693	0.081705	0.073608	0.066314	0.059741975	0.053821599	0.048487927	0.043682817
	Yearly NPV	-249.0303423	-673.055	-505.29653	-364.17768	-246.066	211.14394	190.219762	171.36916	154.3866	139.0871	125.30365	112.8862	101.69925	91.620948	82.541395	74.361617	66.99245	60.35356	54.372574	48.9843	44.13	39.75676	35.8169	32.2675	29.0698	26.189	23.5937	21.25559	19.14918	17.25151	15.5419	14.00171279	12.61415567	11.3641042	10.23793171
	Total NPV	0																																		

8.5 Technical and Economic Feasibility Study- Cost sensitivity study

We conducted a cost sensitivity study of Rice University integrated catalytic ceramic foam CO_2 capture technology. We changed several key parameters and operating factors that will affect the capital cost or operating cost of CCS plant. These parameters include prices of catalytic and non-catalytic ceramic foam, catalyst performance, catalyst longevity, waste heat availability, fuel cost and capacity factor.

8.5.1 Ceramic foam price

Fig. 8-6 shows the CCS plant CAPEX sensitivity to ceramic foam price. The solid blue line is the CCS plant CAPEX as function of ceramic foam price, the red point on the solid line represents CAPEX under current marketing price of ceramic foam, which is 2780 $/m^3$. The dash line is the CAPEX of Fluor Ecoamine CCS plant in DOE Case 10, which is 476.14 Million $. Ceramic foam, as the main component of absorber unit and desorber unit, has a significant influence on CCS plant CAPEX. A linear increase of CCS plant CAPEX can be seen in this Figure as the ceramic foam price increases from 500 $/m^3$ to 8000 $/m^3$. It should be noted is that as ceramic foam price exceeds 4800 $/m^3$, the investment of ceramic foam CO_2 capture plant begin to be higher than that of conventional Fluor Ecoamine CO_2 capture system.

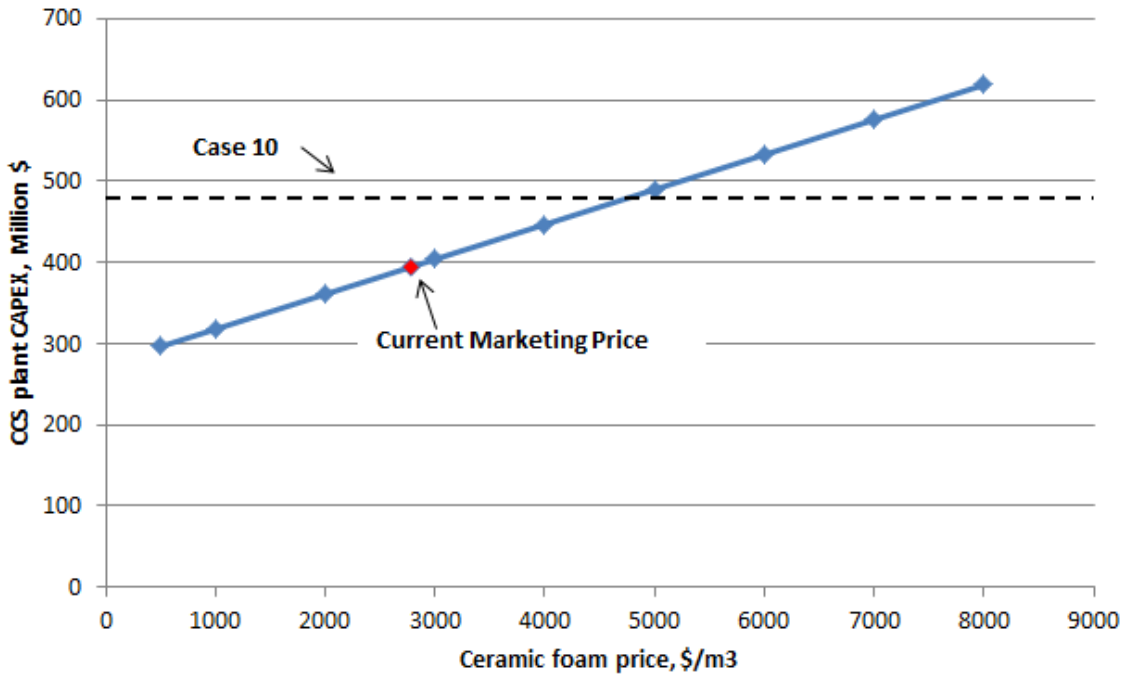

Fig.8-6 CCS plant CAPEX sensitivity to ceramic foam price (catalytic performance: 60%, catalyst longevity: 30 years, capacity factor: 85%, coal cost: $38.18 /ton, waste heat availability: 0%)

Fig. 8-7 exhibits the CAPEX sensitivity of power plant + CCS plant with unit of $/kW to the ceramic foam price. The solid blue line is the total CAPEX of power plant with CCS as function of ceramic foam price. The dash line is the CAPEX of power plant with CCS in DOE Case 10. Power plant with integrated absorber/desorber CO_2 capture unit shows better in economy than DOE Case 10 until ceramic form price higher than 7300 $/m^3.

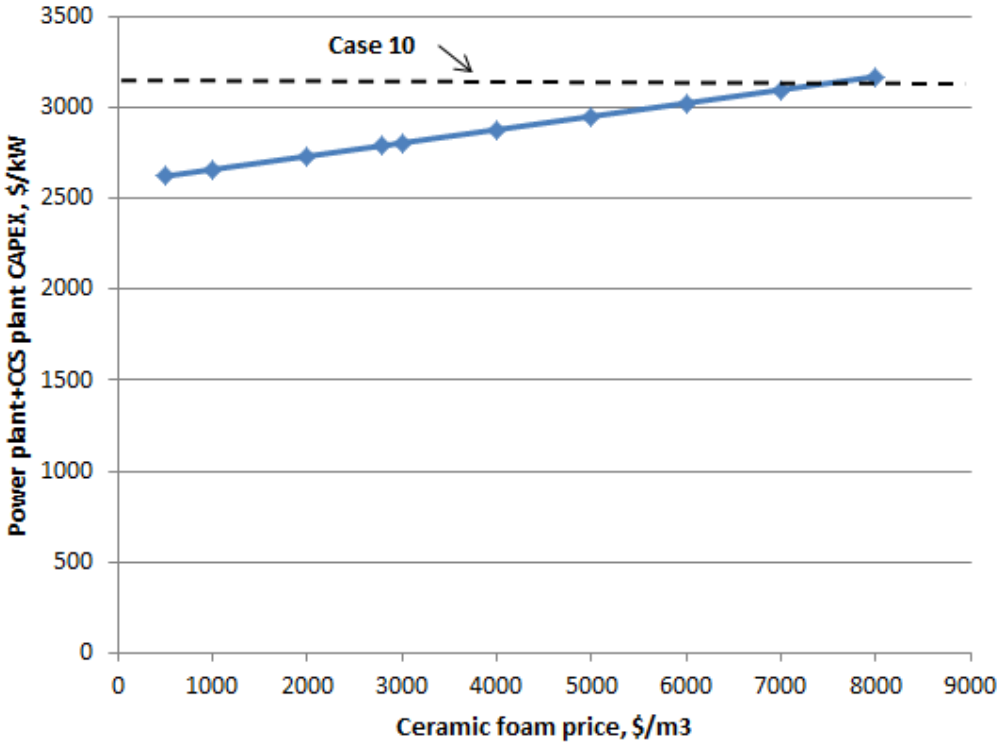

Fig. 8-7 Power plant +CCS plant CAPEX sensitivity to ceramic foam price (catalytic performance: 60%, catalyst longevity: 30 years, capacity factor: 85%, coal cost: $38.18 /ton, waste heat availability: 0%)

The sensitivity of COE to ceramic foam price is shown in Fig. 8-8. Ceramic foam price was changed from $500/m^3 to $9000/m^3. Increasing of ceramic foam price will increase COE apparently. From the breakdown of COE, it can be observed that this increase mainly results from the increase of capital cost and fixed operating & maintenance cost. Change of ceramic foam price doesn't affect the fuel cost, variable cost and TS&M cost in COE. As the ceramic foam price is $9000/m^3, the COE is about $110.67/MWh, which is slightly higher than COE of DOE case 10 ($110.11/MWh).

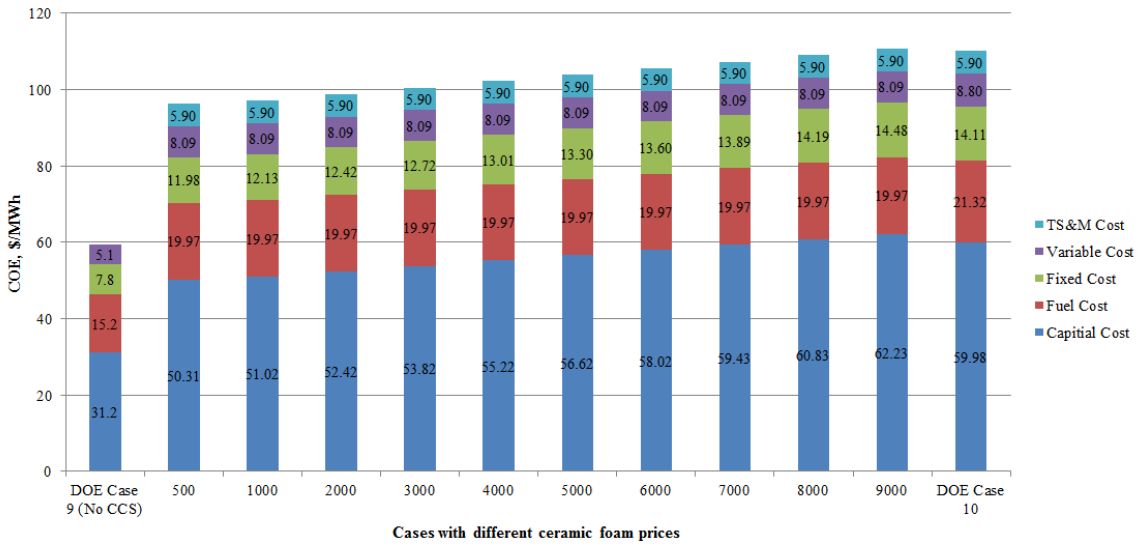

Fig. 8-8 COE sensitivity to ceramic foam price (catalytic performance: 60%, catalyst longevity: 30 years, capacity factor: 85%, coal cost: $38.18/ton, waste heat availability: 0%)

Fig.8-9 further describes the percent increase in COE with different ceramic foam prices compared to DOE case 9. The solid blue line is the percent increase in COE as function of ceramic foam price. The red dash line represents DOE target, less than 35% increase in COE compared to case 9. The black dash line is the percent increase of COE in Case 10. As ceramic foam price lower than 8800 $/m^3, integrated absorber/desorber CO_2 capture technology presents an advantage in terms of COE than Fluor Ecoamine technology. Therefore, it is very important to choose ceramic foam with reasonable price if integrated absorber/desorber CO_2 capture unit is installed in power plant.

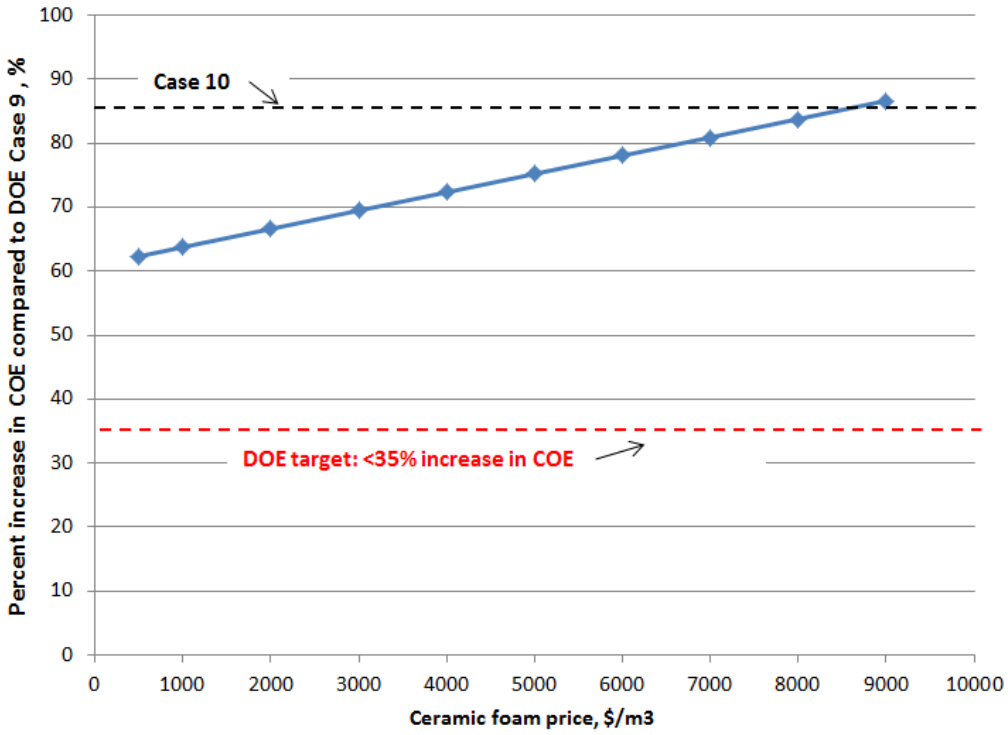

Fig. 8-9 Increase in COE with different ceramic foam prices (catalytic performance: 60%, catalyst longevity: 30 years, capacity factor: 85%, coal cost: $38.18/ton, waste heat availability: 0%)

The influence of ceramic foam price on CO_2 avoided cost is illustrated in Fig.8-10. CO_2 avoided cost is usually defined as the following equation:

$$CO_2 \text{ avoided cost} = \frac{\left\{(COE)_{capture} - (COE)_{ref}\right\} \$/MWh}{\left\{(Emissions)_{ref}^{CO_2} - (Emissions)_{capture}^{CO_2}\right\} tCO_2/MWh} \qquad (8\text{-}9)$$

The red dash line is CO_2 avoided cost of DOE Case 10, which is around $69/ton CO_2. Similar with COE, ceramic foam price has a linear influence on CO_2 avoided cost. The lowest CO_2 avoided cost is only $52/ton CO_2 as ceramic foam price is

$500/m^3$. It can be observed that the integrated absorber/desorber CO_2 capture technology has a higher CO_2 avoided cost than DOE case 10 as the ceramic foam price higher than $8000/m^3$.

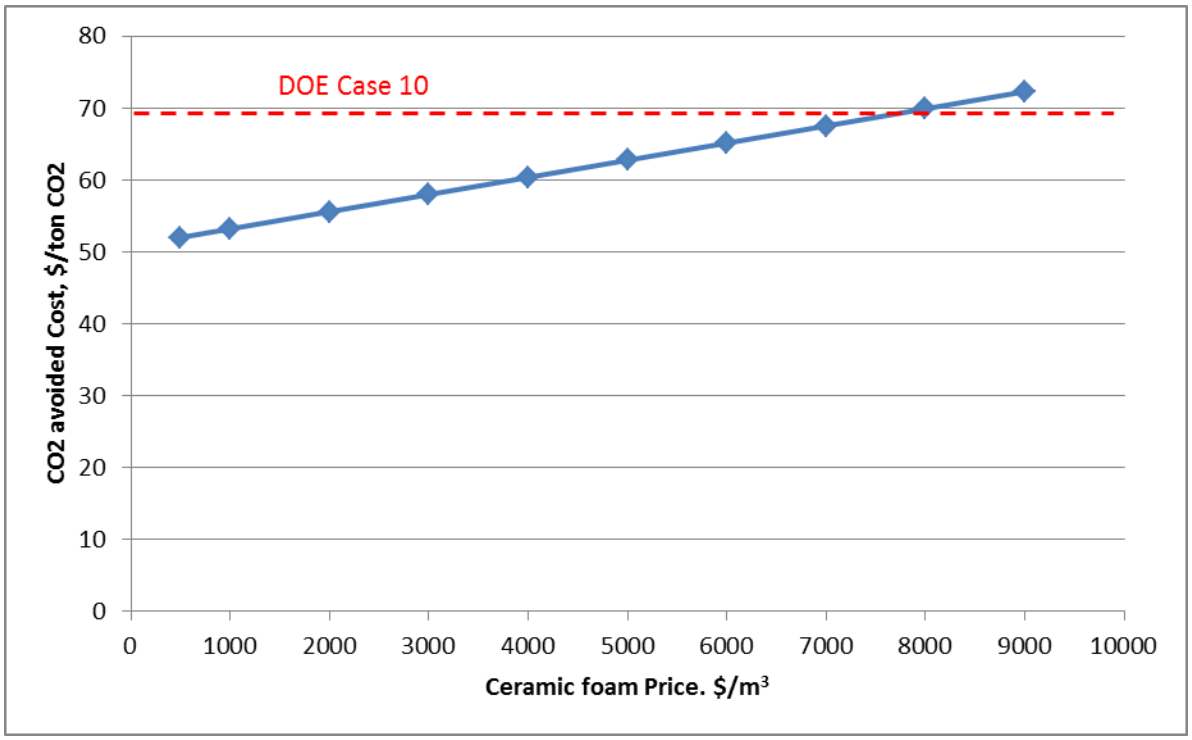

Fig. 8-10 The influence of ceramic foam price on CO_2 avoided cost (catalytic performance: 60%, catalyst longevity: 30 years, capacity factor: 85%, coal cost: $38.18/ton, waste heat availability: 0%)

8.5.2 Catalytic ceramic foam price

For integrated absorber/desorber CO_2 capture technology, regular ceramic foam is packed in absorber side, catalytic ceramic foam is packed in stripper side to enhance CO_2 desorption and lower CO_2 desorption temperature. Fig. 8-11 shows

the effect of catalytic ceramic foam price on COE. X axis is the ratio of catalytic ceramic foam price to ceramic foam price. We investigated the catalytic ceramic foam price from 110% to 1000% of ceramic foam. In the range of 110% to 200%, the increase of catalytic ceramic foam price doesn't present a significant influence on COE. As the catalytic ceramic foam price is 10 times of ceramic foam, COE is \$111.77/MWh which is higher than DOE case 10 (\$110.11/MWh).

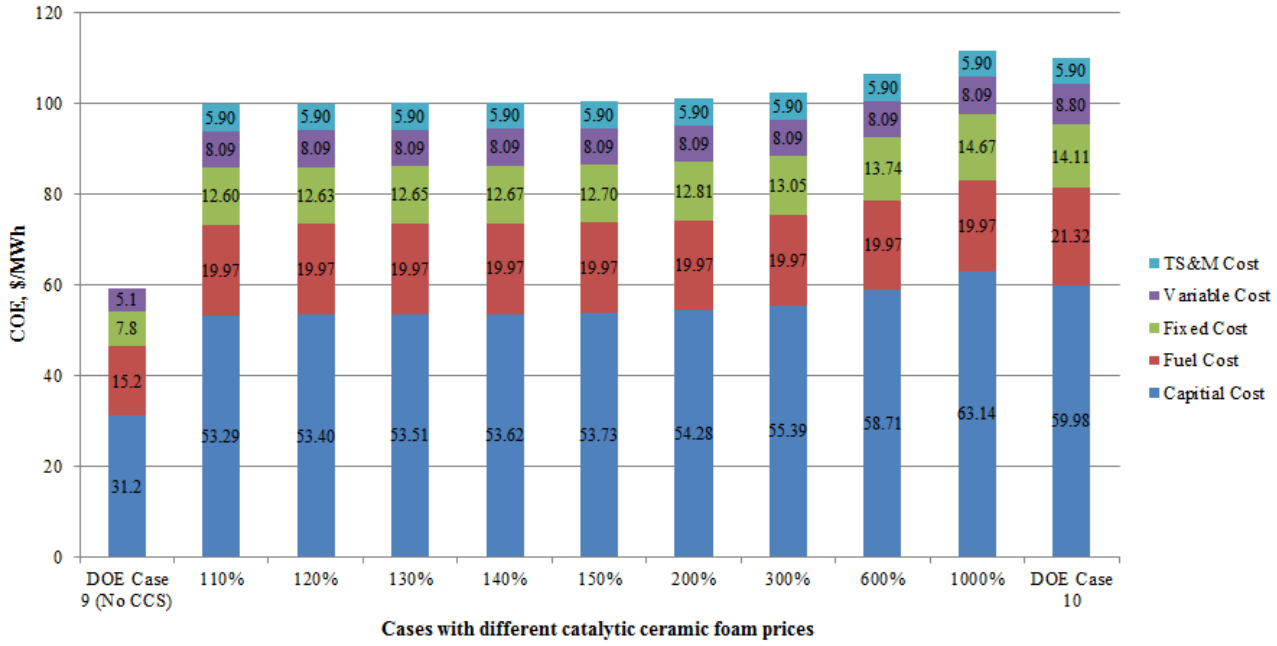

Fig. 8-11 The influence of catalytic ceramic foam price on COE (ceramic foam price: \$2780/m^3 catalytic performance: 60%, catalyst longevity: 30 years, capacity factor: 85%, coal cost: \$38.18/ton, waste heat availability: 0%)

We further investigated the percent increase in COE with different catalytic ceramic foam prices compared to DOE case 9 in Fig. 8-12. The solid blue line is the percent increase in COE as function of ceramic foam price. The red dash line

represents DOE target, less than 35% increase in COE compared to case 9. The black dash line is the percent increase of COE in Case 10. About 86% increase of COE can be found for DOE case 10. The increase of catalytic ceramic foam price results in a higher COE compared to Case 9. In practice, the price of catalytic ceramic foam depends on the cost of catalyst, ratio of catalyst to ceramic foam and fabrication complexity. As the catalytic ceramic foam price 9 times of ceramic foam, integrated absorber/desorber CO_2 capture technology presents higher COE than Fluor Ecoamine technology (DOE case 10).

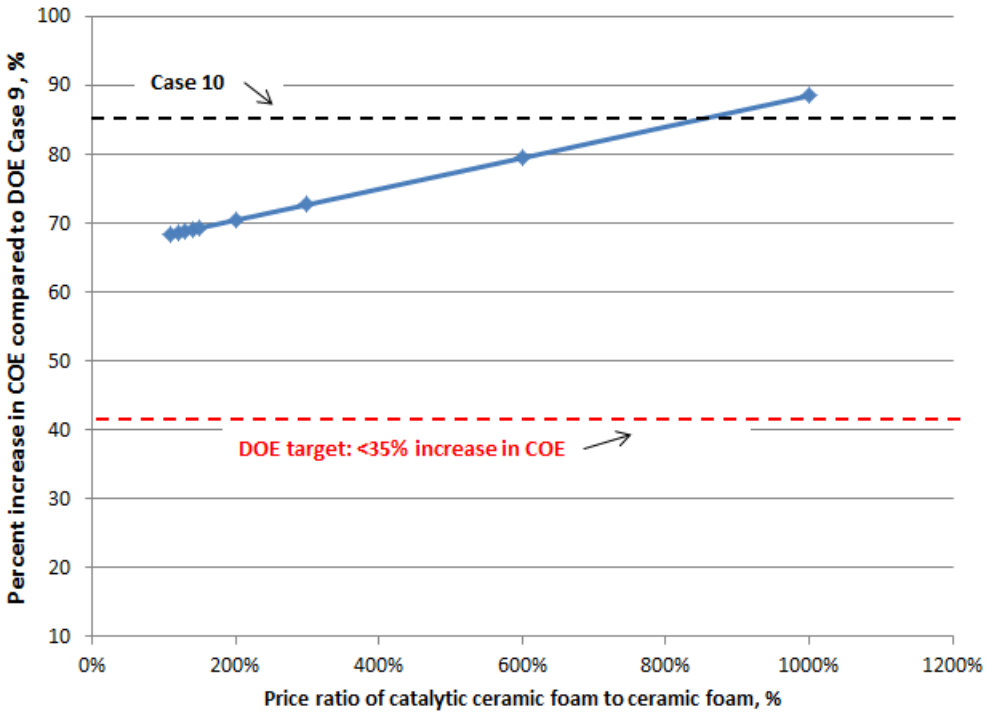

Fig. 8-12 Increase in COE with different catalytic ceramic foam price (ceramic foam price: \$2780/m^3, catalytic performance: 60%, catalyst longevity: 30 years, capacity factor: 85%, coal cost: \$38.18/ton, waste heat availability: 0%)

8.5.3 Catalyst performance sensitivity

In our previous CO_2 catalytic desorption experiments, we found different catalysts may presents varied performances in terms of increasing CO_2 desorption rate. Fig. 8-13 is an example of different catalysts tested for CO_2 desorption in CO_2-rich MEA solvent. Compared to MEA only case, 20% to 70% CO_2 desorption increment can be found for different catalysts in 60 min desorption. Better catalytic capability will lead to the increase of CO_2 desorption rate and decease of regeneration energy required, which both have a close relationship to COE.

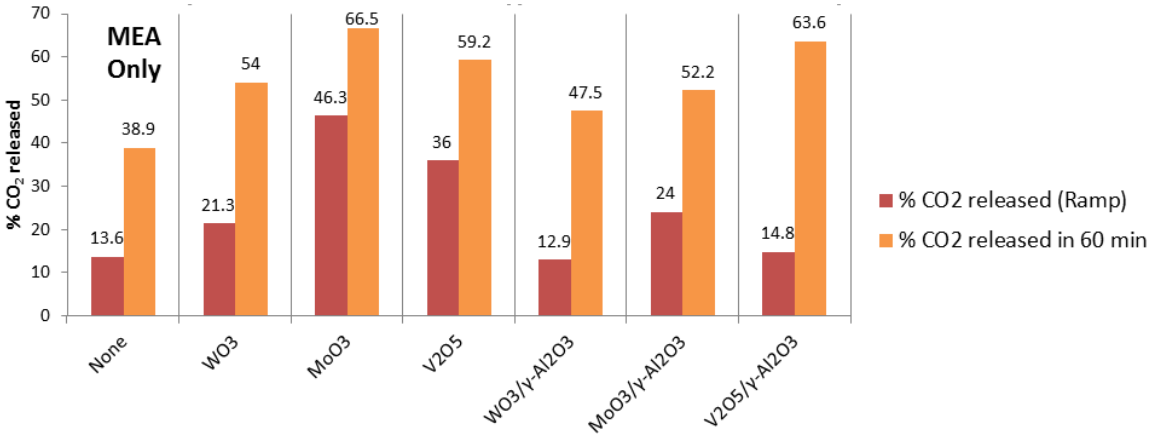

Fig. 8-13 Tested CO_2 desorbed in CO_2-rich MEA solvent with different metal oxide catalysts (all desorption at 85 ^oC, except V_2O_5 /γ-Al_2O_3 desorption at 91 ^oC)

The sensitivity of COE to catalyst performance is shown in Fig. 8-14. Catalyst performance is quantitatively described as the percent increase in CO_2 desorption rate compared to non-catalyst case, from 0% to 2000% in this study. Higher

catalyst performance indicates less energy consumption for CO_2 desorption. It was found that the COE is reduced as the catalytic performance increases.

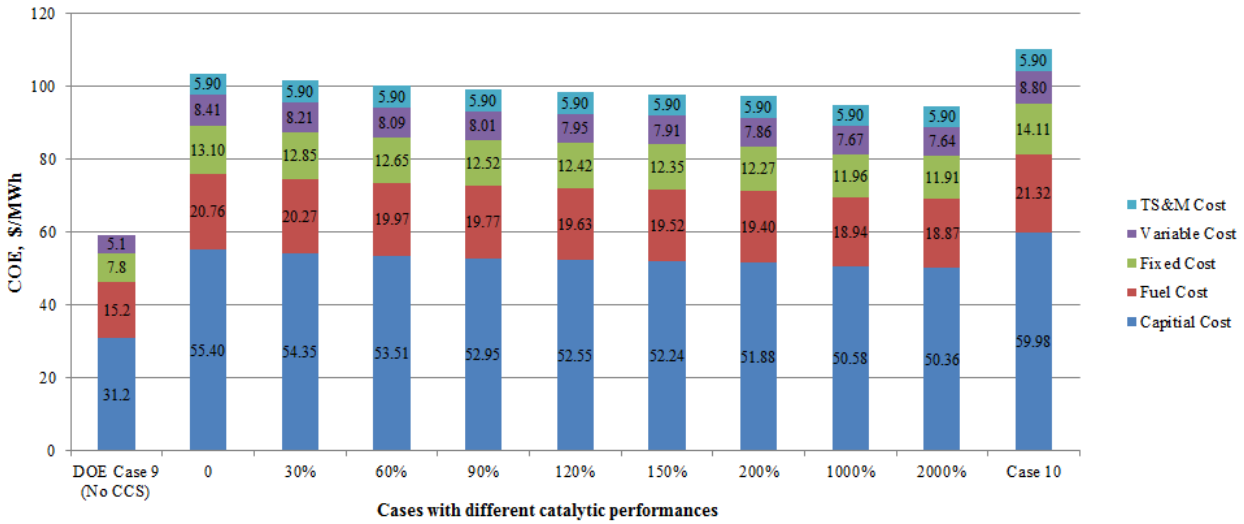

Fig.8-14 COE sensitivity to catalyst performance (ceramic foam price: \$2780/m^3, catalyst longevity: 30 years, capacity factor: 85%, coal cost: \$38.18/ton, waste heat availability: 0%)

Fig.8-15 describes the percent increase in COE compared to DOE case 9 with different catalyst performance. The solid blue line is the percent increase in COE as function of catalyst performance. The red dash line represents DOE target, less than 35% increase in COE compared to case 9. The black dash line is the percent increase of COE in Case 10. A limitation on COE reduction was found if catalyst performance increases infinitely. As the catalyst performance increase from 0% to 200%, a significant reduction on COE can be observed. However, as catalyst performance further increased, this reduction trend become negligible until percent increase in COE reach to 60%.

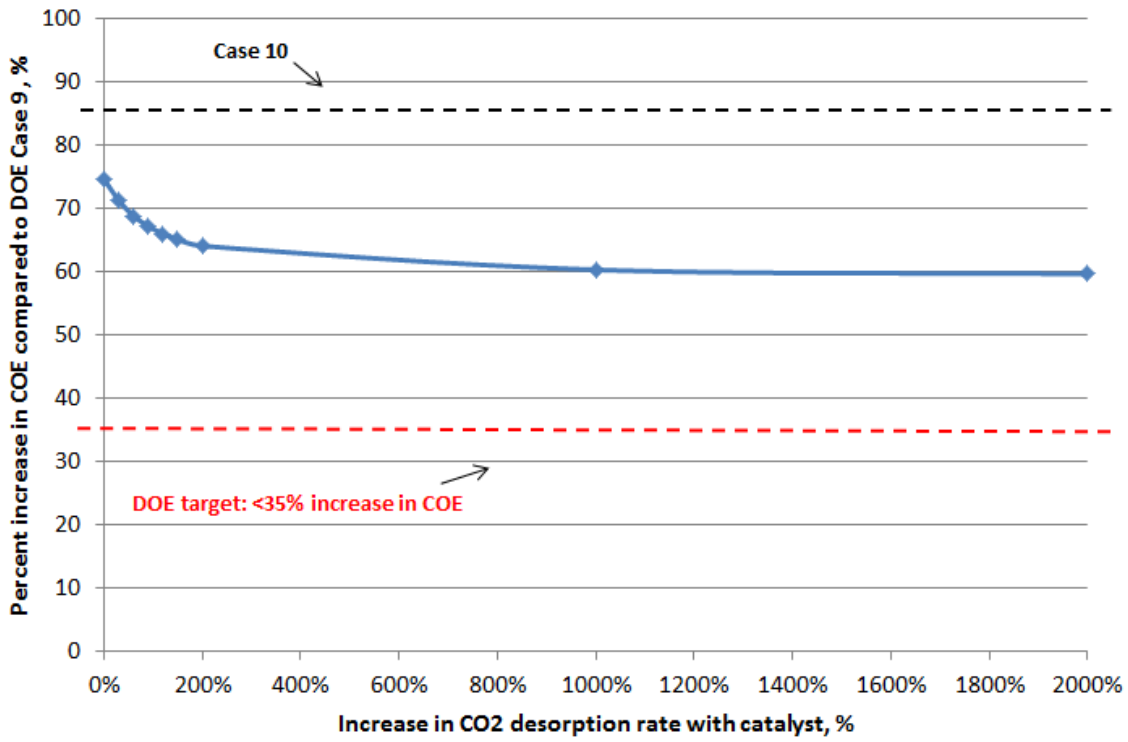

Fig.8-15 Increase in COE with different catalytic performances (ceramic foam price: \$2780/m^3, catalyst longevity: 30 years, capacity factor: 85%, coal cost: \$38.18/ton, waste heat availability: 0%)

8.5.4 Waste heat availability

For Rice University CO_2 capture technology, one of the advantages is to be capable of using some low-grade heat for CO_2 capture due to lower desorption temperature. This low-grade heat includes not only the low-temperature steam from LP, but also some waste heat available in the power plant. One example is to heat recovery from flue gas before FGD. In FGD reactor the temperature is usually 80 ^oC, but the temperature of flue gas before FGD can be as high as 180 ^oC. Therefore, this sensible heat can be utilized for our CO_2 capture system.

Fig.8-16 exhibits the sensitivity of COE to the availability of waste heat, from 0% to 80%. 0% means no waste heat is available to be used to provide heat for the reboiler, 80% means 80% of head duty in the reboiler can be provided by integrating waste heat. As we can see, more waste heat availability will significantly reduce the COE. The contribution of capital cost to COE is also reducing if more waste heat for CO_2 capture is available. This is due to more waste heat availability will not lead to extra equipment cost and an increase on capital cost of CCS plant, but more electricity will be generated in the power plant (less steam will be extracted from turbine). Therefore, the capital cost would go down if more waste heat can be used

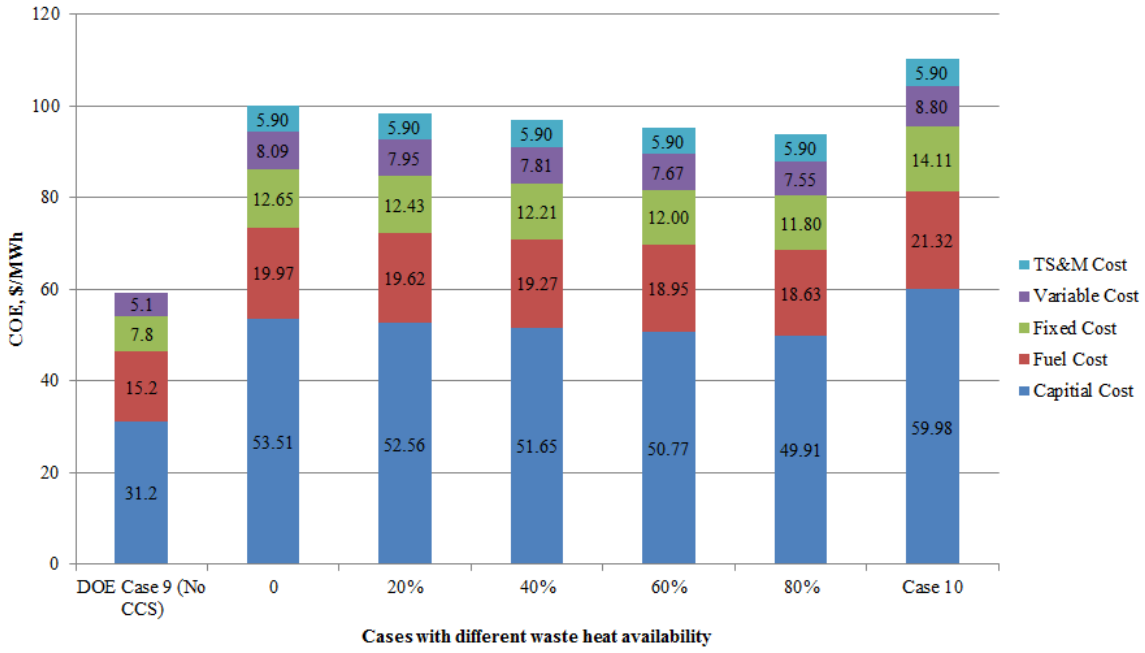

Fig.8-16 COE sensitivity to waste heat availability (ceramic foam price: \$2780/m^3, catalytic performance: 60%, catalyst longevity: 30 years, capacity factor: 85%, coal cost: \$38.18/ton)

Fig.8-17 shows the net plant efficiency of power plant with CCS under different waste heat availabilities. The solid blue line is the net plant efficiency as function of waste heat availability. The red dash line represents the net plant efficiency in Case 10. It can be found that net plant efficiency is a linear increasing function of waste heat availability.

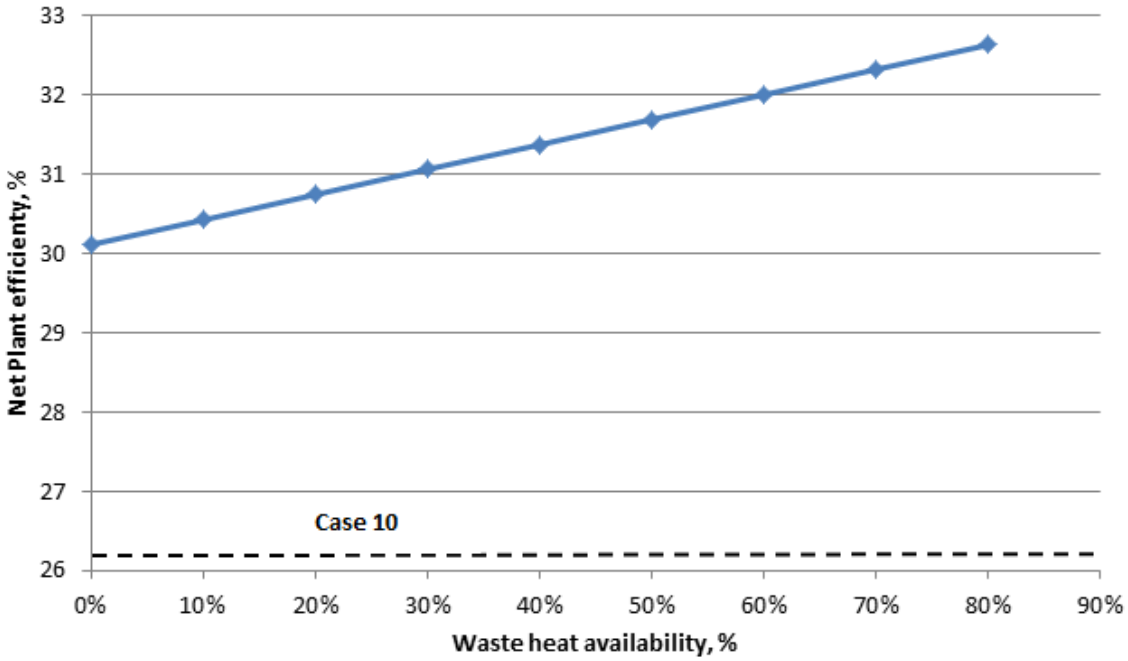

Fig.8-17 Net plant efficiencies in different cases (ceramic foam price: \$2780/m^3, catalytic performance: 60%, catalyst longevity: 30 years, capacity factor: 85%, coal cost: \$38.18/ton)

8.5.5 Longevity of catalytic ceramic foam

The longevity of catalytic ceramic foam is an important factor to cost of CO_2 capture. In practice the catalytic ceramic foam usually has a shorter lifetime than regular ceramic foam. Fig.8-18 shows the COE sensitivity to the lifetime of catalytic ceramic foam. The longevity of catalytic ceramic foam changed from 1

year to 30 years (lifetime of coal power plant). Four different prices of ceramic foam are also investigated, which are \$1000/m^3, \$3000/m^3, \$5000/m^3 and \$8000/m^3. The red dash line represents the COE of DOE case 10, which is \$110.17/MWh. COE decreases with the increase of lifetime of catalytic ceramic foam. If the ceramic foam price was \$8000/m^3, integrated absorber/desorber technology will not be attractive compare to Fluor Ecoamine technology in terms of COE as catalytic ceramic foam life time less than 7 years. And it is very interesting to notice that COE doesn't have obvious change if the catalytic ceramic foam can be used for more than 3 years. Therefore, it is better to choose the catalytic ceramic foam that can be used for more than 3 years for integrated absorber/desorber CO_2 capture technology.

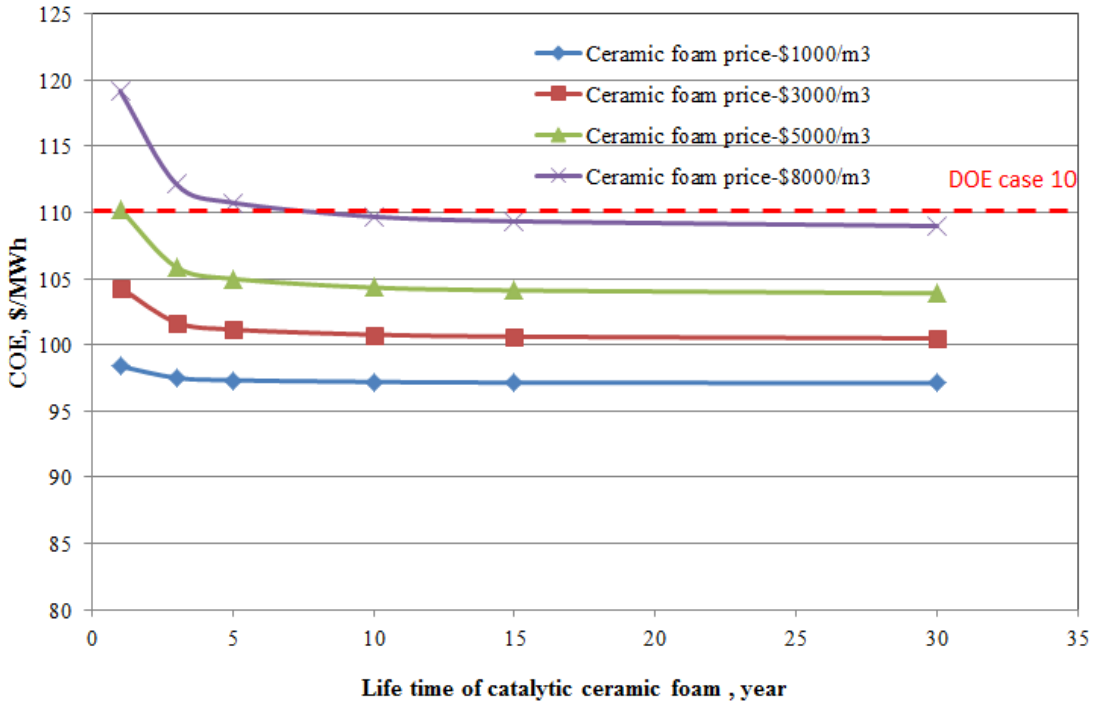

Fig.8-18 COE sensitivity to the lifetime of catalytic ceramic foam (ceramic foam price: $2780/m^3, catalytic performance: 60%, capacity factor: 85%, coal cost: $38.18/ton, waste heat availability: 0%)

Fig. 8-19 investigated the effect of catalytic ceramic foam lifetime on CO_2 avoided cost. Similar to COE, increase the durability of catalytic ceramic foam result in a lower CO_2 avoided cost. A transition point of catalytic ceramic foam lifetime is 3 years. After that, the variation of lifetime doesn't play any significant influence on CO_2 avoided cost.

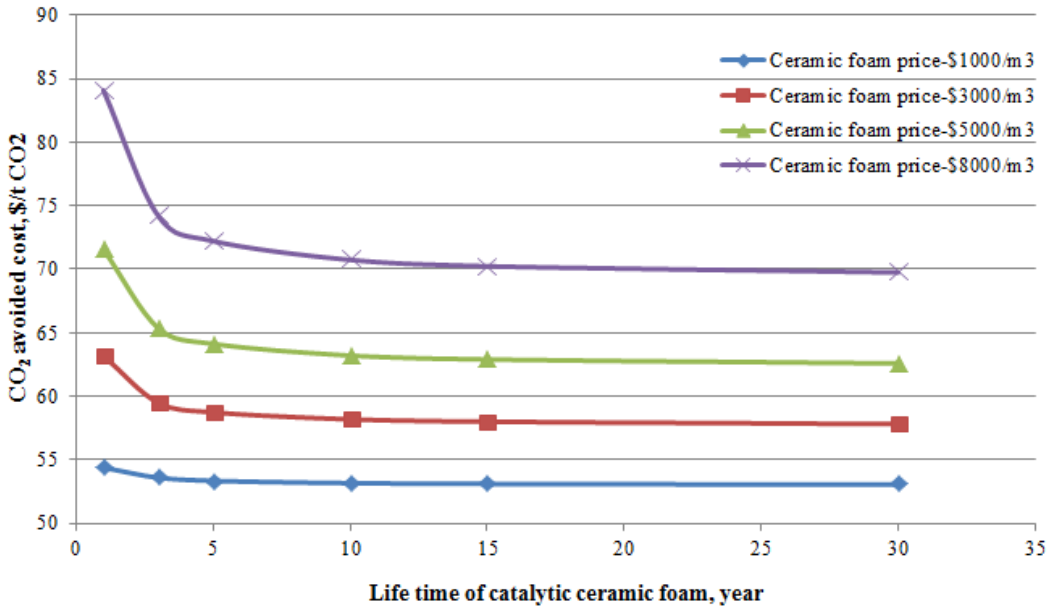

Fig.8-19 CO_2 avoided cost sensitivity to the lifetime of catalytic ceramic foam (ceramic foam price: $2780/m^3, catalytic performance: 60%, capacity factor: 85%, coal cost: $38.18/ton, waste heat availability: 0%)

8.5.6 Capacity factor

The capacity factor of a power plant is the ratio of its actual output over a period of time, to its potential output if it were possible for it to operate at full nameplate capacity continuously over the same period of time. The default capacity factor for CCS plant is assumed to be 85% during the operating years. Fig.8-20 investigates the change of COE with capacity factor from 30% to 95%. It is assumed that a capacity factor of greater than 85 percent can be achieved without the expenditure of additional capital. The COE increases more rapidly at low capacity factor and then increases slowly at high capacity factor. This is because the relatively high capital component is spread over fewer kilowatt-hours of generation. It can be proved by that capital cost is more dominant in COE at low capital cost.

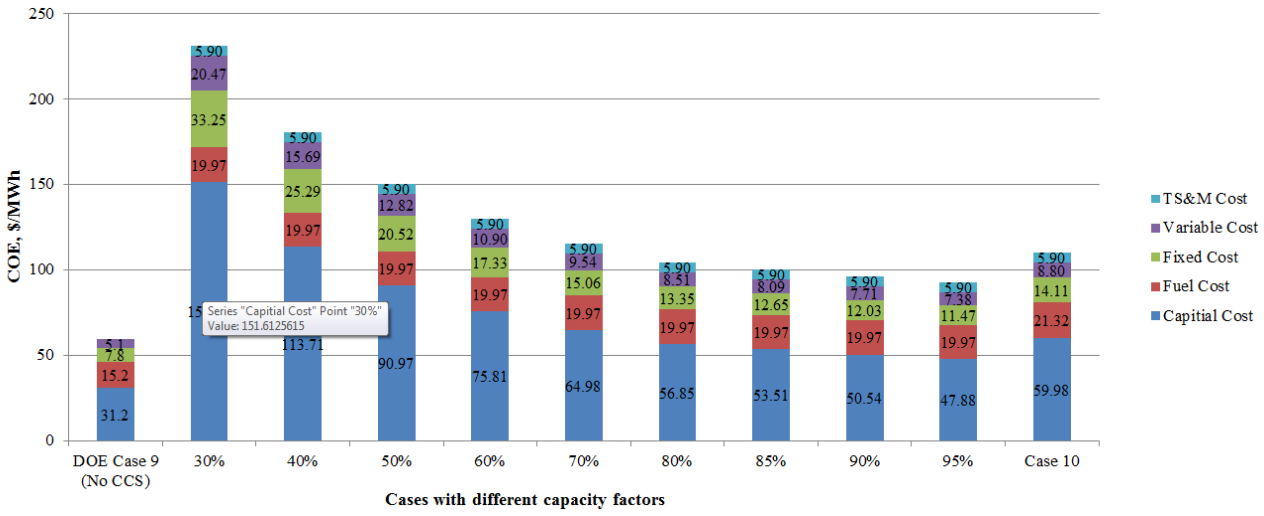

Fig. 8-20 The effect of capacity factor on COE (ceramic foam price: \$2780/m^3, catalytic performance: 60%, catalyst longevity: 30 years, coal cost: \$38.18/ton, waste heat availability: 0%)

The sensitivity of CO_2 avoided cost to capacity factor is shown in Fig.8-21. The dash line is the CO_2 avoided cost of case 10 at 85% capacity factor. CO_2 avoided cost decreases with the increase of capacity factor. Integrated absorber/desorber CO_2 capture technology shows a lower capacity factor to achieve CO_2 avoided cost of \$68/t CO_2 than Fluor Ecoamine technology.

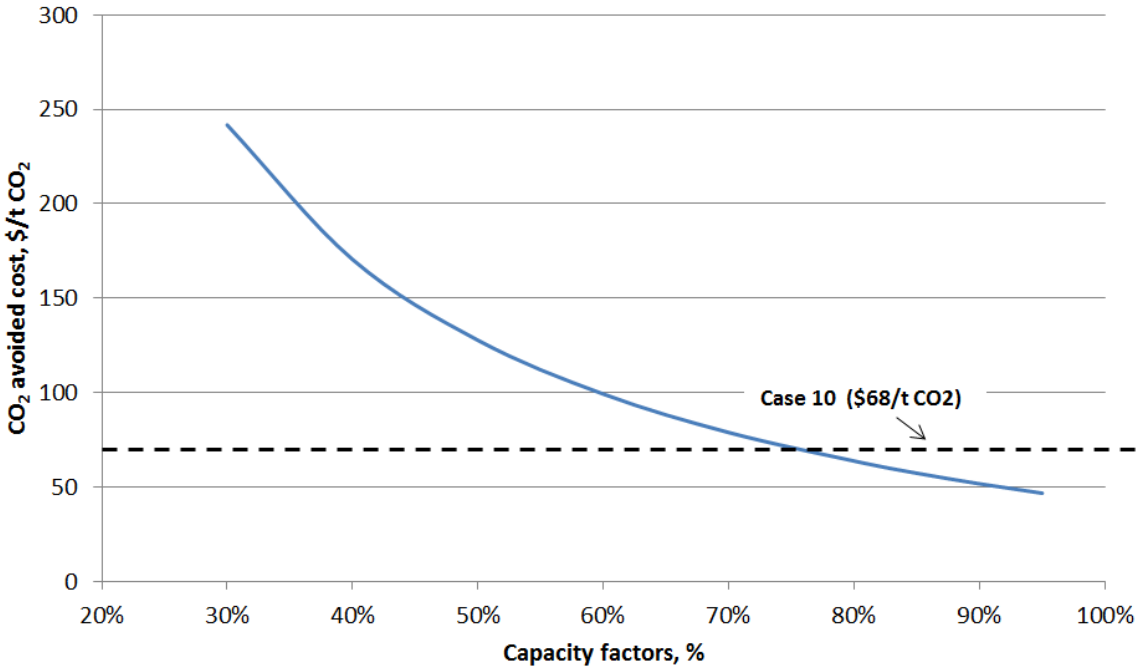

Fig. 8-21 The effect of capacity factor on CO_2 avoided cost (ceramic foam price: \$2780/m^3, catalytic performance: 60%, catalyst longevity: 30 years, coal cost: \$38.18/ton, waste heat availability: 0%)

8.5.7 Coal price

Fig.8-22 shows the sensitivity of COE to the coal price. Higher coal price results in the increase of COE. This is because the increase of fuel cost in COE. And it can be found that the variation of coal price will not affect the capital cost, only fuel cost is influenced by the coal price.

The percent increase of COE with coal price compared to DOE case 9 is described in Fig. 8-23. The solid blue line is the percent increase in COE as function of ceramic foam price. The red dash line represents DOE target, less than 35% increase in COE compared to case 9. The black dash line is the percent increase of COE in Case 10. About 86% increase of COE can be found for DOE case 10. The increase of coal price results in a higher COE compared to Case 9.

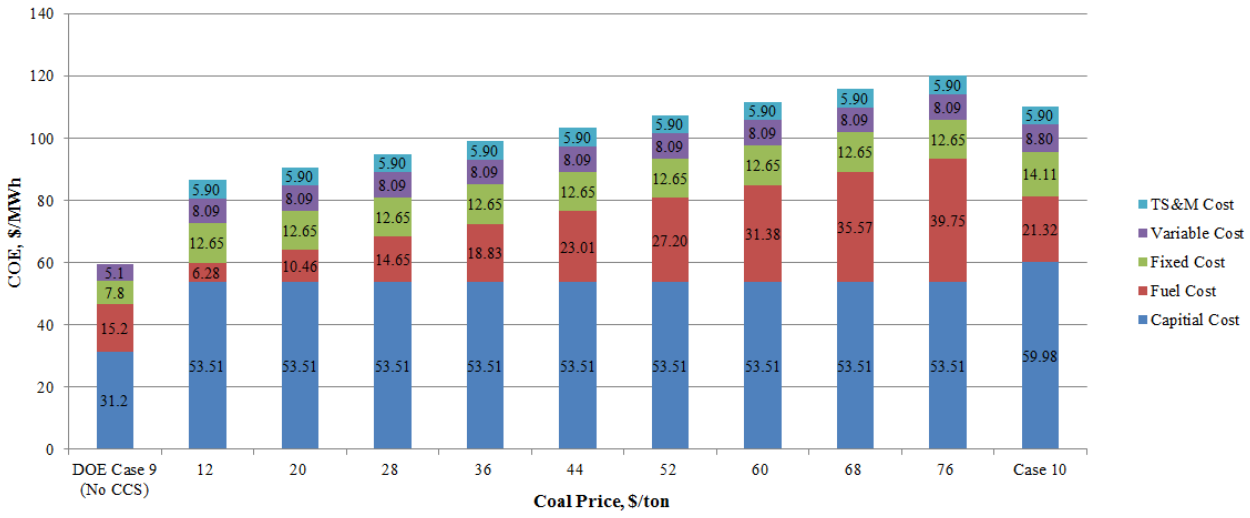

Fig.8-22 The sensitivity of COE to coal price (ceramic foam price: \$2780/m^3, catalytic performance: 60%, catalyst longevity: 30 years, capacity factor: 85%, waste heat availability: 0%)

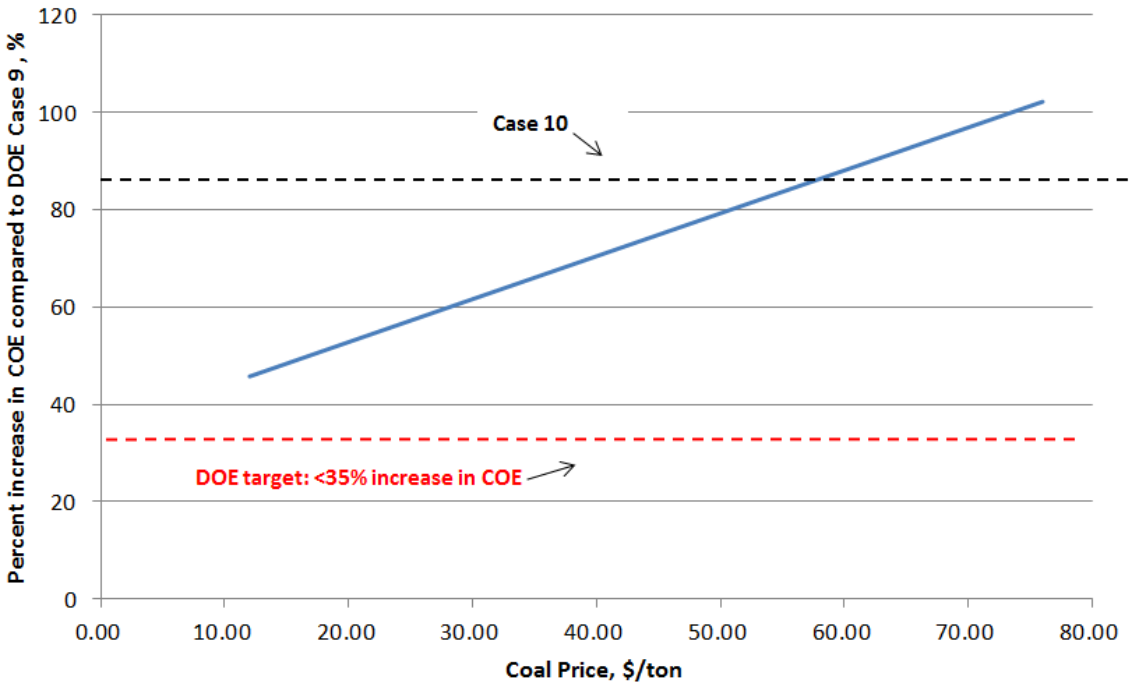

Fig.8-23 Increase in COE with coal price (ceramic foam price: \$2780/m^3, catalytic performance: 60%, catalyst longevity: 30 years, capacity factor: 85%, waste heat availability: 0%)

8.5.8 An optimal case of integrated absorber/desorber CO_2 capture

The target of DOE is to develop a CCS technology which has 90% CO_2 removal with no more than a 35% increase in COE. In order to achieve this goal, we try to optimize some parameters of integrated absorber/desorber technology to reach a reasonable COE that close to DOE's target. Fig. 8-24 shows an optimal case of

integrated absorber/desorber CO_2 capture technology. Two reference cases (DOE Case 9 and Case 10) are also presented to compare with this optimal case. In the optimal case, the ceramic foam price is \$500/m^3, catalytic performance is 200%, catalyst longevity is 30 years, capacity factor is 95%, waste heat availability is 90%, and coal price is \$38.18/ton. For optimal case, the COE is about \$82/MWh, equal to 75% of Case 10. The red dash line in Fig.5-19 is the DOE target. It can be found that the COE of optimal case is very close to DOE 'target.

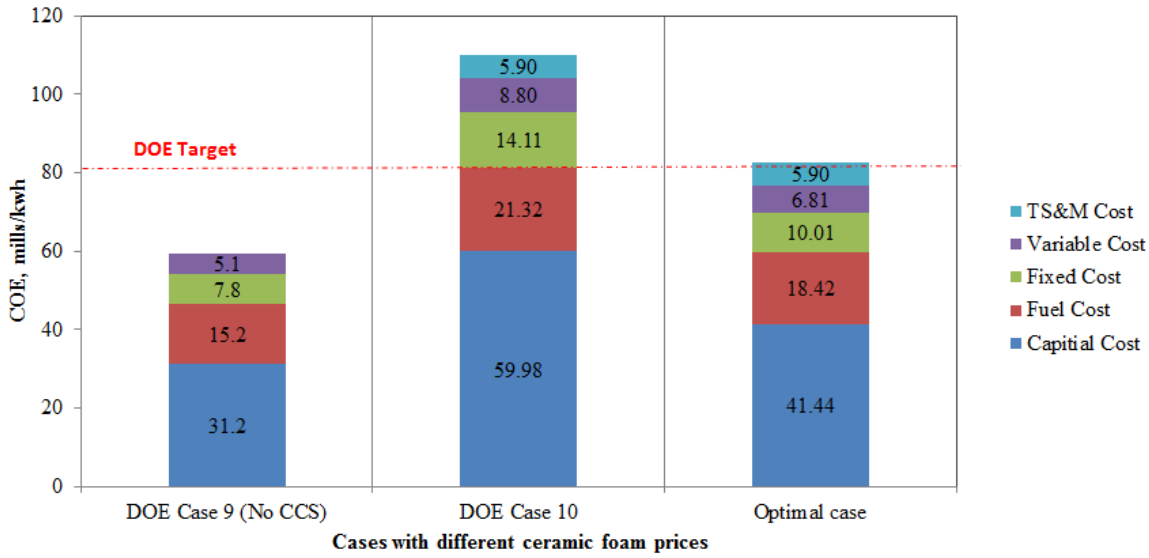

Fig. 8-24 Optimal case of integrated absorber/desorber CO_2 capture (ceramic foam price: \$500/m^3, catalytic performance: 200%, catalyst longevity: 30 years, capacity factor: 95%, waste heat availability: 90%, coal price: \$38.18/ton)

9. EH&S risk assessment study

This section is to present an environmental, health and safety (EH&S) risk assessment of this integrated absorber/desorber post-combustion CO_2 capture process. All potential gaseous, liquid and solid waste emissions from the process will be identified. For any potential hazards, an engineering analysis has been undertaken to identify ways in which they can be eliminated or minimized.

9.1 Process description

The flow diagram of subcritical PC plant with Rice University integrated absorber/desorber PCC process is shown in Fig. 9-1. In this process, SO_X and NO_X concentrations of the flue gas must be further reduced to approximately 10 ppmv to minimize formation of amine heat stable salts (HHS) during the CO_2 absorption process. After DeNO_X and FGD system, the flue gas will be sent to integrated absorber/desorber CO_2 capture system for CO_2 separation. IP/LP steam will be extracted from the steam line between IP turbine and LP turbine to regenerate the rich-amine, but it will lead to a loss of power output of the plant. In addition, CO_2 compression heat can be recovered for the steam turbine (ST) system to offset part of the power loss.

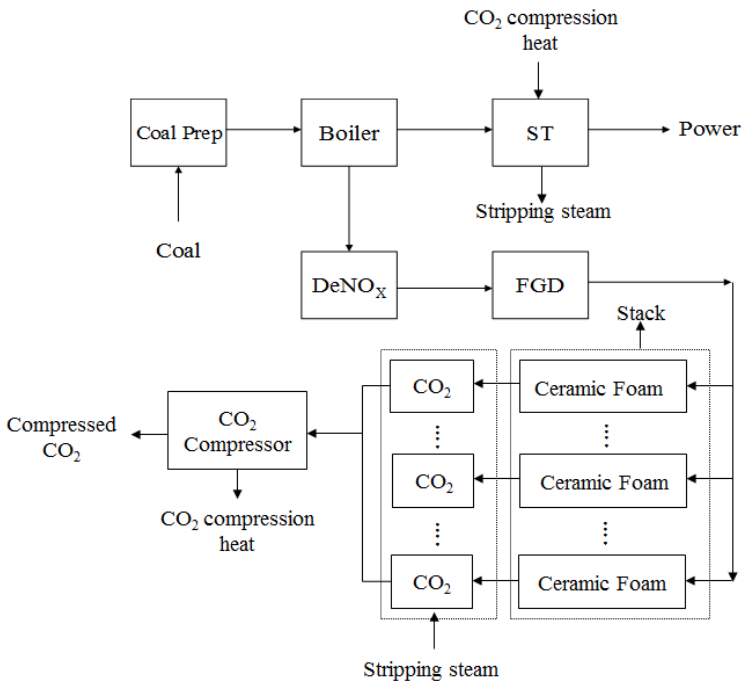

Fig.9-1 Subcritical PC plant with integrated absorber/desorber CO_2 capture process

Fig. 9-2 gives the detailed schematic diagram of integrated absorber/desorber CO_2 capture unit. Flue gas flows into the bottom of the absorption chamber was used as the flue gas stimulant. Absorbent solvent is delivered at the top of the absorption chamber from the solvent reservoir. The decarbonized flue gas exiting the absorption chamber emits to the atmosphere by stack. The absorbent after CO_2 absorption will flow into the desorber chamber for desorption. In order to facilitate the lateral flow of liquid from absorber to stripper, absorption chamber was pressurized and stripper chamber was operated at near-atmospheric pressure. The temperature in stripper side is around 100 C. Steam generated from the reboiler is

introduced into the bottom of stripping chamber for CO_2 desorption. The absorbent solvent after desorption then send back to the absorber chamber for next step absorption.

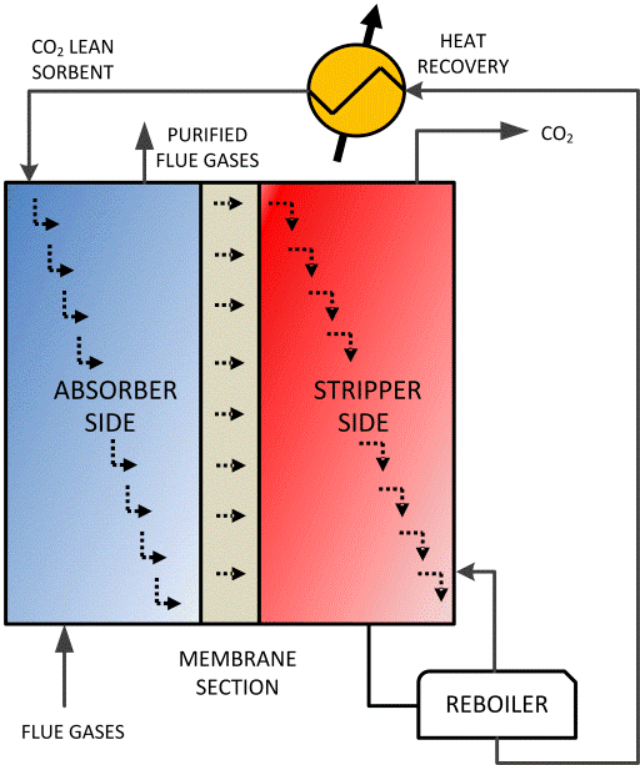

Fig. 9-2 Schematic diagram of integrated absorber/desorber CO_2 capture unit.

Figure 9-3 is the overview of the PCC process with potential species emissions. In this report, the emission during normal steady-state operation is only included, emissions during process upset conditions are not included. Amine absorbent is chosen as the CO_2 absorbent.

9.2 Gaseous emission

For the gaseous emission, all species are expected to be either emitted as a gas or entrained within the gas stream. The boiler is staged for low NO_X production using low NO_X burners (LNB) and overfired air (OFA) technologies and is fitted with SCR for NO_X abatement. In the SCR system, the reactor vessel is designed to allow an appropriate retention time for the ammonia to contact the NO_X in the boiler exhaust gas. Ammonia is injected into the gas immediately prior to entering the reactor vessel. The catalyst contained in the reactor vessel enhances the reaction between the ammonia and the NO_X in the gas. The ammonia storage and injection system consists of the unloading facilities, bulk storage tank, vaporizers, dilution air skid, and injection grid.

A forced oxidation limestone/gypsum wet FGD system that achieves a removal efficiency of 98 percent is installed after $DeNO_X$ unit to reach SO_2 emission standard. The FGD system is a wet limestone forced oxidation positive pressure absorber non-reheat unit, with wet-stack, and gypsum production. The FGD system consists of limestone handling and reagent preparation, FGD scrubber and byproduct dewatering. The calcium sulphate by-product in FGD system after dewatering will be sold as a plaster constituent.

Particulate emissions are controlled using a pulse jet fabric filter, which operates at an efficiency of 99.8 percent. Co-benefit mercury capture results in a 90 percent reduction of mercury emissions.

The integrated absorber/desorber PCC plant is designed to remove 90 percent of CO_2 from flue gas after Direct Contact Cooler (DCC). The captured CO_2 will be ultimately compressed and purified to become the CO2 product which can be utilized for enhanced oil recovery or storage.

The off-gas leaving the top of the absorption side through the stack is the main location that gaseous species and liquids entrained in gases can be emitted during normal operation. The gases are emitted from the absorber side off-gas stack at ambient pressure and a temperature of 40 ^{o}C. In addition to absorber side off-gas stack emissions, unplanned releases can occur from vents or loss of containment.

Nitrogen, argon, oxygen and moisture have been ignored among the species that leaving from the stack, since they are abundant in air and pose no EH&S risks at the plant operating conditions. The remaining expected gaseous species emissions are all similar to the levels that would be emitted from an equivalent PC power plant. An emission control system over the absorber is designed to avoid amine component carry-over and aerosol formation. The emission control system includes demisters and a wash column. The maximum concentration of amine components in the flue gas leaving the emission control system is 10 ppmv.

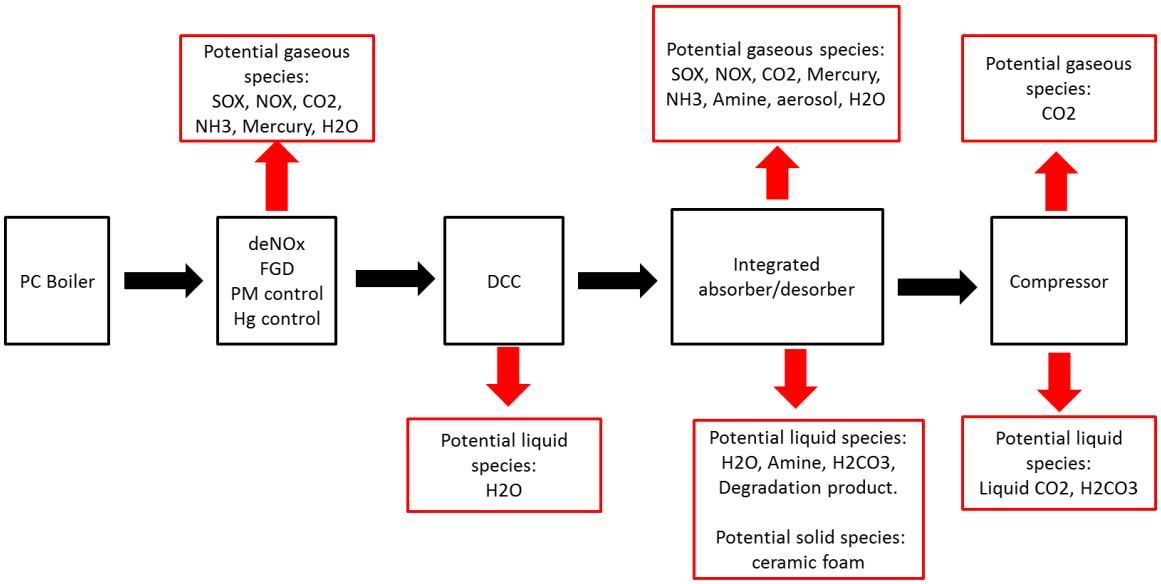

Fig. 9-3 overview of the PCC process with potential species emissions

9.3 Liquid emission

There are four potential sources that liquid emission may exist in the PCC plant. They are DCC system, emission control system (water wash stage) in absorber side, compressor inter-stage coolers and solvent reclaimer.

In the DCC system, the flue gas directly contacts with 40 ^{o}C spray water falling down. The moisture in the flue gas is condensed and leaves the bottom of the DCC along with the spray water. Due to a trace amount of flue gas acidic gases (e.g. SO_2, NO_2) presented in the condensate, these condensed water will be sent to treatment in the PC plant water demineralization plant.

In the emission control system of the CO_2 absorber, the flue gas exiting the absorber of PCC plant will be washed by a water wash loop system to removal any

droplets and aerosol, etc. These waste wash water will be also recycled by sending to water treatment plant for demineralization.

In the compressor inter-stage cooler, some condensate will be removed from pressured CO_2 product stream. These condensates may contain some acid components such as H_2CO3, they will also be sent to water treatment plant for demineralization.

Due to thermal and oxidative degradation of amine solvent, some requires replenishment with fresh amine and removal of produced waste slurry in the solvent reclaimer. The composition of these wet solid and slurry wastes cannot be confirmed; therefore they are usually removed from the plant by specialist contractor for appropriate off-site treatment and disposal.

9.4 Solid waste emission

Accumulated heat stable salts are the major potential for solid waste emission. These heat stable salts can be separated from the solvent by mechanical and activated carbon filters which installed within the solvent circulation loop. Periodic replacement of mechanical and activated carbon filters is required. The used filters disposal is provided by filter suppliers.

Table 9-1 identifies the potentially major emitted species, the sources of emissions, physical states of emissions, the EH&S effects of the species emitted, and the National Fire Protection Association (NFPA) 704 Standard System for the Identification of the Hazards of Materials for Emergency Response categorization.

The NFPA 704 Rating acts as a quick visual reference to the potential hazards with a rating of 0 (Least Hazardous) to 4 (Most Hazardous). The Diamond is formed of four colors - red, blue, yellow and white representing flammability, health, reactivity and any special notices, respectively.

Table 9-1 The list of potentially major emitted species in PCC plant.

Species	Source	State of species	Potential human health effect	Toxicity	Physical properties	NSPA Rating
Carbon dioxide	Stack CO_2 product gas stream Vents	Gas	■ Asphyxiant gas in large concentrations. ■ No harm to skin and eye contact.	Lowest Lethal concentration (LCLO) in humans = 90,000 ppm for 5 minutes	Colorless, odorless gas	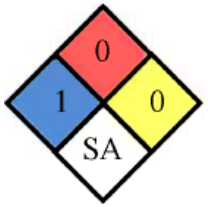
Oxides of Sulfur	Stack Vents	Gas	■ Highly toxic. ■ Life-threatening at high dosage, ■ May irritate eyes and cause inflammation. ■ May burn skin and aggravate existing dermatitis.	Median Lethal concentration (LC50) in rats = 2520 ppm for 1 hour	Colorless, choking gas with irritating odor.	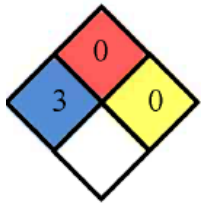
Oxides of Nitrogen	Stack Vents	Gas	■ Highly toxic. ■ May cause burns in presence of moisture. ■ Pulmonary damage and breathing difficulty can occur.	LC50 in rats =870 ppm for 4 hour	Colorless with irritating odor	
Ethanolamine	Reclaimer Stack Vents Drains	liquid	■ Monoethanolamine can cause eye and skin burns ■ Breathing monoethanolamine vapors can be irritating to the respiratory tract ■ Swallowing monoethanolamine can cause severe irritation or chemical burns of the mouth,	Inhalation mouse LC50=2420 mg/m3/2hr	colorless, viscous liquid with an odor reminiscent to that of ammonia	

			throat, esophagus, and stomach			
Mercury	Stack Vents Drains	gas	■ Causes chemical burns to the respiratory tract. ■ Irritation & possible burns. ■ May cause severe and permanent ■ damage to the digestive tract	LD50 = 25.9 mg/kg, rats	Odorless heavy liquid.	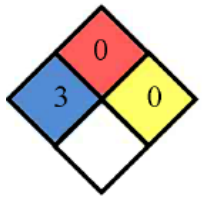

9.5 Management and mitigation

Management and mitigation of gaseous emissions is only considered to be required for the transient condition. For the normal steady-state operation, it is not required. Transient condition may result in more aerosol formation and foaming in PCC plant, which will cause more entrained components emission. The common approach to mitigate this phenomenon is using an emission control system (i.e. water wash column and demister) at the top of the absorber side. To reduce the foam formation, antifoam agent is also recommended to add into amine absorbent.

9.6 Handling and Storage

For gaseous substances, there are no requirements for bulk storage of gaseous substances foreseen as part of the PCC plant. For liquid and solid substances, it is proposed that all solvent is off-loaded in a designated area with its own drainage system to minimize any potential for uncontrolled emissions. Solvent is to be delivered by road tanker and the solvent storage vessels will have nozzles to which the tanker can connect before unloading to minimize the chance for any emissions. The reclaimer waste is passed to a reclaimer waste storage tank and loaded in a designated area with its own drainage system to minimize any potential for uncontrolled emissions. The reclaimer waste tanks will also have nozzles to which the tanker can connect before unloading to minimize the chance for any emissions.

9.7 Potential Risk

Risks associated with PCC plant design, operation, and maintenance, along with related mitigation approaches and actions to satisfy all existing EH&S regulations and guidelines are listed below:

- PCC plant operation safety- All the operators have to undergo a safety and

operation training before work;

- Chemical exposure- multiple eyes wash and emergency showers are required. Vents and blow downs should be located in a safe area. Relief valve, safety valve and other similar devices should be in proper size and installed properly. Alarm system for any chemical leaks during operation is required;
- Solvent handling and storage -Rigorous operating procedures including mandatory usage of Personal Protection Equipment (PPE)

10. Conclusion

In this project, we developed a new concept to capture CO_2 from power plant with lower capital and operating cost by combining absorber and stripper columns into a single, integrated process unit. Ceramic foams with highly-interconnected structures were chosen as the packing material for absorber and desorber. We investigated the hydrodynamic characteristics of α-Al_2O_3 ceramic foam and the performance of CO_2 absorption using aqueous 30 wt% DGA in a gas-liquid counter current column packed. Ceramic foams allowed for higher flow rates of gas and liquid to be used before flooding occurred, compared to random packings. Compared the CO_2-pickup performance of 20-, 30-, and 45-ppi alumina foam with that of 6-mm Raschig rings; also estimated the performance for 25-mm Raschig rings. Estimates show that 20-ppi ceramic foam has a better performance than the 25-mm Raschig rings. A 1-D mathematical model was further developed to simulate the hydrodynamic characteristics and CO_2 absorption performance of ceramic foam. The model predictions agreed well with the experimental results. This study demonstrated ceramic foams are a promising alternative to conventional random packings to improve CO_2 absorption using aqueous amines.

Based on this integrated absorber/ desorber concept, we designed a stainless steel prototype and a steam generator, suitable for conducting the proof-of-concept demonstration. CO_2 capture experiments were conducted in this bench-scale prototype with using 30 wt% diglycolamine and simulated flue gas. Based on the experimental results, it can be concluded that the concept of a performing CO_2 absorption and stripping in a single integrated unit is feasible. More than 90% CO_2 removal can be achieved using the combined absorber/stripper configuration. As a material itself, ceramic foam can be used as a gas-liquid contactor in the combined absorption and stripping unit.

We also developed a 2-D model to simulate gas and liquid flow in the capture process and compare simulation results with experimental measurements. The gas/liquid flow, temperature profile, pressure profile and CO_2 absorption/stripping were predicted. Additionally, an optimization and parametric study for the integrated absorber/desorber ceramic foam reactor, based on 2D model with using 30 wt.% MEA as absorbent were performed. The operating parameters include operating parameters such as CO_2 lean solvent loading, stripper operating temperature and gas flow rate to liquid flow rate ratio, and geometric parameters, such as stripper size, absorber/striper overlapping height and membrane thickness.

In terms of CO_2 catalytic desorption using solid catalysts, a series of materials were tested to enhance the decomposition of MEA-CO_2 complex during regeneration of MEA. Pure metal oxides MoO_3, V_2O_5, and WO_3 and supported metal oxide (on γ-Al_2O_3) have shown to be promising catalytic materials as they increased CO_2 release up to 70% during stripping of CO_2 from MEA. These materials being acidic in nature, catalyze the degradation of CO_2-MEA complex and subsequent release of CO_2. We have observed leaching of these materials. The lowest leaching was observed for WO_x/γ-Al_2O_3. It was found that γ-Al_2O_3 helps in mitigating this issue/problem. This shows that catalyst preparation method can be optimized to fully stop the leaching.

The techno-economic evaluation (TEA) of a subcritical PC power plant with integrated absorber/desorber ceramic foam CO_2 capture process was studied. Integrated absorber/desorber CO_2 capture shows a higher net plant efficiency of 30.10%, than conventional Fluor Econamine CO_2 capture (27.01%). In terms of COE, integrated absorber/desorber CO_2 capture presents a lower COE of 100.12 mills/kWh, than COE 110.11 mills/kWh of Fluor Econamine CO_2 capture. This

indicates integrated absorber/desorber CO_2 capture is a promising technology for future carbon capture from coal fired power plant.

A sensitivity studies based on integrated catalytic ceramic foam CO_2 capture process was performed in this report. Some parameters including prices of catalytic and non-catalytic ceramic foam, catalyst performance, catalyst longevity, waste heat availability, fuel cost and capacity factor, were varied to investigate their effects on COE, CPAEX and CO_2 avoided cost. With optimization of these parameters, $82/MWh of COE can be achieved with using integrated absorber/desorber CO_2 capture technology, which is very close to DOE's target that no more than a 35% increase in COE with CCS.

Environmental, health and safety risk assessment for integrated absorber/desorber post-combustion CO_2 capture plant was estimated. The potential emissions were found to pose no significant EH&S concerns. To reduce the risk of waste emission, some mitigation, handling and storage methods for potential emission have been proposed and described. However, due to this EH&S risk assessment is estimated based on lab-scale test and prediction, some uncertainties exist. Further work on a larger-scale test unit is recommended to reduce the uncertainties on EH&S risk assessment.

Appendix A

B.1 Viscosity of aqueous DGA solvent

The viscosity of aqueous DGA solution is calculated by following correlation that presented by Amr et al.[38].

$$\ln \mu/\mathrm{mPa \cdot s} = \ln \mu_0 + \sum_{k=1}^{n} a_k x_2^k \qquad \text{(B1)}$$

where is μ the viscosity of the binary solution, μ_W is the viscosity of pure water, and x is the mole fraction of DGA.

B.2 CO_2 diffusion coefficient in liquid phase

The diffusivity of CO_2 in DGA solutions was estimated using the modified Stokes-Einstein equation as follows[39]

$$D_{CO2} = D_{CO2,\mathrm{W}} \left(\frac{\mu_W}{\mu_L}\right)^{0.6} \qquad \text{(B2)}$$

where $D_{CO2,W}$ is the diffusivity of CO_2 in pure water, D_{CO2} is the diffusivity of CO_2 in DGA solutions, is μ_W the viscosity of pure water and μ_L is the viscosity of DGA solution.

CO_2 diffusivity $D_{CO2,W}$ in water can be expressed in the following equation ,

$$D_{CO2,W} = 2.35\times10^{-6}\times e^{(-2119/T)} \quad \text{(B3)}$$

For diffusivity of DGA in solvent, it was estimated by following equation[40]

$$D_{DGA} = 2.868\times10^{-12}\,\mu_L^{-0.449}T \quad \text{(B4)}$$

where D_{DGA} is diffusivity of DGA molecule in solvent, m^2/s, and T is temperature in K.

B.3 The Henry's constant for CO_2 in DGA solution

The Henry's law constant for CO_2 in aqueous DGA can be obtained using N_2O analogy[41].

$$H_{CO2,L} = H_{N_2O,L}(H_{CO_2,w} / H_{N_2O,w}) \quad \text{(B5)}$$

In which $H_{N_2O,L}$ is the Henry constant of N_2O in aqueous DGA, $H_{CO_2,W}$ and $H_{N_2O,W}$ are the Henry constant of CO_2 and N_2O in water, respectively.

$H_{CO_2,W}$ and $H_{N_2O,W}$ can be determined in the following equations provided by Versteeg et al.[42]:

$$H_{CO_2,w} = 2.82\times10^{6}\times e^{(-2044/T_L)} \quad \text{(B6)}$$

$$H_{N_2O,w} = 8.55\times10^{6}\times e^{(-2284/T_L)} \quad \text{(B7)}$$

The solubility of N_2O in pure amine solvent was proposed by Wang et al.[43] as follows:

$$H_{N_2O-\text{pure amine}} = b_1 \exp(b_2 / T) \quad \text{(B8)}$$

in which b_1 and b_2 are the parameter for calculating N_2O solubility in pure amine..

The N_2O solubility in the aqueous DGA can be estimated by correlating the excess Henry's coefficient in following correlation[44],

$$X = \ln H_{N_2O,L} - \sum_{i=1}^{n} \Phi_i \ln H_{N_2O,i} \quad \text{(B9)}$$

where Φ_i is the volume fraction of *i*th solvent X is excess Henry coefficient.

B.4 CO_2 diffusivity in gas phase

The diffusivity of gas B in gas F can be calculated by the Maxwell–Gilliland equation[45]

$$D_{\mathrm{B,F}} = \frac{4.36\times10^{-2} T_{\mathrm{G}}^{\,3/2} \sqrt{\dfrac{1}{M_{\mathrm{B}}} + \dfrac{1}{M_{\mathrm{F}}}}}{P\,(v_{\mathrm{F}}^{1/3} + v_{\mathrm{B}}^{1/3})^2} \quad \text{(B10)}$$

where $D_{B,F}$ is diffusion coefficient of gas B in Gas F; P is the pressure in gas phase in Pa; T_G is the gas phase temperature; M_B and M_F are the molecular weight of B and F; v_B and v_F are the molecular volume of gas B and F.

REFERENCES

1. Stemmet, C., et al., *Hydrodynamics of gas–liquid counter-current flow in solid foam packings.* Chemical engineering science, 2005. **60**(22): p. 6422-6429.

2. Caplow, M., *KINETICS OF CARBAMATE FORMATION AND BREAKDOWN.* Journal of the American Chemical Society, 1968. **90**(24): p. 6795-6803.

3. Danckwerts, P.V., *The reaction of CO2 with ethanolamines.* Chemical Engineering Science, 1979. **34**(4): p. 443-446.

4. Glasscock, D.A., J.E. Critchfield, and G.T. Rochelle, *CO2 ABSORPTION DESORPTION IN MIXTURES OF METHYLDIETHANOLAMINE WITH MONOETHANOLAMINE OR DIETHANOLAMINE.* Chemical Engineering Science, 1991. **46**(11): p. 2829-2845.

5. Versteeg, G.F. and W.P.M. Vanswaaij, *ON THE KINETICS BETWEEN CO2 AND ALKANOLAMINES BOTH IN AQUEOUS AND NON-AQUEOUS SOLUTIONS .1. PRIMARY AND SECONDARY-AMINES.* Chemical Engineering Science, 1988. **43**(3): p. 573-585.

6. Abu-Zahra, M.R.M., et al., *CO(2) capture from power plants. Part I. A parametric study of the technical-performance based on monoethanolamine.* International Journal of Greenhouse Gas Control, 2007. **1**(1): p. 37-46.

7. Phan, D.T., et al., *Catalysis of CO2 Absorption in Aqueous Solution by Inorganic Oxoanions and their Application to Post Combustion Capture.* Environmental Science & Technology, 2014. **48**(8): p. 4623-4629.

8. Liu, Q., et al., *Kinetics Studies of CO2 Adsorption/Desorption on Amine-Functionalized Multiwalled Carbon Nanotubes.* Industrial & Engineering Chemistry Research, 2014. **53**(29): p. 11677-11683.

9. Liu, J.Z., et al., *Study on mass transfer and kinetics of CO2 absorption into aqueous ammonia and piperazine blended solutions.* Chemical Engineering Science, 2012. **75**: p. 298-308.

10. Leon, M., et al., *A kinetic study of CO2 desorption from basic materials: Correlation with adsorption properties.* Chemical Engineering Journal, 2011. **175**: p. 341-348.

11. Bishnoi, S. and G.T. Rochelle, *Absorption of carbon dioxide into aqueous piperazine: reaction kinetics, mass transfer and solubility.* Chemical Engineering Science, 2000. **55**(22): p. 5531-5543.

12. Nicholas, N.J., et al., *Use of Vanadium(V) Oxide as a Catalyst for CO2 Hydration in Potassium Carbonate Systems.* Industrial & Engineering Chemistry Research, 2014. **53**(8): p. 3029-3039.
13. Conway, W., et al., *Comprehensive Kinetic and Thermodynamic Study of the Reactions of CO2(aq) and HCO3- with Monoethanolamine (MEA) in Aqueous Solution.* Journal of Physical Chemistry A, 2011. **115**(50): p. 14340-14349.
14. Boettinger, W., M. Maiwald, and H. Hasse, *Online NMR spectroscopic study of species distribution in MEA-H2O-CO2 and DEA-H2O-CO2.* Fluid Phase Equilibria, 2008. **263**(2): p. 131-143.
15. Rochelle, G., et al., *Aqueous piperazine as the new standard for CO2 capture technology.* Chemical Engineering Journal, 2011. **171**(3): p. 725-733.
16. Cantillo, D. and C.O. Kappe, *Immobilized Transition Metals as Catalysts for Cross-Couplings in Continuous Flow-A Critical Assessment of the Reaction Mechanism and Metal Leaching.* Chemcatchem, 2014. **6**(12): p. 3286-3305.
17. Jha, M.K., et al., *Hydrometallurgical recovery/recycling of platinum by the leaching of spent catalysts: A review.* Hydrometallurgy, 2013. **133**: p. 23-32.
18. Epifani, M., et al., *Metal Oxide Nanocrystals from the Injection of Metal Oxide Sols in a Coordinating Environment: Principles, Applicability, and Investigation of the Synthesis Variables in the Case Study of CeO2 and SnO2.* Chemistry of Materials, 2009. **21**(5): p. 862-870.
19. Parks, G.A., *ISOELECTRIC POINTS OF SOLID OXIDES SOLID HYDROXIDES AND AQUEOUS HYDROXO COMPLEX SYSTEMS.* Chemical Reviews, 1965. **65**(2): p. 177-&.
20. Somasundaran, P., *Encyclopedia of Surface and Colloid Science*. 2006, Crc Press.
21. Lee, S.C., et al., *Development of regenerable MgO-based sorbent promoted with K2CO3 for CO2 capture at low temperatures.* Environmental Science & Technology, 2008. **42**(8): p. 2736-2741.
22. Al-Juaied, M. and G.T. Rochelle, *Absorption of CO2 in aqueous diglycolamine.* Industrial & engineering chemistry research, 2006. **45**(8): p. 2473-2482.
23. Pacheco, M.A., S. Kaganoi, and G.T. Rochelle, *CO< sub> 2</sub> absorption into aqueous mixtures of diglycolamine< sup>®</sup> and methyldiethanolamine.* Chemical engineering science, 2000. **55**(21): p. 5125-5140.

24. Alper, E., *Kinetics of reactions of carbon dioxide with diglycolamine and morpholine.* The Chemical Engineering Journal, 1990. **44**(2): p. 107-111.
25. Littel, R., et al., *Modelling of simultaneous absorption of H< sub> 2</sub> S and CO< sub> 2</sub> in alkanolamine solutions: The influence of parallel and consecutive reversible reactions and the coupled diffusion of ionic species.* Chemical engineering science, 1991. **46**(9): p. 2303-2313.
26. Al-Juaied, M. and G.T. Rochelle, *Thermodynamics and equilibrium solubility of carbon dioxide in diglycolamine/morpholine/water.* Journal of Chemical & Engineering Data, 2006. **51**(2): p. 708-717.
27. Edwards, T., et al., *Vapor‐liquid equilibria in multicomponent aqueous solutions of volatile weak electrolytes.* AIChE Journal, 1978. **24**(6): p. 966-976.
28. ASPEN, P., *V7. 2.* Burlington: Aspen Technology, 2010.
29. Maurer, G. *On the solubility of volatile weak electrolytes in aqueous solutions*. in *ACS Symp. Ser*. 1980.
30. Dankworth, D.C. and S. Sundaresan, *A macroscopic model for countercurrent gas‐liquid flow in packed columns.* AIChE journal, 1989. **35**(8): p. 1282-1292.
31. Saez, A. and R. Carbonell, *hydrodynamic parameters for gas‐liquid cocurrent flow in packed beds.* AIChE Journal, 1985. **31**(1): p. 52-62.
32. Stemmet, C., et al., *Solid foam packings for multiphase reactors: modelling of liquid holdup and mass transfer.* Chemical Engineering Research and Design, 2006. **84**(12): p. 1134-1141.
33. Thomeer, J., *Introduction of a pore geometrical factor defined by the capillary pressure curve.* Journal of Petroleum Technology, 1960. **12**(03): p. 73-77.
34. Leverett, M., W. Lewis, and M. True, *Dimensional-model studies of oil-field behavior.* Transactions of the AIME, 1942. **146**(01): p. 175-193.
35. Rocha, J.A., J.L. Bravo, and J.R. Fair, *Distillation columns containing structured packings: a comprehensive model for their performance. 1. Hydraulic models.* Industrial & engineering chemistry research, 1993. **32**(4): p. 641-651.
36. Maćkowiak, J., *Model for the prediction of liquid phase mass transfer of random packed columns for gas–liquid systems.* Chemical Engineering Research and Design, 2011. **89**(8): p. 1308-1320.

37. Longo, G.A. and A. Gasparella, *Experimental and theoretical analysis of heat and mass transfer in a packed column dehumidifier/regenerator with liquid desiccant.* International Journal of Heat and Mass Transfer, 2005. **48**(25): p. 5240-5254.
38. Kister, H.Z., et al., *Realistically predict capacity and pressure drop for packed columns.* AIChe CEP, 2007: p. 28-38.
39. Koonaphapdeelert, S., Z. Wu, and K. Li, *Carbon dioxide stripping in ceramic hollow fibre membrane contactors.* Chemical Engineering Science, 2009. **64**(1): p. 1-8.
40. Kvamsdal, H.M. and G.T. Rochelle, *Effects of the temperature bulge in CO2 absorption from flue gas by aqueous monoethanolamine.* Industrial & Engineering Chemistry Research, 2008. **47**(3): p. 867-875.
41. Mangalapally, H.P., et al., *Pilot plant experimental studies of post combustion CO2 capture by reactive absorption with MEA and new solvents.* Energy Procedia, 2009. **1**(1): p. 963-970.

PRODUCTS

a. PUBLICATIONS, CONFERENCE PAPERS AND PRESENTATIONS

Publications:

1) Warudkar S S, Cox K R, Wong M S, et al. Influence of stripper operating parameters on the performance of amine absorption systems for post-combustion carbon capture: Part I. High pressure strippers[J]. International Journal of Greenhouse Gas Control, 2013, 16: 342-350.

2) Warudkar S S, Cox K R, Wong M S, et al. Influence of stripper operating parameters on the performance of amine absorption systems for post-combustion carbon capture: Part II. Vacuum strippers [J]. International Journal of Greenhouse Gas Control, 2013, 16: 351-360.

3) Wang Z, Gupta M, Warudkar S S, et al. Improved CO2 Absorption in a Gas-Liquid Counter Current Column using a Ceramic Foam Contactor[J]. Industrial & Engineering Chemistry Research, 2016, *55* (5): 1387–1400.

These 3 publications are attached after the final report.

To be published:

1) A manuscript on catalytic desorption of CO_2 is in preparation.
(Title: Improved CO_2 Capture Techonolgy with a Low Temperature Catalytic Desorption; Authors: Mayank Gupta, Zhen Wang, Colin Shaw and Michael S. Wong*.)

2) A manuscript on CO_2 absorption in integrated absorber/desorber unit is in preparation. (Title: Cost reduction of CO_2 capture with using novel integrated absorber/desorber unit)

Presentations:

"Combined Pressure and Temperature Contrast and Surface-Enhanced Separation of Carbon Dioxide for Post-Combustion Carbon Capture," 2015 NETL CO_2 Capture Technology Meeting, Pittsburgh, PA, June, 2015.
https://www.netl.doe.gov/File%20Library/Events/2015/co2captureproceedings/Z-Wang-Rice-U-Combined-Pressure--Temperature--and-Surface-Enhanced-CO2-Separation.pdf

"Combined Pressure and Temperature Contrast and Surface-Enhanced Separation of Carbon Dioxide for Post-Combustion Carbon Capture," 2014 NETL CO_2 Capture Technology Meeting, Pittsburgh, PA, July 2014. http://www.netl.doe.gov/File%20Library/Events/2014/2014%20NETL%20CO2%20Capture/M-Wong-Rice-Combined-Separation-of-CO2-.pdf.

"Combined Pressure and Temperature Contrast and Surface-Enhanced Separation of Carbon Dioxide for Post-Combustion Carbon Capture," 2012 NETL CO_2 Capture Technology Meeting, Pittsburgh, PA, July 2012. http://www.netl.doe.gov/File%20Library/events/2012/CO2%20capture%20meeting/G-Hirasaki-Rice-Combined-Separations.pdf.

"Combined Pressure and Temperature Contrast and Surface-Enhanced Separation of Carbon Dioxide for Post-Combustion Carbon Capture," Project Kick-Off Meeting, November 2011. http://www.netl.doe.gov/File%20Library/Research/Coal/ewr/CO2/Rice-DOE-Kick-off-Meeting-Presentation-Nov-7-8-2011_sanitize.pdf.

b. WEBSITE(S) OR OTHER INTERNET SITE(S)

Nothing to report

c. TECHNOLOGIES OR TECHNIQUES

Nothing to report

d. INVENTIONS, PATENT APPLICATIONS, AND/OR LICENSES

United States Provisional Patent Application: CO2 CAPTURE WITH AMINES AND METAL OXIDES

EXHIBIT 1: MILESTONE STATUS REPORT

Tasks	Milestone Title/Description	Planned Completion Date	Actual Completion Date	Verification Method	Comments (Progress toward achieving milestone, explanation of deviation from plan, etc.)
1	Complete update of Project Management Plan	10/31/2011	1/25/2012	Project Management Plan file	n/a
1	Complete Kick-off Meeting	12/15/2011	11/7/2011	Briefing Document & Meeting Results	n/a
2	Complete preliminary Technical and Economic Feasibility Study	5/31/2012	5/30/2012	Submission of – Preliminary Technical and Economic Feasibility Study	Completed
3	Complete Gas-liquid heat and mass transfer studies on unfunctionalized ceramic foam	5/1/2012	5/1/2012	Quarterly and annual reports	Completed
4	Complete design, fabrication, and setup of the stainless steel prototype of the combined absorption/desorption unit.	9/30/2012	3/31/2013	Photographs of assembled stainless steel experimental prototype	Completed
5	Complete CO_2 capture demonstration using the stainless steel prototype to demonstrate that CO_2 absorption from a CO_2/N_2 mixture can be achieved in the combined absorber/desorber setup	12/31/2012	3/31/2013	Quarterly and annual reports	Completed

6	Catalytic desorption of CO_2 using metal oxides	12/15/2014	12/31/2014	Quarterly and annual reports	Completed
7	Kinetic analysis of CO_2 desorption	12/15/2014	3/31/2015	Quarterly and annual reports	Completed
8	Complete Process modeling and simulation – 1D model	8/31/14	6/30/2014	Quarterly and annual reports	Completed
8	Complete Process modeling and simulation – 2D model	10/30/2014	9/1/2014	Quarterly and annual reports	Completed
9	Complete Technical and Economic Feasibility Study	12/31/2014 (amended from 8/31/14)	9/30/2015	Submission of – Final Technical and Economic Feasibility Study	Completed
10	Complete Technology EH&S Risk Assessment	12/31/2014 (amended from 9/30/14)	12/31/2015	Submission of EH&S Risk Assessment study	Completed

EXHIBIT 2: PROJECT COST PLAN/STATUS

Baseline Reporting Quarter	Budget Period 1							
	10/1/11 - 12/31/11		1/1/12 - 3/31/12		4/1/12 - 6/30/12		7/1/12 - 9/30/12	
	Quarter	Project Total	Quarter	Project Total	Quarter	Project Total	Quarter	Project Total
Baseline Cost Plan								
Federal Share	60,905	60,905	60,905	121,810	60,905	182,715	60,906	243,621
Non-Federal Share	22,368	22,368	22,368	44,736	22,368	67,104	22,369	89,473
Total Planned	83,273	83,273	83,273	166,546	83,273	249,819	83,275	333,094
Actual Incurred Cost								
Federal Share	28,386	28,386	51,063	79,449	83,313	162,762	59,466	222,228
Non-Federal Share	17,832	17,832	23,513	41,345	14,977	56,322	8,400	64,722
Total Incurred Costs	46,218	46,218	74,576	120,794	98,290	219,084	67,866	286,950
Variance								
Federal Share	32,519	32,519	9,842	42,361	(22,408)	19,953	1,440	21,393
Non-Federal Share	4,536	4,536	(1,145)	3,391	7,391	10,782	13,969	24,751
Total Variance	37,055	37,055	8,697	45,752	(15,017)	30,735	15,409	46,144

Baseline Reporting Quarter	Budget Period 2							
	10/1/12 - 12/31/12		1/1/13 - 3/31/13		4/1/13 - 6/30/13		7/1/13 - 9/30/13	
	Quarter	Project Total	Quarter	Project Total	Quarter	Project Total	Quarter	Project Total
Baseline Cost Plan								
Federal Share	81,892	325,513	81,892	407,405	81,892	489,297	81,892	571,189
Non-Federal Share	12,837	102,310	12,837	115,147	12,837	127,984	12,837	140,821
Total Planned	94,729	427,823	94,729	522,552	94,729	617,281	94,729	712,010
Actual Incurred Cost								
Federal Share	48,888	271,116	63,221	334,337	107,445	441,782	61,632	503,414
Non-Federal Share	16,921	81,643	3,280	84,923	9,313	94,236	4,347	98,583
Total Incurred Costs	65,809	352,759	66,501	419,260	116,758	536,018	65,979	601,997
Variance								
Federal Share	33,004	54,397	18,671	73,068	(25,553)	47,515	20,260	67,775
Non-Federal Share	(4,084)	20,667	9,557	30,224	3,524	33,748	8,490	42,238
Total Variance	28,920	75,064	28,228	103,292	(22,029)	81,263	28,750	110,013

Baseline Reporting Quarter	Budget Period 2	
	10/1/13 - 12/31/13	
	Quarter	Quarter
Baseline Cost Plan		
Federal Share	0	571,189
Non-Federal Share	0	140,821
Total Planned	0	712,010
Actual Incurred Cost		
Federal Share	55,698	559,112
Non-Federal Share	8,668	107,251
Total Incurred Costs	64,366	666,363
Variance		
Federal Share	(55,698)	12,077
Non-Federal Share	(8,668)	33,570
Total Variance	(64,366)	45,647

Baseline Reporting Quarter	Budget Period 3							
	1/1/14 - 3/31/14		4/1/14 - 6/30/14		7/1/14 - 9/30/14		10/1/14 - 12/31/14	
	Quarter	Project Total	Quarter	Project Total	Quarter	Project Total	Quarter	Project Total
Baseline Cost Plan								
Federal Share	49,364	620,553	49,364	669,917	81,892	571,189	49,365	768,647
Non-Federal Share	12,836	153,657	12,836	166,493	12,837	140,821	12,835	192,163
Total Planned	62,200	774,210	62,200	836,410	94,729	712,010	62,200	960,810
Actual Incurred Cost								
Federal Share	0	559,112	1,483	560,595	58,130	618,725	69,676	688,401
Non-Federal Share	0	107,251	13,008	120,259	3,854	124,113	31,573	155,686
Total Incurred Costs	0	666,363	14,491	680,854	61,984	742,838	101,249	844,087
Variance								
Federal Share	49,364	61,441	47,881	109,322	(8,765)	100,557	(20,311)	80,246
Non-Federal Share	12,836	46,406	(172)	46,234	8,891	55,215	(18,738)	36,477
Total Variance	62,200	107,847	47,709	155,556	216	155,772	(39,049)	116,723

Baseline Reporting Quarter	Budget Period 3 (Non-cost Extension)							
	1/1/15 - 3/31/15		4/1/15 - 6/30/15		7/1/15 - 9/30/15		10/1/15 - 12/31/15	
	Quarter	Project Total	Quarter	Project Total	Quarter	Project Total	Quarter	Project Total
Baseline Cost Plan								
Federal Share	0	768,647	0	768,647	0	768,647	0	768,647
Non-Federal Share	0	192,163	0	192,163	0	192,163	0	192,163
Total Planned	0	960,810	0	960,810	0	960,810	0	960,810
Actual Incurred Cost								
Federal Share	21,572	709,973	23,214	733,187	21,098	754,285	14,362	768,647
Non-Federal Share	11,644	167,330	22,716	190,046	1,358	191,404	759	192,163
Total Incurred Costs	33,216	877,303	45,930	923,233	22,456	945,689	15,121	960,810
Variance								
Federal Share	(21,572)	58,674	(23,214)	35,460	(21,098)	14,362	(14,362)	0
Non-Federal Share	(11,644)	24,833	(22,716)	2,117	(1,358)	759	(759)	0
Total Variance	(33,216)	83,507	(45,930)	37,577	(22,456)	15,121	(15,121)	0